A SIMULATION TOOL FOR THE ANALYSIS AND DESIGN OF LEAKY WAVE ANTENNAS IN LATERALLY SHIELDED PLANAR TECHNOLOGY WITH APPLICATION TO METAMATERIALS

by

MARTA PADILLA PARDO

Supervisor: Professor J.(Yiannis) C. Vardaxoglou

September 2011

Wireless Communications Research Group (WiRC)

SCHOOL OF ELECTRONIC, ELECTRICAL AND SYSTEMS ENGINEERING

Loughborough University

Loughborough University

CERTIFICATE OF ORIGINALITY

This is to certify that I, Marta Padilla Pardo, am responsible for the work submitted in this thesis, that the original work is my own except as specified in acknowledgements or in references, and that neither the thesis nor the original work contained therein has been submitted to this or any other institution for a higher degree.

…… (Signed)

…… (Date)

To my Mother,

who taught me pain is often unavoidable

but suffering is optional.

ABSTRACT

Leaky-waves have been a topic of increasing interest in the last years, with diverse practical applications in many different engineering fields. From periodic, FSS, EBG or even metamaterial leaky-wave based antennas to waveguide filters and higher efficiency energy guiding, they all share a common base structure: a travelling-wave propagating within a metal encapsulation, which can be open or closed, and altered by a planar metallization of periodic nature, from which the energy may radiate. Due to the fact that these antennas are usually electrically large and the periodic printed circuit requires a certain grade of complexity, simulations of such antennas using 3D commercial software are prohibitively time consuming. Also, the homebrew methods developed up to this day are either not rigorous and accurate enough or unable to deal with complex periodic geometries. At this point, the evolution of leaky-wave antennas needs a solid, efficient and versatile tool where to base the future design research on.

In this work a novel simulation tool for waveguide embedded leaky-wave antennas is presented. It is based on a full-wave Method of Moments applied to the spectral domain Green Functions for a rigorous modal analysis of the finite structure. The use of Subdomain basis functions allows the software to model complex periodic geometries, overcoming a main limitation, and the analytical nature of the method combined with its 2.5D approach, results in a significant computing time reduction. It is built on a modular coding philosophy and provided with a user-friendly graphical interface, and an intuitive working procedure, making the program not only fast and accurate, but also easy to use and extendable to new geometries. Finally, the educational potential of this new analysis software is remarkable, since it identifies higher order effects such as bandgaps and multi-harmonic radiation from a complete and simple modal approach.

KEYWORDS

Leaky-wave antennas, periodic antennas, simulation tool, Method of Moments, FSS, EBG, computer aided design.

A SIMULATION TOOL FOR THE ANALYSIS AND DESIGN OF LEAKY WAVE ANTENNAS IN LATERALLY SHIELDED PLANAR TECHNOLOGY WITH APPLICATION TO METAMATERIALS

INDEX

CHAPTER 1 - INTRODUCTION

Where the reader gets in contact with the basic knowledge necessary to situate this work in its proper background and to ease the full understanding of the concepts that will come in following chapters.

1.1. Leaky Waves and Antennas: Review.

Leaky wave antennas belong to the category of **TRAVELLING WAVE ANTENNAS (**[Walter 1965] and [Milligan 2005] ch. 10), together with *surface wave antennas* and *slot arrays*. This whole family is based on the radiation of a propagative mode in a basic guiding structure (usually a waveguide of some sort), but the radiation mechanism changes drastically from one sub-category to another. The longitudinal propagation constant of any mode propagating along any waveguide is:

$$k_y = \beta_y - j\alpha_y$$

where β is the **phase constant** in rad/m, and α is the **attenuation constant** in nep/m, that accounts for both radiation and material losses, if existing any of them. As will be seen in detail in Chapter 2, the expression for the propagation constant in the transversal direction, i.e., into free space, is given by:

$k_z = \sqrt{k_0^2 - k_y^2}$ that can be either $k_z = -j\alpha_z$ → slow-wave or **surface-wave**

$k_z = \beta_z$ → fast-wave or **leaky-wave**

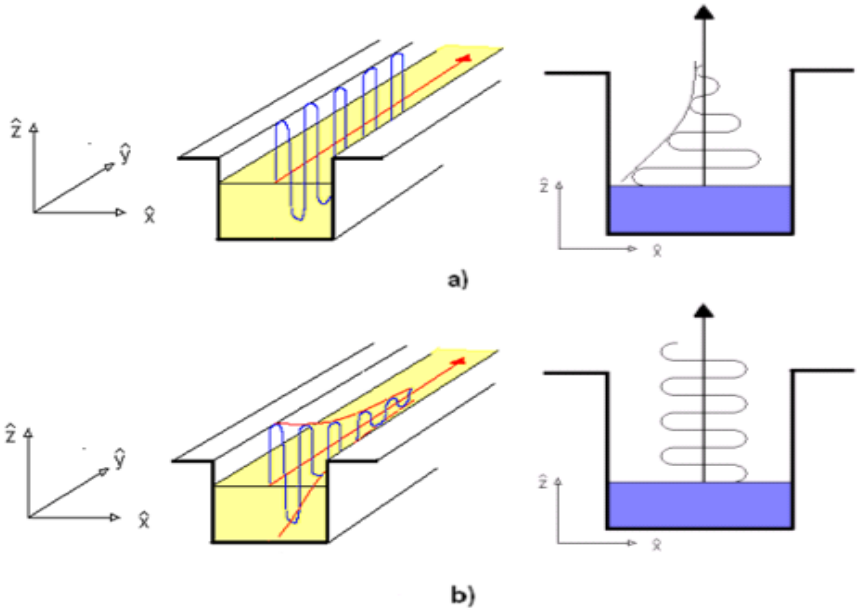

Figure 1.1.1 Longitudinal and transversal fields: a) Surface wave and b) Leaky wave.

Surface-wave modes propagate energy along the longitudinal direction in dielectric waveguides, with only the losses related to the material, which will be considered as none from now on, for simplicity's sake. This way, the longitudinal propagation constant is $k_y = \beta_y$ and $k_z = -j\alpha_z$, meaning the fields surrounding the guide are reactive, decaying exponentially in the transversal direction and producing no radiation (see Figure 1.1.1 a). The only way a surface-wave may radiate is at curvatures or at resistive discontinuities, which can exist in an open waveguide, for example at its very end, in contrast with the either inductive or capacitive discontinuities in closed waveguides. This property was applied to the dielectric waveguide to obtain the so called **surface-wave antennas,** which are basically end-fire antennas. An excellent overview of these type of structures can be found in [Johnson 1993], ch. 12 and [Volakis 2007] ch. 10, both written by F.J. Zucker.

Leaky-wave modes radiate while propagating along the structure. Leaky waves have been extensively treated in the literature, [Tamir 1963-I] [Tamir 1963-II] [Johnson 1993] [Volakis 2007] [Balanis 2008]. A. Oliner defines a **leaky-wave antenna (LWA)** as a waveguiding structure that possesses a mechanism that permits it to leak power all along its length. The propagation constant is now complex, $k_y = \beta_y - j\alpha_y$, counting now with an attenuation constant that correspond to the energy leakage per unit length, see Figure 1.1.1 b). The propagation features in its longitudinal direction are defined by its phase constant β and its leakage constant α. The value of the phase constant will determine the radiation angle θ_m, also, large values of the leakage constant will produce short effective apertures and broad beams, while low values of α will result in very narrow beams, provided the antenna is long enough. These two parameters depend on the frequency and the cross-sectional geometry. Once are known, the radiation features for an antenna of length L_{WG} can be directly obtained by a set of very simple approximations:

$$\sin\theta_m \approx \frac{\beta_y}{k_0} \tag{1.1.1}$$

$$\Delta\theta \approx \frac{1}{(L/\lambda_0)\cos\theta_m} \tag{1.1.2}$$

Where θ_m is the angle of maximum of the beam, measured from broadside direction, $\Delta\theta$ is the beamwidth and the k_0 is the free-space wavenumber. The directivity of the antenna depends mainly on the length, but also on the value of the attenuation constant along said length, which will determine the aperture illumination. It is also well-known the **scan-angle behaviour** with frequency of LWA. They start scanning at broadside right above cut-off and the pointing angle moves towards endfire as the frequency increases.

One important aspect about leaky waves is its **'improper' or 'nonspectral' behaviour,** observed in [Goldstone 1959] . By examining the wavenumbers, it can be seen how the amplitude of the forward leaky wave increases transversely away from the aperture of the guiding structure, which mean that the radiation at the infinite will not be zero, but extremely more intense than in the origin. This obviously, violates a basic physical law in

electromagnetics, but there is a simple explanation for this phenomenon [Balanis 2008] based on the ray diagram in Figure 1.1.2. In this plot, the closer the rays are, the higher level of the power flow in the direction of the arrows, so in the case of the forward wave, this power increases exponentially as the observation point moves vertically further from the structure.

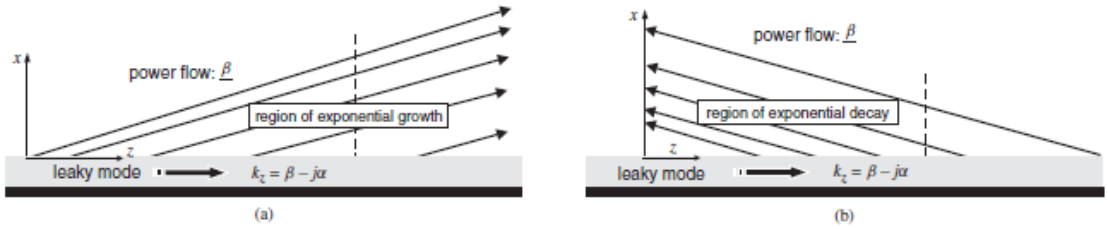

Figure1.1.2 Ray interpretation for leaky-waves [Balanis 2008].
a)Fordward wave and b) Backward wave.

In the real case, when a feeding is considered as the source point, a '*shadow boundary*' exists, where this improper nature indeed occurs. But above the limit of this boundary, $\theta > \theta_m$, the field level decreases very quickly, being consistent with the radiation condition at infinite. This is shown in Figure 1.1.3, where the '*shadow boundary*' (a) and a contour plot (b) of the field magnitude for a LWA radiating at $\theta_m = 30^o$ with an $\frac{\alpha_y}{k_0} = 0.02$ is calculated.

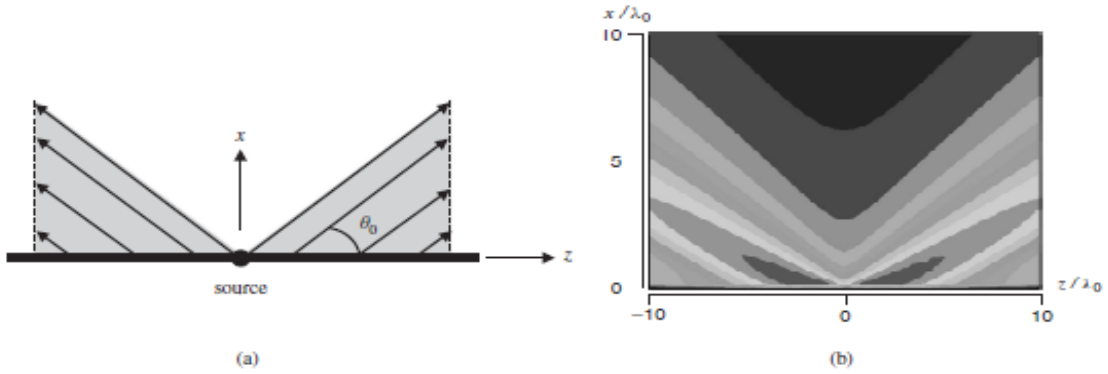

Figure 1.1.3 Real case with a feeding source [Balanis 2008].
a) Shadow boundary and b) Field magnitude.

Regarding the radiation, as previously mentioned, it is determined by the values of β_y and α_y, and depends on the frequency and the geometrical cross-section of the open waveguide. For a LWA with its geometrical parameters uniform along its length, α_y and β_y do not change and the aperture distribution has an exponential illumination. This corresponds with a high side lobe level for high directivity, since the antenna cannot be extremely long. It is therefore desirable some kind of **tapering on the antenna**, to control the alpha along the longitudinal direction by modifying geometrical parameters while maintaining beta constant, in order to obtain a specific aperture illumination with a convenient sidelobe performance.

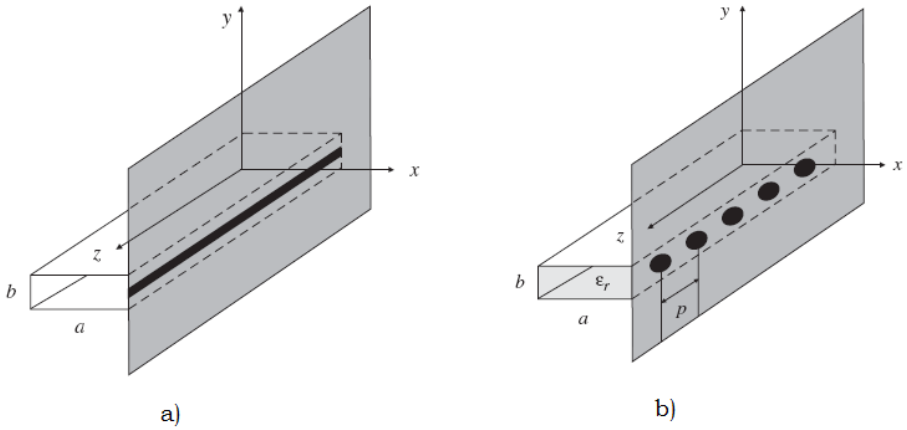

Figure 1.1.4 First LWAs [Balanis 2008]. a) Inset of Hansen and b) Holey WG.

Leaky-wave antennas can be classified following several criteria, the most important being the distinction between uniform and periodic antennas. Also, they can be either 1D or 2D, and based on a closed or open waveguide. The different classifications came as a result of the evolution in the study and design of LWA, topic of much interest since the 1950s. The first known LWA was presented by Hansen [Hansen 1940], and it was a rectangular waveguide with a longitudinal slot along the narrow wall, see Figure 1.1.4. Most of the initial studies of LWA were done on closed waveguides with **uniform geometries**. Uniform LWAs produce scannable beams with frequency, but limited to the forward quadrant, since the values for the phase constant β_y will be always positive. The Hansen antenna had a very high leakage rate and therefore very low directivities. Another main drawback of these first attempts was the high losses. In consequence, the studies were focused on open waveguides, to reduce metal related loss. These antennas were based on non-radiative structures due to its inherent symmetry, working with surface

waves, and introducing some kind of asymmetry, the radiation of a leaky mode was achieved. This **radiation mechanism by asymmetry** will be explained in more detail in following chapters. A very complete overview of the evolution of uniform LWA can be found in [Volakis 2007].

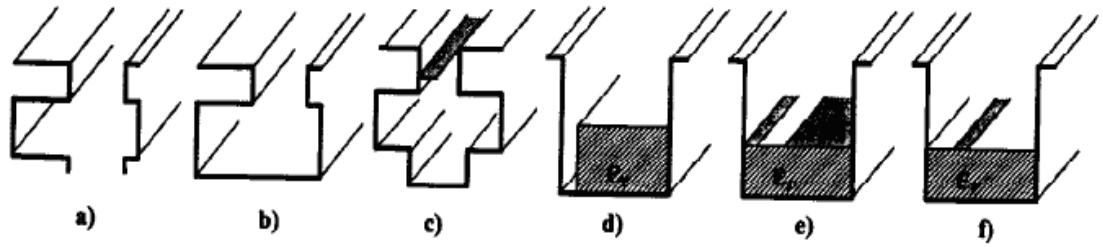

Figure 1.1.5: Several configurations for uniform LWAs.

Just to mention some of them, the offset groove-guide (see Figure 1.1.5 a) and the stub-loaded rectangular waveguide (see Figure 1.1.5 b) were studied respectively in [Lampariello 1987] and [Lampariello 1998], using both a single mode Transverse Equivalent Network (TEN) for the main Parallel Plate Waveguide (PPW) mode (m=0) and full wave Mode Matching technique, in which the whole spectrum of PPW modes was considered but only the main PPW mode radiation was modelled. The groove guide with an asymmetrical conductor strip (Figure 1.1.5 c) was first studied in [Lampariello 1985], where again only m=0 PPW mode was considered to radiate. A more accurate full-wave method [Ma 1994], based on mode matching procedure, took into account all higher order PPW modes in propagation, but just the main PPW mode for radiation. Also the Non- Radiative Dielectric (NRD) leaky-wave antenna was (Figure 1.1.5 d) was studied with a multi-mode Equivalent Transverse Network, but the radiation impedance was applied only to the main PPW mode [Shigesawa 1986]. Printed circuit versions of these types of LWA have not been studied with so much detail. The slot-line leaky-wave antenna (Figure 1.1.5 e) was presented for the first time in 1987 [Lampariello 1987], considering the stub height was infinite. An infinite stub structure do not allow for a practical design. The problem is that the finite height of the stub allowed the propagation of a set of undesired channel-guide leaky-modes, which can deteriorate the performance of the antenna [Shigesawa 1994]. The properties of the slot-line infinite stub loaded leaky wave mode were studied with more detail [Lampariello 1990] by using the Equivalent Resonance procedure. The Mode Matching technique for planar laterally-shielded slot-

line (Figure 1.1.5 e) or the laterally-shielded microstrip line (Figure 1.1.5 f) has also been used to study the dispersion characteristics of leaky-waves modes [Ma 1994]. Again, only the main PPW mode radiation was modelled in the equivalent circuit.

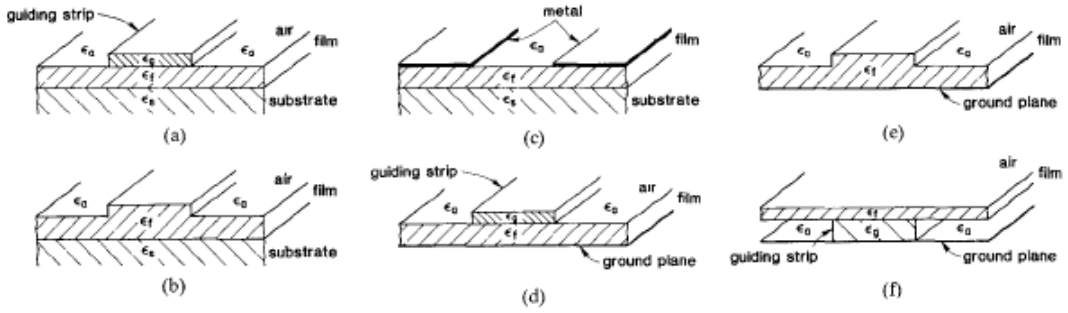

Figure 1.1.6: Some examples of open dielectric LWA.

Another less popular group of uniform LWA is the non laterally shielded *Open Dielectric Waveguides*, some examples studied using the Mode Matching technique can be found in [Peng 1981-I] and [Peng 1981-II] and are showed in Figure 1.1.6. As can be seen, since the classical slotted rectangular waveguide [Goldstone 1959], many original open waveguide structures were studied. Most of these configurations have in common that are formed by Parallel- Plate waveguides. It is important to notice that all of them share a stub at the top; the reasons for this will be discussed in further chapters.

One step forward from the uniform structures, the **periodic LWAs** exhibit interesting features, such as frequency scanning capability, high directivity and large radiations bandwidths. These are structures which have been periodically modulated in some fashion in the longitudinal direction. This periodic modulation creates a guided wave that consists of an infinite number of space harmonics (Floquet waves). The antenna is usually designed so the second order Floquet harmonic is a fast wave, and hence radiative. These higher order harmonics posses a main beam that can point in either the backwards or forward direction. This **backward radiation** mechanism has been known for many ages [Johnson 1993]. Despite its many advantages, it has not been so widely studied as the uniform LWA, and the references in the literature are not as abundant. One of the first known periodic LWA appears in [Goldstone 1959], called the ´holey waveguide' (see Figure 1.1.4). As happened with Hansen LWA, the radiation from this antenna was uncontrollable. But it was not until the 1970s that systematic experimental and theoretical investigations were carried out. Different technologies have been used, as

the microstrip line [Tzuang 2000], the dielectric grating guide [Schwering 1983] [Jacobsen 1970], the strip loaded dielectric slab [Jacobsen 1970] [Mittra 1981] [Encinar 1990], see Figure 1.1.7 below, and the strip-loaded inset waveguide [Guglielmi 1989] [Guglielmi 1991], see Figure 1.1.8 a).

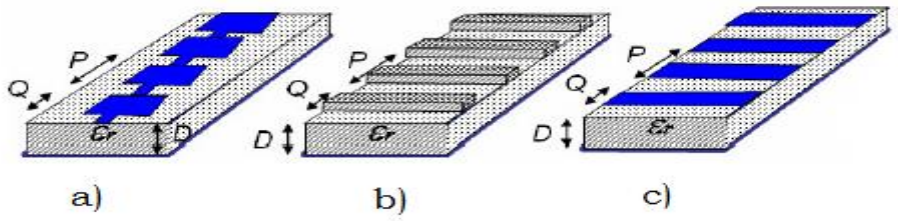

Figure 1.1.7: Some examples of periodic LWA technologies:
a) Microstrip line, b) dielectric grating guide and c) strip dielectric slab.

A hybrid planar waveguide technology, which makes use of a laterally-shielded top-open dielectric rectangular waveguide, in which a uniform strip o slot is asymmetrically located to provide radiation, was proposed in [Gómez June-2004I] [Gómez September-2005] to design tapered uniform or periodic leaky-wave antenna for the millimetre waveband. Some differences arise between the method proposed in [Gómez September-2005] and the techniques used in and [Guglielmi 1991]. In [Guglielmi 1989], Guglielmi and Boccalone proposed a more accurate Transverse Equivalent Network (TEN) to represent the unit cell of the PLWA, which is used to design a novel dielectric inset PLWA in [Guglielmi 1991]. The method proposed in [Guglielmi 1989] and [Guglielmi 1991], although accurate, has two important restrictions which are overcome by the full-wave analysis technique proposed in [Gómez September-2005]. The first restriction of [Guglielmi 1989], [Guglielmi 1991] is that only one-dimensional (1-D) periodic discontinuities can be studied, leading to the strip loaded PLWA shown in Figure 1.1.8 a) (the dielectric-inset PLWA). The novel PLWA shown in Figure 1.1.8 b) and c) allow the introduction of two-dimensional (2-D) perturbations to obtain interesting taper properties. The second difference is that the TEN developed in [Guglielmi 1989] and [Guglielmi 1991] is valid only for the TE_{01} mode excitation, horizontally polarized electric field, as shown in Figure 1.1.8 a), so it did not modelled the effect of higher order parallel-plate modes in the antenna performance.

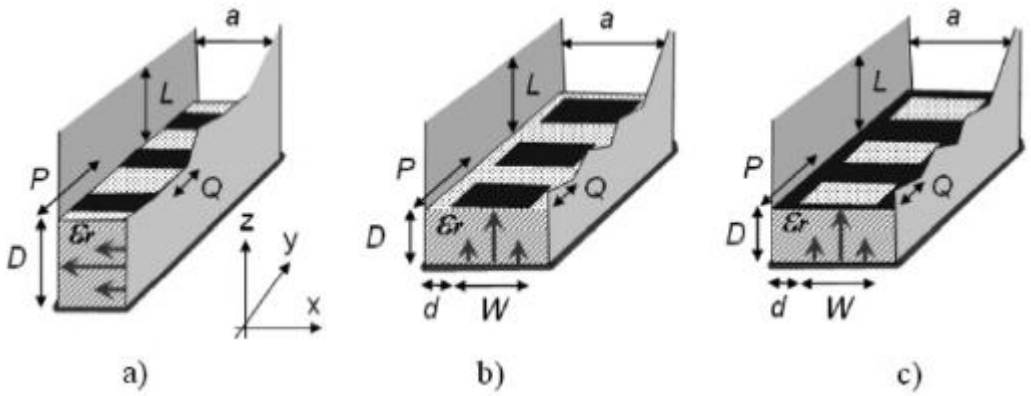

Figure 1.1.8: Some examples of periodic LWA technologies:

The capability to control the leakage rate without varying the pointing angle for LWA as the one showed in Figure 1.1.8 c) was probed in [Gómez September-2005], and a tapered PLWA based on a rectangular slot was presented. The main drawback of the Gomez technique is that it is limited to the analysis of rectangular patches or slots. The present work is based on the studies of Gomez and Melcón for periodic leaky wave antennas, to create a rigorous method able to analyze open waveguides loaded with printed circuits of complex shape, as crosses and loops, accounting for the higher order modes effects on radiation.

1.2. FSS and EBGs: Review and Differentiation.

As a general definition, **Electromagnetic Band Gap** (EBG) stands for 1-D, 2-D or 3-D periodic structures that prevent the propagation of the electromagnetic waves in a specific band of frequency, ideally for all angles and all polarizations. In these structures, two phenomena can be observed. First, the *interference* of waves reflected on the periodic array of elements, either printed circuits or apertures, which will produce pass-bands or stop-bands. The variation of the partially reflective properties will depend mostly on the periodicity, and may occur within large bands of frequency. Second, the *resonant interaction* of waves with the elements of the periodic structure, which will result in bandgaps at the resonance frequencies. This may be useful when working very close to the resonance frequency, in a very narrow band. In this case, the variation of the partially reflective properties of the structure will depend mostly of the physical parameters of the

single element geometry, such as the length in a resonant dipole. In Chapter 4, these two different effects will be identified as *'interference bandgaps'* and *'resonant bandgaps'*.

Usually, when talking about EBGs, all these frequency phenomena are contemplated. There are other terms that belong to the category of EBGs but have slightly different connotations that must be taken into account. **Frequency Selective Surfaces** (FSS) are EGBs that work on a limited range of incidence angles of the wave and a certain polarization. This term is generally used in microwave terminology and can be also called **Partially Reflective Surfaces** (PRS). In optics, the preferred term is **Photonic Band Gap** (PBG).

The objective of this section is not to present the reader with all the studies and lines of work that have been carried out in the last decades about EBGs, nor to list all the different geometries analysed as FSSs. It is to explain the close relation these periodic surfaces have with leaky wave antennas, and the wide field of applications they, in combination, may be used for.

1.2.1. Electomagnetic Bandgap Strucures

EBG are periodic structures that are composed of dielectric or metallic elements. They are capable of controlling the electromagnetic waves in the same way semiconductors control the propagation of electrons. This control over the waves lies on its bandgap property. Based on [Yang 2009], by properly choosing the geometrical parameters, the EBGs have three main application fields:

- **High Impedance Surfaces** (HIS) to suppress the surface wave, responsible for reducing the efficiency in antenna applications, see Figure 1.2.1.1 a) ([Gonzalo 1999], [Yang 2003]) and undesired leakage in guided-wave circuits [Yang 1999-I].

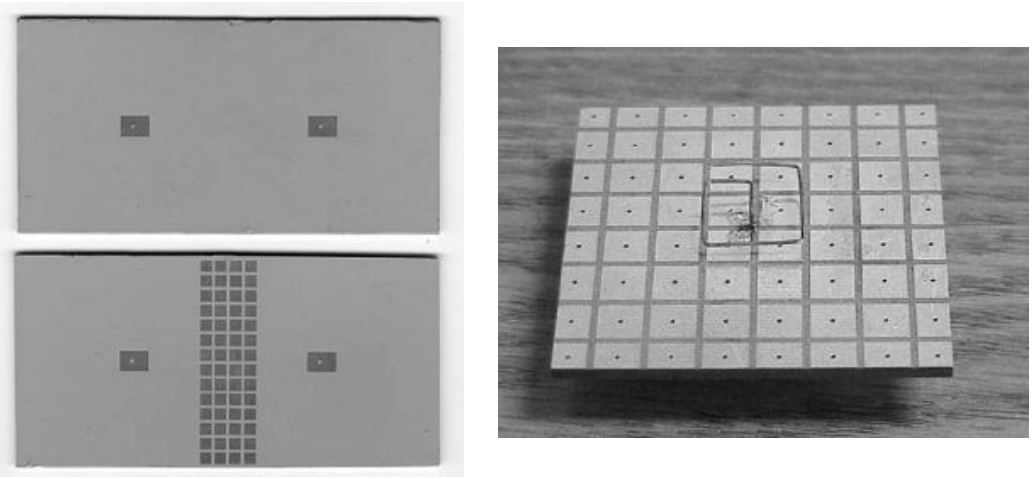

a) b)

Figure 1.2.1.1 a) Avoiding coupling btw patches [Yang 2003] and
b) Low profile antenna [Yang 2001]

- **Artificial Surfaces**, such as *Perfect Magnetic Conductors* (PMC) acting as substrates to design low profile antennas, as the one presented in Figure 1.2.1.1 b) ([Sievenpiper 1999], [Yang 2001]) and create TEM waveguides ([Yang 1999-II], [Maci 2005]). There is also a very complete overview in [Balanis 2008] ch. 15 about Artificial Impedance Surfaces (AIS) for those interested.

- **High Gain Resonator Antennas,** with an EBG acting as a superstrate increasing the effective aperture and hence the gain. There are several configurations that can be used to produce this highly directive antennas: *multilayer dielectric plates* [Jackson 1993], [Thevenot 1999], [Neto 2007], [Kanso 2009], *multilayer of dielectric* [Thevenot 1999] [Lee 2005] *or metallic rods* [Diblanc 2005], and *single or multilayer frequency selective surfaces*. See Figure 1.2.1.2 below for an example of different types of high gain resonator LWA.

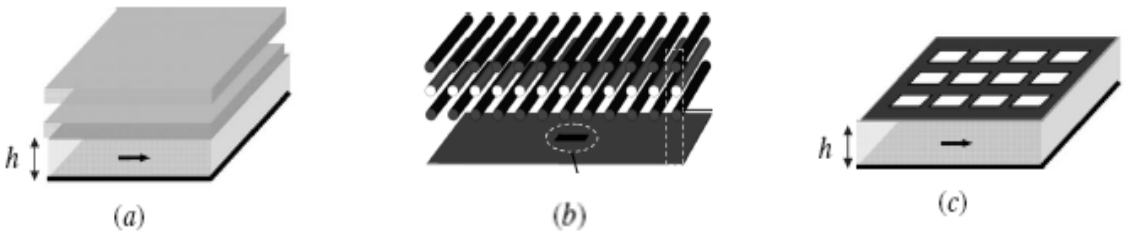

Figure 1.2.1.2 a) Dielectric layers LWA, b) Dielectric Rods LWA and c) FSS LWA.

High gain resonator antennas are basically broadside 2D periodic leaky wave antennas. The general principles and formulas that model their behaviour can be found in [Jackson 1985], [Zhao 2005-I], [Zhao 2005-II], [Zhao 2005-III], [Volakis 2007] chapter 11 and [Balanis 2008] chapter 7. They consist of a metal ground plane, a dielectric layer on it (may be air) and an FSS covering it. The FSS is used to create a leaky parallel plate waveguide region, with the leakage or radiation constant controlled by the reflectivity of the FSS. The antenna behaves as a **Fabry-Perot resonator** [Trentini 1956], increasing the directivity, since the reflection on the FSS is designed such as to increase the effective aperture and to achieve 'in phase' leakage, see Figure 1.2.1.3 a). In [Feresidis 2001] can be found the methodology to design said 'in phase' radiation, based on a metallic dipole FSS. In the community, the FSS used as a superstrate in this kind of antennas are called *Partially Reflective Surfaces* (PRS), since the decisive parameter is the reflection coefficient they present. It can be deduced that the phase constant, and therefore the main bean pointing angle, will depend mainly on the thickness of the substrate, and the attenuation constant on the properties of the PRS. Figure 1.2.1.3 shows the radiation for b) a pencil beam at $\theta_m = 0^o$ and c) a conical beam for $\theta_m > 0^o$. They are typically excited by a simple source (a dipole, patch or waveguide), but multiple feeding has been probed to produce purer polarization and lower side lobes performances [Iriarte 2009].

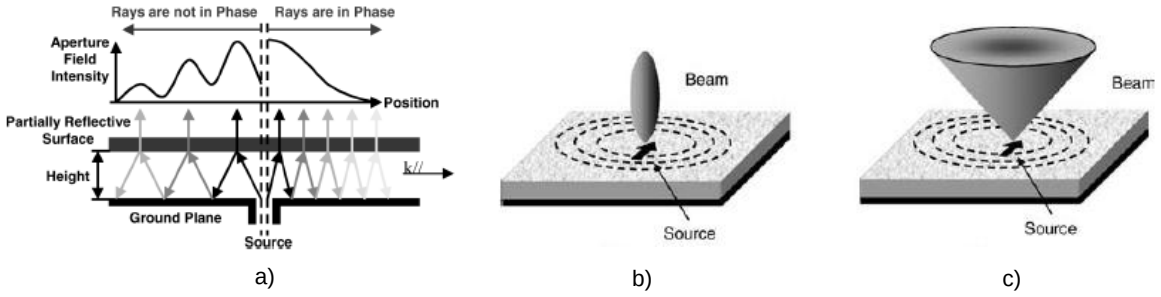

Figure 1.2.1.3 a) Fabry-Perot resonator [Iriarte 2009] , b) pencil beam and c) conical beam.

The 2D PLWA structure supports both TE and TM modes, so in order to produce a omnidirectional narrow pencil beam in broadside, the phase constant and the attenuation constant must be the same for both polarizations:

$$\beta^{TE} \approx \alpha^{TE} \approx \beta^{TM} \approx \alpha^{TM} \qquad (1.2.1.1)$$

When the antenna is optimized to radiate at $\theta_m = 0^o$, the above condition (1.2.1.1) is automatically satisfied, even if the PRS of the LWA has very different periodicities in each dimension. As the main beam increases from $\theta_m = 0^o$, the response of the PRS to the TE and TM polarizations becomes increasingly differing and the beamwidths become different in the principal planes.

Examples of **single PRS 2D periodic LWA** can be found in [Macci 2005] for printed dipoles, [Guerin 2006] for a single metallic grid, [Goussetis 2006] for metallic square patches, [Kosmas 2007], [Chantalat 2008] for circular holes and [Iriarte 2009] for square holes lattice. These antennas work at one frequency and the PRS is situated at about 0.5λ above the ground plane to produce the 2π offset in phase required. To increase the operating bandwidth, a second layer of PRS has to be added on top of the existing one, to produce a defect in the latter PRS and create an allowed band in the forbidden frequency band. The **multilayer PRS LWA** shows enhanced gain within the frequency defect band. This phenomenon is explained in detail in [Moustafa 2009] with a double layer EBG composed of a square loop FSS and a double square loop FFS on top, reaching a 8% of bandwidth. The ring resonator and round holes are combined in [Oses 2009] with similar results.

Dual band PRS LWA require two PRS stacked one on top of another, with a separation of 0.5λ, with gives a total height of the antenna of a wavelength, without the feeding. To produce more compact dual band LWA, [Lee 2007] proposes a new superstrate composed by a thin dielectric supporting layer with PRSs of different periodicity printed on top and bottom of it.

Combinations of **FSS and PMC LWA** have been used to reduce significantly the profile of the antenna, see Figure 1.2.1.4. The metallic ground plane, until now a Perfect Electric Conductor (PEC), is replaced with a PMC, to reflect the incident wave in phase. This approach can be found in [Feresidis 2005], [Wang 2006] and [Mateo 2011] for metallic patches with different lattice and [Kelly 2008] for a combination of metal patches with a metallic mesh. It was probed that with this technique the cavity height can be reduced to a fourth of the wavelength.

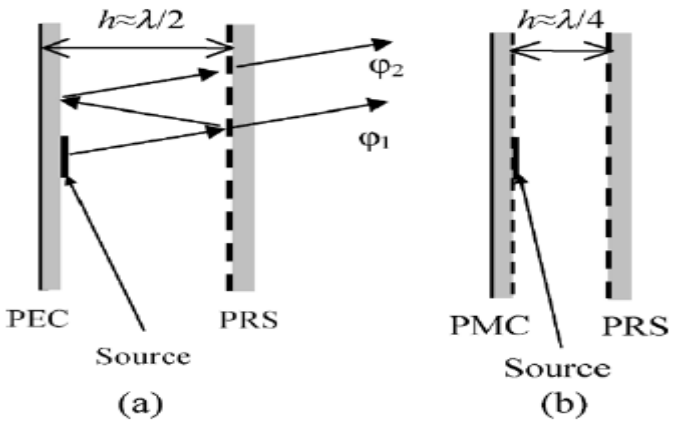

Figure 1.2.1.4 a) PEC ground plane LWA and b) PMC ground plane LWA, [Feresidis 2005].

The first EBG structures were analyzed using simple **Lumped Elements Equivalent models**, describing the periodic circuit in terms of LC resonant circuits. It is obvious that such a simplification could not render very accurate results. Another popular method is the **Equivalent Transmission Line method**, where the FSS or PRS is described by its equivalent admittance (see Figure 1.2.1.5), and then the equivalent transmission line modelling the cross-section of the LWA is solved by conventional numerical techniques. This resolution can be found in [Maci 2005], and in [Luukkonen 2008] for metal strips or patches. This method is simple and relatively accurate for the calculation of the reflection coefficient, but it considers an infinite structure, and cannot produce a Floquet modal dispersion results as a full-wave method would.

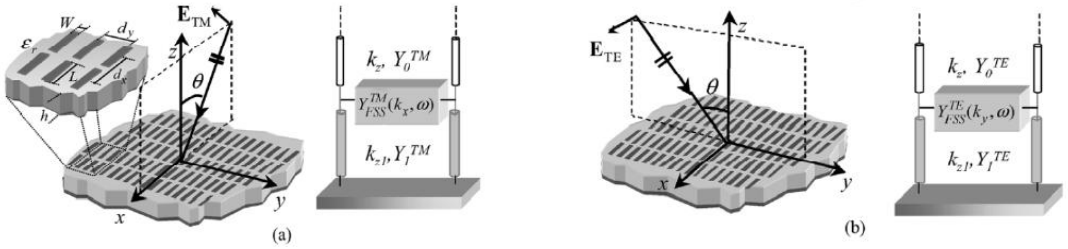

Figure 1.2.1.5 a) TM Equiv.Tx. Line and b) TE Equiv. Tx. Line [Macci 2005].

More complex and rigorous methods appeared as the computing technology grew. **Finite Difference Time Domain** (FDTD) method seems to be the more popular to analyze 2D PLWA, as can be seen in [Thevenot 1999], [Sauleau 1999] [Yang 2003] [Kosmas 2007] and [Kelly 2008]. Nevertheless, lately, the frequency domain **Method of Moments** is being applied to the analysis of 2D PLWA, based on Floquet modal expansion and Entire Domain basis functions, see [Goussetis 2006] and [Mateo 2011]. In Chapter 5 it will be

discussed how to apply the method developed in the present work to 2D PLWA to produce more rigorous and significant results that will account for the finite extension of the antenna and higher order radiation effects.

1.2.2. Frequency Selective Surfaces

In 1919, Marconi patented the first known periodic structure, [Marconi 1919]. But it was not until the 1960s that frequency selective surfaces were intensively studied. Since then, thousands of papers have come into light, in which the FSSs have evolved to more complex structures, its fields of application have been multiplied and new terminology and classification of such structures was settled. There are excellent books devoted to FSS [Wu 1995], [Vardaxoglou 1997] and [Munk 2000], and dedicated chapters in [Balanis 2008] ch.16 and [Volakis 2007] ch.56. FSS can be defined basically as **frequency filters**, able to produce the four standard filter responses: *high-pass* or inductive (metallic mesh with holes [Lee 1982] [Cwik 1987]), *low-pass* or capacitive (array of metallic patches [Lee 1982]), *band-stop* (arrays of metallic resonant geometries [Mittra 1988] [Tsao 1984]) and *band-pass* (periodic apertures of resonant elements [Mitra 1988]). Combinations of these four types will result in tailored frequency responses [Wang 1999].

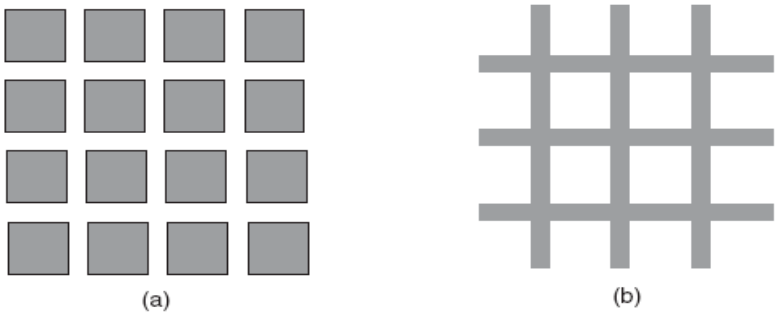

Figure 1.2.2.1 a) metal patches (low-pass) and b) metal grid (high-pass).

Complementary apertures and metallizations will result in complementary filter responses as shown graphically in Figure 1.2.2.2, provided the structure is symmetric and no substrate is present, by direct application of **Babinet´s principle**, assuming the electric field has also a complementary polarization.

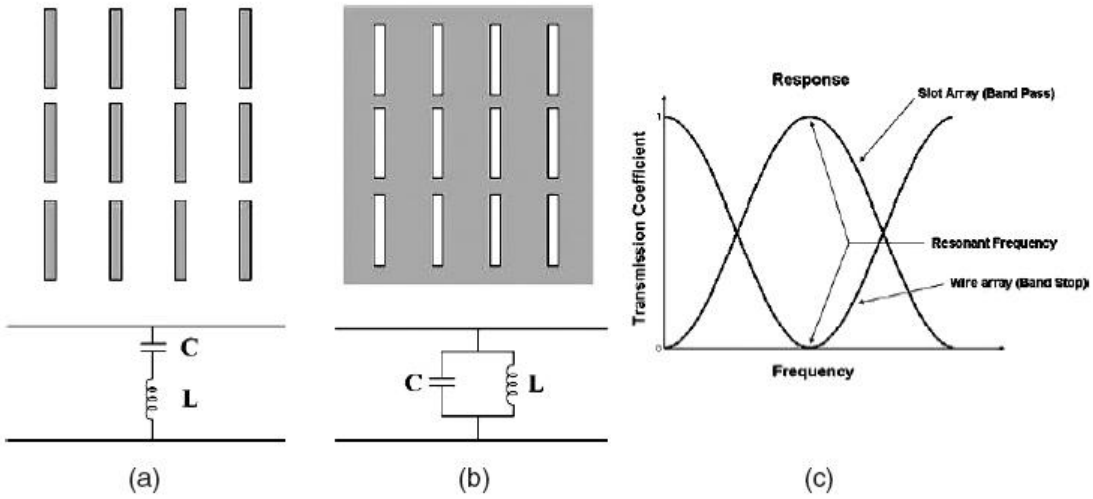

Figure 1.2.2.2 Babinet´s Principle [Volakis 2007].
a) Dipole array, b) slot array and c) frequency response.

Typically, FSSs work on its **resonance frequency**, which is determined mainly by the geometry of the single periodic element. However, the behaviour, both in frequency and radiation, of the FSS will depend on several factors:

- The geometry of the single element.
- The period of the structure.
- The conductivity of the metallic material.
- The permittivity of the dielectric material acting as substrate (if existing).
- The finite number of cells.
- The frame surrounding the FSS.
- The number of layers and separation in stacked compositions.

When designing 1D LWA, as seen in the previous section, the working frequency band does not have to be close to the resonance frequency of the geometrical element of the single cell, the reflectivity of the interface with the open air for a single frequency can be controlled by any of the geometrical parameters listed above, while maintaining the pointing angle fixed. To taper the antenna illumination it is necessary to count with enough grades of liberty, that is to say, geometrical dimensions, which will be only possible introducing more complex elements, as those showed in Figure 1.2.2.3. This is applicable too for those LWA designed specifically on their resonant frequency, the basic mode of operation in 2D broadside LWAs.

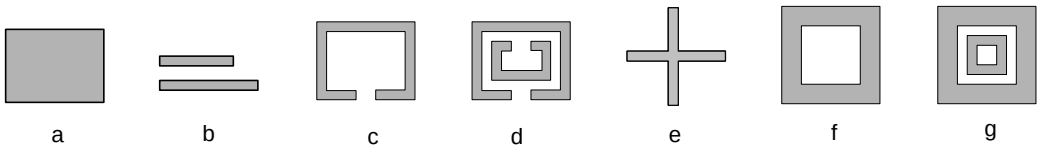

Figure 1.2.2.3 Some of the most common geometries in FSS. a) patch, b) double dipole, c) split ring, d) double split ring, e) cross, f) square loop and g) double square loop.

The first numerical analyses of FSSs were based on the **Mode Matching Technique** [Zarrillo 1987] and **Equivalent Circuit Method** [Lee 1982] [Wang 1999], since these approaches were not too demanding in terms of computational cost. Said methods were not too accurate, as they assumed a plane wave incidence, with no possibility of modelling the effect of higher order modes at the aperture.

As computers became more powerful, said methods became more refined [Wang 1991] [Ma 1994] and other techniques were developed, more rigorous and accurate, based on the **Integral Equation Method** and the induced currents on the metal expansion. This integral can be formulated by using *Spatial-domain approach* [Montgomery 1975] [Johnson 1993] [Gomez Sept-2005] or *Spectral domain approach* [Montgomery 1978] [Mittra 1988] [Becks 1992] [Wu 1995] [Vardaxoglou 1997]. Once the integral is formulated, the most well-known technique to solve it is the **Method of Moments** (MoM) [Chen 1970] [Wang 1991] [Bozzi 2005]. It is able of giving details of the frequency and polarization responses of the FSS, together with a physical understanding of their operation. It also can handle angles of arbitrary incidence. Briefly, due to the periodic nature of the structure, the fields can be expanded into a set of Floquet spatial harmonics. The electric field on the metallic surfaces must be zero, so an integral equation can be solved. In order to do so, the currents on the metal will be expanded into a set of complete orthogonal basis functions and the coefficients will be calculated by applying the MoM.

Depending on the geometry under study, the MoM may take considerable amount of computing time and memory. The memory requirements can be reduced by using iterative methods, as the **Conjugate Gradient Method** (CGM) [Wang 1991], to solve the integral equation. A very illustrative summary of the use of MoM and CGM can be found in [Mittra 1988].

The method developed in this thesis is based on the **Spatial MoM combined with Parallel Plate modal expansion** in a laterally shielded structure. For this kind of structure Spatial-domain approach is more suitable than Spectral-domain, since the Fourier transforms needed to model this geometry are very complex, and the computational requirements would be too high. This new method will be seen in detail in Chapter 2.

1.3. Metamaterials: Review.

In 1967, Russia, the physician **Victor Veselago** wrote a paper speculating about the existence of materials with negative permeability and permittivity, and the properties these substances would exhibit [Veselago 1967]. It was him who coined the term Left-Handed to express that the electric field, magnetic field and the phase constant would form a left handed triad, opposite to the conventional right handed triad. It took more than 30 years for the first artificial metamaterial to be developed by **Smith** [Smith 2000]. It was a combination of metal thin wires with split ring resonators, resulting in a new material with negative constitutive parameters over a small range of frequency, as the negative refraction index probed in the experimental demonstration. This was the trigger that started the numerous studies on metamaterials up to this day.

Metamaterials (MTM) are artificial effectively homogeneous electromagnetic structures with unusual properties not readily available in nature. The effective-homogeneity condition is ensured by choosing an average cell size P much smaller than the guided wavelength λ_g, at least a quarter of it. Any material is defined basically by its constitutive parameters, the *permittivity* ε and the *permeability* μ. These in turn define the *refractive index n* by

$$n = \pm\sqrt{\varepsilon_r \mu_r} \qquad (1.3.1)$$

where $\varepsilon_r = \varepsilon / \varepsilon_0$ and $\mu_r = \mu / \mu_0$, being ε_0 and μ_0 the permittivity and permeability of free space respectively. Based on these two parameters, there are four combinations: $(+\varepsilon,+\mu)$, $(-\varepsilon,+\mu)$, $(+\varepsilon,-\mu)$ and $(-\varepsilon,-\mu)$, as can be seen in Figure 1.3.1. The latter is referred as **Left-Handed Materials** (LHM) or **Negative Refractive Index materials** (NRI). By definition they have antiparallel phase and group velocities.

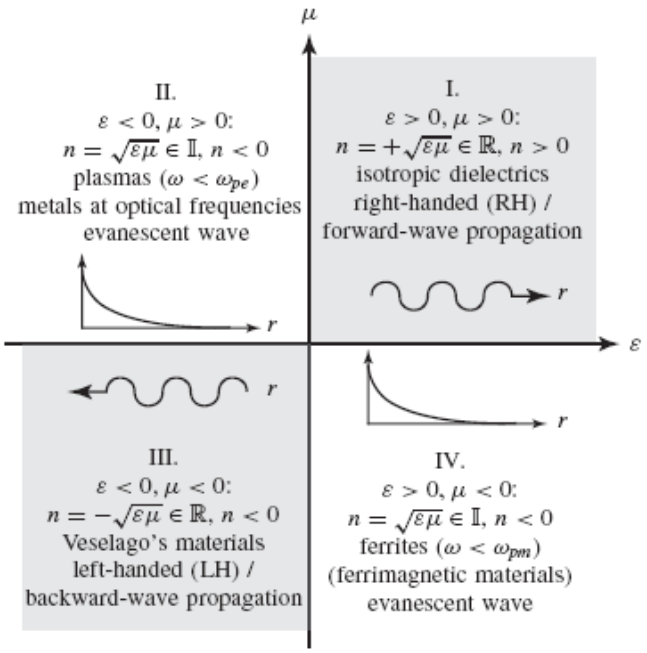

Figure 1.3.1 Permittivity- permeability diagram from [Caloz 2006].

The first metamaterials worked on the resonant frequency, which means high loss and very narrow bandwidth. The need for a different approach to obtain alternative structures resulted in the introduction of the **Transmission Line (TL) Analysis method** in 2002 by three different research groups: **Eleftheriades** [Grbic 2002-I], [Grbic 2002-II], [Eleftheriades 2003], [Eleftheriades 2007] and [Balanis 2008] ch.14, **Oliner** and **Caloz** [Liu 2002], [Sanada 2004], [Lim 2004-I], [Lim 2004-II] [Caloz 2005] and [Caloz 2008]. In the last years, both Eleftheriades and Caloz have published a book devoted to metamaterials, see [Eleftheriades 2005] and [Caloz 2006]. They are a compendium of advances in the fields and a detailed explanation of the basic principles, but in equality of technical completeness, the author considers Caloz approach makes complex concepts simple and easily understandable by graphics, and because of this, will be the reference whenever possible.

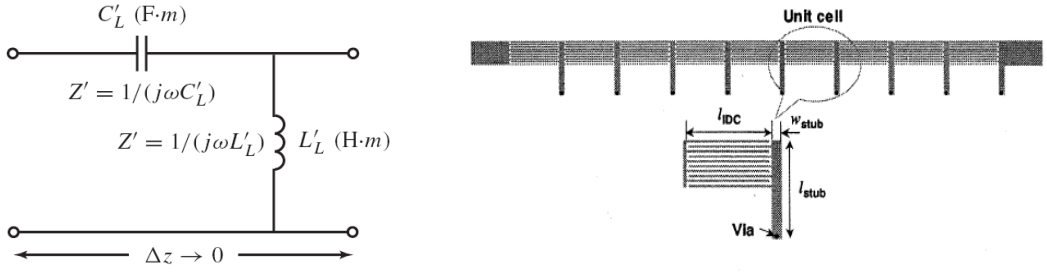

Figure 1.3.2 a)Transmission line model for the ideal LH metamaterial [Caloz 2006] and b) LH microstrip strucuture [Liu 2002].

The basic model of the TL method is presented in Figure 1.3.2. a). By studying the characteristics of the LC transmission line, it was deduced that a structure could be conceived based on this model to achieve a left-handed medium with a non resonant nature, working on a selected bandwidth with low loss (demonstration may be found in [Caloz 2006]). One of the first examples is the microstrip line presented in [Liu 2002], constituted by a series of interdigital capacitors C_L and shunt stub inductors L_L as shown in Figure 1.3.2 b).

The LC circuit used to model the left handed metamaterial is ideal. The associated currents and voltages in the real circuit induce other effects, as series inductance L_R in the interdigital capacitor and a shunt capacitance C_R between the upper printed circuit and the ground plane. A pure LH structure can not exist, for there always are side RH contributions. This concept of **Composite Right/Left Handed** (CRLH) is introduced in [Sanada 2004], and the equivalent transmission line model can be seen in Figure 1.3.3 a). In Figure 1.3.3 b), the dispersion diagram for the real TL model is presented in green line. At low frequencies the C_L and L_L are dominant and the phase constant is negative, also at higher frequencies L_R and C_R are dominant and the phase constant is positive. ω_{se} and ω_{sh} are the series and shunt resonances respectively. For comparison, the dispersion for a pure LH structure ($L_R = C_R = 0$) and a pure RH structure ($C_L = L_L = 0$) are shown too in blue and red curves.

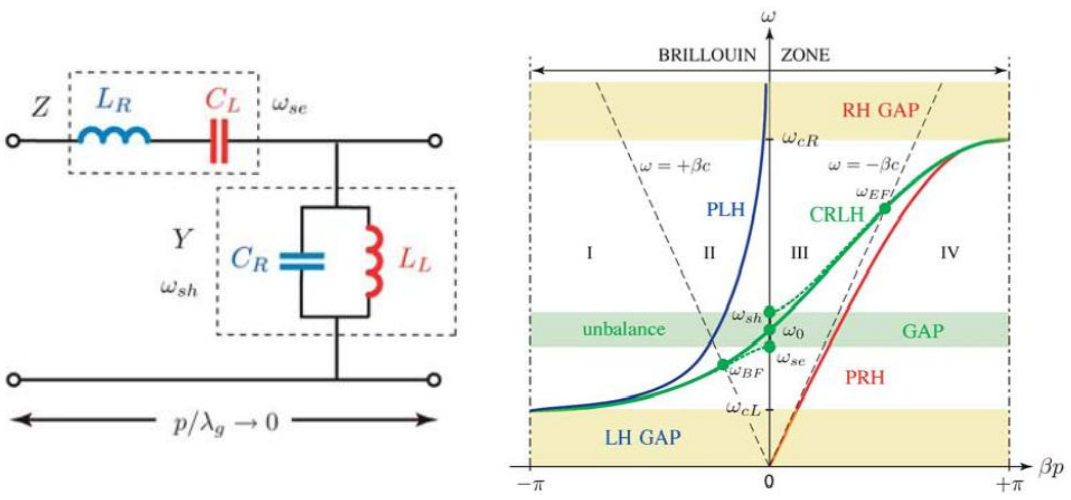

a) b)

Figure 1.3.3 a)Transmission line model for the real LH metamaterial [Caloz 2008] and b) corresponding dispersion diagram.

1.3.1. Periodic LWA vs. Metamaterial LWA.

Both antennas are based on leaky-wave propagation and posses the capability of **backward radiation**, but the mechanism to achieve it differs greatly between them. In the *conventional PLWA*, the radiation in negative angles is well known and is associated to the higher order negative harmonics in the Floquet modes expansion, characteristic of periodic structures. The cell period in these structures is typically one or several half guided wavelengths, since it is essential to generate leaky space harmonics.

The *Metamaterial LWAs*, on the other hand, have periods much smaller than the guided wavelength, and the structure becomes a different material with an effective permittivity and permeability, chosen by design. The leaky-wave propagating within this effective material exhibits backward radiation in its main fundamental mode. In these LWAs, the periodicity is not implemented to obtain higher order Floquet harmonics to radiate backwards, but to obtain the LH effective material. In fact, the periodicity is not necessary, since it is working in its fundamental mode.

Figure 1.3.1.1 shows the dispersion diagram of the fundamental mode of a balanced CRLH TL. The behaviour is similar to that of the first high order negative Floquet harmonic, as will be explained in following chapters. It must be noticed that the circuit is designed for the resonance frequencies $\omega_{se} = \omega_{sh} = \omega_0$. This is called *balance condition*, and it allows the antenna to radiate in broadside, avoiding the gap in the scanning region characteristic of the PLWAs. The dashed lines represent the air-lines. The first crossing of the dispersion curve with the air-line occurs at ω_{BF} when the phase constant is equal to the free space propagation constant $-\beta = k_0$. At this point the fundamental mode transforms from a guided wave to a leaky wave radiating at backward endfire. As the frequency increases, the negative angle scans towards broadside. In broadside $\beta = 0$, since the antenna is balanced, there is no bandgap. After this, the angle becomes positive and scans towards forward enfire, reaching it at ω_{EF}, where $\beta = k_0$ and the leaky wave becomes a surface wave below cut-off again.

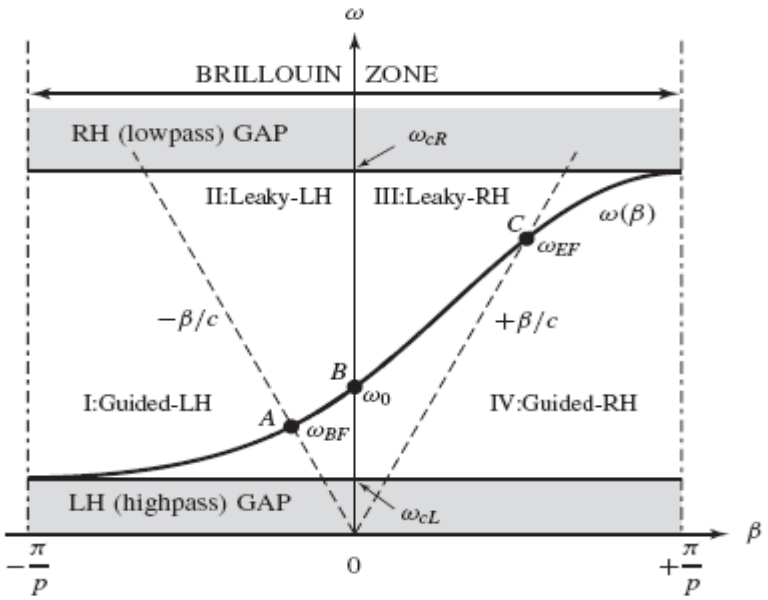

Figure 1.3.1.1 Dispersion diagram for a balanced CRLH [Caloz 2006].

This **backfire-to-endfire frequency scanning capability of the fundamental mode** in a balanced CRLH structure was presented for the first time in [Liu 2002]. Its main advantages are that it achieves broadside radiation and that the feeding for this antenna can be simple and efficient, since it works with its fundamental mode.

It is clear how the use of metamaterials in combination with leaky-waves offers a series of advantageous behaviours, that should be studied oriented to radiation performances. The software tool developed in the present work will be able to support geometries that have been probed to exhibit LH properties, opening the door to an infinite number of possibilities in the field of PLWA, metamaterial based or not. This will be possible thanks to the rigorous full wave analysis method and the radiation study based on Parallel Plate modes, able to model higher order effects on the radiation pattern.

1.4. Objective.

It is clear that the future of periodic leaky wave antennas research is oriented to the introduction of more **complex elements in the periodic surfaces** and the combination with **metamaterial** structures. Also, it has to take into account that real physical antennas are finite and usually encapsulated in some kind of metal box, both for structural reasons and performance requirements. The application of high lateral walls to suppress currents that may deteriorate the radiation pattern is commonly used in antennas. The effect of the height of these walls must be introduced in the analysis method, as well as the possibility of analyze unit cells of arbitrary shape.

The objective of this thesis is to develop a simulation tool which is versatile, fast but still accurate and rigorous. This novel full wave method is based on the Space Domain PPW Modes expansion in combination with Subdomain basis functions. With it, the discrete PPW radiation spectrum can be related directly to the continuous radiation spectrum of this type of open-waveguide leaky modes, in an attempt to unify the theory of guiding and radiation phenomena.

The advantages of using laterally shielded structures are many and well known:

- Structurally, the antenna is more rigid and protected.
- Pure horizontal polarization is easier to obtain, since the height will ensure higher order modes do not reach the aperture.

- Surface waves propagating in the substrate are eliminated, avoiding secondary lobes by diffraction.

Previous methods that could deal with complex unit cell geometries for leaky wave antennas did not take into account the effect of the lateral walls. This is one of the main novelties, among others. Also, radiation patterns so far were deduced from approximations and took not into account the effect of higher order modes.

For the first time a method that accounts for all the properties listed below is presented. This **novel simulation tool** is:

- a rigorous and accurate full wave method, based on MoM. It is able to analyze modes separately, even propagation of higher order modes.
- highly efficient, since most of operations are analytical and presents very good absolute convergence. It simplifies a 3D problem into a 2D one. It will be shown that it is considerably faster than commercial software.
- able to model the effect of the interference between different modes (bandgaps).
- able to model finite height of lateral stubs at the top of the structure.
- flexible, since it allows several dielectric layers and periodicity on either the narrow or broad waveguide wall.
- able to rigorously calculate the radiation pattern, taking into account the contribution of higher order modes. It also gives a useful comparison between the propagating spectra of modes and the radiating spectra.
- and, most important, able to model complex FSS geometrical elements, based on the use of Subdomain Functions.

This software is the **major novel contribution** of the present work, not only because it is faster than other software, like HFSS, but also due to the wide range of information provided in the form of graphical results, based on the modal study of the structure. It will be shown how the results obtained with commercial software cannot explain most of times what is truly happening inside the structure. A **second contribution** will be the modal study of a LWA with printed elements of certain complexity. Such an in-depth analysis on said kind of antenna has not been done before.

This thesis represents the first step towards a novel approach to the research of periodic leaky wave antennas, since it produces as a final result the simulation software needed for said study. Usually, this initial stage involves a full and deep understanding of the maths related to the problem and dealing with abstract and arid concepts. The obtained results from all this effort is a powerful simulation tool, not a final optimized design of a practical antenna, since this will require a whole separate research on a chosen geometry, now that the program is ready to use. Many different lines of research are proposed at the end of this work, and some of them will be followed in Loughborough University or through collaboration with other universities, and to the author, it is extremely fulfilling to have made it possible with the present contribution.

1.5. Structure of this PhD.

The present work is divided into five chapters. **Chapter 1** is an introduction that will guide the reader along the evolution of *leaky-wave antennas* and will establish the basic knowledge necessary to comprehend the concepts that will be treated throughout this thesis. An overview of the state of art and the trends in the research of LWA, as well as the previously coded methods was necessary to provide a background to the creation of the novel method presented in following chapters.

Chapter 2 is a complete and systematic presentation of the *Spatial Domain Method of Moments* combined with Parallel Plate modes expansion and, as the main innovation, the use of Sub-domain basis functions to model the induced currents on the metallic printed circuits. The maths working out related to the analysis method is explained in depth, as well as the advantages that presents in comparison with other similar methods.

Chapter 3 is dedicated to the presentation of *Basis Functions* and its kinds. Both Entire-domain and Sub-domain basis functions are discussed in detail, since the simulation tool will support both approaches. Issues as suitability, meshing criteria and convergence will be dealt with, and last, validation of results obtained with this new method in comparison with previously studied LWA and precedent methods will be presented.

The developed simulation software will be introduced in **Chapter 4**. A periodic leaky wave antenna based on an open laterally shielded waveguide loaded with square metallic loops on a dielectric ground will be studied and will serve as an example to discover the features of this analysis tool. It is the first time a complete full-wave modal study of a PLWA of this kind has taken place, since the previous studies were limited to rectangular patches or slots. Dispersion curves, current and fields results will be obtained. But the main objective of the software is not only generate accurate solutions, but to produce information enough for the user to reason and comprehend the inside workings of the electromagnetic structure. This way, several phenomena related to periodic structures will be identified and discussed. The radiation of the LWA will be analyzed based on the PPModes expansion and the equivalent magnetic currents they induce on the aperture, so the effect of higher order modes that may reach the aperture will be taken into account in the radiation pattern. Also, it will be shown that the program is extremely flexible and easy to extend in order to analyze other new geometries.

And last, **Chapter 5** will show the versatility of the developed simulation tool by presenting a selection of potential applications. Each of these applications may be future lines of interesting research, and WELAST will be the key in the analysis and also the design of new devices. The possibilities are endless. To finish, some extensions and improvements for the coded program, that the author had not the time to implement, are proposed.

CONFERENCES AND PUBLICATIONS

A list of publications written along the carrying out of this PhD is presented below:

M. Padilla, J.C. Vardaxoglou, " Analysis of a Metamaterial Based Leaky Wave Antenna with Laterally Shielded Planar Technology", EuCAP 2007, Edinburgh, UK, Nov. 11-16, 2006.

M. Padilla, J.C. Vardaxoglou, " Versatile Analysis Method for Metamaterial Leaky-Wave Antennas in Hybrid Waveguide-Printed Circuit Technology", 2nd Young Scientist Meeting on Metamaterial,s YSMM'08, Barcelona, Spain, Feb. 7-8, 2008.

M. Padilla, J.C. Vardaxoglou, " Versatile Analysis Method for Leaky-Wave Antennas in Hybrid Waveguide-Printed Circuit Technology", Loughborough Antennas & Propagation Conference, LAPC 2008, Loughborough, UK, Mar. 17-18, 2008.

M. Padilla, J.C. Vardaxoglou, " Versatile Analysis Method for Laterally-Shielded Planar Technology Leaky-Wave Antennas", IEEE APS-URSI 2008, San Diego, California, USA, Jul. 5-11, 2008.

Two papers are currently being written, presenting the method and the simulation program developed in this PhD:

"An Efficient Full-Wave Modal Method for the Analysis of Laterally Shielded Leaky-Wave Antennas based with Periodic Printed Circuit of Arbitrary Shape", on progress.

"A Novel Simulation Software for the Modal Analysis and Design of Periodic Leaky-Wave Antennas: WELAST", on progress.

AUTHOR´S NOTE

Experienced researchers may find that the present work is explained in too much detail. The author has done purposely so, since it is her intention that this thesis may be understood and used by any student interested in microwaves, not only those specialised in the field of LWAs. It was always present during the development of the simulation software WELAST that the most important result, at the end of the day, was to truly understand the 'what is happening inside the structure and why'. Getting to know in depth the inside working mechanism of the radiating device is not only a source of great satisfaction and personal achievement for any engineer, but a logical and efficient way to approach the analysis and design of any antenna. This is the reason why this work starts with the most basic concepts and moves from there to some maths of high complexity. Also, this software was conceived to be extended as need may arise to try new geometries. This objective could not have been fulfilled if all the information and explanations, necessary to understand the core of the program, would not had been given to the reader fully detailed.

CHAPTER 2 - THE METHOD

Where the consistency and rigorousity of the full-wave numerical technique, specifically developed to analyze waveguide embedded LWA, are presented.

The characterization of leaky-wave antennas requires the calculation of the dispersion diagram of the modes supported by the periodic structure. The electromagnetic analysis of periodic structures (FSSs, PRSs, EBGs…) can be based on several different methods, roughly divided in three main branches: **Time Domain** Methods, **Spectral Domain** Methods and **Spatial Domain** Methods, as discussed in Chapter 1. Traditionally, the preferred technique for open planar structure was the formulation of Green Functions in the Spectral Domain, for both 2D [Mittra 1988] and 3D problems [Becks 1992]. The infinite nature of the periodic structures yielded to continuous wavenumbers in the spectral domain, and Fourier transforms could be applied. However, the required Fourier integrals are complex and come with a high numerical cost. When analyzing laterally shielded structures, the wavenumber must be treated in a discrete modal approach, so the method can be directly derived in the space domain, avoiding any kind of complicated Fourier transform. This is due to the existence of Parallel Plate modes and the correspondent modal expansion in the electromagnetic solution of the open transmission line, as will be explained in this chapter.

Independently of the method, all 3D problems are tedious to model, with a high computational cost. An equivalent simplified circuit will be used in this work to move from the analysis of a 3D structure to a 2.5D structure (that is to say, a problem where the fields are considered variable in 3 dimensions and the currents are considered variable only in 2D, in a plane transversal to the propagation direction of the structure), reducing severely the complexity of the formulation.

Finally, there is a consideration, depending on the type of structure to analyze, an EBG or an FSS. Besides the pros and drawbacks of each method, when determining the dispersion curve is not really a big deal which, since most of the methods used for the analysis of FSSs can be used on the EBGs. But there is a fundamental difference: while in the FSS there is an incident plane wave with a specific angle causing a response, in the EBG there is not incident field and therefore no independent term in the analysis, and this leads to a **homogeneous problem** [Bozzi 2005]. The latter case is the one this thesis deals about.

Focusing now specifically on the analysis methods for LWA, three main approaches have been used to study the complex leaky modes travelling along these structures:

- The first one, [Lampariello 1987] and [Guglielmi 1991], was the use of the **Transverse Resonance Equation** on an equivalent network obtained for the main Parallel Plate Mode, responsible for the radiation. As a drawback, this method could not model the effect of higher order modes and the approximation of the equivalent network was not accurate enough for all the cases.

- The second one, [Ma 1994], was a full wave approach for the entire PPM spectrum using the **Mode-Matching** technique. This method in the case of laterally shielded structures is accurate, but it requires solving the mode-matching integrals in each discontinuity using a high number of Parallel Plate Modes (PPM). In this case, the main drawbacks were the computation cost and the problems with relative-convergence.

- The third one is the **Spatial domain Method of Moments** in [Gomez Sept-2005]. This technique did not require complicated Fourier Integrals and had full-wave nature, so it did not have restrictions regarding the PPM order. It is also remarkable the modal

approach to the Markuvitz Radiation Impedance, enabling the radiation not only of the main PPM, but the simultaneous radiation of Floquet armonics and higher order PPM, as well as other modes supported by the structure [Gomez March-2006]. This method modelled discontinuities in both directions of the transversal plane where the printed circuit was situated, allowing for tapered illuminations of the antenna. However, the main limitation of this technique was the use of simple Entire Domain basis functions, so that it can only model planar metallizations of regular geometries, that is to say, rectangular slots or patches.

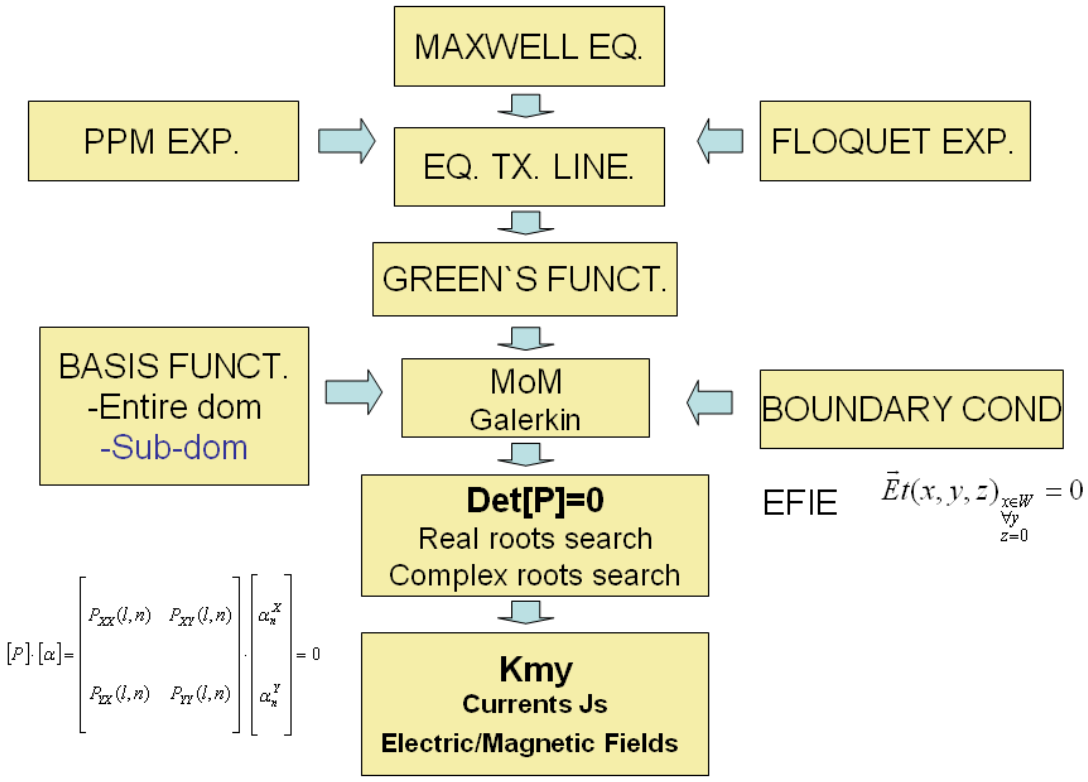

Figure 2.1: Basic layout of the proposed method.

The work undertaken throughout this thesis is based on the third method. It will analyze the properties of the modes (leaky or not) existing in dielectric waveguide periodically loaded with planar metallizations (see Figure 2.1.1). To overcome the limitations of the previous computed models, the novel method proposed in this present work will be based on the **Spatial Domain Method of Moments + Subdomain Approach of the geometry**. By developing an equation system based on the number of subcells in which the basic periodic geometry is divided, this analysis is able to model the currents induced on a non-

regular planar metallization. This way, it becomes a versatile general method for arbitrary printed geometries. As will be illustrated in later chapters, this method can study not only dipole and patch based LWAs, but also based on other well-known geometries as cross-dipoles, square loops, double square loops, split rings, and so on. This novel contribution opens the door to a field of possibilities: the study of the arbitrary printed circuits applied to the shielded leaky wave antenna.

The flow chart in Figure 2.1. shows an overview of the whole method. The Maxwell equations for the fields in the structure are expanded in a sum of Parallel-Plates modes, which will make possible to take into account the layered media (dielectric-air) and the radiation condition at the aperture, through an equivalent transmission line of the transversal section of the PPW. The same way, a Floquet modes expansion will model the periodicity along the propagation direction. The currents induced on the metallization will be represented as a current source in the equivalent transmission line, and this will be expressed in terms of spatial Green functions. Appling the Method of Moments to the Green function, the currents can be expanded in term of a set of basis functions. **Subdomain functions** will be used for the first time to analyze this kind of laterally-shielded leaky wave antennas, allowing for non-regular metallizations (see Chapter 3) as the main novelty of this method. Once the currents are expanded, the Electric Field Integral Equation (EFIE) is imposed to make the transverse electric field zero on the metallic patch (boundary condition). This way, a homogeneous problem is obtained and solved forcing the determinant of the MoM matrix to be zero. The longitudinal propagation constant is the result of this homogeneous system. After this, the currents, fields and radiation pattern can be calculated.

Most mathematical workouts have been incorporated into the Appendix A, at the end of this work, for completeness. In order to make it easy to consult this added information at any point of the chapter, the reference numbers of the equations have been kept in the order in which they were developed (meaning the order is shared by both documents and jumps from one to the other), making it possible, for those interested, to follow the natural flow of the full working out of this method.

2.1. From Maxwell's Equations.

The basic structure to analyse is presented in Figure 2.1.1. It consists of an open parallel-plate waveguide filled with dielectric material, and a planar metallization of arbitrary shape supported by the dielectric layer, which is the source of the electric currents. The coordinates system used for the mathematical formulation is presented as well, and it will be settled as such for the remaining of the present work. The transversal section (z-x plane) and the longitudinal direction of propagation (y-direction) will be treated with different approaches:

- Transverse-longitudinal notation will be used in relation to the z-axis, that is to say, the z-axis will stand as the longitudinal direction during the initial analysis, although the modal propagation constant will be determined by the y-axis for the final structure. The **z-axis stands for the propagating direction of** the modal vector functions of the **Parallel-Plate Waveguide** (see next section), so this expansion will make possible to analyse in a simplified way the multilayered media (air-dielectric) and the radiation condition (both within the z direction). The x-y plane will be considered in this first approach as the transversal plane.

- The propagation direction cannot be considered as a homogeneous medium due to its periodicity. So periodicity in the y-axis will be modelled using a **Floquet modes expansion** (see 2.3 section). For each Floquet mode, the associated PPM expansion will exist, resulting in a complete full-wave analysis method for the whole structure.

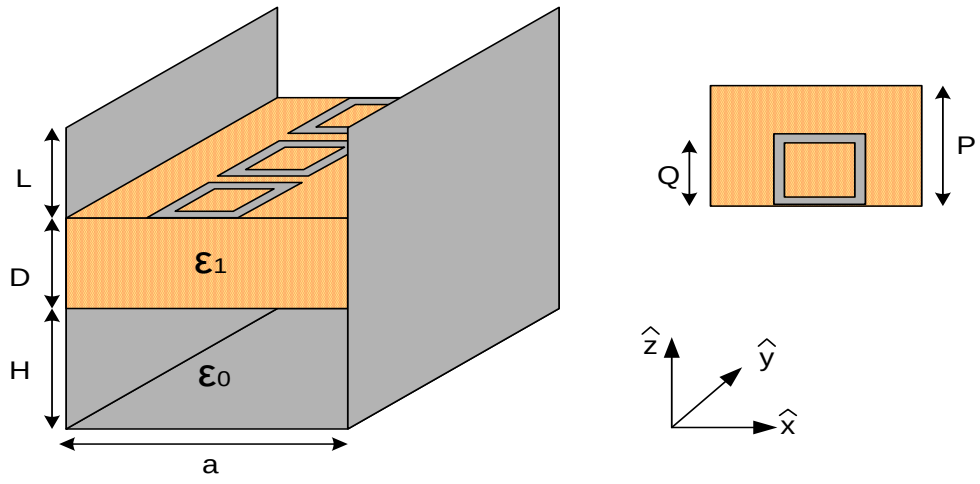

Figure 2.1.1: Basic structure.

The starting point will be Maxwell's Equations for time-harmonic (steady-state sinusoidal) fields when surface currents do exist in a simple medium (linear, isotropic and homogeneous). The temporal dependence will not be explicitly specified, it is assumed to be $e^{j\omega t}$ from now on.

$$\vec{\nabla}\times\vec{E} = -j\omega\mu\vec{H} \qquad (2.1.1)$$

$$\vec{\nabla}\times\vec{H} = \vec{J}_s + j\omega\varepsilon\vec{E} \qquad (2.1.2)$$

Where $\vec{E}$ and $\vec{H}$ are vector field phasors and $\vec{J}_s$ is the superficial source phasor, all of them containing information on direction, magnitude and phase.

As previously mentioned, it is along the z-axis where the multilayered media and the aperture to open space lay, so in order to take these discontinuities into account, it is necessary to assume the z-direction as the initial propagation direction for the Maxwell's Equations (2.1.1) and (2.1.2). With this aim, the previous equations will be split into their **transversal components** (x-y plane) and **longitudinal components** (z-axis). The expression of the fields using this transverse-longitudinal notation is:

$$\vec{E} = \vec{E}_t + \hat{z}E_z \qquad (2.1.3)$$

$$\vec{H} = \vec{H}_t + \hat{z}H_z \qquad (2.1.4)$$

From each Maxwell's Equation is derived a pair of longitudinal-transverse equations, which are summarised below. For the complete mathematical workout, see Appendix A Workout 1.

$$\vec{\nabla}_t\times\vec{E}_t = -j\omega\mu\hat{z}H_z \qquad (2.1.9)$$

$$\frac{\partial\vec{E}_t}{\partial z} - \vec{\nabla}_t E_z = -j\omega\mu\left(\vec{H}_t\times\hat{z}\right) \qquad (2.1.16)$$

$$\vec{\nabla}_t\times\vec{H}_t = +j\omega\varepsilon\hat{z}E_z \qquad (2.1.20)$$

$$\frac{\partial\vec{H}_t}{\partial z} - \vec{\nabla}_t H_z = -j\omega\varepsilon\left(\hat{z}\times\vec{E}_t\right) - \hat{z}\times\vec{J}_t \qquad (2.1.29)$$

As it can be seen, the transverse component equations (2.1.16) and (2.1.29) depend also on the longitudinal fields E_z and H_z. The objective is to obtain a set of transverse

equations independent of the longitudinal component. For this purpose it is needed to express the longitudinal fields in terms of the transverse fields. The complete process can be found in Appendix A Workout 2, obtaining the following set of transverse Maxwell's equations:

$$\frac{\partial \vec{E}_t}{\partial z} = -j\omega\mu\left(\vec{H}_t \times \hat{z}\right) + \frac{1}{j\omega\varepsilon}\vec{\nabla}_t\left[\vec{\nabla}_t(\vec{H}_t \times \hat{z})\right] \qquad (2.1.40)$$

$$\frac{\partial \vec{H}_t}{\partial z} = -j\omega\varepsilon\left(\hat{z} \times \vec{E}_t\right) + \frac{1}{j\omega\mu}\vec{\nabla}_t\left[\vec{\nabla}_t(\hat{z} \times \vec{E}_t)\right] - \hat{z} \times \vec{J}_t \qquad (2.1.41)$$

This pair of equations shows the general relation between the transverse current $\vec{J}_t$ and the coupled transverse fields $\vec{E}_t$ and $\vec{H}_t$ that it generates. As shown in Figure 2.1.1, the planar metallization extends on the x-y plane, so the only surface currents existing in the structure will be those induced on the patches and will be, using this notation, transversal currents.

2.2. Parallel Plate Modes Expansion

They are one of the main keys to the simplicity of the present method, allowing the modelling of the propagating fields within the structure in the space domain directly. It is fundamental to understand their nature and properties as a complete function set.

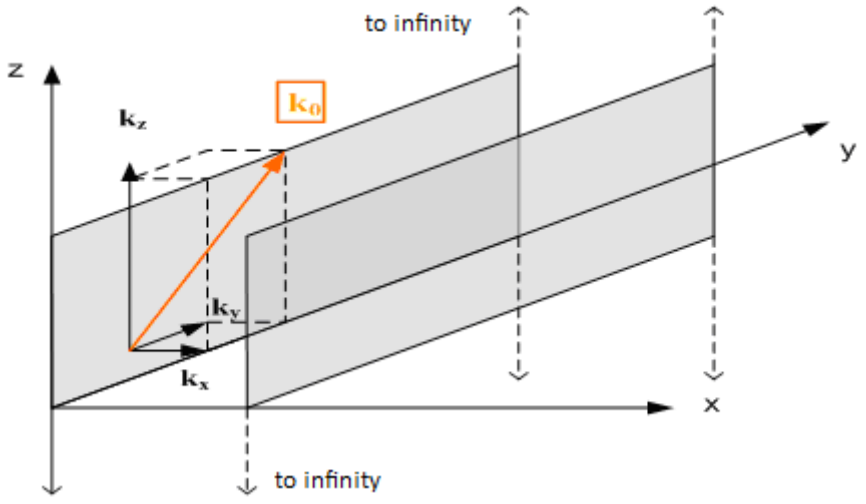

Figure 2.2.1: Parallel – Plate Basic configuration.

A Parallel-Plate transmission line consists of two parallel conducting plates separated by a dielectric slab of uniform thickness and width "a" (see Figure 2.2.1). In this sort of structure, Parallel- Plate modes propagate in form of plane waves ([Cheng 1989], [Cheng 1997]). Each of them propagates in a certain direction and with a certain wavenumber vector:

$$\vec{k}_0 = k_x\hat{x} + k_y\hat{y} + k_z\hat{z} \qquad (2.2.1)$$

And each of them must satisfy the boundary conditions of the parallel plates, so the propagation constant in the x axis is determined by:

$$k_{mx} = m\frac{\pi}{a}(rad/m) \qquad (2.2.2)$$

where $m = 1, 2..\infty$ is the modal index, meaning the number of harmonic variations in the x direction. This set of modes forms a complete base for the parallel plate structure, so any field existing within this structure can be defined as a contribution of these modes.

The structure that is being analysed is a modification of the basic parallel plate waveguide (Figure 2.2.1). The transverse fields which can exist in this type of structure can be expanded as series of the vector mode functions of the parallel plate waveguide, since these modal functions satisfy the boundary conditions of the metal side walls, in which the multilayered media is contained. But, due to its complexity, the new boundary conditions (multilayered media, planar metallization, metallic bottom wall...) cannot be satisfied by these PPM alone. In following sections, it will be shown how these discontinuities are taken into account in the expansion and how its development will lead to the equivalent modal transmission lines.

The following equations show the standard procedure to express the modal solutions of the structure in a sum of PPM, using the transverse-longitudinal notation. The z direction is chosen as the longitudinal propagating direction of the PPW. As the cross section of the PPW with a horizontal homogeneous dielectric slab of a given permittivity is uniform for each z position (in any point of the x-y plane), an analysis in the z direction can be done to account for the dielectric discontinuities, as it will be shown in later sections. The $e^{-jk_z z}$ variation on the longitudinal axis z is assumed, so it will be omitted within this development.

TE MODES

$$Ez = 0$$

$$Hz_m = \phi_m^{TE} = -\cos(k_{xm}x)e^{-jk_{ym}y}, \text{m=0,1,2...}$$

$$\vec{Ht}_m = -\vec{\nabla}t \cdot \phi_m^{TE} = \left[-k_{xm}\sin(k_{xm}x)\hat{x} - jk_{ym}\cos(k_{xm}x)\hat{y}\right]e^{-jk_{ym}y}$$

$$\vec{Et}_m = \frac{\vec{Ht}_m \times \hat{z}}{Z_{TE}} = \frac{1}{Z_{TE}}\left[-jk_{ym}\cos(k_{xm}x)\hat{x} + k_{xm}\sin(k_{xm}x)\hat{y}\right]e^{-jk_{ym}y}$$

$$\vec{e}_m(x,y) = \frac{-jk_{ym}\cos(k_{xm}x)\hat{x} + k_{xm}\sin(k_{xm}x)\hat{y}}{N_m}e^{-jk_{ym}y} \qquad (2.2.3)$$

TM MODES

$$Hz = 0$$

$$Ez_m = \phi_m^{TM} = -\sin(k_{xm}x)e^{-jk_{ym}y}, m = 1,2...$$

$$\vec{Et}_m = -\vec{\nabla}t \cdot \phi_m^{TM} = \left[+k_{xm}\cos(k_{xm}x)\hat{x} - jk_{ym}\sin(k_{xm}x)\hat{y}\right]e^{-jk_{ym}y}$$

$$\vec{e}_m(x,y) = \frac{+k_{xm}\cos(k_{xm}x)\hat{x} - jk_{ym}\sin(k_{xm}x)\hat{y}}{N_m}e^{-jk_{ym}y} \qquad (2.2.4)$$

It is important to note that, the same way the propagation coefficient k_{mx} is expanded as series of vector mode functions, where "mx" stands for the Parallel Plate mode order, the propagation factor k_{my} is expanded too, but as series of Floquet Modes using the same expansion index "my". The meaning of this second expansion will be developed thoroughly in the next section.

Equations (2.2.3) and (2.2.4) express the normalized modal transverse vector electric functions (the expression for the normalization coefficient N_m will be deduced further on in this section). The dependence with the y coordinate that has been taken into consideration for the whole development of these expressions is that of a plane wave propagating in an infinite medium in the y axis, $e^{-jk_{ym}y}$, and this scalar function can be separated from the modal vector functions dependence with the x coordinate:

$$\vec{e}_m^{(p)}(x,y) = \vec{e}_m^{(p)}(x) \cdot e^{-jk_{ym}y} \qquad (2.2.5)$$

This reasoning applied to equations (2.2.3) and (2.2.4) leads to the expression of the transverse vector functions for the electric fields:

$$\vec{e}_m^{\,TE}(x) = \frac{-jk_{ym}\cos(k_{xm}x)\hat{x} + k_{xm}\sin(k_{xm}x)\hat{y}}{N_m} \qquad (2.2.6)$$

$$\vec{e}_m^{\,TM}(x) = \frac{+k_{xm}\cos(k_{xm}x)\hat{x} - jk_{ym}\sin(k_{xm}x)\hat{y}}{N_m} \qquad (2.2.7)$$

The relationship between the electric and the magnetic normalized transverse vector mode functions is presented below:

$$\vec{h}_m^{(p)}(x,y) = \hat{z} \times \vec{e}_m^{(p)}(x,y) \qquad (2.2.8)$$

$$\vec{e}_m^{(p)}(x,y) = \vec{h}_m^{(p)}(x,y) \times \hat{z} \qquad (2.2.9)$$

Applying equation (2.8) on expressions (2.6) and (2.7), the transverse vector functions for the magnetic fields are obtained:

$$\vec{h}_m^{TE}(x) = \frac{-k_{xm}\sin(k_{xm}x)\hat{x} - jk_{ym}\cos(k_{xm}x)\hat{y}}{N_m} \qquad (2.2.10)$$

$$\vec{h}_m^{TM}(x) = \frac{+jk_{ym}\sin(k_{xm}x)\hat{x} + k_{xm}\cos(k_{xm}x)\hat{y}}{N_m} \qquad (2.2.11)$$

The modal vector functions $\vec{e}_m^{(p)}(x,y)$ and $\vec{h}_m^{(p)}(x,y)$ are the different type of plane waves (p=1, 2 for TE and TM) which can propagate in the PPW shown in Figure 2.2.1, with no other discontinuity but the two side metal walls. Before adapting them to the new structure, the inner product will be used in order to set these modal vector functions as a complete base.

The definition of the **inner product** in terms of the scalar product of either electric fields or magnetic fields will be used to establish the concept of orthogonal coordinate system of a vectorial space. This orthogonality relation probes the completeness property of a set of normal modes. The establishment of this base is necessary to expand the fields as a linear combination of PPM (base vectors). The general expression of the inner product is showed below:

$$I_{P_m Q_n^*} = \int_{x=0}^{a} \vec{e}_m^{\,(p)}(x) \cdot \vec{e}_n^{\,(q)*}(x) \cdot \partial x = \int_{x=0}^{a} \vec{h}_m^{\,(p)}(x) \cdot \vec{h}_n^{\,(q)*}(x) \cdot \partial x = \\ = \int_{x=0}^{a} \vec{e}_m^{\,(p)}(x) \times \vec{h}_n^{\,(q)*}(x) \cdot \hat{z} \cdot \partial x \qquad (2.2.12)$$

where m,n= 0,1… ∞ is the order of the PPM and p,q=TE or TM.

This definition has been studied before by many authors due to its importance to expand any electromagnetic field inside a given geometry [Collin 1960]. Note that the last expression corresponds with the density of power propagating in z. This way the inner product gives the idea of how much energy is coupled between modes (m and n modes with any polarization). This is especially important, since in the case of an open structure, the propagation constant becomes complex, and the inner product definition probes that the PPM base is not orthogonal [Gómez March-2004]. This is because PPM TE^z and TM^z leaky modes have not only a complex k_z propagating factor, but also a complex k_y propagating factor, due to the unbounded z and y directions.

Evaluating in the first place the inner product between modes with electric fields with the same polarization, it results as follows:

$$I = \int_0^a \vec{e}_m^{\,TE}(x) \cdot \vec{e}_n^{\,TE*}(x) dx = \int_0^a \vec{e}_m^{\,TM}(x) \cdot \vec{e}_n^{\,TM*}(x) dx = \\ = \begin{cases} \frac{1}{2} a \frac{|k_{ym}|^2 + k_{xm}^{\,2}}{|N_m|^2} & \text{if m=n>0} \\ a \frac{|k_{ym}|^2 + k_{xm}^{\,2}}{|N_m|^2} & \text{if m=n=0} \\ 0 \quad \text{if } m \neq n \quad \text{(orthogonal)} \end{cases} \qquad (2.2.13)$$

It can be seen that those modes with the same polarization and different modal index are orthogonal. The **normalization coefficient** N_m is defined so that the set of modal vector functions is not only orthogonal, but orthonormal, obtaining:

$$\boxed{N_m = \sqrt{\frac{a}{2}} \delta \cdot \sqrt{k_{xm}^{\,2} + |k_{ym}|^2}} \quad \text{with } \delta = 1 \text{ if m=n>0 or } \delta = 2 \text{ if m=n=0} \qquad (2.2.14)$$

Evaluating now the inner product between modes with electric fields with different polarization, and taking into account that the k_{xm} conjugate is equal to k_{xm}, since it is a real number, it results as follows:

$$I=\int_0^a \vec{e}_m^{\,TE}(x)\cdot\vec{e}_n^{\,TM*}(x)dx=\begin{cases}-\frac{1}{2}\,jk_{xm}a\,\frac{k_{ym}{}^2-\left|k_{ym}\right|^2}{k_{ym}\cdot\left|N_m\right|^2}=\frac{-jk_{xm}(k_{ym}-k_{ym}^*)}{\left|N_m\right|^2}\frac{a}{2} & \text{if m=n>0}\\ \frac{-jk_{xm}(k_{ym}-k_{ym}^*)}{\left|N_m\right|^2}a & \text{if m=n=0}\\ 0 & \text{if } m\neq n \text{ (orthogonal)}\end{cases} \qquad (2.2.15)$$

Just as in the case with the same polarization, the base vectors with different modal index are orthogonal among them, but in this case, it can be appreciated how the inner product between the same modal index PPM is not an unitary scalar, but a certain expression. This expression will be defined as the **coupling coefficient** C_m, as shown:

$$\boxed{C_m=\frac{jk_{xm}(k_{ym}-k_{ym}^*)}{\left|N_m\right|^2}\frac{a}{2}\delta} \quad \text{with } \delta=1 \text{ if m=n>0 or } \delta=2 \text{ if m=n=0} \qquad (2.2.16)$$

It is interesting to notice that only in the case that k_{ym} is a real number, the coupling coefficient will be zero, and the basis will be orthonormal,

Introducing the normalization and the coupling coefficients into the previous results and resuming both cases, those with same and different polarization, into one single expression leads to the next relation of orthonomality that the PPM fulfil according to the **inner product definition** in (2.2.12):

$$I_{P_mQ_n^*}=\int_0^a \vec{e}_m^{\,(p)}(x)\cdot\vec{e}_n^{\,(q)*}(x)dx=\begin{cases}1 & \text{if p=q and m=n}\\ 0 & \text{if } m\neq n\\ C_m & \text{if } p\neq q \text{ and m=n}\end{cases} \qquad (2.2.17)$$

The equation (2.2.17) can be explained under a physical point of view, knowing that the inner product express the cross power among modes that propagates in the z axis, that is to say, the coupled energy between different PPM. It was stated before that C_m was zero

only if the propagation constant in the longitudinal direction k_{ym} was real. In other words, when there are no losses in the y direction (closed structure or non radiating modes), the PPM are orthogonal (there is no coupled energy). However, if there is any type of losses or attenuation in the longitudinal direction, k_{ym} will be complex and the coupling coefficient will have a certain value. This means that the modes TE and TM of the same order will be coupled and will not be orthogonal between them. This aspect must be taken into account when developing the analysis method, and will lead to a coupled set of equivalent transmission lines in the z-direction (section 2.5).

It was expected that the modal vector functions $\vec{e}_m^{(p)}(x,y)$ and $\vec{h}_m^{(p)}(x,y)$ are no more solutions in the new more complex structure, since they separately do not satisfy the new boundary conditions imposed in the z axis (bottom metal wall, metallization strips, multilayered media...). The key is that the fields which can exist in this structure can be expanded by a series of these modal functions adding an scalar amplitude for each mode ($V_m^{(p)}(z)$ for TE and $I_m^{(p)}(z)$ for TM) that will take into account the discontinuities in the z axis as will be shown in section 2.5. The following couple of equations model the PPM expansion for the complex structure:

$$\vec{E}t(x,y,z) = \sum_{p}^{TE,TM} \sum_{m=0}^{\infty} V_m^{(p)}(z) \cdot \vec{e}_m^{(p)}(x) \cdot e^{-jk_y y} \qquad (2.2.18)$$

$$\vec{H}t(x,y,z) = \sum_{p}^{TE,TM} \sum_{m=0}^{\infty} I_m^{(p)}(z) \cdot \vec{h}_m^{(p)}(x) \cdot e^{-jk_y y} \qquad (2.2.19)$$

It must be noticed that originally, the z dependence of the PPM was defined by $e^{-jk_z z}$, as a plane wave propagating freely in the z direction. In the new structure, more complex dependency in the z axis was needed to model wave reflections at the discontinuities, so new functions have been introduced for the expansion. The second thing to remember is that every mode propagating in the y direction (these Floquet modes will be seen in the next section), has a PPM expansion in the z-x plane, so those parallel-plate modes will share the same propagation constant in y axis, k_{my}, the longitudinal direction of the final structure.

2.3. Floquet Modes Expansion

Along the longitudinal y direction of the structure, the antenna presents a periodicity P which determines the unit cell length. The analysis of this sort of structure can be made applying Floquet theory ([Brillouin 1946], [Brillouin 1960], [Vardaxoglou 1997]). In [Gomez Sept-2005] it was used to analyze for the first time laterally-shielded periodic leaky-wave antennas.

The electromagnetic fields in a periodic structure (periodic boundary conditions) are periodic with the exception of a propagation coefficient in the periodicity direction, k_{y0}, called **bloch-wavenumber**. Assuming periodicity along y direction, they can be expressed:

$$\vec{E}(x,y,z) = e^{-jk_{y0}y}\vec{E}_p(x,y,z) \qquad (2.3.1)$$

$$\vec{H}(x,y,z) = e^{-jk_{y0}y}\vec{H}_p(x,y,z) \qquad (2.3.2)$$

The fields in each unit cell can be expanded using spatial harmonics in the y direction ([Oliner 1993], [Tzuang 2000], [Schwering 1983]), the so called **Floquet Modes**:

$$\vec{E}_p(x,y,z) = \sum_{p}^{TE,TM}\sum_{my=-\infty}^{\infty}\vec{E}_{my}^{(p)}(x,z)e^{-jk_{ym}y} \qquad (2.3.3)$$

$$\vec{H}_p(x,y,z) = \sum_{p}^{TE,TM}\sum_{my=-\infty}^{\infty}\vec{H}_{my}^{(p)}(x,z)e^{-jk_{ym}y} \qquad (2.3.4)$$

So, it all can be resumed:

$$\vec{E}(x,y,z) = e^{-jk_{y0}y}\sum_{p}^{TE,TM}\sum_{my=-\infty}^{\infty}\vec{E}_{my}^{(p)}(x,z)e^{-jk_{ym}y} = \sum_{p}^{TE,TM}\sum_{my=-\infty}^{\infty}\vec{E}_{my}^{(p)}(x,z)e^{-jk_{my}y} \qquad (2.3.5)$$

$$\vec{H}(x,y,z) = e^{-jk_{y0}y}\sum_{p}^{TE,TM}\sum_{my=-\infty}^{\infty}\vec{H}_{my}^{(p)}(x,z)e^{-jk_{ym}y} = \sum_{p}^{TE,TM}\sum_{my=-\infty}^{\infty}\vec{H}_{my}^{(p)}(x,z)e^{-jk_{my}y} \qquad (2.3.6)$$

where $\boxed{k_{my} = k_{y0} + k_{ym} = k_{y0} + my\frac{2\pi}{P}}$ (2.3.7)

It is important to note that due to radiation losses of the leaky waves, the bloch-wavenumber k_{y0} becomes complex, having a **phase constant** β_{y0} and an **attenuation constant** α_y. In this way, the leakage effect makes the propagation constant of any space harmonic k_{my} complex:

$$k_{my} = k_{y0} + k_{ym} = (\beta_{y0} - j\alpha_y) + my\frac{2\pi}{P} = \left(\beta_{y0} + my\frac{2\pi}{P}\right) - j\alpha_y \qquad (2.3.8)$$

In the last section, the Parallel Plate Modes were introduced to expand the fields in the structure, and as showed below, a mode expansion in the y direction was taken into account, but not yet explained. Now that k_{my} is defined, the Floquet modes expansion can be easily introduced in the expressions of the fields:

$$\vec{E}^z(x,y,z) = \sum_{p}^{TE,TM} \sum_{mx=0}^{\infty} \sum_{my=-\infty}^{\infty} V_{mx,my}^{(p)}(z)\vec{e}_{mx}^{(p)}(x)e^{-jk_{my}y} \qquad (2.3.9)$$

$$\vec{H}^z(x,y,z) = \sum_{p}^{TE,TM} \sum_{mx=0}^{\infty} \sum_{my=-\infty}^{\infty} I_{mx,my}^{(p)}(z)\vec{h}_{mx}^{(p)}(x)e^{-jk_{my}y} \qquad (2.3.10)$$

In these expressions the notation can be changed as shown below. This will be useful in later sections.

$$\vec{e}_{mx,my}^{(p)}(x,y) = \vec{e}_{mx}^{(p)}(x)e^{-jk_{my}y} \qquad (2.3.11)$$

$$\vec{h}_{mx,my}^{(p)}(x,y) = \vec{h}_{mx}^{(p)}(x)e^{-jk_{my}y} \qquad (2.3.12)$$

To probe that the series of Floquet modes are an orthogonal coordinate system of a vectorial space, the definition of the **inner product** (in terms of the scalar product of either electric fields or magnetic fields) will be used, in a similar way that it was done for the PPM. The general expression of the inner product and its resolution are showed below:

$$I_{P_{my}Q_{ny}^*} = \int_{x=0}^{P} e^{-jk_{my}y} \cdot e^{+jk_{ny}y}\partial y = \begin{cases} 0 \rightarrow my \neq ny \\ P \rightarrow my = ny \end{cases} \qquad (2.3.13)$$

where $k_{my} = k_{y0} + my\frac{2\pi}{P}$ and $k_{ny} = k_{y0} + ny\frac{2\pi}{P}$.

The **normalization coefficient** N_m is defined so that the set of modal vector functions is not only orthogonal, but orthonormal. It can easily be deduced from (2.3.13):

$$\boxed{N_m = \sqrt{\frac{1}{P}}} \qquad (2.3.14)$$

The conclusion is that there's no coupling between any mode or polarization in this expansion, since the Floquet modes are orthonormal by definition, even for complex propagation constants.

2.4. Radiation Condition

The open laterally-shielded leaky-wave antenna may or may not radiate, depending on certain conditions. This was one of the main improvements that [Gomez August-2005] introduced, opening the structure on the wide side of the rectangular waveguide. This simple change made a huge difference, from the previously studied LWA [Guglielmi 1991] that radiated in any case and without any control, to the tapered continuous LWA in which the illumination, and so the radiation pattern, could be modified at will.

The radiation mechanism is achieved, from the non-radiative open waveguide structure in which the transversal field would be defined by the TE_{10} mode, by introducing a spatial asymmetry in the $\hat{x}$ direction, in such a way that the fundamental PPW mode m=0 is excited. This fundamental mode is a non-homogeneous plane wave with horizontal polarization, that is to say, its electric field is perpendicular to the side walls.

The physical explanation is that the asymmetrically located patch induces a difference of charge (unbalanced coupling of the TE_{10} to the side walls). This way, the vertically polarized TE_{10} mode is transformed into a horizontal field in the parallel-plate region. This horizontal field can propagate, reaching the aperture at the top and inducing radiation. This mechanism is clearly illustrated by means of field lines on Figure 2.4.1.

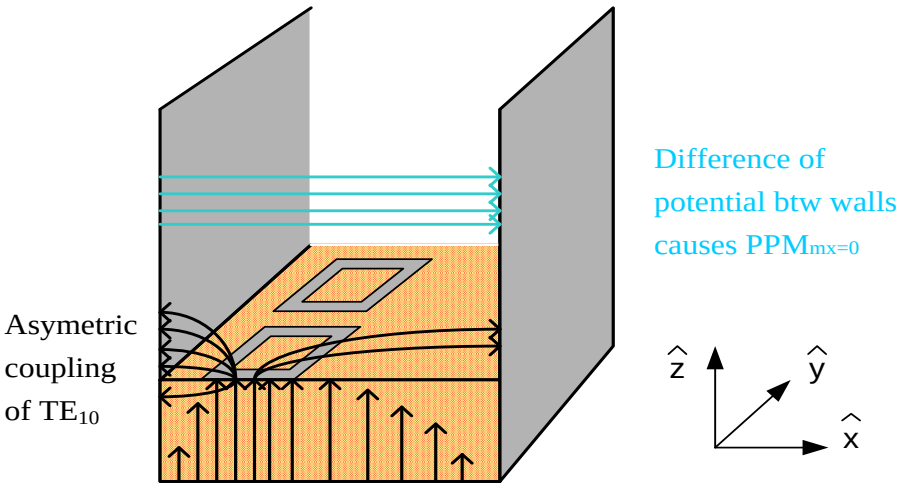

Figure 2.4.1: Radiation Mechanism.

At this point, it is interesting to remember that in the first attempts of the leaky-wave antenna, as in the INSET of Guglielmi, the mode responsible for the radiation was the TE_{01}, which was able to radiate without the need of introducing any asymmetry due to its inherent horizontal polarization. It simply escaped from the open waveguide. This is an extremely important difference; it has evolved from a structure that radiated by intrinsic mechanism to a second one in which the radiation is intentionally caused by a variable parameter, the asymmetry. It is precisely that variability what provides tuneable control means for the radiation, and therefore, makes it possible to do taper designs with fixed aiming angle of the main lobe at a specific frequency.

As probed in [Gomez 1994], the only mode responsible for the radiation is the PPW m=0, while the rest of higher order modes (m>0) spoil the radiation performance. The conditions for the fundamental PPW mode to be the only mode excited and responsible for the radiation, are given by the geometrical parameters.

Once the PPW mode m=0 is excited, it has to meet a second condition in order to radiate, since this excitation by itself is not enough. The mentioned mode must have a propagative k_z, what is known as fast wave. To achieve it, it is necessary k_z to be a real number.

$$m=0 \rightarrow \quad k_x = \sum_{m=0}^{m=\infty} k_{x,m} = \sum_{m=0}^{m=\infty} m\frac{\pi}{a} = 0 \qquad (2.4.1)$$

$$k_x^2 + k_y^2 + k_z^2 = k_0^2 \rightarrow k_z = \sqrt{k_0^2 - k_x^2 - k_y^2}$$

$$k_z = \sqrt{k_0^2 - k_y^2} \qquad (2.4.2)$$

There are two possibilities:

a) The propagation constant in the direction $\hat{z}$ is an imaginary number:

$$k_0^2 - k_y^2 \le 0 \qquad (2.4.3)$$

$$\left|\frac{k_y}{k_0}\right| \ge 1 \rightarrow \quad \boxed{k_z = -j\alpha_z} \qquad (2.4.4)$$

This is the case of a **slow wave** and therefore, it does not radiate. The energy decreases exponentially in the $\hat{z}$ direction and fades away before it can get out of the parallel plates of the waveguide.

b) The propagation constant in the direction $\hat{z}$ is a real number:

$$k_0^2 - k_y^2 \ge 0 \qquad (2.4.5)$$

$$\left|\frac{k_y}{k_0}\right| \le 1 \rightarrow \quad \boxed{k_z = \beta_z} \qquad (2.4.6)$$

In this case k_y is within the **fast wave** zone and k_z is real and propagative. It is called so, "fast wave" because the longitudinal phase velocity is bigger than the speed of light. The PPM mx=0 is able to propagate towards the aperture. It can be probed that the higher order PPM are evanescent in the structure, applying the same procedure:

$$m=1 \rightarrow \quad k_x = \sum_{m=0}^{m=\infty} k_{x,m} = \sum_{m=0}^{m=\infty} m\frac{\pi}{a} = \frac{\pi}{a} \qquad (2.4.7)$$

$$k_x^2 + k_y^2 + k_z^2 = k_0^2 \rightarrow k_z = \sqrt{k_0^2 - k_x^2 - k_y^2}$$

$$k_z = \sqrt{k_0^2 - \left(\frac{\pi}{a}\right)^2 - k_y^2} = k_0\sqrt{1 - \left(\frac{\pi}{ak_0}\right)^2 - \left(\frac{k_y}{k_0}\right)^2} \qquad (2.4.8)$$

In order for the PPM mx=1 not to propagate along the parallel plates it is necessary that:

$$\frac{k_y}{k_0} \geq \sqrt{1-\left(\frac{\pi}{ak_0}\right)^2} \qquad (2.4.9)$$

The propagation constant of the TE_{10}, propagating in the y direction, can be approximated for that of a PPM mx=1 (as both have the same harmonic variation). For a waveguide filled with dielectric, as will be the case either partially or completely, this propagation constant can be written as:

$$\frac{k_y^{TE_{10}}}{k_0} \geq \sqrt{\varepsilon_r-\left(\frac{\pi}{ak_0}\right)^2} \qquad (2.4.10)$$

It can be easily seen that, since $\varepsilon_r \geq 1$, the PPM mx=1 will be evanescent in the z-direction, and therefore so will be any other higher PPM.

Figure 2.4.2 shows the theoretical behaviour of the three first Floquet harmonics associated to the PPM mx=0, in terms of how the normalized propagation constant increases with the frequency. The blue line represents the first Floquet harmonic, which after cut-off radiates only forward from broadside. The plot is focused on the radiation zone or fast-wave region of the second harmonic my=-1, in green. Said harmonic radiates while its normalised propagation constant is between [-1, 1]. This picture will help the reader to understand how the aiming angle of the leaky mode varies with the frequency from backward endfire to broadside, and finally to forward endfire and how it becomes a surface wave afterwards. These concepts will be dealt in depth in the final chapters, when analyzing the obtained results.

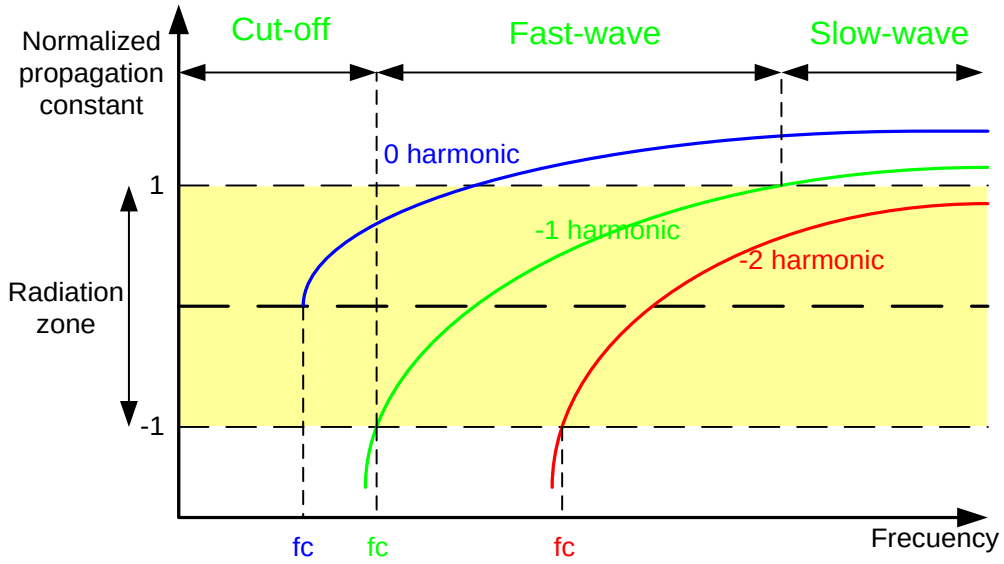

Figure 2.4.2 Theoretical propagation of a periodic LWA

Summarizing:

To produce a radiating TE_{10} mode it is necessary to meet two conditions:

1.- The PPW m=0 mode must be excited $\rightarrow$ asymmetry in $\hat{x}$.

2.- k_y must be within the *fast wave* zone.

2.5. Equivalent Transmission Line

In order to obtain the desired Green Functions of an elemental electric source in a structure consisting of a parallel plate waveguide with a stratified dielectric media, it is necessary to express the equivalent modal transmission line equations of this structure. For this purpose, the transverse Maxwell equations (2.1.40) and (2.1.41), and the transverse-fields modal expansions (2.3.9) and (2.3.10), obtained in previous sections, will be combined in this section.

$$\frac{d\vec{E}_t}{dz} = -j\omega\mu\left(\vec{H}_t \times \hat{z}\right) + \frac{1}{j\omega\varepsilon}\vec{\nabla}_t\left[\vec{\nabla}_t(\vec{H}_t \times \hat{z})\right] \quad (2.1.40)$$

$$\frac{d\vec{H}_t}{dz} = -j\omega\varepsilon\left(\hat{z} \times \vec{E}_t\right) + \frac{1}{j\omega\mu}\vec{\nabla}_t\left[\vec{\nabla}_t(\hat{z} \times \vec{E}_t)\right] - \hat{z} \times \vec{J}_t \quad (2.1.41)$$

$$\vec{E}_t(x,y,z) = \sum_{p}^{TE,TM}\sum_{mx=0}^{\infty}\sum_{my=-\infty}^{\infty} V_{mx,my}^{(p)}(z)\vec{e}_{mx}^{(p)}(x)e^{-jk_{my}y} = \sum_{p}^{TE,TM}\sum_{mx=0}^{\infty}\sum_{my=-\infty}^{\infty} V_{mx,my}^{(p)}(z)\vec{e}_{mx,my}^{(p)}(x,y)$$

(2.3.9)

$$\vec{H}_t(x,y,z) = \sum_{p}^{TE,TM}\sum_{mx=0}^{\infty}\sum_{my=-\infty}^{\infty} I_{mx,my}^{(p)}(z)\vec{h}_{mx}^{(p)}(x)e^{-jk_{my}y} = \sum_{p}^{TE,TM}\sum_{mx=0}^{\infty}\sum_{my=-\infty}^{\infty} I_{mx,my}^{(p)}(z)\vec{h}_{mx,my}^{(p)}(x,y)$$

(2.3.10)

Remember that the indexes *mx* and *my* stand for the PPM order and Floquet modes order respectively. The modal expansions of the transverse fields are introduced into the transverse Maxwell Equations, resulting in the expressions showed below. First from (2.1.40):

$$\sum_{p}^{TE,TM}\sum_{mx=0}^{\infty}\sum_{my=-\infty}^{\infty}\frac{dV_{mx,my}^{(p)}(z)}{dz}\vec{e}_{mx,my}^{(p)}(x,y) = -j\omega\mu\left(\sum_{p}^{TE,TM}\sum_{mx=0}^{\infty}\sum_{my=-\infty}^{\infty} I_{mx,my}^{(p)}(z)\left(\vec{h}_{mx,my}^{(p)}(x,y)\times\hat{z}\right)\right) +$$

$$+\frac{1}{j\omega\varepsilon}\vec{\nabla}_t\left[\vec{\nabla}_t\left(\sum_{p}^{TE,TM}\sum_{mx=0}^{\infty}\sum_{my=-\infty}^{\infty} I_{mx,my}^{(p)}(z)\left(\vec{h}_{mx,my}^{(p)}(x,y)\times\hat{z}\right)\right)\right] \quad (2.5.1)$$

Second from (2.1.41):

$$\sum_{p}^{TE,TM}\sum_{mx=0}^{\infty}\sum_{my=-\infty}^{\infty}\frac{dI_{mx,my}^{(p)}(z)}{dz}\vec{h}_{mx,my}^{(p)}(x,y) = -j\omega\varepsilon\left(\sum_{p}^{TE,TM}\sum_{mx=0}^{\infty}\sum_{my=-\infty}^{\infty} V_{mx,my}^{(p)}(z)\left(\hat{z}\times\vec{e}_{mx,my}^{(p)}(x,y)\right)\right) +$$

$$+\frac{1}{j\omega\mu}\vec{\nabla}_t\left[\vec{\nabla}_t\left(\sum_{p}^{TE,TM}\sum_{mx=0}^{\infty}\sum_{my=-\infty}^{\infty} V_{mx,my}^{(p)}(z)\left(\hat{z}\times\vec{e}_{mx,my}^{(p)}(x,y)\right)\right)\right] -$$

$$-\sum_{p}^{TE,TM}\sum_{mx=0}^{\infty}\sum_{my=-\infty}^{\infty} j_{mx,my}^{(p)}(z)\left(\hat{z}\times\vec{e}_{mx,my}^{(p)}(x,y)\right) \quad (2.5.2)$$

Where the transverse current $\vec{J}_t(x,y,z)$ has suffered both modal expansions as well:

$$\vec{J}_t(x,y,z) = \sum_{p}^{TE,TM} \sum_{mx=0}^{\infty} \sum_{my=-\infty}^{\infty} j_{mx,my}^{(p)}(z)\vec{e}_{mx}^{(p)}(x)e^{-jk_{my}y} = \sum_{p}^{TE,TM} \sum_{mx=0}^{\infty} \sum_{my=-\infty}^{\infty} j_{mx,my}^{(p)}(z)\vec{e}_{mx,my}^{(p)}(x,y)$$

(2.5.3)

The procedure applied on these two previous equations (2.5.1) and (2.5.2) can be found in Appendix A Workout 3, and it includes the following steps:

1. The two different polarizations, TE and TM, will be separately considered and referred by a superscript index as (p) or (q), depending on the case.

2. By applying the definition of the inner product for the Parallel Plates modes on each polarization's expression, the summation in terms of "x" will be eliminated, obtaining the following set of equations:

$$\sum_{my=-\infty}^{\infty} \frac{dV_{mx,my}^{(p)}(z)}{dz}e^{-jk_{my}y} + \sum_{my=-\infty}^{\infty} \frac{dV_{mx,my}^{(q)}(z)}{dz}C_m e^{-jk_{my}y} =$$

$$= -j \sum_{my=-\infty}^{\infty} Z_{0m}^{(p)} k_{zm} I_{mx,my}^{(p)}(z)e^{-jk_{my}y} - j \sum_{my=-\infty}^{\infty} C_m Z_{0m}^{(q)} k_{zm} I_{mx,my}^{(q)}(z)e^{-jk_{my}y}$$

(2.5.15)

$$\sum_{my=-\infty}^{\infty} \frac{dI_{mx,my}^{(p)}(z)}{dz}e^{-jk_{my}y} + \sum_{my=-\infty}^{\infty} \frac{dI_{mx,my}^{(q)}(z)}{dz}C_m e^{-jk_{my}y} = -j\frac{k_z^2}{Z_{0m}^{(p)}} \sum_{my=-\infty}^{\infty} V_{mx,my}^{(p)}(z)e^{-jk_{my}y} -$$

$$- \sum_{my=-\infty}^{\infty} j_{mx,my}^{(p)}(z)e^{-jk_{my}y} + C_m\left(-j\frac{k_z^2}{Z_{0m}^{(q)}} \sum_{my=-\infty}^{\infty} V_{mx,my}^{(q)}(z)e^{-jk_{my}y} - \sum_{my=-\infty}^{\infty} j_{mx,my}^{(q)}(z)e^{-jk_{my}y}\right)$$

(2.5.25)

3. By applying the definition of the inner product for the Floquet modes on each polarization's expression resulting from the step no.2, the summation in terms of "y" will be eliminated.

$$\frac{dV_{mx,my}^{(p)}(z)}{dz} + \frac{dV_{mx,my}^{(q)}(z)}{dz}C_m = -jZ_{0m}^{(p)}k_{zm}I_{mx,my}^{(p)}(z) - jC_m Z_{0m}^{(q)}k_{zm}I_{mx,my}^{(q)}(z) \qquad (2.5.27)$$

$$\frac{dI_{mx,my}^{(p)}(z)}{dz} + \frac{dI_{mx,my}^{(q)}(z)}{dz}C_m = -j\frac{k_z^2}{Z_{0m}^{(p)}}V_{mx,my}^{(p)}(z) - j_{mx,my}^{(p)}(z) + C_m\left(-j\frac{k_z^2}{Z_{0m}^{(q)}}V_{mx,my}^{(q)}(z) - j_{mx,my}^{(q)}\right)$$

(2.5.29)

4. Due to the previous steps, a pair of coupled equations in terms of polarization is obtained. The next step will be to decouple these expressions.

The equations (2.5.27) and (2.5.29) describe the behaviour of the modal functions $V_m^{(p)}(z)$ and $I_m^{(p)}(z)$, first introduced in the PPM expansion in section 2. At first sight, these equations remind of the system of differential equations from a transmission line, as shown in the Figure 2.5.1 below:

$$\begin{cases} \dfrac{\partial V_m^{(p)}(z)}{\partial z} = -jZ_{0m}^{(p)} \cdot k_{zm} \cdot I_m^{(p)}(z) \\ \dfrac{\partial I_m^{(p)}(z)}{\partial z} = -j\dfrac{1}{Z_{0m}^{(p)}} \cdot k_{zm} \cdot V_m^{(p)}(z) - j_m^{(p)}(z) \end{cases}$$

$$k_{zm} = \sqrt{k_o^2 \varepsilon_r - k_{cm}^2} = \sqrt{k_o^2 \varepsilon_r - k_{xm}^2 - k_y^2} = \sqrt{k_o^2 \varepsilon_r - \left(m\frac{\pi}{a}\right)^2 - k_y^2}$$

$$\begin{cases} Z_{0m}^{TE} = \dfrac{\omega\mu}{k_{zm}} \\ Z_{0m}^{TM} = \dfrac{k_{zm}}{\omega\varepsilon} \end{cases}$$

p=TE,TM m=0,1,2..

Figure 2.5.1 Equations for the Equivalent Tx line

This transmission line has as the propagation direction the z axis and an electric source in parallel, $j_m(z)$. It can be physically interpreted as shown in Figure 2.5.2, where an equivalent transmission line is created from the structure.

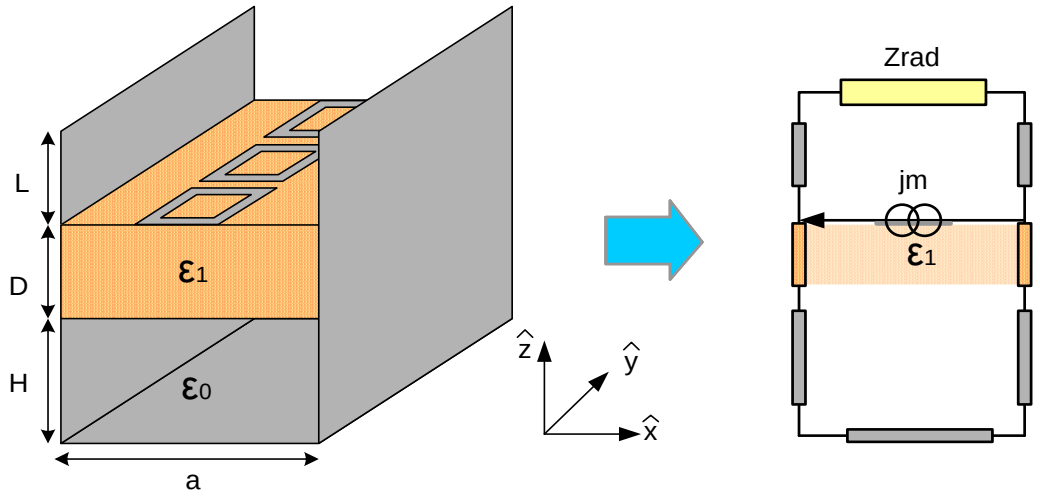

Figure 2.5.2: Equivalent transmission line.

However, in the equations (2.5.27) and (2.5.29) obtained from the analysis done so far, the TE and TM modes do not appear uncoupled, so the equivalent transmission line for the structure under study will not correspond exactly to the one in Figure 2.5.2, since that one does not take into account couplings. Next step is to consider separately both polarizations to get to a pair of coupled differential equations.

If the two possible combinations of polarizations are taken into account, the following expressions are obtained from (2.5.27) and (2.5.29):

p=TE and q=TM

$$\frac{d}{dz}\left(V_{mx,my}^{(TE)}(z)+V_{mx,my}^{(TM)}(z)C_m\right)=-jk_{zm}\left(Z_{0m}^{(TE)}I_{mx,my}^{(TE)}(z)+C_mZ_{0m}^{(TM)}I_{mx,my}^{(TM)}(z)\right) \quad \text{(A)}$$

$$\frac{d}{dz}\left(I_{mx,my}^{(TE)}(z)+I_{mx,my}^{(TM)}(z)C_m\right)=-jk_{zm}\left(\frac{V_{mx,my}^{(TE)}(z)}{Z_{0m}^{(TE)}}-C_m\frac{V_{mx,my}^{(TM)}(z)}{Z_{0m}^{(TM)}}\right)-\left(j_{mx,my}^{(TE)}(z)+C_mj_{mx,my}^{(TM)}(z)\right) \quad \text{(B)}$$

p=TM and q=TE

$$\frac{d}{dz}\left(V_{mx,my}^{(TM)}(z)+V_{mx,my}^{(TE)}(z)C_m\right)=-jk_{zm}\left(Z_{0m}^{(TM)}I_{mx,my}^{(TM)}(z)+C_mZ_{0m}^{(TE)}I_{mx,my}^{(TE)}(z)\right) \quad \text{(C)}$$

$$\frac{d}{dz}\left(I_{mx,my}^{(TM)}(z)+I_{mx,my}^{(TE)}(z)C_m\right)=-jk_{zm}\left(\frac{V_{mx,my}^{(TM)}(z)}{Z_{0m}^{(TM)}}-C_m\frac{V_{mx,my}^{(TE)}(z)}{Z_{0m}^{(TE)}}\right)-\left(j_{mx,my}^{(TM)}(z)+C_mj_{mx,my}^{(TE)}(z)\right) \quad \text{(D)}$$

$A-C_m\cdot C\Rightarrow$

$$\frac{d}{dz}\left(V_{mx,my}^{(TE)}(z)-C_m^2V_{mx,my}^{(TE)}(z)\right)=-jk_{zm}Z_{0m}^{(TE)}\left(I_{mx,my}^{(TE)}(z)-C_m^2I_{mx,my}^{(TE)}(z)\right) \quad (2.5.30)$$

$B-C_m\cdot D\Rightarrow$

$$\frac{d}{dz}\left(I_{mx,my}^{(TE)}(z)-C_m^2I_{mx,my}^{(TE)}(z)\right)=-j\frac{k_{zm}}{Z_{0m}^{(TE)}}\left(V_{mx,my}^{(TE)}(z)-C_m^2V_{mx,my}^{(TE)}(z)\right)-\left(j_{mx,my}^{(TE)}(z)-C_m^2j_{mx,my}^{(TE)}(z)\right) \quad (2.5.31)$$

$C-C_m\cdot A\Rightarrow$

$$\frac{d}{dz}\left(V_{mx,my}^{(TM)}(z)-C_m^2V_{mx,my}^{(TM)}(z)\right)=-jk_{zm}Z_{0m}^{(TM)}\left(I_{mx,my}^{(TM)}(z)-C_m^2I_{mx,my}^{(TM)}(z)\right) \quad (2.5.32)$$

$D-C_m\cdot B\Rightarrow$

$$\frac{d}{dz}\left(I_{mx,my}^{(TM)}(z)-C_m^2I_{mx,my}^{(TM)}(z)\right)=-j\frac{k_{zm}}{Z_{0m}^{(TE)}}\left(V_{mx,my}^{(TM)}(z)-C_m^2V_{mx,my}^{(TM)}(z)\right)-\left(j_{mx,my}^{(TM)}(z)-C_m^2j_{mx,my}^{(TM)}(z)\right) \quad (2.5.33)$$

Equations (2.5.30) and (2.5.31) for the TE, and (2.5.32) and (2.5.33) for the TM obtained above, are two systems of decoupled differential equations, corresponding to a transmission line for each polarization. Both transmission lines are related by C_m, which has the couplings effects in it. This situation is represented graphically in the Figure 2.5.3 below:

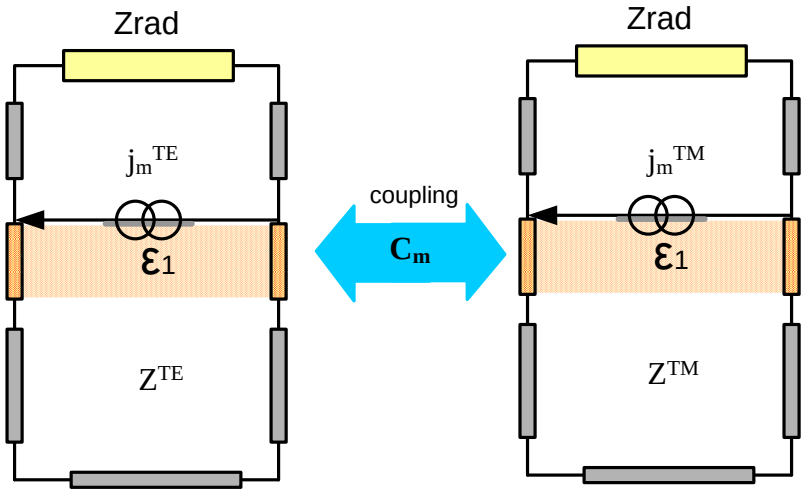

Figure 2.5.3: Coupling between TE and TM equivalent tx. Lines.

Now it is defined, where $m = mx, my$:

$$V_{mTOTAL}^{(p)} = V_{mx,my}^{(p)}(z) - C_m^2 V_{mx,my}^{(p)}(z) \qquad (2.5.34)$$

$$I_{mTOTAL}^{(p)} = I_{mx,my}^{(p)}(z) - C_m^2 I_{mx,my}^{(p)}(z) \qquad (2.5.35)$$

$$j_{mTOTAL}^{(p)} = j_{mx,my}^{(p)}(z) - C_m^2 j_{mx,my}^{(p)}(z) \qquad (2.5.36)$$

So the expressions (2.5.30)-(2.5.33) can be resumed and renamed as follows:

$$\frac{dV_{mTOTAL}^{(p)}}{dz} = -jk_{zm}Z_{0m}^{(p)}I_{mTOTAL}^{(p)} \qquad (2.5.37)$$

$$\frac{dI_{mTOTAL}^{(p)}}{dz} = -j\frac{k_{zm}}{Z_{0m}^{(p)}}V_{mTOTAL}^{(p)} - j_{mTOTAL}^{(p)} \qquad (2.5.38)$$

Two systems of uncoupled equations, or what is equivalent, two transmission lines of different polarization coupled with each other, have been obtained $\Rightarrow$ this can be solved as a usual transmission line (see section 7).

To complete the fields expansion, three unknown expressions must be found:

- Modal voltage functions, $V_{mx,my}^{(p)}(z)$

- Modal current functions, $I_{mx,my}^{(p)}(z)$

- Current source functions, $j_{mx,my}^{(p)}(z)$

Voltage and current modal functions will be derived by solving the transmission line in section 2.7. Current source functions will be obtained using the Green's Functions in section 2.6.

At this point, and before deriving the Green functions, the author considers it necessary to clarify what has been established so far. Three different approaches have been applied to each of the dimensions of the periodic initial structure in order to express the fields in the open waveguide as expansions of modal functions. In the x dimension the variation of the fields has been modelled through the *PPM expansion*. The stratification and the aperture of the guide, on the z dimension, has been treated as an *equivalent transmission line*, and finally, the periodicity in the y dimension is contemplated in the form of *Floquet modes*. This will allow obtaining a modal solution for the modes that propagate along the y-direction that takes into account the shape of the metallization and the discontinuities in the z-direction. This procedure is graphically illustrated on Figure 2.5.4 below. The currents modelled as a current source in the transmission line will be studied in the next section.

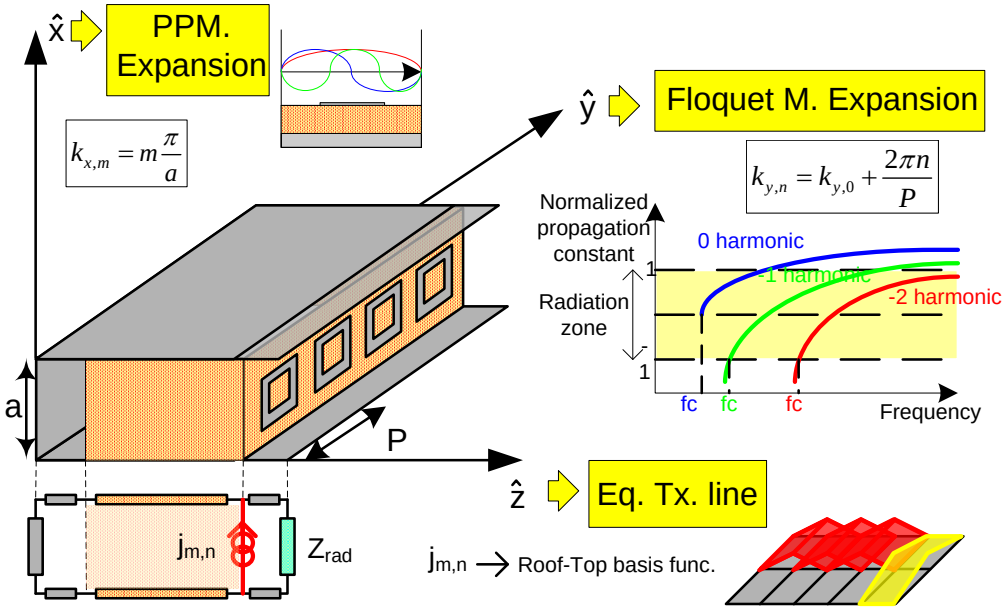

Figure 2.5.4: 3 dimensions → 3 approaches.

2.6. Deriving Green's Functions

The next step is to find the value of the currents that appear in the Transmission Line Model developed in the previous section, that's to say, the value of the coefficients $j_{mx,my}^{(p)}(z)$ of the expanded expression of the current existing in the planar metallic design on the dielectric layer. These values will depend on the chosen current distribution applied to feed the structure. This distribution was expanded in (2.5.3) as shown below, taking into account that it is a Parallel Plate guide containing a periodic circuit in the longitudinal direction $\hat{y}$.

$$\vec{J}_t(x,y,z) = \sum_{p}^{TE,TM} \sum_{mx=0}^{\infty} \sum_{my=-\infty}^{\infty} j_{mx,my}^{(p)}(z)\vec{e}_{mx}^{(p)}(x)e^{-jk_{my}y} = \sum_{p}^{TE,TM} \sum_{mx=0}^{\infty} \sum_{my=-\infty}^{\infty} j_{mx,my}^{(p)}(z)\vec{e}_{mx,my}^{(p)}(x,y)$$

(2.5.3)

For this purpose, the Green's functions, necessary to express the Integral Equation which relates the fields in any structure with the electric currents which exist inside it, will be used. In order to obtain these Green's functions, it is considered a unitary element of transverse electric current, periodic in the $\hat{y}$ direction with a propagating factor k_{y0}, and directed in both $\hat{x}$ and $\hat{y}$ direction. It can be expressed as:

$$\vec{J}_t^{\,x} = \delta(x-x')\cdot\delta(z-z')\cdot\delta(y-y')e^{-jk_{y0}y}\hat{x} \qquad (2.6.1)$$

$$\vec{J}_t^{\,y} = \delta(x-x')\cdot\delta(z-z')\cdot\delta(y-y')e^{-jk_{y0}y}\hat{y} \qquad (2.6.2)$$

The x´, z´ and y´ coordinates are the position of the elementary source in the z-x plane and that elementary source will be the same in each unitary cell but for the distance P in the $\hat{y}$ direction (see figure 2.1.1). This current has only transverse components in $\hat{x}$ and $\hat{y}$ since it only exists on the metallic planar circuit. As a reminder, the dependence in $\hat{y}$ is:

$$k_{my} = k_{y0} + k_{ym} = k_{y0} + my\frac{2\pi}{P} \qquad (2.3.7)$$

The modal coefficients $j_{mx,my}^{(p)}(z)$ can be calculated, since equations (2.6.1) and (2.6.2) must be equal for each elementary source, directed in both $\hat{x}$ and $\hat{y}$ direction. In the first case, it is considered a **elemental current source directed on** $\hat{x}$:

$$\vec{J}_t(x,y,z) = \vec{J}_t^{\,x} \qquad (2.6.3)$$

Applying the definition of the inner product for PPM and Floquet modes and decoupling each polarization (see Appendix A Workout 4), it is obtained:

$$j_{mx,my}^{x,TE}(z) = \frac{e^{+j(my\frac{2\pi}{P})y'}}{P}\frac{\vec{e}_{mx}^{\,x,TE*}(x) - C_m\vec{e}_{mx}^{\,x,TM*}(x)}{1-C_m^2}\delta(z-z') \qquad (2.6.13)$$

$$j_{mx,my}^{x,TM}(z) = \frac{e^{+j(my\frac{2\pi}{P})y'}}{P}\frac{\vec{e}_{mx}^{\,x,TM*}(x) - C_m\vec{e}_{mx}^{\,x,TE*}(x)}{1-C_m^2}\delta(z-z') \qquad (2.6.14)$$

It is important to notice that the superscript has been modified in order to indicate that these expressions are to be considered for the variation in $\hat{x}$. Again, the effect of the coupling between the modes TE^z and TM^z is reflected in the coefficient C_m.

If the same process is repeated again but this time for **the elementary source directed in** $\hat{y}$ (2.6.2), $\vec{J}_t(x,y,z) = \vec{J}_t^{\,y}$, the following results are obtained:

$$j_{mx,my}^{y,TE}(z) = \frac{e^{+j(my\frac{2\pi}{P})y'}}{P}\frac{\vec{e}_{mx}^{\,y,TE*}(x) - C_m\vec{e}_{mx}^{\,y,TM*}(x)}{1-C_m^2}\delta(z-z') \qquad (2.6.15)$$

$$j_{mx,my}^{y,TM}(z) = \frac{e^{+j(my\frac{2\pi}{P})y'}}{P}\frac{\vec{e}_{mx}^{\,y,TM*}(x) - C_m\vec{e}_{mx}^{\,y,TE*}(x)}{1-C_m^2}\delta(z-z') \qquad (2.6.16)$$

The $\delta(z-z')$ term means that the source of current $j_{mx,my}^{(p)}(z)$ can only exist in the position $z=z'$ (the height of the metallization), that is to say, it is situated within the metallic strip. Taking that into account, that term can be omitted from now on, until the moment to apply the boundary condition in the next section arrives.

The transversal electric and magnetic fields (2.3.9) and (2.3.10) inside the structure were obtained in previous sections. In them appear the expressions of modal voltage $V_{mx,my}^{(p)}(z)$ and current $I_{mx,my}^{(p)}(z)$ functions of the equivalent transmission line.

$$\vec{E}_t(x,y,z) = \sum_{p}^{TE,TM} \sum_{mx=0}^{\infty} \sum_{my=-\infty}^{\infty} V_{mx,my}^{(p)}(z)\vec{e}_{mx}^{(p)}(x)e^{-jk_{my}y} = \sum_{p}^{TE,TM} \sum_{mx=0}^{\infty} \sum_{my=-\infty}^{\infty} V_{mx,my}^{(p)}(z)\vec{e}_{mx,my}^{(p)}(x,y)$$

(2.3.9)

$$\vec{H}_t(x,y,z) = \sum_{p}^{TE,TM} \sum_{mx=0}^{\infty} \sum_{my=-\infty}^{\infty} I_{mx,my}^{(p)}(z)\vec{h}_{mx}^{(p)}(x)e^{-jk_{my}y} = \sum_{p}^{TE,TM} \sum_{mx=0}^{\infty} \sum_{my=-\infty}^{\infty} I_{mx,my}^{(p)}(z)\vec{h}_{mx,my}^{(p)}(x,y)$$

(2.3.10)

In order to derive the Green Function, it is required to express those fields in terms of the elementary current. The modal functions for voltage and current are normalized with respect to the current source. These elementary voltage $\hat{V}_m^{(p)}(z)$ and current $\hat{I}_m^{(p)}(z)$ can be calculated from the resolution of the equivalent transmission line. The final expressions for the **transversal-longitudinal Green Functions** are presented below (see Appendix A Workout 5).

$$\bar{\bar{G}}_{EJ}^{tt}(r,r') = \sum_{p}^{TE,TM} \sum_{mx=0}^{\infty} \sum_{my=-\infty}^{\infty} \vec{X}_m^{(p)}(x')Y_m^{(p)}(y')\hat{V}_m^{(p)}(z)\,\vec{e}_{mx}^{(p)}(x)e^{-jk_{my}y} \quad (2.6.25)$$

$$\bar{\bar{G}}_{HJ}^{tt}(r,r') = \sum_{p}^{TE,TM} \sum_{mx=0}^{\infty} \sum_{my=-\infty}^{\infty} \vec{X}_m^{(p)}(x')Y_m^{(p)}(y')\hat{I}_m^{(p)}(z)\,\vec{h}_{mx}^{(p)}(x)e^{-jk_{my}y} \quad (2.6.26)$$

$$\bar{G}_{EJ}^{zt}(r,r') = \frac{1}{j\omega\varepsilon} \sum_{mx=0}^{\infty} \sum_{my=-\infty}^{\infty} \hat{I}_m^{TM}(z)\vec{X}_m^{TM}(x')Y_m^{TM}(y')k_{cm}^2\hat{\phi}_{mx}^{TM}(x)e^{-jk_{my}y} \quad (2.6.40)$$

$$\bar{G}_{HJ}^{zt}(r,r') = \frac{1}{j\omega\mu} \sum_{mx=0}^{\infty} \sum_{my=-\infty}^{\infty} \hat{V}_m^{TE}(z)\vec{X}_m^{TE}(x')Y_m^{TE}(y')k_{cm}^2\hat{\phi}_{mx}^{TE}(x)e^{-jk_{my}y} \quad (2.6.41)$$

Where:

$$\vec{X}_m^{(p)}(x') = \frac{\vec{e}_{mx}^{(p)*}(x') - C_m\vec{e}_{mx}^{(q)*}(x')}{1-C_m^2} \quad (2.6.23) \qquad Y_m^{(p)}(y') = \frac{e^{+j(my\frac{2\pi}{P})y'}}{P} \quad (2.6.24)$$

And $m = mx, my$, which are the order of the PPM and Floquet modes respectively.

In matricial form, it can be resumed as follows:

$$\bar{\bar{G}}_{EJ} = \begin{pmatrix} \bar{\bar{G}}_{EJ}^{tt} \\ \bar{G}_{EJ}^{zt} \end{pmatrix} = \begin{pmatrix} \bar{G}_{EJ}^{xt} \\ \bar{G}_{EJ}^{yt} \\ \bar{G}_{EJ}^{zt} \end{pmatrix} = \begin{pmatrix} G_{EJ}^{xx} & G_{EJ}^{xy} \\ G_{EJ}^{yx} & G_{EJ}^{yy} \\ G_{EJ}^{zx} & G_{EJ}^{zy} \end{pmatrix} \quad (2.6.42)$$

$$\bar{\bar{G}}_{HJ} = \begin{pmatrix} \bar{\bar{G}}_{HJ}^{tt} \\ \bar{G}_{HJ}^{zt} \end{pmatrix} = \begin{pmatrix} \bar{G}_{HJ}^{xt} \\ \bar{G}_{HJ}^{yt} \\ \bar{G}_{HJ}^{zt} \end{pmatrix} = \begin{pmatrix} G_{HJ}^{xx} & G_{HJ}^{xy} \\ G_{HJ}^{yx} & G_{HJ}^{yy} \\ G_{HJ}^{zx} & G_{HJ}^{zy} \end{pmatrix} \quad (2.6.43)$$

And the electric and magnetic fields created in the structure due to any transverse current distribution will be given by:

$$\vec{E}(r) = \int_{r'} \bar{\bar{G}}_{EJ}(r,r') \cdot \vec{J}_t(r') dr' \quad (2.6.44)$$

$$\vec{H}(r) = \int_{r'} \bar{\bar{G}}_{HJ}(r,r') \cdot \vec{J}_t(r') dr' \quad (2.6.45)$$

As a reminder, the only existing currents are the transverse currents:

$$\vec{J}_t(x',y') = J^x(x',y')\hat{x} + J^y(x',y')\hat{y}, \quad (2.6.46)$$

since the currents induced in the lateral walls (parallel-plates) were taken into account in the PPM expansion, which fulfil the boundary condition imposed by those walls. Also, the currents induced on the bottom metallic wall is contemplated in the equivalent transmission line, through $\hat{V}_m^{(p)}(z)$ and $\hat{I}_m^{(p)}(z)$.

2.7. Equivalent Transmission Line Solution

In order to express the variation of the fields in the z-direction, Maxwell´s equations led to a system of differential coupled equations, which were identified as the equations from **two coupled transmission lines** of different polarization.

$$\frac{dV_{mTOTAL}^{(p)}}{dz} = -jk_{zm}Z_{0m}^{(p)}I_{mTOTAL}^{(p)} \qquad (2.5.37)$$

$$\frac{dI_{mTOTAL}^{(p)}}{dz} = -j\frac{k_{zm}}{Z_{0m}^{(p)}}V_{mTOTAL}^{(p)} - j_{mTOTAL}^{(p)} \qquad (2.5.38)$$

where $m = mx, my$, and will be so for the remaining of the chapter.

$$V_{mTOTAL}^{(p)} = V_{mx,my}^{(p)}(z) - C_m^2 V_{mx,my}^{(p)}(z) \qquad (2.5.34)$$

$$I_{mTOTAL}^{(p)} = I_{mx,my}^{(p)}(z) - C_m^2 I_{mx,my}^{(p)}(z) \qquad (2.5.35)$$

$$j_{mTOTAL}^{(p)} = j_{mx,my}^{(p)}(z) - C_m^2 j_{mx,my}^{(p)}(z) \qquad (2.5.36)$$

The general solution for a transmission line consist of a standing wave which is the sum of a progressive wave travelling in the propagation direction (remember it was the z-direction to take into account the stratification) and a regressive wave travelling in the opposite direction. This can be described with next equations:

$$V_m^{(p)}(z) = V_{om}^{(p)^+} e^{-jk_z z} + V_{om}^{(p)^-} e^{+jk_z z} \qquad (2.7.1)$$

$$I_m^{(p)}(z) = I_{om}^{(p)^+} e^{-jk_z z} - I_{om}^{(p)^-} e^{+jk_z z} = = \frac{1}{Z_{0m}^{(p)}}\left[V_{om}^{(p)^+} e^{-jk_z z} - V_{om}^{(p)^-} e^{+jk_z z}\right] \qquad (2.7.2)$$

$$k_{zm} = \sqrt{k_o^2 - k_{cm}^2} = \sqrt{k_o^2 - k_{mx}^2 - k_{my}^2} = \sqrt{k_o^2 - \left(mx\frac{\pi}{a}\right)^2 - k_{my}^2} \qquad (2.7.3)$$

$$Z_{0m}^{TE} = \frac{\omega\mu}{k_{zm}} \qquad (2.7.4)$$

$$Z_{0m}^{TM} = \frac{k_{zm}}{\omega\varepsilon} \qquad (2.7.5)$$

Therefore, to express the modal scalar functions $V_m^{(p)}(z)$ and $I_m^{(p)}(z)$, the equivalent transmission line must be solved, in which the stratified medium is transformed in a equivalent network in the z-direction, see Figure 2.7.1 below for clarification.

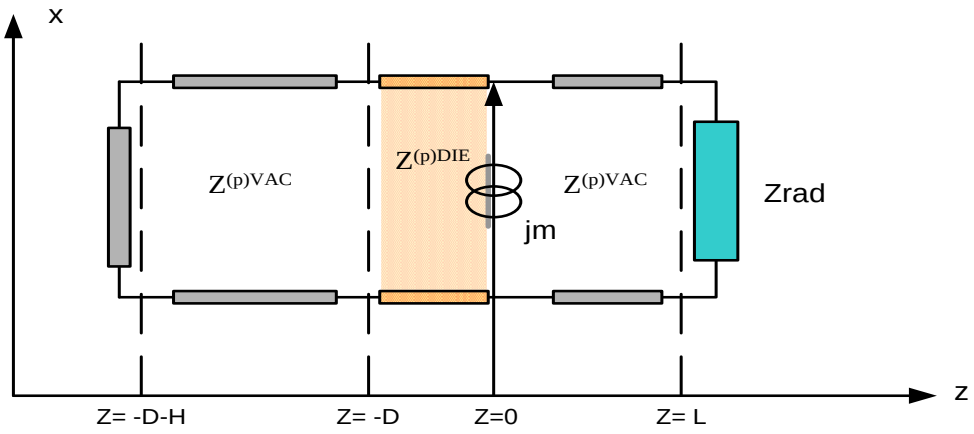

Figure 2.7.1: Equivalent Transmission Line.

Since the transverse electric currents only appear in the metal strip, the equivalent current sources are located in that position, which is also the origin point in the z direction, that is z=0. The dielectric substrate has a width of "D", and it is at a distance "L" from the top wall and a height “H” from the bottom metallic wall. The metallization width is "W", and it must be thin enough to neglect the thickness, and therefore not consider any current in z-direction. The width of the PPW side walls is "a". The mathematics related to the transmission line resolution can be found in Appendix A Workout 6.

The impedances for each medium and propagation constants are defined as showed below:

$$Z_{0m}^{TE^{VAC}} = \frac{\omega\mu_0}{k_{zm}^{VAC}} \qquad (2.7.36)$$

$$Z_{0m}^{TE^{DIE}} = \frac{\omega\mu_0}{k_{zm}^{DIE}} \qquad (2.7.38)$$

$$Z_{0m}^{TM^{VAC}} = \frac{k_{zm}^{VAC}}{\omega\varepsilon_0} \qquad (2.7.39)$$

$$Z_{0m}^{TM^{DIE}} = \frac{k_{zm}^{DIE}}{\omega\varepsilon_0\varepsilon_r} \qquad (2.7.40)$$

$$k_{zm}^{VAC} = \sqrt{k_0^{VAC^2} - k_{cm}^{\ 2}} = \sqrt{\omega^2\mu_0\varepsilon_0 - \left(m\frac{\pi}{a}\right)^2 - k_y^{\ 2}} \qquad (2.7.41)$$

$$k_{zm}^{DIE} = \sqrt{k_0^{DIE^2} - k_{cm}^{\ 2}} = \sqrt{\omega^2\mu_0\varepsilon_0\varepsilon_r - \left(m\frac{\pi}{a}\right)^2 - k_y^{\ 2}} \qquad (2.7.42)$$

The aperture at the top of the waveguide will be modelled as the **Markuvitz radiation impedance**, based on the studies developed in [Markuvitz 1951]. This impedance was modified in [Gomez Jan-2005] to extend it to higher order PPM of both polarizations, resulting in the modal impedance $Z_m^{(p)RAD}$.

With this working out, the solutions for the normalized modal functions $\hat{V}_m^{(p)}(z)$ and $\hat{I}_m^{(p)}(z)$ are obtained. Note that the resolution of the transmission line will obtain a different solution for each PPM and Floquet mode, since it depends on the indexes mx and my. This way, this method presents the advantage of being able to study the effect on the radiation of higher order modes. At this point, the only unknowns left to solve are the propagation in the longitudinal direction of the LWA and the currents induced on the planar metallization. Both will be dealt with in the next section.

2.8. Method of Moments

In this section, the integral equation technique developed throughout this chapter will be used to solve a general case of the shielded microstrip-line structure under study. The particular transmission line model was derived and now the appropriate boundary conditions will be imposed to formulate the Electric Field Integral Equation (EFIE). Finally, the Method of Moments (MoM) will be used to solve the EFIE.

2.8.1. Boundary Conditions

Equations in the previous section model the voltage and current standing waves created in the equivalent transmission line represented in figure 2.7.1. They were developed in Appendix A Workout 6 and can be summarized as follows:

$$V_{\substack{m \\ z\geq 0}}^{(p)}(z) = j_m^{(p)} \cdot \frac{Z_{Lm}^{(p)} \cdot Z_{Dm}^{(p)}}{Z_{Lm}^{(p)} + Z_{Dm}^{(p)}} \cdot \frac{e^{-jk_{zm}^{VAC} z} - e^{+jk_{zm}^{VAC} z} \cdot e^{-j2k_{zm}^{VAC} L}}{1 - e^{-j2k_{zm}^{VAC} L}} \quad (2.8.1.1)$$

$$V_{\substack{m \\ z\le 0}}^{(p)}(z) = j_m^{(p)} \cdot \frac{Z_{Lm}^{(p)} \cdot Z_{Dm}^{(p)}}{Z_{Lm}^{(p)} + Z_{Dm}^{(p)}} \cdot \frac{e^{+jk_{zm}^{DIE} z} - e^{-jk_{zm}^{DIE} z} \cdot e^{-j2k_{zm}^{DIE} D}}{1 - e^{-j2k_{zm}^{DIE} D}} \quad (2.8.1.2)$$

$$I_{\substack{m \\ z>0}}^{(p)}(z) = j_m^{(p)} \cdot \frac{Z_{Dm}^{(p)}}{Z_{Lm}^{(p)} + Z_{Dm}^{(p)}} \cdot \frac{e^{-jk_{zm}^{VAC} z} + e^{+jk_{zm}^{VAC} z} \cdot e^{-j2k_{zm}^{VAC} L}}{1 + e^{-j2k_{zm}^{VAC} L}} \quad (2.8.1.3)$$

$$I_{\substack{m \\ z<0}}^{(p)}(z) = -j_m^{(p)} \cdot \frac{Z_{Lm}^{(p)}}{Z_{Lm}^{(p)} + Z_{Dm}^{(p)}} \cdot \frac{e^{+jk_{zm}^{DIE} z} + e^{-jk_{zm}^{DIE} z} \cdot e^{-j2k_{zm}^{DIE} D}}{1 + e^{-j2k_{zm}^{DIE} D}} \quad (2.8.1.4)$$

It can be checked how the voltage is zero on the top and bottom metal walls while the current reaches a maximum. These functions also satisfy the boundary conditions with the current source in z=0. It is also remarkable to say that, while the voltage is continuous in z=0 ($V(z=0^+)=V(z=0^-)$), the current is not, since the current of the source is split into $I(z=0^+)$ and $I(z=0^-)$. Note also the sign minus in equations (2.8.1.4), since the direction of the equivalent current must not be changed for a correct analysis.

All the functions needed in the integral equations can be expressed analytically, which will translate into a low computational cost. For the problem we are interested in, the fields described with the integral equations satisfy all the next boundary conditions:

- Side metal walls in the x axis due to the modal vector functions of the PPW.
- Stratified medium in z axis and top and bottom metal walls due to the modal scalar amplitude functions of the equivalent transmission line.
- Maxwell´s equations, including coherence with the electric source located at z=0 and propagation phenomena in all directions (including the y-axis).

The only boundary condition which is not satisfied yet is the field behaviour on the printed circuit, at z=0, since:

1. On the metallization strip located in z=0 with a width "W", the transverse electric field Et must be zero, and this condition is not satisfied by the modal vector functions $V_m^{(p)}(z)$ at z=0. In fact, although these scalar modal functions are not zero at z=0 individually, the modal summation should make the total transverse field be zero, accordingly to equation (2.6.32). The longitudinal magnetic field Hz, must be zero over the metallization as well, but as can be seen by equation (2.6.34), the behaviour of Hz is closed related to the variations of Et, and both boundary conditions are dependent.

2. The transverse magnetic field Ht is discontinuous at z=0, as we have just seen by equations (2.8.1.3) and (2.8.1.4). This discontinuity is due to the excitation source located at z=0, and therefore must exist only on the metal strip and must be coherent with the electric current density. The longitudinal electric field Ez must be also discontinuous since electric charge density might exist on the metal surface, but this boundary condition is again dependent on that of Ht, since the Continuity Equation relates the electric charge density variation with its corresponding electric current density.

3. Therefore, outside the metallization of width "W", the transverse magnetic field Ht must be continuous, since no electric current density can exist. From equations (2.8.1.3) and (2.8.1.4), it can be seen that $I_m^{(p)}(z)$ at z=0 is not a continuous function, and again, the modal summation must make the total field be zero outside the metallization.

These three **boundary conditions** must be satisfied to find a valid solution for the electromagnetic fields in the shielded microstrip line. These conditions can be written mathematically as follows:

$$\begin{cases} 1. & \vec{E}t(x,y,z)_{\substack{x\in W \\ \forall y \\ z=0}} = 0 & (2.8.1.5) \\ 2. & \vec{H}t(x,y,z)_{\substack{x\in W \\ \forall y \\ z=0^+}} - \vec{H}t(x,y,z)_{\substack{x\in W \\ \forall y \\ z=0^-}} = \hat{z}\times\vec{J}t & (2.8.1.6) \\ 3. & \vec{H}t(x,y,z)_{\substack{x\notin W \\ \forall y \\ z=0^+}} - \vec{H}t(x,y,z)_{\substack{x\notin W \\ \forall y \\ z=0^-}} = 0 & (2.8.1.7) \end{cases}$$

All of these equations are integral equations, since an integral between the Green´s functions (obtained in section 2.6) and the transverse currents Jt must be performed to obtain the fields. The first is called **Electric Field Integral Equation (EFIE)**, while the second and the third equations are **Magnetic Field Integral Equations (MFIE)**.

In this way, we can write the EFIE which describes the electromagnetic problem of the shielded microstrip transmission line using the expression for the transversal electric field that was obtained through the Green function in (2.6.32), in the Appendix A:

$$\vec{E}t(x,y,z)_{\substack{x\in W \\ \forall y \\ z=0}} = \sum_{p}^{TE,TM} \sum_{mx=0}^{\infty} \sum_{my=-\infty}^{\infty} A_m^{(p)} \hat{V}_m^{(p)}(0) \cdot \vec{e}_{mx}^{(p)}(x) e^{-jk_{my}y} = 0 \qquad (2.8.1.8)$$

Where the coefficient $A_m^{(p)}$ is given in (2.6.31), and accounts for the contributions of each PPM and Floquet mode to the fields in the structure. This term also contains the transversal currents. Again, now that the problem has already been formulated, it is important to remark that the transverse distribution of current on the metal strip, **Jt**, is still unknown, and also the wave number in the y direction, $\mathbf{k_{my}}$.

2.8.2. MoM - Galerkin.

The **Method of Moments (MoM),** introduced in Chapter 1, will be used to express the current density and obtain a homogeneous system of linear equations which can be solved only for certain k_{my} solutions, leading to the valid current and field distributions. The EFIE will be transformed to a matrix equation by the use of MoM, and the solution of the matrix equation will yield the surface current distribution on the microstrip.

To discretize the EFIE (2.8.1.8), the unknown transverse current density Jt will be expanded with a set of basis functions. These functions are separated in two, $f_{nx}(x')$ for the dependence in x and $g_{ny}(y')$ for the dependence in y, being nx and ny the coordinates where the basis functions exists. Depending on the nature of these basis functions (Entire Domain or Subdomain functions), the formulation of the problem will have a different approach. The use of **Roof-top basis functions** will be the main novelty introduced in the method developed throughout this thesis, and will be the object of study in next chapter. For now, a subdomain general case will be considered.

$$\vec{Jt}(x',y') = \sum_{Bx=0}^{C_x} \left\{ \beta_{Bx}^{X} \cdot f_{nx}^{X}(x') g_{ny}^{X}(y') \cdot \hat{x} \right\} e^{-jk_{y0}y'} + \sum_{By=0}^{C_y} \left\{ \beta_{By}^{Y} \cdot f_{nx}^{Y}(x') g_{ny}^{Y}(y') \cdot \hat{y} \right\} e^{-jk_{y0}y'} \quad (2.8.2.1)$$

Next modal coefficients are obtained:

$$A_m^{(p)} = \int_{S'} \frac{\vec{e}_{mx}^{x,(p)*}(x') - C_m \vec{e}_{mx}^{x,(q)*}(x')}{1 - C_m^2} Y_m^{(p)}(y') J_t^{x}(r') + \int_{S'} \frac{\vec{e}_{mx}^{y,(p)*}(x') - C_m \vec{e}_{mx}^{y,(q)*}(x')}{1 - C_m^2} Y_m^{(p)}(y') J_t^{y}(r') =$$

$$= \sum_{Bx=0}^{Cx} \beta_{Cx}^{X} \int_{S'} \frac{\vec{e}_{mx}^{x,(p)*}(x') - C_m \vec{e}_{mx}^{x,(q)*}(x')}{1 - C_m^2} Y_m^{(p)}(y') f_{nx}^{X}(x') g_{ny}^{X}(y') e^{-jk_{y0}y'} +$$

$$+ \sum_{By=0}^{Cy} \beta_{By}^{Y} \int_{S'} \frac{\vec{e}_{mx}^{y,(p)*}(x') - C_m \vec{e}_{mx}^{y,(q)*}(x')}{1 - C_m^2} Y_m^{(p)}(y') f_{nx}^{Y}(x') g_{ny}^{Y}(y') e^{-jk_{y0}y'} \quad (2.8.2.2)$$

It can be seen how the continuous EFIE (2.8.1.8) has been transformed into a discrete equation in which now it appears $(Cx + Cy)$ unknown coefficients, namely β_{Bx}^{X} and β_{By}^{Y}. The number of basis functions Cx and Cy, and therefore the number of coefficients needed, will depend on the number of cells necessary to describe the geometry, that is to say, the convergence of the problem, and will be dealt particularly for each structure.

To solve those $(Cx + Cy)$ unknown current coefficients, it is needed $(Cx + Cy)$ independent equations. As it was explained, the third step in the MoM procedure (after expressing the integral equation and discretizing the unknown function using basis functions) is to use **test functions** to obtain a set of "weaker" boundary conditions.

The **Galerkin** technique, which employs identical basis and weighting functions, yields to more accurate and rapidly convergent numerical results than other testing methods, see [Wang 1991] and [Chan 1990]. It also leads to a simple analytic basis and test integrals and allows the re-use of code, reducing the computation time.

$$\boxed{\int_r \vec{E}t(x,y,0)\cdot f_{lx}(x)\cdot g_{ly}(y)\cdot \partial r = 0} \Rightarrow \begin{cases} \int_r \vec{E}t(x,y,0)\cdot f_{lx}^{X}(x)\cdot g_{ly}^{X}(y)\cdot \partial r = 0 \\ \int_r \vec{E}t(x,y,0)\cdot f_{lx}^{Y}(x)\cdot g_{ly}^{Y}(y)\cdot \partial r = 0 \end{cases}$$

(2.8.2.3)

Basis and test integrals derived from equation above are defined as follows. For the complete mathematical solution, see Appendix A Workout 7.

Basis Integrals

$$\begin{cases} I_{BX}^{EX} = \int_{x'} \bar{X}_m^{(p)}(x')\cdot \hat{x}\cdot f_{nx}^{X}(x')dx' & (2.8.2.6) \\ I_{BY}^{EX} = \int_{y'} Y_{my}(y')\cdot g_{ny}^{X}(y')\cdot e^{-jk_0 y'}dy' & (2.8.2.7) \\ I_{BX}^{EY} = \int_{x'} \bar{X}_m^{(p)}(x')\cdot \hat{y}\cdot f_{nx}^{Y}(x')dx' & (2.8.2.8) \\ I_{BY}^{EY} = \int_{y'} Y_{my}(y')\cdot g_{ny}^{Y}(y')\cdot e^{-jk_0 y'}dy' & (2.8.2.9) \end{cases}$$

Test Integrals

$$\begin{cases} I_{TX}^{EX} = \int_x e_{mx}^{(p)}(x)\cdot \hat{x}\cdot f_{lx}^{X}(x)dx & (2.8.2.10) \\ I_{TY}^{EX} = \int_y e^{-jk_{my}y}\cdot g_{ly}^{X}(y)dy & (2.8.2.11) \\ I_{TX}^{EY} = \int_x e_{mx}^{(p)}(x)\cdot \hat{y}\cdot f_{lx}^{Y}(x)dx & (2.8.2.12) \\ I_{TY}^{EY} = \int_y e^{-jk_{my}y}\cdot g_{ly}^{Y}(y)dy & (2.8.2.13) \end{cases}$$

Note that the indexes lx and ly stand for each different equation obtained when using the corresponding test functions. To understand the difference between them and the basis functions indexes, it must be clear that:

- n_x and n_y stand for the spatial coordinates where the basis functions, that model the currents that produce the fields, exist (in other words, where the cell is located).
- l_x and l_y stand for the spatial coordinates where the test functions, that average the observed field, exist.

Note also that the integration variable in the test is "r" and not "r´", since the integration is performed in the domain where the electric field is evaluated, and not in the current domain, where the variable is "r´". In order to make clear the physical meaning of these integrals, a brief description of them could be:

I_{BX}^{EX} stands for the current that varies on $\hat{x}'$ and depend on $\hat{x}'$.

I_{BY}^{EX} stands for the current that varies on $\hat{x}'$ but depend on $\hat{y}'$.

I_{BX}^{EY} stands for the current that varies on $\hat{y}'$ but depend on $\hat{x}'$.

I_{BY}^{EY} stands for the current that varies on $\hat{y}'$ and depend on $\hat{y}'$.

I_{TX}^{EX} stands for the field that varies on $\hat{x}$ and its dependence on $\hat{x}$ is being tested.

I_{TY}^{EX} stands for the field that varies on $\hat{x}$ but its dependence on $\hat{y}$ is being tested.

I_{TX}^{EY} stands for the field that varies on $\hat{y}$ but its dependence on $\hat{x}$ is being tested.

I_{TY}^{EY} stands for the field that varies on $\hat{y}$ and its dependence on $\hat{y}$ is being tested.

Both equations (2.8.2.4) and (2.8.2.5) are expressed using an infinite amount of modal functions of the PPW and the Floquet modes. However, these infinite series cannot be handled by a computer, and therefore the series must be truncated by a number "Mx" of modal functions (Mx for TE^z and Mx for TM^z modes) for the PPW and a number “My” of modal functions (again My for TE^z and My for TM^z modes) for the Floquet modes. This truncation problem will be dealt with when studying the convergence of specific geometries.

The matrix "P" is called the **Moment Matrix** and it is defined as shown below in equation (2.7.2.18). By its application, equations (2.8.2.4) and (2.8.2.5) can be rewritten in following matricial form:

$$P_{JX}^{EX} = \sum_{p}^{TE,TM} \sum_{mx=0}^{\infty} \sum_{my=-\infty}^{\infty} \hat{V}_m^{(p)}(0) \cdot I_{BX}^{EX} \cdot I_{BY}^{EX} \cdot I_{TX}^{EX} \cdot I_{TY}^{EX} \qquad (2.8.2.14)$$

$$P_{JY}^{EX} = \sum_{p}^{TE,TM} \sum_{mx=0}^{\infty} \sum_{my=-\infty}^{\infty} \hat{V}_m^{(p)}(0) \cdot I_{BX}^{EY} \cdot I_{BY}^{EY} \cdot I_{TX}^{EX} \cdot I_{TY}^{EX} \qquad (2.8.2.15)$$

$$P_{JX}^{EY} = \sum_{p}^{TE,TM} \sum_{mx=0}^{\infty} \sum_{my=-\infty}^{\infty} \hat{V}_m^{(p)}(0) \cdot I_{BX}^{EX} \cdot I_{BY}^{EX} \cdot I_{TX}^{EY} \cdot I_{TY}^{EY} \qquad (2.8.2.16)$$

$$P_{JY}^{EY} = \sum_{p}^{TE,TM} \sum_{mx=0}^{\infty} \sum_{my=-\infty}^{\infty} \hat{V}_m^{(p)}(0) \cdot I_{BX}^{EY} \cdot I_{BY}^{EY} \cdot I_{TX}^{EY} \cdot I_{TY}^{EY} \qquad (2.8.2.17)$$

$$\boxed{(P)(\beta) = \begin{pmatrix} P_{JX}^{EX} & P_{JY}^{EX} \\ P_{JX}^{EY} & P_{JY}^{EY} \end{pmatrix} \begin{pmatrix} \beta_{nx,xy}^{X} \\ \beta_{nx,ny}^{Y} \end{pmatrix} = 0} \qquad (2.8.2.18)$$

In a **homogeneous system of linear equations**, in order to ensure non trivial solution of the system, the determinant of P matrix must be equal to zero. It is in that assumption where the resolution of the electromagnetic problem, and therefore the solution for the k_{my} lies, since all the functions involved in the problem are analytical functions which depend on the unknown variable k_{my}. Note that this variable stands for the propagation constant of the transmission line in its longitudinal direction.

Since the determinant is a complex function which depends on the complex variable k_{my}, the search for the solution will become a **search for a zero in the complex plane**. For this purpose, the iterative algorithm developed in [Gomez Jan-2005] is used. The search starts with the real solution of k_{my} for the completely closed structure and gradually, the top-wall is changed from the impedance of a short-circuit to the final modal Markuvitz radiation impedance, corresponding to the completely open structure. This transformation must be carried out in small steps in order to provide a smooth transition to the accurate solution. It is important to note that for a given PPM order, the Floquet harmonics will have a different phase constant β_{my} but share the same attenuation constant α_{my}, since all the family of harmonics belonging to the same PPM are 'coupled'. This complex search is the only numerical calculation required in the present method, representing the highest computational cost of this technique. All the expressions derived in this chapter and those expressions to calculate the currents, fields and radiation pattern from the complex value of k_{my} are analytical.

CONCLUSION

In conclusion, the main **advantages of the method** developed in this chapter are:

- The Spatial Domain approach avoids dealing with complex Fourier transforms.

- The use of modal expansions (PPM, thanks to shielded nature of the structure) avoids the numerical resolution of the problem, since all the expressions will be analytical.

- Galerkin technique allows for simple analytical expressions for the basis and test integrals, and a direct relation between them.

- The solutions are accurate since it is a full-wave method: it accounts for all the PPM, not only the main one, responsible for the radiation. This is possible since the series of PPM are orthogonal (it is contemplated the case in which it is not as coupling between modes) and so are the Floquet modes.

- The method allows the simultaneous radiation of Floquet harmonics, higher order PPM and other modes. This is important, since other modes radiating, apart from the main PPM, will lead to secondary lobes and degrade the radiation pattern.

Until now, previously developed methods to analyze and design laterally shielded LWA were limited to the use of Entire Domain basis function to model the transversal currents in the structure. In this work, **Subdomain basis functions** are proposed for the first time to build a novel full wave method able to deal with arbitrary geometries for the planar metallization, which was not possible with the previous methods (restricted to rectangular patches or slots). Next Chapter is exclusively dedicated to the study and discussion of the Subdomain basis functions that will be introduced in this method, as well as to validate those results with this new approach.

CHAPTER 3 - BASIS FUNCTIONS

Where a novel combination of Spatial Domain Method of Moments + Subdomain basis functions is developed and validated.

In Chapter 2, the EFIE was defined and the MoM applied to it, modelling the currents with a set of basis functions and the corresponding set of unknown coefficients (β), therefore discretizing the problem into the matrix equation $(P)(\beta)=0$. At this point, the propagation constant is obtained by solving $\det(P)=0$, and after that, the calculation of the currents coefficients is straight forward. The maths were developed for a general case of subdomain basis functions. In the present chapter, different options for the basis functions are discussed: those used in previous computed models (Entire domain) and a new approach to analyze this type of LWA, the **Subdomain basis functions**. The latter will be the key to the high versatility of the proposed method.

The choice of the appropriate set of basis functions and test functions is decisive to solve the electric currents density on the metallic printed circuit (or magnetic currents in the case of apertures), a priori unknown, with enough accuracy and at reasonable computing

cost. The basis and test functions will determine the complexity and size of the MoM matrix. There are two main families of these functions that can be found in the literature:

- *Entire domain functions*: They have support on the whole structure or object under analysis. It is plain that there's no need to mesh the geometry. Examples of this kind of functions are polynomial functions (Tchebycheff), sinusoidal functions, Legendre functions, Maclaurin functions...

- *Sub-domain functions*: In this case the functions only exist within a cell defined by a mesh on the geometry of the structure. There are several types of mesh, as rectangular, triangular etc. Or even more, it can be uniform or not.

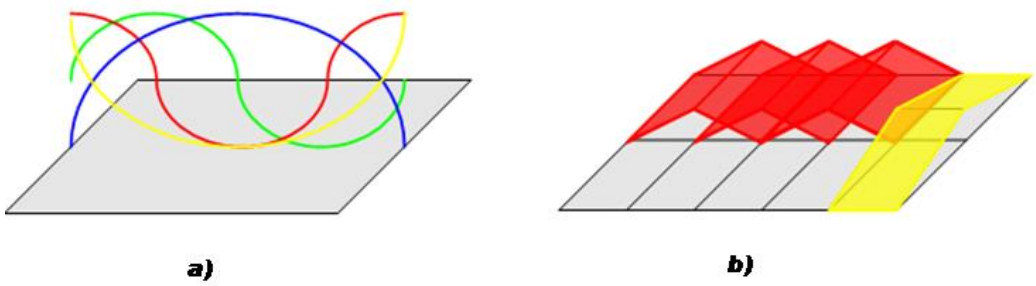

Figure 3.1: a) Entire Domain basis functions and b) Sub-domain basis functions.

3.1. Entire domain Basis Functions

These are complete domain functions, since **they exist on the entire element** under analysis. Each function overlaps with itself and the rest of the functions of the set, since they share the domain, and they present a good convergence in **simple regular geometries**. They can be seen as "current modes", so the coefficients β_i are complex scalars defining the amplitude and phase of the corresponding current mode. This type of basis functions is more adequate when the shape of the unknown function is known a priori, although not the exact form.

To build a consistent and versatile analysis tool and to check its results with previous computed models, the method was first developed for a set of Entire domain basis and test functions. These functions must satisfy the **boundary conditions of the currents at the edges** of the metallization. Figure 3.1.1 shows the distributions of the currents induced on a periodic metallic patch on a LWA structure (see picture of the structure on Figure 3.3.1), obtained with a simulation with 5 basis functions for each x and y directions.

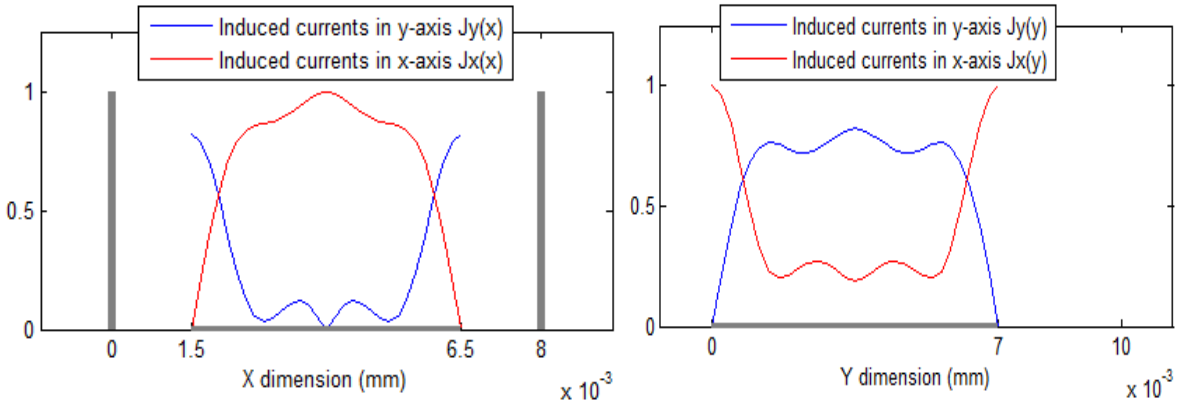

Figure 3.1.1: Normalized surface currents for a metallic patch.

The chosen set of basis functions is **sinusoidal**, as shown in the next equations. Due to the periodic nature of the structure, each of the current distributions on the patch ($\overline{J}_x$ and $\overline{J}_y$) possesses two components. The upper index refers to the direction of the current that the basis functions models, either $\overline{J}_x$ or $\overline{J}_y$.

$$f_{nx}^{X}(x') = \sin\left(nx\frac{\pi}{W}x'\right) \quad (3.1.1)$$

$$f_{nx}^{Y}(x') = \cos\left(nx\frac{\pi}{W}x'\right) \quad (3.1.2)$$

$$g_{ny}^{X}(y') = \cos\left(ny\frac{\pi}{Q}y'\right) \quad (3.1.3)$$

$$g_{ny}^{Y}(y') = \sin\left(ny\frac{\pi}{Q}y'\right) \quad (3.1.4)$$

Where nx and ny are the order of the sinusoidal basis functions, and W and Q are the width and length of the metallic patch, respectively. The expanded currents using the basis functions are of the form:

$$\vec{J}(x',y') = \vec{J}_x(x',y') + \vec{J}_y(x',y') = \qquad (2.8.2.1)$$

$$\sum_{nx=0}^{N_x}\sum_{ny=0}^{N_y}\left\{\beta_{nx,xy}^{X}\cdot f_{nx}^{X}(x')g_{ny}^{X}(y')\cdot\hat{x}+\beta_{nx,ny}^{Y}\cdot f_{nx}^{Y}(x')g_{ny}^{Y}(y')\cdot\hat{y}\right\}e^{-jk_{y0}y'}$$

As explained in the previous section, the **Galerkin method** of resolution uses the same functions for the basis and for the test. The difference lies in the space where the functions are defined or evaluated, (x´, y´) in the case of the basis functions and (x,y) in the test functions. In the same way, the indexes that define the functions are named differently. It is important to notice that, while the indexes nx and ny in the case of the basis functions represent the harmonic variation of the functions that model the currents, the indexes lx and ly stand for the harmonic variations of the test functions that average the observed field in the integral equation. It can be seen how **the meaning of the indexes in the Entire domain changes drastically from** the one presented in Chapter 2 section 2.8.2 for **the Subdomain general case**. While the index of the basis functions for the SD formulation depends on the cell which the function exists physically on, in the Entire domain case, it represents the order of the basis function, making a summation that will model the current. For a structure simulated with Nx basis functions in the x direction (nx =0,1..Nx) and Ny basis functions for the y direction (ny =0,1..Ny), the sizes of the matrices used to calculate the determinant of the MoM matrix, [P], presented in Chapter 2 section 2.8.2 are shown in Table below:

$I_{BX}^{EX}\ I_{BX}^{EY}\ I_{TX}^{EX}\ I_{TX}^{EY}$	(N_x+1) by (Floquet and PPM modes)
$I_{BY}^{EX}\ I_{BY}^{EY}\ I_{TY}^{EX}\ I_{TY}^{EY}$	(N_y+1) by (Floquet and PPM modes)
$P_{JX}^{EX}\ P_{JY}^{EX}\ P_{JX}^{EY}\ P_{JY}^{EY}$	$(N_x+1)(N_y+1)$ by $(N_x+1)(N_y+1)$
$(P)=\begin{pmatrix} P_{JX}^{EX} & P_{JY}^{EX} \\ P_{JX}^{EY} & P_{JY}^{EY} \end{pmatrix}$	$2(N_x+1)(N_y+1)$ by $2(N_x+1)(N_y+1)$

Table 3.1.1 Matrix dimensions for Entire Domain basis functions.

The complete working out of the final expressions for both the basis and test integrals using the ED basis functions can be found in the Appendix A Workout 8.

The purpose of developing the method for ED basis functions was double. First, to make the software even more flexible, since the user can choose the suitable type of basis functions depending on the geometry to analyze (an advantage when the geometry is simple and the computing resources are limited), and second, as a milestone to verify part of the coded method before changing to a more complex kernel to add the Subdomain functionality. This is why the same set of sinusoidal basis functions than in [Gómez March-2006] was chosen. Along this Chapter, several simple structures analyzed in articles by said author and others will be studied for illustrative and verification purposes.

To validate the results obtained with the ED basis functions, a periodic LWA analyzed by Guglielmi in 1991 using the Transverse Equivalent Network method [Guglielmi 1991] will be studied. This structure is presented at the top of Figure 3.1.2. The dimensions of this antenna are: a=1.4mm, D=1.4mm, L=2.8mm, P=3.38mm, Q=2.366mm and ε_r =9. In the same Figure, the radiation angle of the main beam (left-hand figure) and the attenuation constant (right-hand figure) are shown. The results obtained with the method developed in the previous chapter using ED functions are plotted together with those obtained by Guglielmi. There is an excellent agreement between both results. Same analysis was developed in [Gomez March-2006], using the method for the ED functions, and the results obtained were practically identical to those shown in 3.1.2. The phenomenon of backward scanning and bandgap, which can be appreciated in both dispersion curves, will be introduced and explained in depth in later chapters.

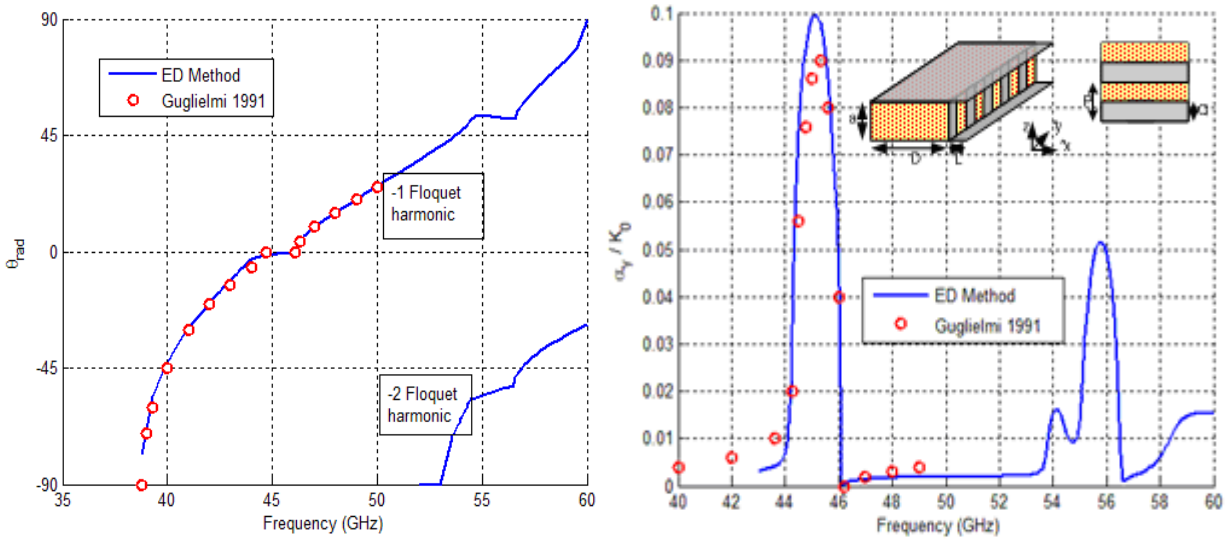

Figure 3.1.2 Dispersion curves for ED based Method vs. results from Guglielmi structure.

In Figure 3.1.3 the normalized surface currents induced on the metallic patch are modelled for the Guglielmi antenna using Entire Domain sinusoidal basis functions, at 40GHz. It can be checked that the current distribution obtained by this method fulfils the required boundary conditions. The currents in the longitudinal y direction are negligible while the currents in the x direction are not zero at the edges of the metallic patch, since it is touching the metallic side walls of the waveguide. On the right hand side of the same Figure, the transversal electric field at the same frequency is illustrated. As was previously explained in Chapter 2, it can be seen how the TE_{10} has an inherent horizontal polarization that radiates even if the planar geometry is perfectly symmetric.

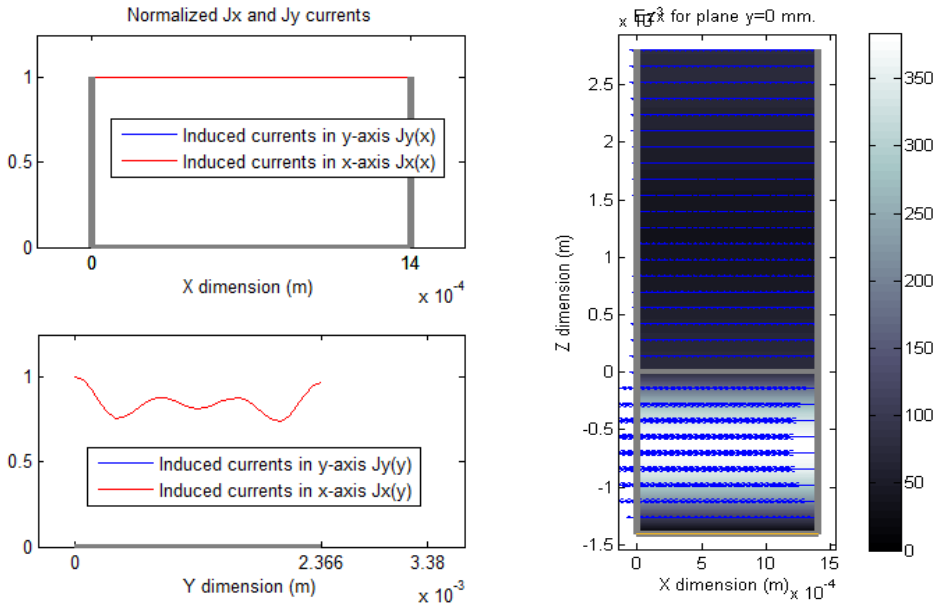

Figure 3.1.3 Normalized surface currents on the metallization and transversal electric field.

The Entire Domain basis functions based method, results and convergence were extensively checked and validated in the literature (reader may refer to all [Gomez *] references). It can be seen that the **developed code matches perfectly with these previous results**, fulfilling the goal of this first step, which was to settle a solid base as a starting point to increase the complexity of the method. By extending the mathematical workout presented in Chapter 2, this method will be able to deal with general purpose basis functions, the main novelty in the analysis of this type of leaky-wave antennas presented in this work.

3.2. Subdomain Basis Functions

The use of Entire Domain basis functions allows a significant reduction in the MoM matrix size compared to the case where Subdomain type functions are employed, provided the geometry is limited to a simple rectangular strip or slot. Geometries of light complexity as the cross-dipole, square loop and Jerusalem cross have been successfully modeled with the use of more elaborated Entire domain functions, tailored specifically for each one of those geometries, see [Tsao 1984] and [Bozzi 2005], resulting in extremely fast algorithms. An excellent overview of this element specific ED functions can be found in [Mittra 1988]. The major drawback is that the developed code is only applicable for the specific geometry; for any new geometry, a new set of suitable ED basis functions must be found, if ever possible, and introduced in the analytical integrals to create a new simulation code.

Entire Domain functions appear as the logical choice to solve problems for electrically large structures, since the computing cost will be the main concern. However, as was detailed in Chapter 2, the analytical nature of the proposed method together with the simplification of the whole 3D problem into the analysis of a 2D current distribution (a general 2.5D problem) represents a more than considerable reduction of the computational cost. Also, matricial treatment of the data will speed up the calculations when using Matlab, as will be explained in Chapter 4. Furthermore, for arbitrary geometries, suitable ED basis functions are not, most of the times, available. Based on these premises, the way to move forward in the field of study of the LWA, was to open the door to the subdomain approach. The present work is aimed to be a **general-use method**, so the capability to analyze arbitrary shaped printed circuits, thanks to the Subdomain approach, has been chosen over the extreme reduction of computational cost, inherent to the use of ED functions.

The most popular sub-domain functions found in literature are Pulse, Roof-Top and RWG basis functions. Pulse functions are uniform on each cell, which leads to discontinuities problems when modelling the current density. Roof-Top and RWG functions are not affected by this issue since they overlap on adjacent cells.

The use of sub-domain functions requires meshing the geometry of the structure under study. Different types of meshing can be applied depending on the chosen sub-domain basis functions, in order to get an acceptable accuracy modelling the contour of the geometry. For the development of the proposed method, **rectangular mesh with Roof-Top basis functions** will be applied.

3.2.1. Roof-tops basis functions

The Roof-Top functions ([Becks 1992], [Mittra 1988]) are defined as the product of triangular or piecewise linear functions along the direction of the current flow (over two cells) and of step or piecewise constant functions in the orthogonal dimension (over one cell). The centres of the functions directed in x and directed in y, represented by red circles and black crosses respectively, are offset by $\left(\frac{\Delta x}{2}, \frac{\Delta y}{2}\right)$. This type of functions are the most commonly used due to its good performance in convergence and accuracy in the estimation of the current density, unknown a priori, with a relative small number of basis and test functions.

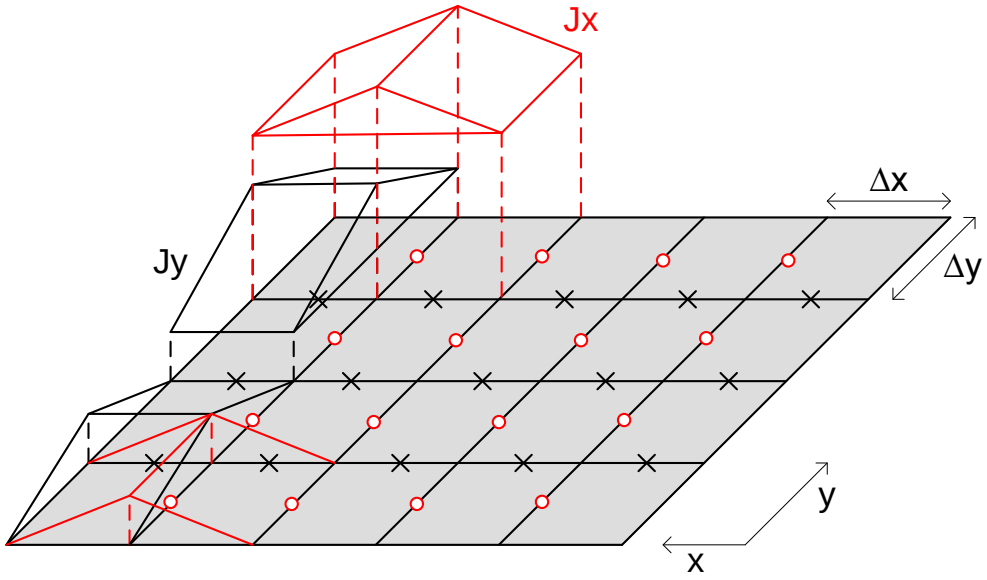

Figure 3.2.1.1 Roof-Top functions on a metallic patch.

J_x expansion functions

$$\begin{cases} \Lambda^X(x_{nx}) = \begin{cases} 1 - \dfrac{|x - x_{nx}|}{\Delta x}, & |x - x_{nx}| < \Delta x \\ 0, & \textit{elsewhere} \end{cases} \\ \Pi^X(y_{ny}) = \begin{cases} 1, & |y - y_{ny}| < \dfrac{\Delta y}{2} \\ 0, & \textit{elsewhere} \end{cases} \end{cases}$$

J_y expansion functions

$$\begin{cases} \Lambda^Y(y_{ny}) = \begin{cases} 1 - \dfrac{|y - y_{ny}|}{\Delta y}, & |y - y_{ny}| < \Delta y \\ 0, & \textit{elsewhere} \end{cases} \\ \Pi^Y(x_{nx}) = \begin{cases} 1, & |x - x_{nx}| < \dfrac{\Delta x}{2} \\ 0, & \textit{elsewhere} \end{cases} \end{cases}$$

Where nx and ny are the indexes for the cells in the x and y direction, respectively, and Δx and Δy are the lengths of the cell in each direction. Traditionally, it had to be necessarily an N x N cells mesh, so the FFT could be applied, which is not necessary in the present method. Since the **method is developed in the spatial domain**, it is possible to have a different number of cells in each direction.

The current expansion for Subdomain basis functions varies from the one used in the case of the Entire Domain. Now **the current** is evaluated in each cell of the grid, so **in the nth cell** it can be expressed:

$$\vec{J}(x', y') = \vec{J}_x(x', y') + \vec{J}_y(x', y') = \left(\beta_x f(x') f(y') \hat{x} + \beta_y f(x') f(y') \hat{y}\right) e^{-jk_{0y}y'}$$

The **basis and test integrals** needed in the Green Functions obtained in Chapter 2 are now defined as shown in Table 3.2.1.1, introducing the roof-top expansion functions in expressions from (2.8.2.6) to (2.8.2.13). The analytical expressions for the basis integrals can be found in Appendix A Workout 9.

Basis Integrals	Test Integrals
$I_{BX}^{EX} = \int_{x'} \bar{X}_m^{(p)}(x') \cdot \hat{x} \cdot \Lambda_{nx}^{X}(x') dx'$	$I_{TX}^{EX} = \int_{x} e_{mx}^{(p)}(x) \cdot \hat{x} \cdot \Lambda_{lx}^{X}(x) dx$
$I_{BY}^{EX} = \int_{y'} Y_{my}(y') \cdot \Pi_{ny}^{X}(y') \cdot e^{-jk_0 y'} dy'$	$I_{TY}^{EX} = \int_{y} e^{-jk_{my} y} \cdot \Pi_{ly}^{X}(y) dy$
$I_{BX}^{EY} = \int_{x'} \bar{X}_m^{(p)}(x') \cdot \hat{y} \cdot \Pi_{nx}^{Y}(x') dx'$	$I_{TX}^{EY} = \int_{x'} e_{mx}^{(p)}(x) \cdot \hat{y} \cdot \Pi_{lx}^{Y}(x) dx$
$I_{BY}^{EY} = \int_{y'} Y_{my}(y') \cdot \Lambda_{ny}^{Y}(y') \cdot e^{-jk_0 y'} dy'$	$I_{TY}^{EY} = \int_{y'} e^{-jk_{my} y} \cdot \Lambda_{ly}^{Y}(y) dy$

Table 3.2.1.1 Roof-Tops basis and test integrals

Test integrals are more easily solved following a similar workout, producing similar results. They are not shown in the Appendix, since it does not present anything new. As can be figured out, there is a direct relation between basis functions integrals and test function integrals, which will make possible the re-use of modules of code, decreasing the computational cost.

3.2.2. Edge conditions and current continuity.

The current induced on a metallic patch is expected to have certain edges conditions. In order to minimize the number of functions required to model accurately the current, it is desirable that these functions satisfy the appropriate edge conditions.

Some authors have suggested having an irregular grid for both dimensions, [Glisson 1980] and [Pearson 1985], meaning the meshing is such that half a cell is left out of the analysis at the edges of the structure, so that the centers where the functions are evaluated do not fall along the edges (nor on corners or bends), where the charge is singular. This mesh can be used satisfactorily when using pulse or triangular basis functions, which are not separable in each dimension and do not satisfy the edge conditions by themselves. This mesh is not recommendable when using Roof-Tops, which have a different variation for the x-directed and for the y-directed currents.

For a metallic patch, the *Roof-top triangles* approach zero in the direction of flow at the patch edges, and the *Roof-top steps* are non zero in the direction of flow parallel to the

edges, allowing for the representation of the edge singularity. As can be seen on Figure 3.2.1.1, to satisfy this edge condition and generate correct results, the centers of the x-directed and the y-directed roof-top functions need to be offset [Park 1998].

Each subsection of the current (the triangle-step doublet) extends over two cells of the grid, longer in the direction of the current, with at least one x-directed and y-directed roof-top overlaying at each cell, ensuring the current continuity.

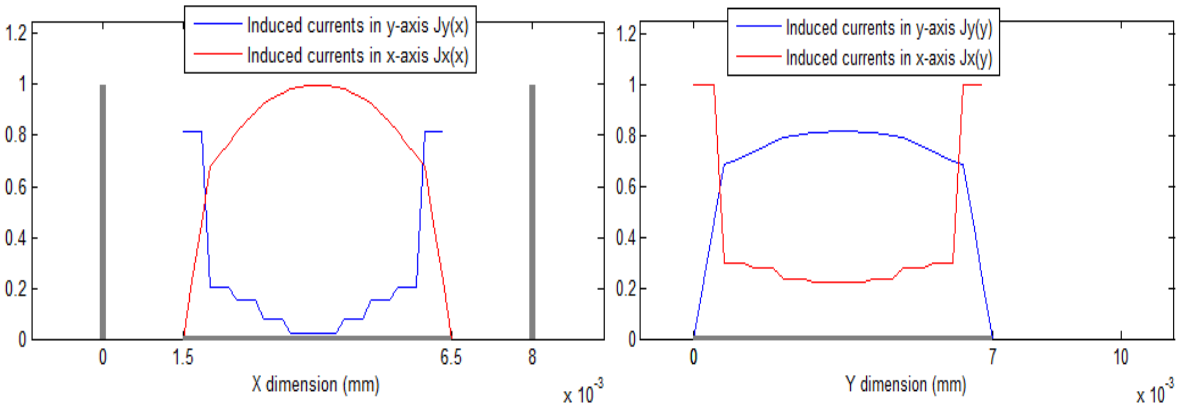

Figure 3.2.2.1 Current distributions on the metallic patches.

Figure 3.2.2.1 shows the obtained currents distributions for the periodic metallic patch structure using Roof-Tops at 10 GHz for a uniform mesh of 10x10 cells. It can be seen how the currents are continuous functions that fulfil the edge conditions discussed above. In previous section, Figure 3.1.1 showed the currents distributions modelled with sinusoidal Entire Domain basis functions for exactly the same patch geometry at 10 GHz too. Comparing both results, it can be easily seen that they have a very good agreement on normalized value and shape, validating the use of Roof-Tops with the MoM method. In any case, modelling the currents with the use of triangle and pulse variations over a meshed geometry results in less smooth plots, unless we use a very large number of cells. This is unnecessary in order to obtain accurate results, given that in the present example, a mesh of 5 by 5 cells of the metallic patch was enough to produce correct numerical results in terms of propagation constant and fields. The 10 by 10 mesh was merely used to present a matching between the ED and SD modelled currents plots.

3.2.3. Meshing criteria.

The Roof-Top basis functions have been used for decades now, but there is still some confusion when it comes to choose the correct mesh or where exactly to place the function upon the cell. In this section it is intended to contemplate several options from the literature and contrast the results.

The first issue to assess is the use of a uniform or non-uniform rectangular mesh. The first one will produce an N x N grid for each direction of the current. When working with Spectral Domain methods, this allows the use of the FFT for the summation in the MoM matrix. In [Mittra 1988] it was established that an N x N grid was strictly necessary, although two years later, the same authors extended the possibility to use the FFT for N x M grids [Chan 1990]. On the other hand, by choosing freely the size of the grid (Nx x Ny), the mesh can be optimized to accurately model the geometry with a minimum number of cells. As said previously, since the proposed method applies the Spacial Domain Green functions, there is no need for considerations about the grid being the same size for both dimensions, so Nx and Ny may be of different size.

A general meshing for Roof-Top functions is presented in [Rubin 1983] and [Park 1998], illustrated in Figure 3.2.1.1, where a grid of (Nx x Ny) cells is applied, with uniform size of the cells defined by Δx and Δy, so the same set of cells is applied for calculating both the distribution of current along the x-axis and y-axis. For geometries in which the metal extends across periodic cell boundaries, Roof-Top functions are placed such that the current is directed across the boundary into the adjacent periodic cell. Since the currents at both sides of the periodic boundary are related by Floquet, it is only necessary to analyze one of them.

Figure 3.2.3.1 below shows the Ny by Nx cells mesh for the metallic square loop printed circuit. From the 132 total cells, only 76 of them are metal filled, pictured in gray. Only those will be considered for the existence of basis functions. This way, each blue filled cell will allocate a Roof-top basis function (in red), making a total of Cx=58 basis functions for the currents directed in x. Likewise, a basis function directed in y will exist on each pink shadowed cell, computing Cy=56 functions or unknowns.

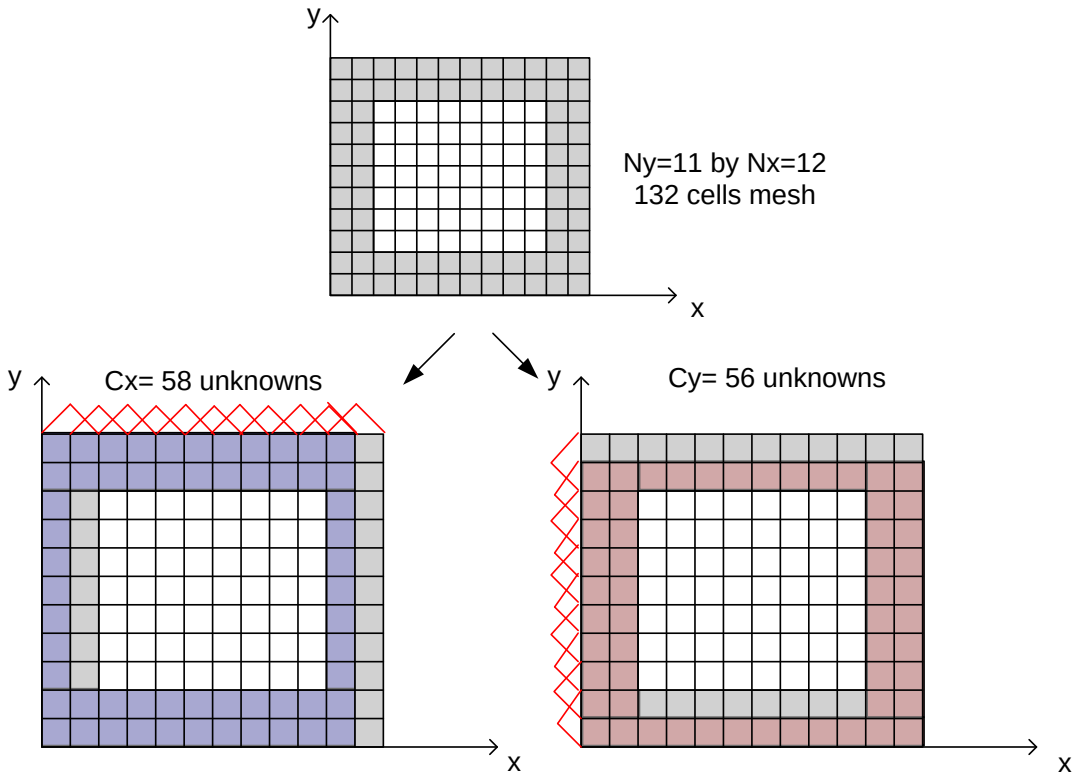

Figure 3.2.3.1 Mesh for the Roof-Top basis funtions.

For calculating the determinant of the MoM matrix, [P] must be square (see Chapter 2). Considering the case of a periodic metallization that do not extend to adjacent cells and a mesh of (Nx x Ny) cells, the sizes of the matrices used in the MoM are:

$I_{BX}^{EX}\ I_{BX}^{EY}\ I_{TX}^{EX}\ I_{TX}^{EY}$	C_x by (Floquet and PPM modes)
$I_{BY}^{EX}\ I_{BY}^{EY}\ I_{TY}^{EX}\ I_{TY}^{EY}$	C_y by (Floquet and PPM modes)
P_{JX}^{EX}	C_x by C_x
P_{JY}^{EX}	C_x by C_y
P_{JX}^{EY}	C_y by C_x
P_{JY}^{EY}	C_y by C_y
$(P)=\begin{pmatrix} P_{JX}^{EX} & P_{JY}^{EX} \\ P_{JX}^{EY} & P_{JY}^{EY} \end{pmatrix}$	C_x+C_y by C_x+C_y

Table 3.2.3.1 Matrix dimensions for rectangular uniform mesh.

C_y and C_x are the number of unknown coefficients for the y directed current J_y and the x directed current J_x, and those will depend directly on the geometry. Note that the matrix dimensions containing the PPM and Floquet modes are not shown, since they are non-dependant on the planar metallization mesh. It can be seen that a square matrix P is obtained, for a rectangular mesh with any value of Nx and Ny.

Comparing the matrix dimensions obtained for the Roof-top basis functions case with the Entire domain case, previously mentioned in Table 3.1.1, it can be easily noticed how the matrices of the basis and test integrals are significantly larger in the subdomain approach: considering the example above in Figure 3.2.3.1 for the square loop, I_{BX}^{EX} is of the order of 58 by (Floquet and PPM modes) versus the size in the case of working with Entire domain and assuming a square metallic patch, 6 by (Floquet and PPM modes). This is the reason for the rise in the computational cost in the case of Subdomain basis functions approach, since the calculation of the analytical expressions of these integrals represents a considerable part of the code. In Chapter 4, a way-round this inconvenience will be presented, with a formulation midway between the Entire Domain and the Subdomain approach.

3.2.4. Convergence.

As seen in Chapter 2, the fields inside the structure were expanded in a set of PPModes in the x-direction and, for each PPM, in a set of Floquet armonics in the y-direction, where the periodicity lies. When using sub-domain functions, as the number of cells increases, the number of PPW modes and Floquet modes needed to reach convergence grows exponentially. This is so because when the number of cells increases, so does the number of basis functions and more variations are contemplated in the currents expansion. It is logical that a larger number of PPM and Floquet modes are necessary to model the fields that those currents generate. Specifically for Roof-Top functions, it is documented that Galerkin procedure converges much faster than other testing procedures [Chan 1990].

Figure 3.2.4.1 shows the variation of the function determinant of the MoM matriz P with the number of PPM and Floquet modes, for the rectangular patch analyzed in Figure 3.2.1.2., at 10 GHz. Each determinant function is normalized so all the graphs could be plot on the same axis. Each line corresponds to a different number of cells, Nx for the divisions on the x-direction and Ny for those on the y-directions, resulting in lines for 16, 25, 36 and 49 cells respectively, which are more than enough for this simple geometry. This type of convergence study is quite fast since it does not require a search in the complex plane and gives a very good first idea of the number of expansion modes that a certain number of cells needs to obtain accurate results. It can be observed how, as the number of cells increases, the number of modes does too in order to converge. In the case of the patch, for 25 cells (blue dashed line), by visual inspection, it is enough with 75 PPM and 50 Floquet modes, for 36 cells it increases to 125 PPM and 75 Floquet modes and finally for 49 cells it reaches about 150 PPM and 100 Floquet modes. It seems an excessively large number of required modes, given that the number of cells is relatively small.

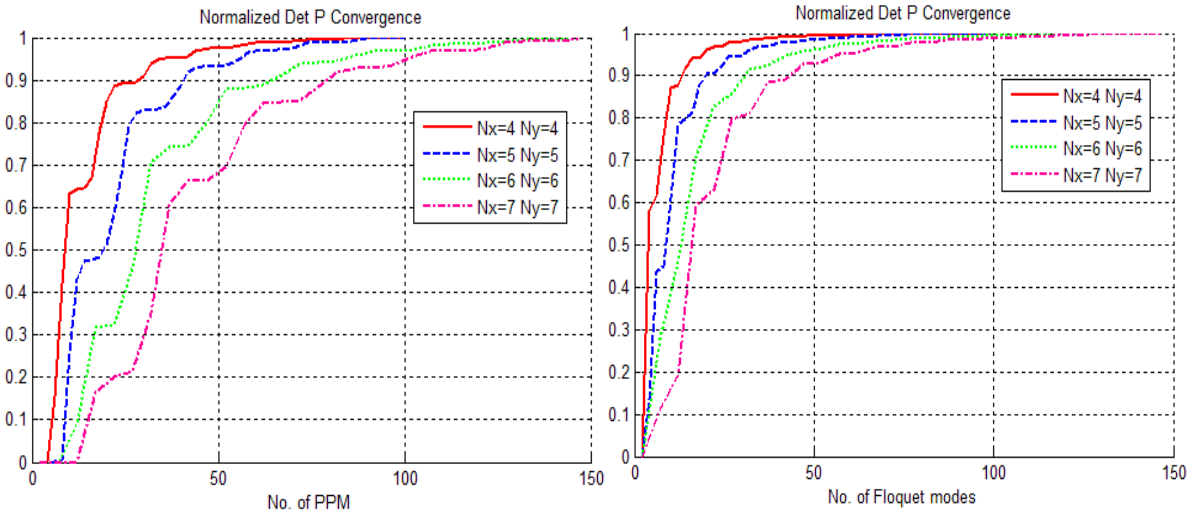

Figure 3.2.4.1 Convergence of the function Det(P).

This phenomenon should not be confused with the concept introduced by [Mittra 1963] of relative convergence that occurs using the Mode-Matching technique, in which unless an optimum number of modes was selected, correct results could not be obtained, even when using large numbers of modes. After [Mittra 1972], some authors believed that this effect was also applicable to integral equations solved by the Moment Method. Although it is

true that when using discontinuous basis functions convergence problems may arise, Mittra himself established in [Mittra 1990] that there was no proof that this phenomenon was applicable for the analysis of FSS and shielded microstrip configurations (similar to the structure analyzed in this work), and to obtain accurate results it is necessary to rely on **absolute convergence**. In other words, since the present method uses continuous basis functions that fulfil the edge conditions, the number of those basis functions and modes necessary to converge must be obtained by experience, increasing the number of modes until the variation is practically non-existent.

Although the study of the determinant of P variation was a good approximation to the number of modes required to reach accurate results in those previous works developed for the Entire Domain [Gomez March-2006], the author considers it is not so reliable for the case of subdomains functions. By practical experience, analyzing different geometries with the method presented in this work, it was probed that the amount of modes that resulted in convergent values for the propagation constant was far less than those predicted by the convergence study of the det(P).

Figure 3.2.4.2 shows the new proposed convergence study, directly in the complex plane, where the search for the zero of the determinant takes place. Both graphs represent how the complex zero moves in the complex plane for the same patch structure, at 10GHz, for a mesh of 25 cells. Figure 3.2.4.2 a) represents the variation of the modal solution as the number of Floquet modes My increases from 5 to 60 (following the direction of the arrow). Figure 3.2.4.2 b) represents the same variation but for the number of PPM, from Mx=10 to Mx=80. It is important to remember that, while the number of PPM expands from 0 to Mx, the Floquet modes are defined from -My to +My. This is the reason why a smaller number of Floquet modes is always taken. From these results, it can be seen that with 40 PPM and 20 Floquet modes it is more that enough to obtain an accurate solution for the 25 cells patch. Comparing this with the previous estimation from the det(P), 75 PPM and 50 Floquet modes, it can be concluded that the determinant function variations with the number of modes is superior to the variation of the position of the zero in the complex plane, and therefore, not to take into account when working with subdomain functions.

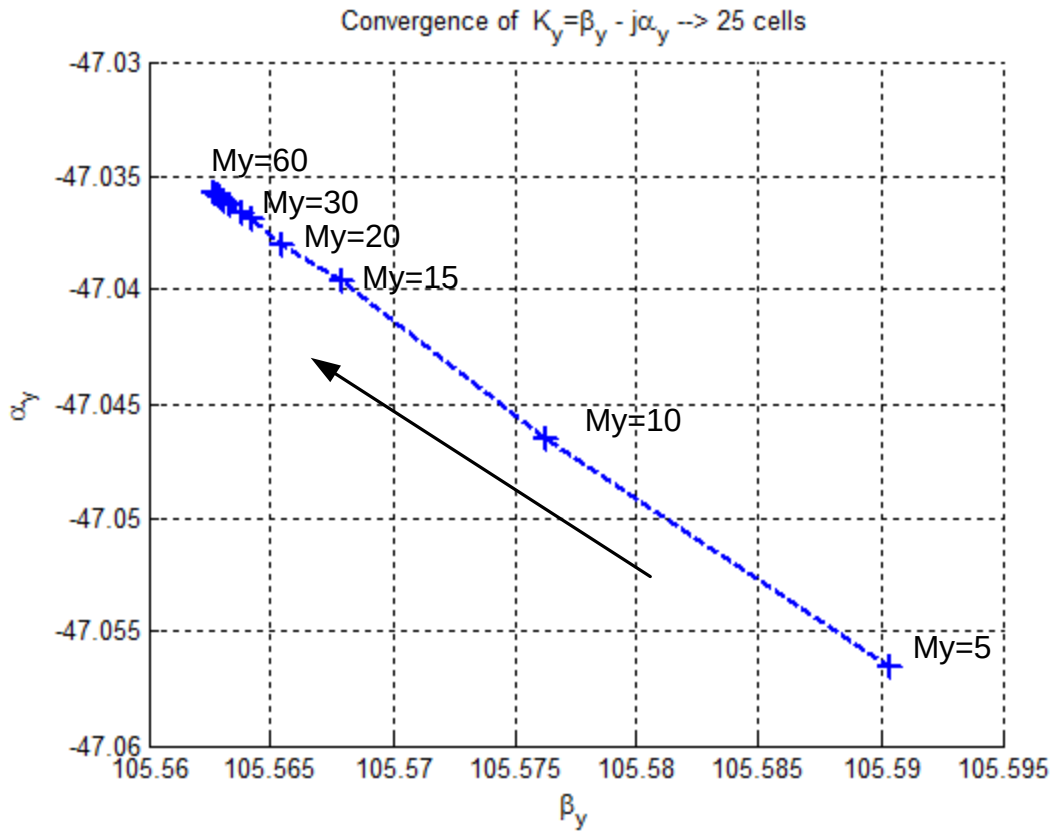

Figure 3.2.4.2 Convergence in the complex plane. a) My =Floquet modes.

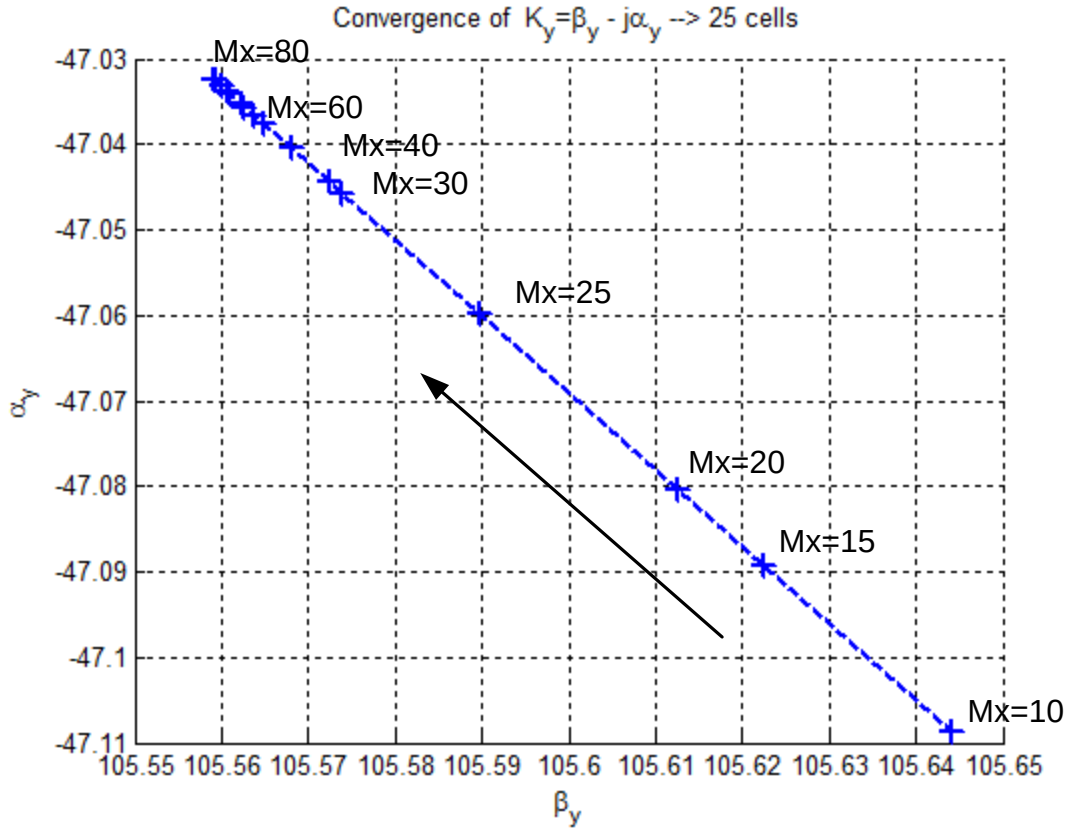

Figure 3.2.4.2 Convergence in the complex plane. b) Mx =PPM.

The convergence for subdomain based techniques depends mostly on the number of cells in which the planar metallization is meshed, which is not applicable to the entire domain dependence to the number of basis functions. In Figure 3.2.4.3 and 3.2.4.4, the same previous convergence study in the complex plane is extended to different number of cells. The blue dashed line for the 25 cells mesh from Figure 3.2.4.2 is exactly the same that the one in the next two figures. As expected, the more number of cells, the more modes to model the fields are needed, although given the scale of the axis, the variation is very low. It can be seen again that a larger number of PPM than Floquet modes is required for each of meshes.

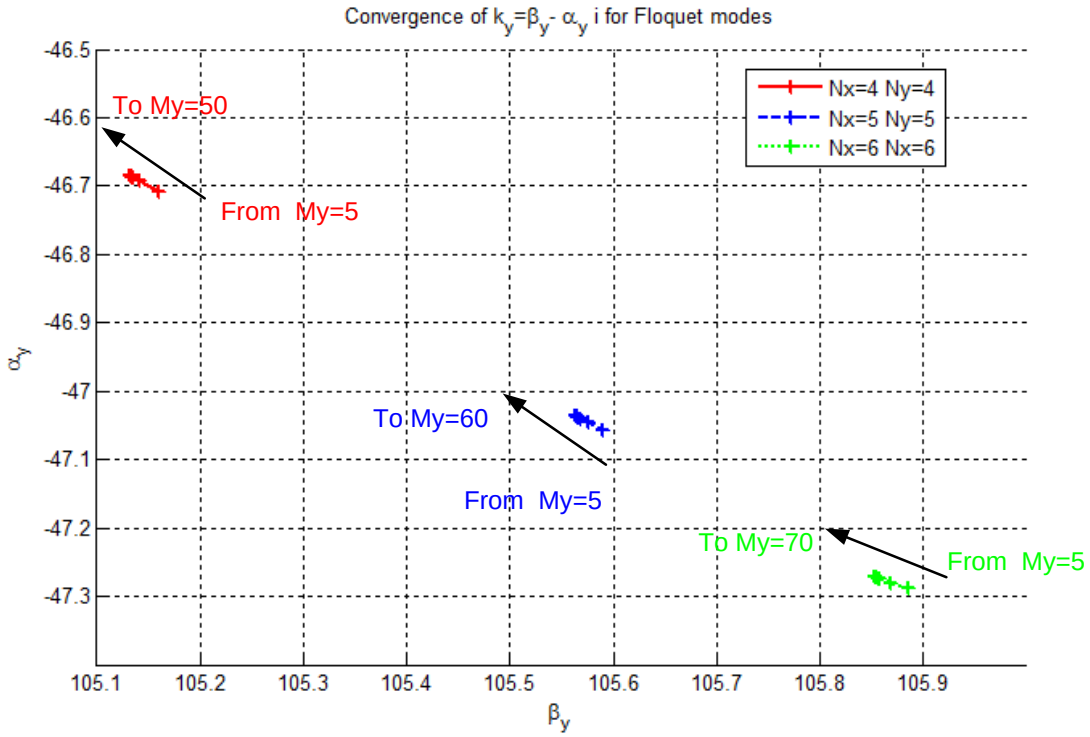

Figure 3.2.4.3 Modal solution convergence in the complex plane for Floquet modes.

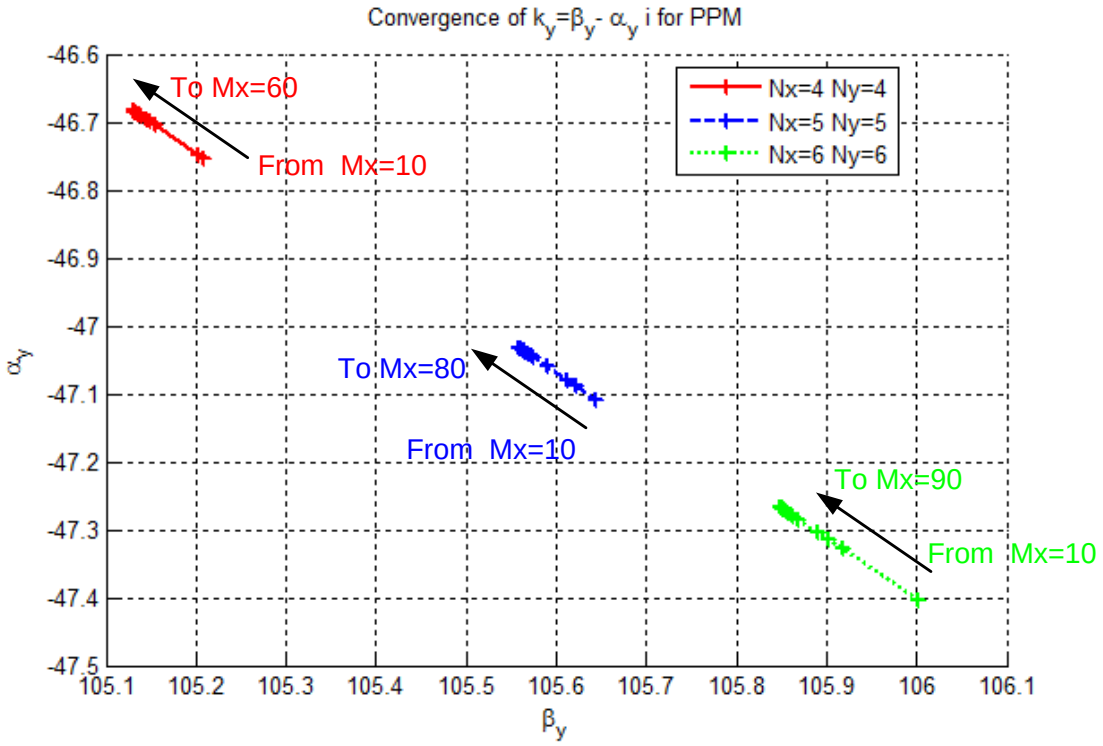

Figure 3.2.4.4 Modal solution convergence in the complex plane for PPM.

When working with Entire Domain basis functions, it was demonstrated in [Gomez March-2006] that the solution of the mode depended little with the number of basis functions used, it was much more dependant on the number of PPM and Floquet modes to converge. In the Subdomain approach, Figure 3.2.4.3 and 3.2.4.4 show how the number of PPM and Floquet modes affect relatively little to the result, in comparison with the effect that the number of cells has on it, which will be dominant and dependant on the geometry. Even more, due to the simplicity of the patch, in this case there is not a significant difference in the propagation constant results obtained for the 5 by 5 grid and the 7 by 7 grid. This little variation with the number of cells is best observed in Table 3.2.4.1 below:

Ny \ Nx	5	6	7
5	105.5738 - 47.0365i	105.8320 - 47.2794i	106.0229 - 47.4522i
6	105.5859 - 47.0301i	105.8540 - 47.2719i	106.0448 - 47.4440i
7	105.6038 - 47.0279i	105.8718 - 47.2690i	106.0674 - 47.4428i

Table 3.2.4.1 Modal solution convergence with the number of cells.

To give a rough idea of how little variation exists between these results, the aiming angle of the main beam for the 5 by 5 mesh solution is 30.27º and for the 7 by 7 mesh, it is 30.42º. After the results of these studies, it can be concluded that the proposed technique presents a **good numerical convergence** behavior. In any case, before initiating the study of any new geometry, a convergence analysis must be done, in a certain order:

- First, the number of cells must be chosen adequately to the geometry complexity. A study similar to that presented in Figures 3.2.4.3 and 3.2.4.4 is perfect for this purpose.

- Second, truncating the PPM and Floquet modes summatories, by including more and more PPM and Floquet modes until the result does not change. Again, these results are included in the study of Figure 3.2.4.2. By zooming in, it can be decided the number of modes from which the variation in the complex plane for a given number of cells is negligible.

3.3. Validation Results

A very simple LWA will be analysed in order to validate the results of the Subdomain code versus the Entire domain method based on the PAMELA software, and already checked in previous section. In this structure the width of the aperture a = 8 mm and the periodicity P =10 mm. A graphical description of the structure is presented at the top of Figure 3.3.1. and it is based on the one studied in [Vardaxoglou Apr-1997]. The metal patches are 5 mm x 7 mm, the dielectric (ε_r =3) is 0.37 mm thick and the length of the stubs at the top of the waveguide is L= 7mm. The Table 3.3.1 below shows the number of Floquet/PPM basis functions for the Entire domain and the number of cells in the Subdomain case used in the simulation. Also the number of PPW modes and Floquet modes needed to reach convergence in the solution $k_y = \beta - \alpha i$ using sinusoidal basis functions and in the case of Roof-Tops functions respectively.

	ED_ Sinusoidal	SD_ Roof-Tops
	1/4 Basis functions	25 cells
No. PPW modes	10	50
No. Floquet modes	41	61

Table 3.3.1 Convergence comparison Entire Domain/ Sub-domain

The Figure 3.3.1 presents the results obtained for the normalized phase constant and the normalized attenuation constant in the longitudinal direction of the first two TE modes, for the sinusoidal Entire domain basis functions vs. Subdomain basis functions (Roof-Tops). It can be seen how in this range of frequencies both modes are within the radiation zone (fast-wave modes). The main beam moves towards endfire as the frequency increases. The radiation constant decreases as the main beam approaches endfire (β / β_0 close to 1) as expected, and eventually it will become a surface wave that propagates and is bounded within the waveguide.

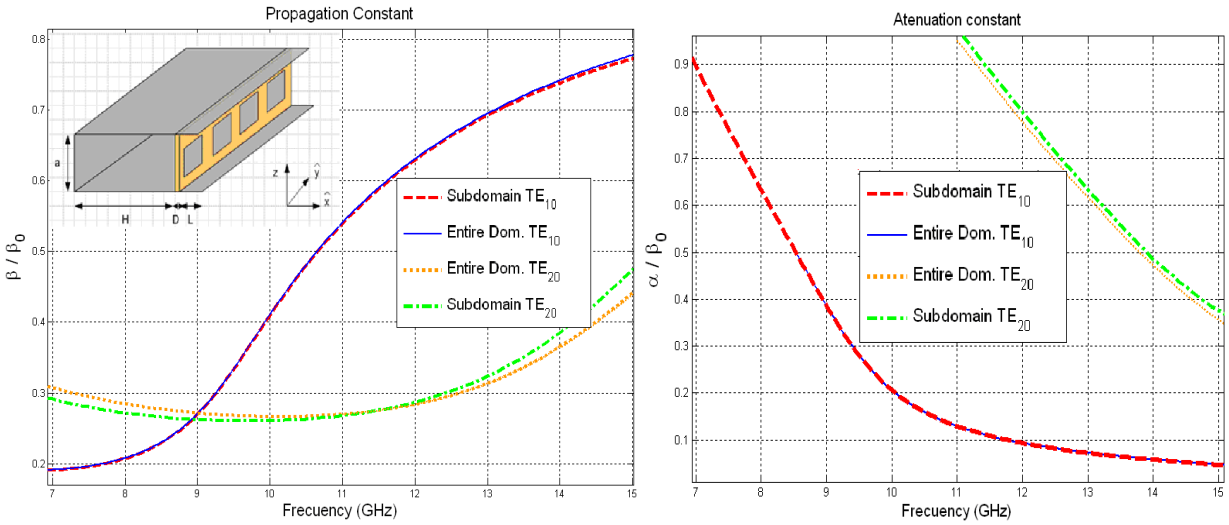

Figure 3.3.1 Complex propagation constant.

Upon inspecting the results, it can be seen a perfect agreement between the results obtained using entire domain and Roof-Tops basis functions. The slight difference in the values at higher frequencies was expected. As the frequency increases the electrical size of the cell also increases, reducing the accuracy. For this reason, as the analysis goes higher in frequency, a smaller cell size would be required, with the consequent rise in simulation time.

Figures 3.3.2 and 3.3.3 present the induced currents on the metallic printed circuit obtained with the use of Roof-tops basis functions and sinusoidal Entire domain functions respectively. It can be appreciated that both results match perfectly, considering the differences between the different basis functions shape.

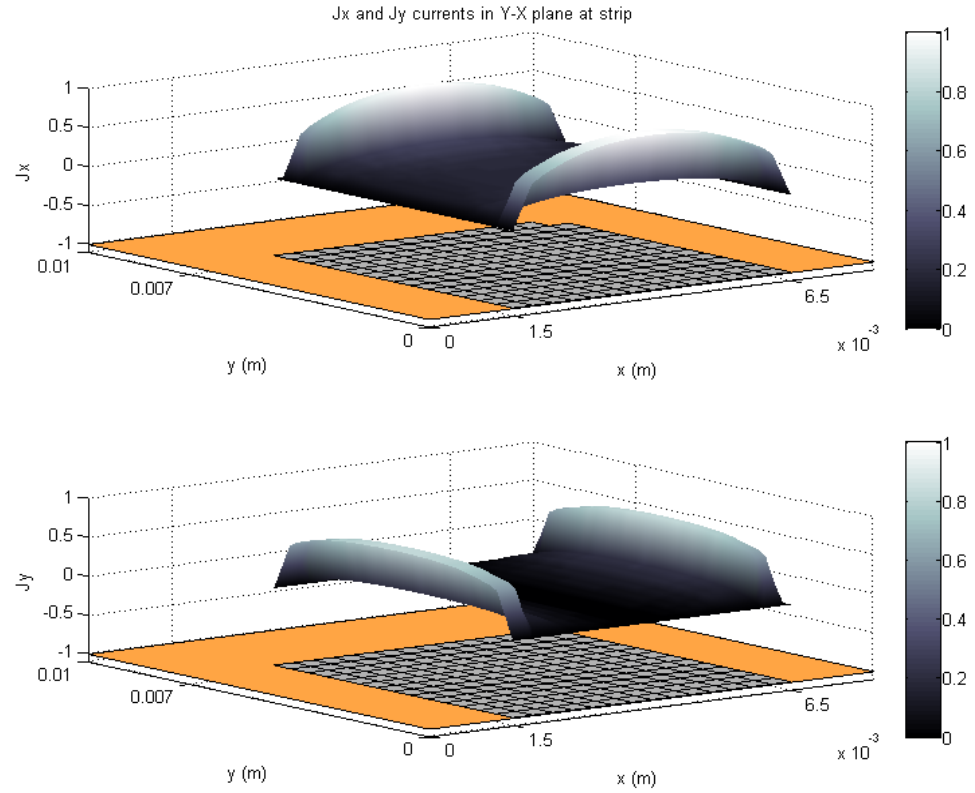

Figure 3.3.2 Induced currents for the Subdomain method.

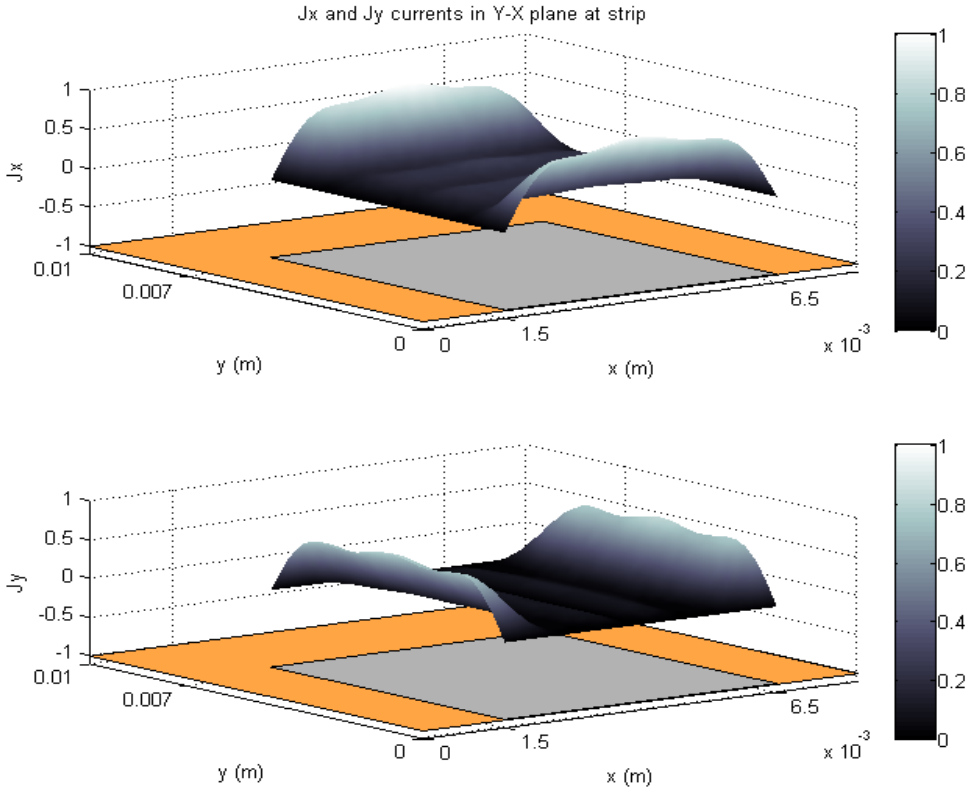

Figure 3.3.3 Induced currents for the Entire domain method.

CONCLUSION

In this Chapter, the Spatial Domain MoM technique to analyze LWAs embedded inside a waveguide, developed in Chapter 2, has been completed with the combination of Roof-Tops basis functions to model the currents on the planar metallizations, developing a novel method able to study the modal solutions of LWAs with non-regular printed circuits. This new approach makes the present method much more versatile, and opens the door to different applications for this type of antennas, based on more complex geometries and the modified scanning behavior that those geometries may enforce. The results have been validated with previously computed models and measurements from literature, assuring its reliability. The consistency of this new approach has been taken into account, in terms of continuity and edge conditions. Finally, the convergence analysis demonstrated that the developed method is rapidly convergent providing accurate results.

Now that the method is completely defined and formulated, it must be efficiently coded into a simulation tool. Next chapter will be dedicated to this software and its graphical interface, how to use it and how the user may extend its capabilities due to its full modular structure.

CHAPTER 4 - THE SOFTWARE

Where an original study of a printed square loop PLWA using WELAST is presented and the novel capabilities and consistency of this new developed software is probed.

The main objective of the present PhD was to create a novel and versatile simulation tool, able to analyse laterally shielded structures that may had any periodic printed circuit of arbitrary shape on the inner dielectric. Previous simulation programs found in literature, p.e. P.A.M.E.L.A. [Gómez Aug-2006], were very limited, only capable of modelling simple rectangular metallic patches or slots. As will be explained in this chapter, although both programs count with common points, as the use of MoM and the chosen coding language Matlab, a completely new approach on modelling the 2D printed circuit of the PLWA is applied. The complexity of this new approach will allow dealing with the induced currents on arbitrary printed circuit geometries. The key for this evolution lies on the use of Sub-domain basis functions, instead of Entire domain basis functions, as was explained in previous chapters. This conceptual change will open the door to a new range of leaky wave antennas and their different behaviours, due to the printed circuit shape, to be studied and comprehended.

Another aspect is the educational interest of the software. The study of the modal spectrum of closed waveguides (rectangular, circular or coaxial) is compulsory and extensively treated by any electrical engineer. However, surface and leaky-wave modes

existing in open waveguides, filled or not with dielectric, are not so well documented in literature. Recently, novel applications for open dielectric waveguides in millimetre wave technologies to reduce conductor loss have retaken this forgotten topic. As was previously discussed in Chapter 1, commercial simulation software, such as HFSS, produces reliable results in terms of field distribution and radiation pattern, but as a global result. A full understanding of those results can only come from a **rigorous modal analysis** of the structure. New analysis tools are necessary to efficiently study and design new kinds of LWAs, to obtain good results knowing the reason behind them. And now, with the arise of the EBGs and PRSs, the software presented in this work will become a key tool to understand the theoretical and practical working principles of leaky-waves, and the conditions under they may exist in these open structures.

This chapter has a double goal. It will present the **major contribution** of this work, the **developed simulation tool for periodic LWAs**, including how to use its friendly graphical interface, its capabilities and how to easily extend it to new geometries, thanks to its modular nature. At the same time, through this software internal working tutorial, a **novel periodic LWA will be analyzed** in full depth. The chosen geometry is the **square loop printed circuit**. Although it is simple enough for the illustrative purpose of this chapter, to the author knowledge, there is no previous modal analysis of this kind of antenna. This chapter will provide with a full understanding of the propagating modes supported by the structure and their individual contribution to the total radiation pattern, as well as how the geometrical parameters of the loop affect to specific performance effects, as Bandgaps or unwanted modes.

4.1. Previous computed models: P.A.M.E.L.A.

It is the predecessor of the software created in this thesis, and, in the author eyes, its 'little sister'. The acronym stands for 'Program for Modal Analysis of Laterally Shielded Structures', in Spanish. It was the first interactive environment created for the analysis of leaky-wave modes in certain types of open waveguides. This program was presented for educative purposes [Gómez Aug-2006], to teach advanced concepts related to the

electromagnetic theory in open waveguides, since the study of leaky wave modes has been often underestimated in the academic formation of microwave engineers. P.A.M.E.L.A. studies the propagation characteristics of those modes supported by the open structure, both surface and leaky wave modes. Once a solution for the propagation constants (phase and attenuation) in the longitudinal direction of the waveguide is found, the field and currents inside, as well as the radiation pattern, are obtained.

This tool was based on the use of sinusoidal Entire Domain basis functions to model the induced currents on the metallization. The advantage of this type of basis functions is that they converge rapidly with a reduced number of functions and, as a direct consequence, a small number of PPM and Floquet modes. This fact, combined with the analytical nature of the full wave method, made it possible to develop a fast and accurate software to analyze LWAs. The program was coded in Matlab, using its matrix based environment to speed up the calculations. Results of this software can be found in [Gomez Sept-2005].

As has been already mentioned in Chapter 3, this predecessor had a major limitation. The Entire Domain approach, although simple and fast, can only support regular geometries, such as rectangular strips or slots. This main drawback exists no longer in the present work, where the new Subdomain approach allows for complex shapes printed on this PLWA configuration.

Also, previous works used an approximation for the radiated pattern, based on an infinite radiating wire, which did not produce closed and rigorous expressions. In the present work, said expressions will be obtained for both E and H radiating planes, taking into account the higher order PPM contribution, as will be seen by the end of this Chapter.

Also, it is important to highlight that the software developed this thesis was first coded using the same Entire Domain approach as its predecessor with a double purpose: first, to validate results, see Chapter 3, and second to build a complete simulation tool that offers the possibility to analyze simple structures using either type of basis functions.

4.2. A novel simulation tool: W.E.L.A.S.T.

The acronym stands for 'Waveguide Embedded Leaky-wave Antenna Simulation Tool'. The analysis with this program is interactive, with graphic results in real time and a sequential procedure in order to help the user to understand the inside workings of the leaky-wave modes.

4.2.1. Novel subdomain approach and coding philosophy.

The introduction of Subdomain basis functions opens the possibilities from the rectangular metallic patch to an infinite number of geometries that may be used as planar metallization inside the dielectric open waveguide. Some of the most popular geometries are showed in Figure 4.2.1.1, and their slots counterparts. These geometries, single and double square loops, split loops and so on, have been extensively studied as frequency selective surfaces (FSS) ([Wu 1995], [Vardaxoglou 1997]), and even some of them as LWAs, analyzing practical measurements in order to characterize the antenna. For the first time, a full-wave method developed for the modal analysis of laterally shielded periodic LWAs is able to integrate these more complex unit cells. This chapter will explain how the software allows the study of surface and leaky-wave modes that these metallizations may induce in the open dielectric waveguide, and the conditions necessary for them to radiate, even considering higher order modes and their unwanted effects on efficiency and radiation.

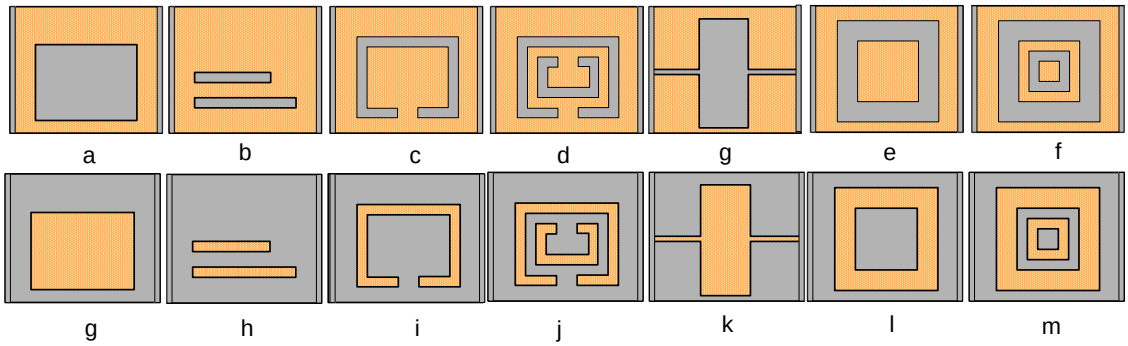

Figure 4.2.1.1 Subdomain basis functions supported geometries: strips and apertures.

The method is coded in Matlab v7. This programming language is well-known for its high-speed matricial treatment of the data and easy-to-build graphical interface tools. The fact that Roof-top basis functions are a complete set of continuous functions that fulfil the edge conditions of the currents, ensures the convergence of the solution with a reasonably small number of basis functions and PPM and Floquet modes associated to each of those functions. This translates into bearable matrix sizes in Matlab environment, which is crucial for a fast and efficient computation. The mathematical expressions for the basis and test integrals that conform the MoM matrix are completely analytical for the Rooftop basis functions, as presented in Chapter 3. It is important to remember that the only numerical calculation will be the complex search of the determinant zero.

To apply the Roof-tops basis functions on the metallization, it must be meshed into a grid. The metal patch will be uniformly divided into a number of cells of dimensions Δx by Δy. Each rectangular cell will have associated its corresponding test and basis integrals, as seen in Chapter 3. At this point, based on the novel Subdomain approach in combination with the matricial treatment of the data, two different ways to deal with the MoM matrix are proposed.

a) **Unknowns-based matrix**.

The periodic unit cell is divided into an N_x by N_y mesh, but only those cells that contain metal are considered in order to fill the MoM matrix. This way the number of unknowns will be C_x for the J_x currents and C_y for the J_y currents. This was explained in depth in the previous chapter, section 3.2.3, for the square loop with a mesh of 11 by 12 cells. This discrimination between cells takes computational time, together with the fact that the basis and test integrals are not of N_x or N_y size, but of a much larger C_x or C_y size, as explained in Table 3.2.3.1. Although this method is applicable to any arbitrary geometry covered by the rectangular mesh, it will not be the most efficient option in a range of cases.

b) **Spatial-based matrix**.

In section 3.2.3, it was discussed how the basis and integral matrices for the Subdomain method were considerably larger than those in the Entire domain approach (Table 3.1.1). The spatial-based MoM matrix [P] stands halfway, using a meshing for the Roof-tops functions, and at the same time, keeping the integral matrices to a minimum size, comparable to that of Entire domain ones. Figure 4.2.1.3 shows this approach for the same square loop with the same mesh that in the unknowns based matrix. Instead of placing the basis functions only on those cells filled with metal, all the mesh will be considered, considering a value of zero for the empty cells. The MoM matrix is built following the same order of the mesh in the physical space. This is possible since all the cells in the same row share the same basis and test integrals dependent on x, and the cells in the same column share the same basis and test integrals dependent on y. The only operations are permutations and combinations of small (N_x or N_y size) integral matrices, applied to all cells without distinction.

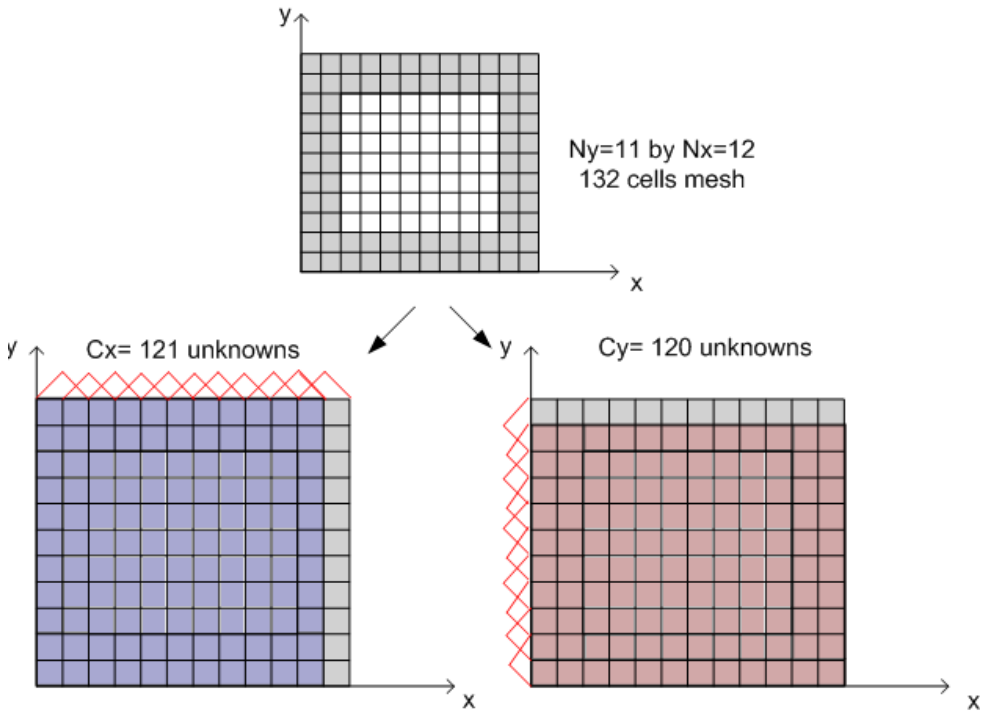

Figure 4.2.1.3 Mesh for the Roof-Top basis funtions.

Table 4.2.1.1 shows the dimensions for the matrices following the spatial-based method. It can be seen how the integral matrices are smaller than in the unknown-based approach, but at the same time, the size of the auxiliary P matrices are larger. Depending on this compromise, computations with spatial-based matrices will be much more efficient when the total number of cells is not too high.

MATRICES	SIZE
$I_{BX}^{EX}\ \ I_{TX}^{EX}$	(N_x-1) by (Floquet and PPM modes)
$I_{BX}^{EY}\ I_{TX}^{EY}$	N_x by (Floquet and PPM modes)
$I_{BY}^{EX}\ \ I_{TY}^{EX}$	N_y by (Floquet and PPM modes)
$I_{BY}^{EY}\ I_{TY}^{EY}$	(N_y-1) by (Floquet and PPM modes)
P_{JX}^{EX}	$N_y(N_x-1)$ by $N_y(N_x-1)$
P_{JY}^{EX}	$N_y(N_x-1)$ by $(N_y-1)N_x$
P_{JX}^{EY}	$(N_y-1)N_x$ by $N_y(N_x-1)$
P_{JY}^{EY}	$(N_y-1)N_x$ by $(N_y-1)N_x$
$(P)=\begin{pmatrix} P_{JX}^{EX} & P_{JY}^{EX} \\ P_{JX}^{EY} & P_{JY}^{EY} \end{pmatrix}$	$N_y(N_x-1)+(N_y-1)N_x$ by $N_y(N_x-1)+(N_y-1)N_x$

Table 4.2.1.1 Matrix dimensions for the spatial-based matrices.

Both methods can be used to solve any kind of geometries. The reason to include this second method in the software, is that it is much faster for a wide range of geometries of light complexity, that will not need a large number of cells to be accurately modelled and convergent. For comparison purposes, Table 4.2.1.1 shows the time in seconds to fill in the MoM matrix P for different sizes of mesh, for the same example of the metallic square loop. All cases consider the same 40 PPM and 20 Floquet modes for computation.

Nx x Ny	No. of unknowns		Time (sec)	
	Spatial-based	Unknowns-based	Spatial-based	Unknowns-based
6 x 6	60	48	0.182	0.273
8 x 8	112	72	0.337	0.441
10 x 10	180	96	0.661	0.791
12 x 12	264	120	1.328	0.954
14 x 14	364	144	3.138	1.273
16 x 16	480	168	5.889	1.671
18 x 18	612	192	10.965	2.095
20 x 20	760	216	19.402	2.516

Table 4.2.1.2 Time to fill the MoM matrix comparison in seconds.

In this specific square loop geometry, it is more efficient to use the spatial-based approach, up to roughly a mesh of 12 by 12 cells. After a convergence study, the results obtained with meshes of 8 or 10 cells were acceptable. Depending on the physical dimensions of the metallization, and the relation of empty cells with those containing metal, one method will be more efficient than the other. It is up to the user to assess the structure under study, maybe do a couple of trials and decide.

4.2.2. User´s guide: General working description.

To work with W.E.L.A.S.T. the user will have to follow a series of simple steps, in a logical order, to obtain the complete modal spectrum of the PLWA based on the chosen geometry. This sequence will lead the analysis from the closed WG structure to the final open LWA. The following sections will initiate the reader through the correct use of the program, making the most of its capabilities, as a new periodic LWA based on single square loops is presented throughout this chapter. Figure 4.2.2.1 shows the internal working of the software. First of all, the **geometrical description** of the structure to analyze must be introduced, from the type of metallization (strip or aperture), to the size of the waveguide containing the LWA. Also, the **numerical parameters**, depending on the method of analysis to apply (Entire Domain or Subdomain approach), such as the

number of PPModes, Floquet modes, etc. After the structure has been defined, the user shall start the **complex search** of the solution, in which the kernel will compute the determinant of the MoM matrix to obtain the value of the longitudinal propagation constant that makes it zero. Based on the obtained results, the user may find it necessary to undertake a **convergence study**, and readjust the numerical parameters previously introduced (number of basis functions or modes to model the fields) to produce accurate results. Once the program is satisfactorily tuned, the search for the solution will start again, for the modes supported by the closed structure and, from those, the complex modes corresponding to the solutions for the open LWA. For any given solution, the user may **plot results** for current, fields, power distribution and radiation pattern associated to it. A **dispersion analysis** can be also done, not only by sweeping the propagation constant with the frequency, but by sweeping any chosen geometrical parameter.

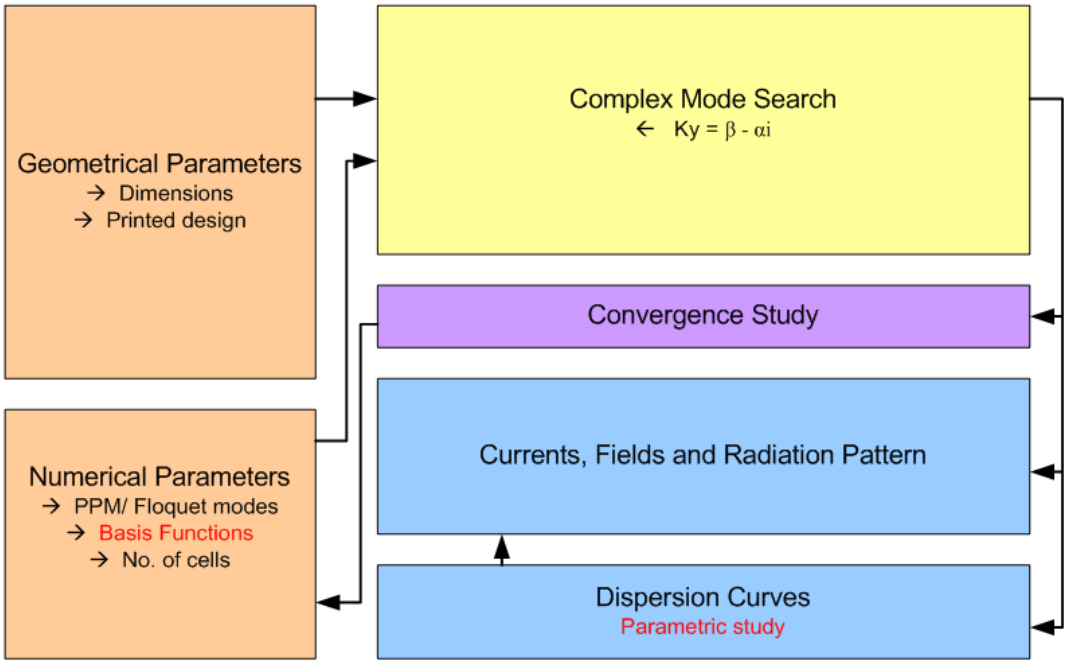

Figure 4.2.2.1 Program functional block diagram

The program counts with an intuitive **Graphical Interface**, which makes it even more agile to interact with. This GUI was developed using the tool GUIDE of Matlab v7. Each part of the main window will be presented and explained in detail. Figure 4.2.2.2 shows a direct correspondence between the functional block diagram illustrated in the figure above and the GUI of the software.

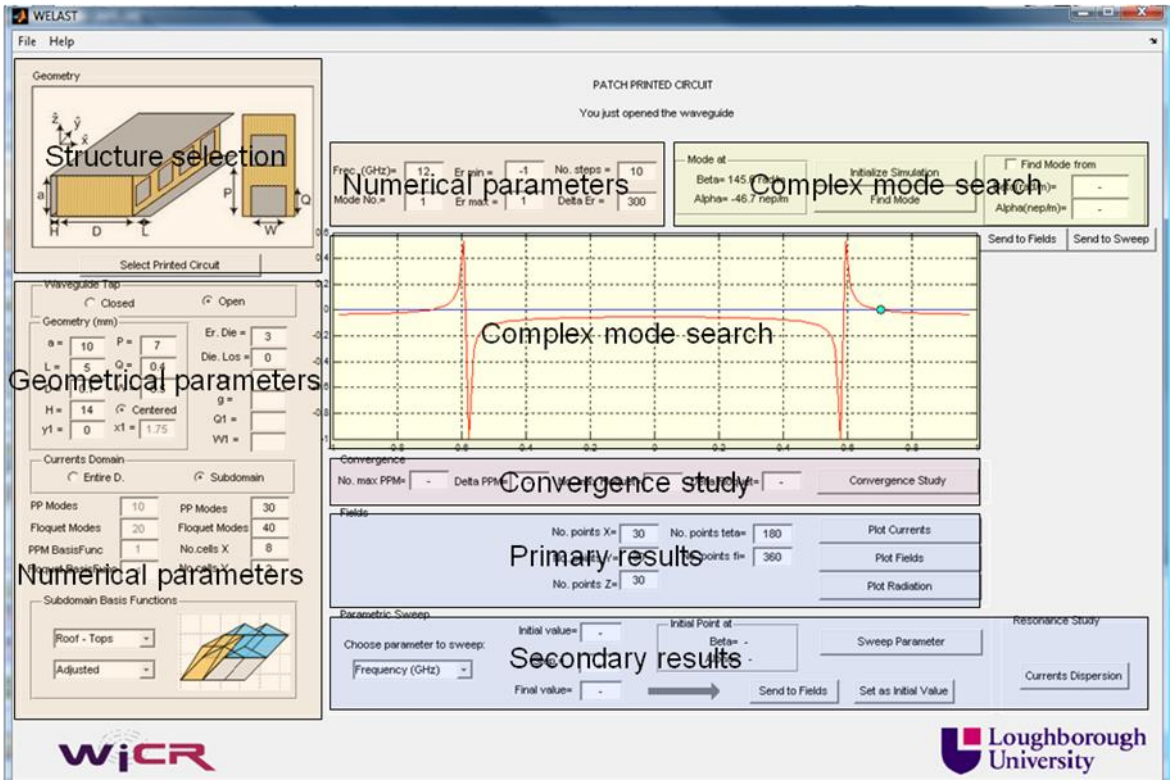

Figure 4.2.2.2 Program interface and correspondent functionality

4.2.3. User´s guide: Closed Structure.

The chosen LWA under analysis will be an open dielectric waveguide with a periodic planar metallization along the longitudinal direction, in the shape of single square loops. Figure 4.2.3.1 shows said structure. As explained in Chaper 2, the main mode of this type of structures (those in which the short wall has been removed) is the TE_{01}, and the only desired mode responsible for radiation. This mode has an intrinsic horizontal polarization between the parallel walls and is, therefore, radiative, even when the geometry is symmetric. This geometry is inspired in the work of Vardaxoglou and Blanos [Vardaxoglou Apr-1997], although slightly modified for illustrative purposes.

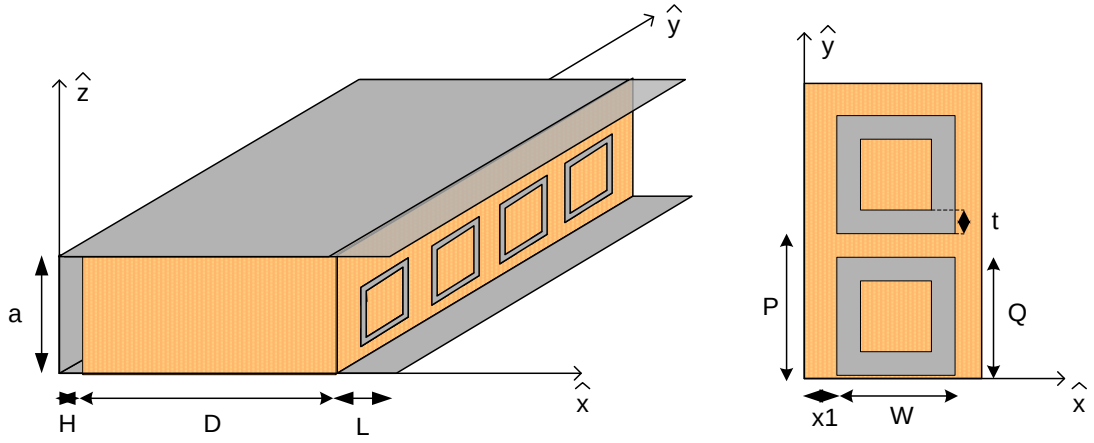

Figure 4.2.3.1 New PLWA under study.

To introduce the geometrical definition of the antenna, the user must first choose the inner printed circuit, using the button *Select Printed Circuit*, at the top left of the main window. This will lead to several options, as the dialog window in Figure 4.2.3.2 below opens.

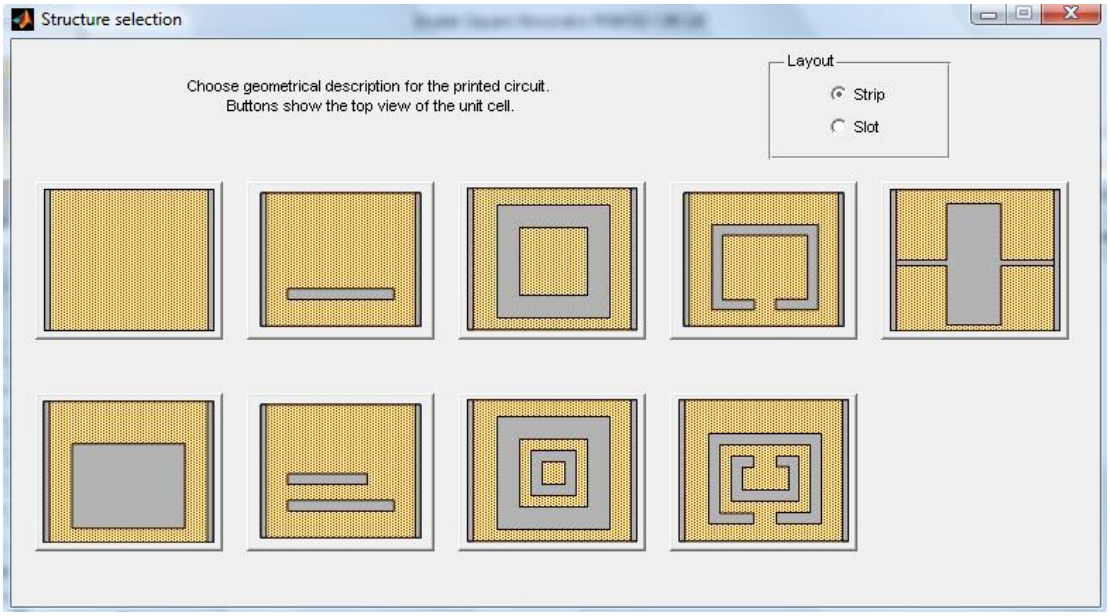

Figure 4.2.3.2 Printed circuit selection dialog window.

Each of the buttons showed above relates directly with a specific .m file, which will use the geometrical and numerical parameters introduced by the user to provide the proper rectangular mesh of the geometry. Some of the most known geometries modules are already implemented. This modular nature of the software allows the introduction of new periodic circuits whenever necessary. The corresponding meshing file must be loaded to

the program, making it extremely easy to extend the code at any time. How to widen the capabilities of the program will be discussed later in depth. Since the geometry of interest is a single metallic square loop, it is only necessary to press that option. The geometry mesh file will be uploaded and the picture at the top left of the main window is updated with the chosen geometry. It is important to notice that the structure is always loaded in a closed waveguide, since the analysis will begin in this form (see Figure 4.2.3.3 a). Below this picture, there is the option to open the structure, which will be used in the next section. Secondly, the user must fill the values of the **geometrical and numerical parameters**. Figure 4.2.3.3 shows the dimensions of the selected structure, and those parameters necessary for the numerical analysis.

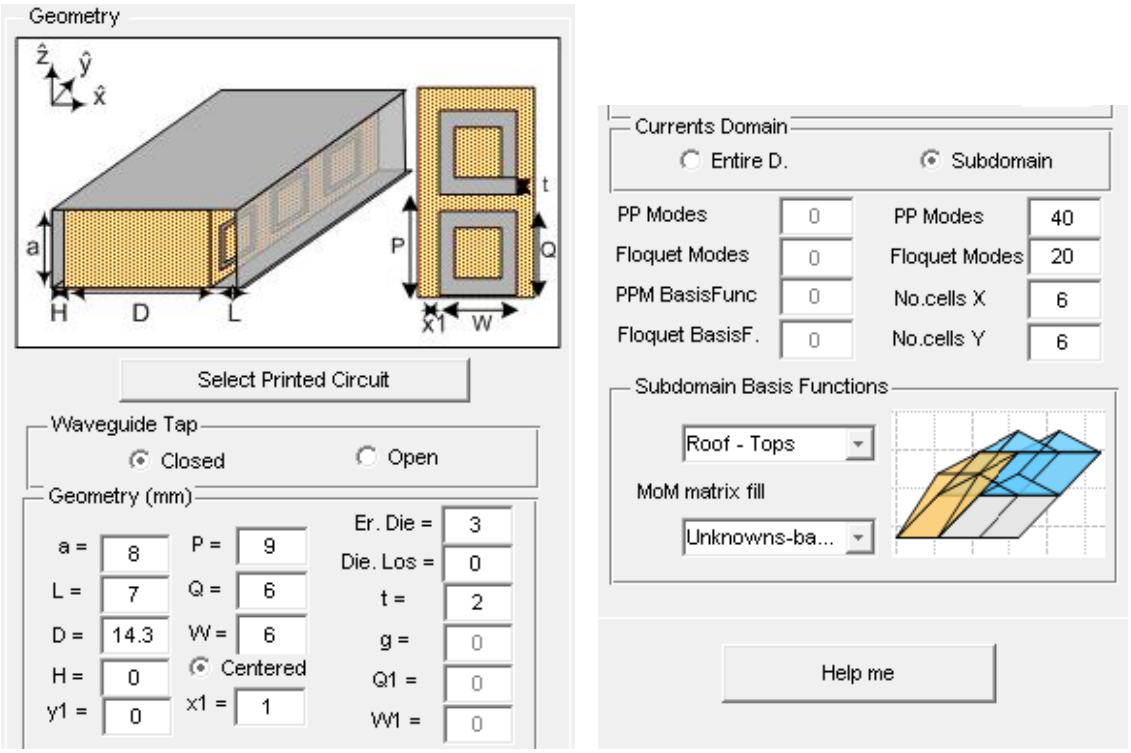

Figure 4.2.3.3 Geometrical and numerical input.

In the **Currents Domain** section, the user must decide which method will be used to analyze the geometry, and include an appropriate fine meshing and a sufficiently large number of basis functions to assure convergence. Note that it is the absolute responsibility of the user to provide with a consistent mesh for the physical dimensions. As discussed in previous sections, for the square ring, the only option is the Subdomain approach, with the spatial-based procedure to fill in the MoM matrix. In the File menu, the user will find the

option to **Save** this configuration of the antenna as a data file (.mat), in order to **Open** it at a later time.

Before starting the search for the real values of the propagation constant of the modes supported by the closed structure, a working frequency must be chosen. When the structure is new, as is the case, it is sometimes difficult to decide where to start. Since the structure is a closed waveguide partially filled with dielectric, it can be deduced that the TE_{01} mode must have a cut-off frequency f_c between the f_c expected for the empty rectangular WG and the f_c for the completely filled with dielectric WG. Pressing the *Help me* button, the user may obtain a valuable information relating the f_c for the first five modes that the structure supports, see Figure 4.2.3.4. Since the dielectric extends over more than two thirds of the waveguide and the fact that the field tends to confine itself more in the dielectric as its permittivity increases, it is expected that the main mode will appear soon after 4 GHz and before 7 GHz. It is also useful to know that the next mode will not appear until after 8GHz, so any other mode appearing before that, apart from the main TE_{01} mode, will be an unwanted mode (surface modes, channel-modes…) and must be avoided, not only because it may degrade the radiation pattern if radiative, but also for efficiency reasons. In any case, this table is only orientative, since the size of the periodic cell will have a considerable impact on the LWA behaviour with frequency.

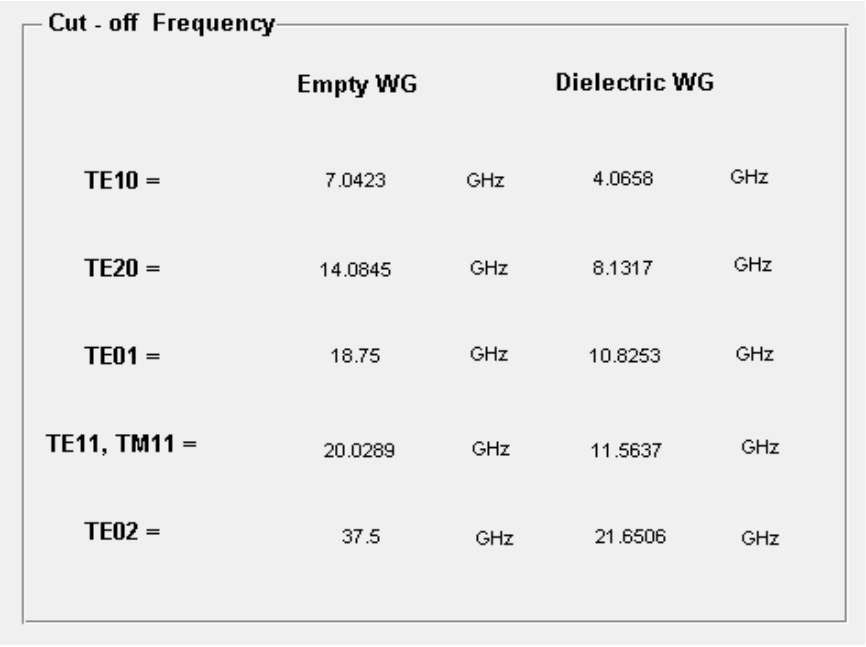

Figure 4.2.3.4 Orientative cut-off frequencies.

For illustrative purposes, the frequency of analysis will be at 11GHz. When pressing the button *Initialize Simulation* the program will calculate the determinant of the MoM matrix P for those values of k_y between the input parameters $\varepsilon_{r\min}$ and $\varepsilon_{r\max}$, given the relation :

$$k_y = k_0\sqrt{\varepsilon_r} \qquad (4.2.3.1)$$

Where ε_r is the dielectric constant effective for the whole inhomogeneous closed waveguide. This constant will be a value between ε_0 (permittivity for the empty WG) and ε_{die} (permittivity of the completely filled with dielectric WG). Choosing the values for $\varepsilon_{r\min}$ =-3 and $\varepsilon_{r\max}$ = 3, the function Det(P) will be calculated for all possible values of k_y in which the ε_r of this structure is comprehended. The resulting function will be showed as a graph in the middle of the main window. The real part and the complex part of the determinant will be plotted versus the ε_r separately, in the form of the continuous blue and red lines that appear in Figure 4.2.3.6.

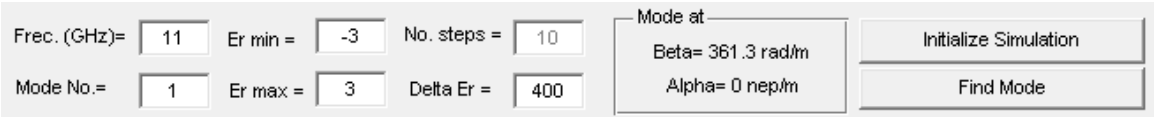

Figure 4.2.3.5 Simulation parameters.

Clicking the button *Find Mode* the program will obtain the solutions for the modes propagating at the chosen frequency. Since the 'Closed' option for the Waveguide was selected in the geometrical parameters (see Figure 4.2.3.3), the zeros of the function Det(P) will correspond to real values of k_y, that is to say, $k_y = \beta_y$ with no complex part corresponding to attenuation. As showed in Figure 4.2.3.6, the program sweeps the real values of k_y until it finds a zero for both real and complex part of the function determinant. Those **real solutions** are marked with a turquoise dot. The user may specify the order of the mode to search, since several modes may be propagating simultaneously at a given frequency. In Figure 4.2.3.5 can be seen how the first mode at 11GHz has a propagation constant of β_y = 361.3 rad/m and α_y = 0 nep/m. Eight modes were found in total as real solutions of Det(P) =0. As the order of the mode increases, the value for the real solutions β_y of the mode decreases, as can be seen in the numbers of Figure 4.2.3.6. (ignore the small arrows for the time being).

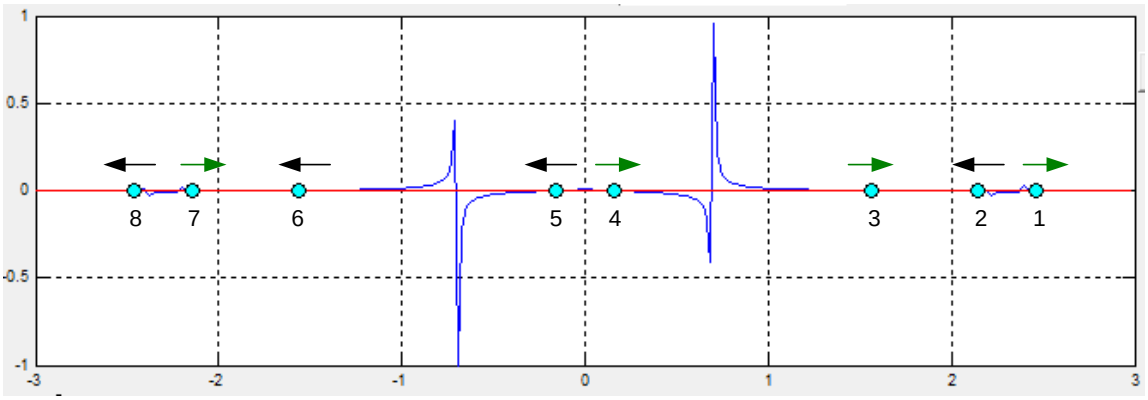

Figure 4.2.3.6 Determinant of the MoM matrix P.

It is important to notice that negative values of ε_r, and therefore β_y, were selected to compute the determinant. This is a direct consequence of the periodic nature of the structure, as explained in Chapter 2, where the propagating modes are composed by **families of Floquet harmonics** related by the spatial period P. For the closed structure, this relation is given by:

$$k_y(my) = k_0 + my\frac{2\pi}{P} \rightarrow \beta_y(my) = \beta_{y0} + my\frac{2\pi}{P}, \quad \text{for } my = [-\infty, \infty] \qquad (4.2.3.2)$$

The propagation constant may take negative values of β_y, since *my* can be a negative number. By observing the eight results and taking the mode 1 as the main mode *my*=0, it can be calculated for the next harmonic *my*=-1:

$$\beta_y(my) = \beta_{y0} + my\frac{2\pi}{P} = 361.3 - 1\frac{2\pi}{0.009} = -336.9 rad/m \qquad (4.2.3.3)$$

This is exactly the propagation constant of mode 7, from which it can be concluded that mode 1 and mode 7 are different harmonics belonging to the same propagative mode. The rest of the modes are checked and no other relation results, apart that the solutions of the positive part of the graph are exactly the same value that those in the negative part of ε_r, so, intuitively, they must be related somehow. This is answered by both, mathematical and physical reasons. As a mathematical method, it gives the theoretical solutions that would exist when the waveguide is infinitely large, no specific feeding applied. In this hypothetical and unreal case, it is well known that two types of waves will be supported, **progressive waves** with positive phase velocity and **regressive waves** with negative phase velocity. The real case being analyzed has a feeding source from which

the waves will travel towards the positive longitudinal direction, assuming the antenna is long enough for most of the energy to be radiated before reaching the end of the waveguide. The only solutions with physical meaning are those in which the energy is propagating in the positive y-direction. It is known that the direction of the energy propagation is given by the **group velocity**:

$$V_{group} = \left(\frac{\partial \beta}{\partial \omega} \right)^{-1} \qquad (4.2.3.4)$$

To discriminate which modes exist physically in the structure, the variation of the propagation constant with the frequency must be obtained. By repeating the real mode search for a slightly higher frequency, 11.1 GHz, it can be obtained the direction the real solutions β_y are moving towards with the frequency. The arrows above the modes in Figure 4.2.3.6 indicate the movement direction of the solutions. Only those modes with green arrows have a positive group velocity and, therefore, travel in the +y-direction. Only the solutions 1, 3, 4 and 7 are valid zeros for the real structure. From these modes with positive group velocity, 1, 3 and 4 have positive β_y and only mode 7 has a negative propagation constant. The **phase velocity** of the first 3 modes is positive and they will be **radiating forward**. The phase velocity of mode 7 is negative, meaning that the energy is travelling in the opposite direction that the wave-front, and this mode will be **radiating backwards**. These type of 'backwards waves' inherent to periodic structures have been studied for years, see for example [Oliner 1993], [Johnson 1993], [Schwering 1983] and [Gomez Aug-2006].

Once the modes that truly exist in the structure have been discriminated, the next step is to recognize the TE mode that each of them represent, since only the radiation due to the TE_{01} mode is desired. To obtain this, the distribution of the fields must be plotted. With the *Plot Fields* button, the 2D graphs for a transversal section of the waveguide will appear for both electric and magnetic field. The user must introduce the number of points to calculate the fields in each dimension and the position in the y direction where the transversal cut will take place, if different from $y_0 = 0$. The options for the representation of the radiated fields will be seen in next section.

Figure 4.2.3.7 shows the electric field in the x and z directions for the modes propagating in the waveguide. By visual inspection, it is deduced that modes 1 and 7 correspond to TE_{01}, mode 3 is a TE_{02} mode and mode 4 corresponds to the typical strip-mode that goes from the inner conductor to the outer. All the field distributions are affected by the presence of the metallic square loop printed on the dielectric layer, as can be seen in the coupling of the field lines at z=0mm.

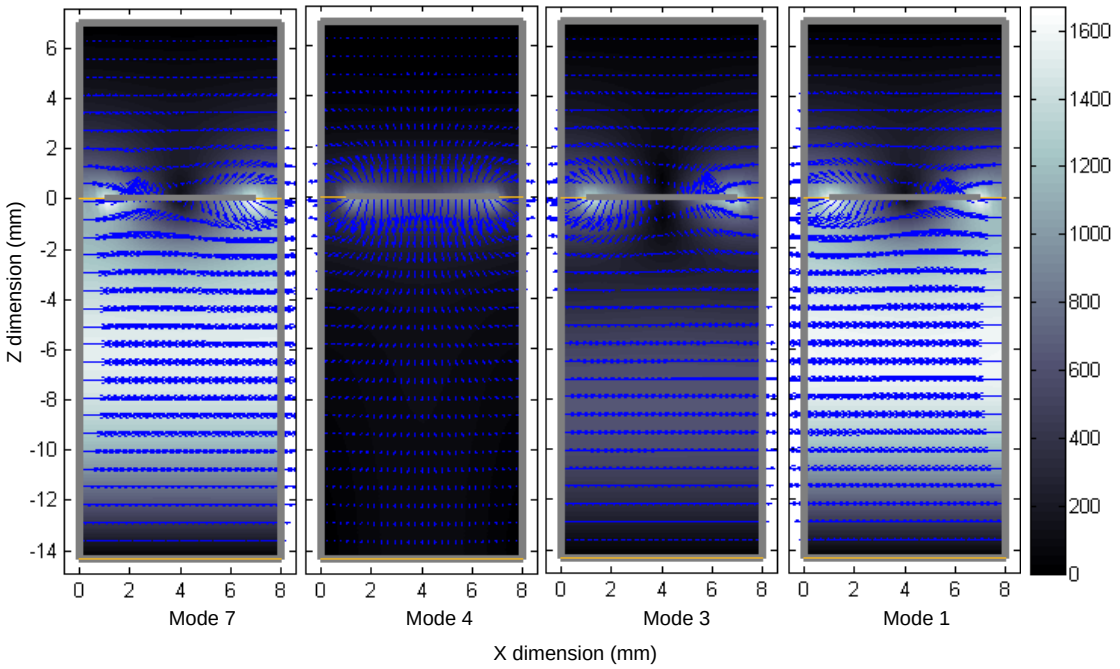

Figure 4.2.3.7 Transversal electric field.

This way the initial representation of the real solutions of the closed waveguide can be interpreted as showed in Figure 4.2.3.8, where one can see that the two first harmonics for the dominant TE mode are propagating, as well as the first harmonic of the TE_{02} mode and last, the strip mode due to the existence of two conductors.

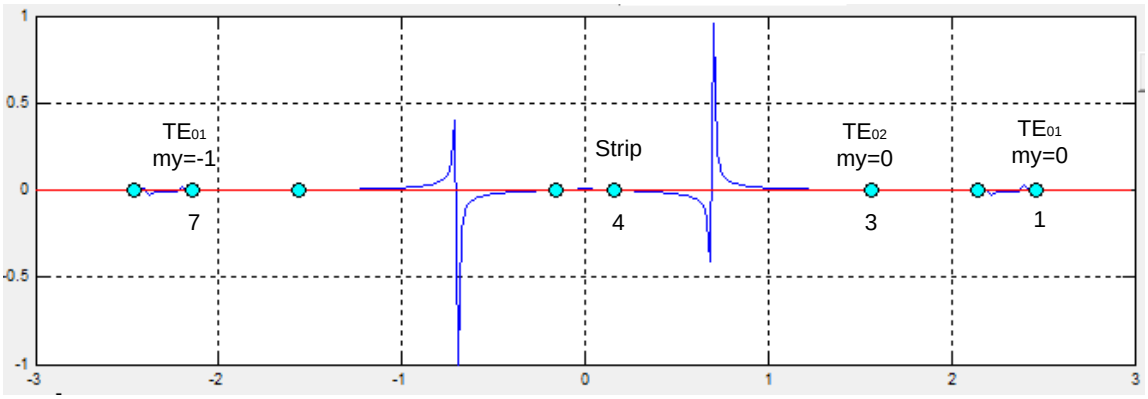

Figure 4.2.3.8 Modes existing in the closed WG.

To clarify how to distinguish between modes when analyzing the solutions obtained for one frequency, Tables 4.2.3.1 and 4.2.3.2 below resume what has been done in this section:

Mode no.	β_y	Group velocity	Meaning energy travelling …	Exists?
1	361.3 rad/m	+	Towards +y (progressive)	Yes
2	336.9 rad/m	-	Towards -y (regressive)	NO
3	288.3 rad/m	+	Towards +y (progressive)	Yes
4	91.9 rad/m	+	Towards +y (progressive)	Yes
5	-91.9 rad/m	-	Towards -y (regressive)	NO
6	-288.3 rad/m	-	Towards -y (regressive)	NO
7	-336.9 rad/m	+	Towards +y (progressive)	Yes
8	-361.3 rad/m	-	Towards -y (regressive)	NO

Table 4.2.3.1 Mode discrimination

Mode no.	β_y	Phase velocity	Meaning it may be radiating …	Field distribution	Floquet armonic
1	361.3 rad/m	+	forwards	TE_{01}	my= 0
3	288.3 rad/m	+	forwards	TE_{02}	my= 0
4	91.9 rad/m	+	forwards	Strip	my= 0
7	-336.9 rad/m	-	backwards	TE_{01}	my= -1

Table 4.2.3.2 Classification of existing modes.

4.2.4. User´s guide: Open Structure.

In last section the propagating modes supported by the closed waveguide were obtained. In this section, the top wall will be removed to obtain the leaky modes radiating along the open waveguide. For illustrative purposes, it is preferable to show several Floquet harmonics close enough to understand their behaviour, for this reason P is increased to 12mm in this section. The first step is opening the structure, changing the option for the Waveguide Tap showed in Figure 4.2.3.3. The short-circuit at the top of the waveguide is

substituted by the **modal Markuvitz radiation impedance** introduced in Chapter 2. In the open structure, some of the modes that were propagating in the closed WG, will radiate while propagating. This means that the propagation constant for those modes will have a real part β_y, the *phase constant*, and an imaginary part α_y as the *attenuation constant*:

$$k_y = \beta_y - \alpha_y \tag{4.2.4.1}$$

The conditions under a propagative mode becomes a leaky-wave mode in an open structure were discussed in Chapter 2. As a quick reminder:

- The PPM mx=0 has to be excited.
- The mode has to be propagating in the fast-wave zone or radiation zone:

$$-1 \le \frac{k_y}{k_0} \le 1 \quad \Rightarrow \quad -1 \le \sqrt{\varepsilon_r} \le 1 \tag{4.2.4.2}$$

None of the propagative modes found at 11GHz seem to fulfil the second condition (see Figure 4.2.3.8), since they are outside of the -1,1 range of dielectric permittivity. The only solution that exists in the fast-wave zone is the strip mode, which does not posses the horizontal polarization necessary to radiate, nor excites the PPM mx=0 by asymmetry. For this reason, the open structure analysis will take place at a lower frequency, 4.5GHz, where the main mode was still radiating. The function determinant of the MoM matrix P at this new frequency for the closed structure is showed in Figure 4.2.4.1 a), where the TE_{01} is in the fast-wave zone. As the top wall is removed, by ticking the appropriate option on the GUI, the complex values of the radiation impedance that models the aperture will force the function determinant to have real and complex parts different from zero, as can be seen in Figure 4.2.4.1 b). When the WG is open, the solution for the TE_{01} is no longer in the real axis of k_y, but in the complex plane, becoming a leaky-wave mode, that is radiating at a certain angle.

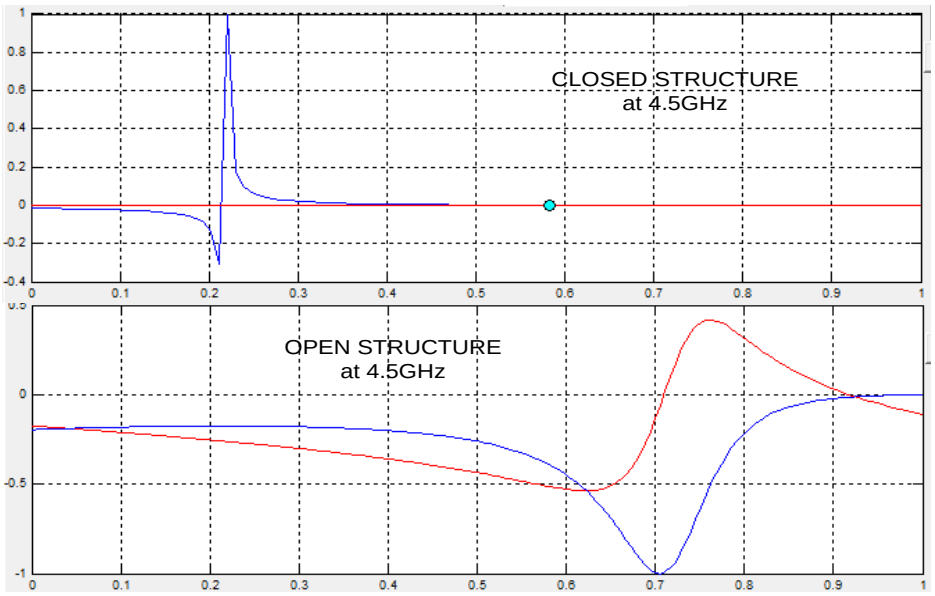

Figure 4.2.4.1 Function Det(P)for a)closed WG and b) open WG

The search for the solutions of leaky-wave modes must take place in the complex plane. Tackling the complex solution search problem directly would require an enormous amount of computations and time, and it might not lead to a proper solution. For this reason, the program applies an **iterative search in the complex plane** implemented for the first time by [Gomez Jan-2005] for laterally shielded structures. This method uses as a starting point the real solution for the completely closed structure. After that, the top wall impedance is gradually changed from that of a perfect metallic wall to the final modal Marcuvitz radiation impedance. Figure 4.2.4.3 illustrates this iterative search for the complex solution, taking as a starting point the one obtained in Figure 4.2.4.1 a) at 4.5GHz. After pressing *Find Mode*, in fifteen steps, the real solution at β_y =74.24 rad/m follows a path through the complex plane until it reaches the final complex solution for the open LWA at k_y =27.6 - 133.8i. This smooth evolution is the key to reach correct results, so it is important to make sure that the number of steps is large enough for the minimization algorithm not to end in a local minimum or to snap to other mode solution that may exist nearby.

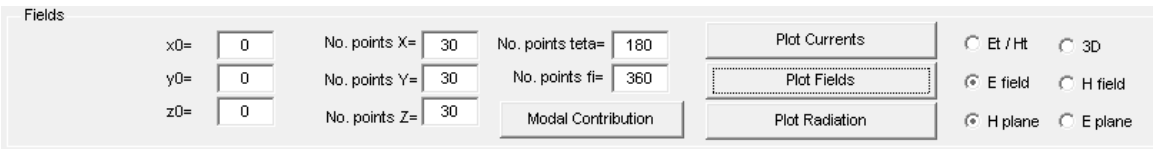

Figure 4.2.4.2 Currents, Fields and Radiation dialog box.

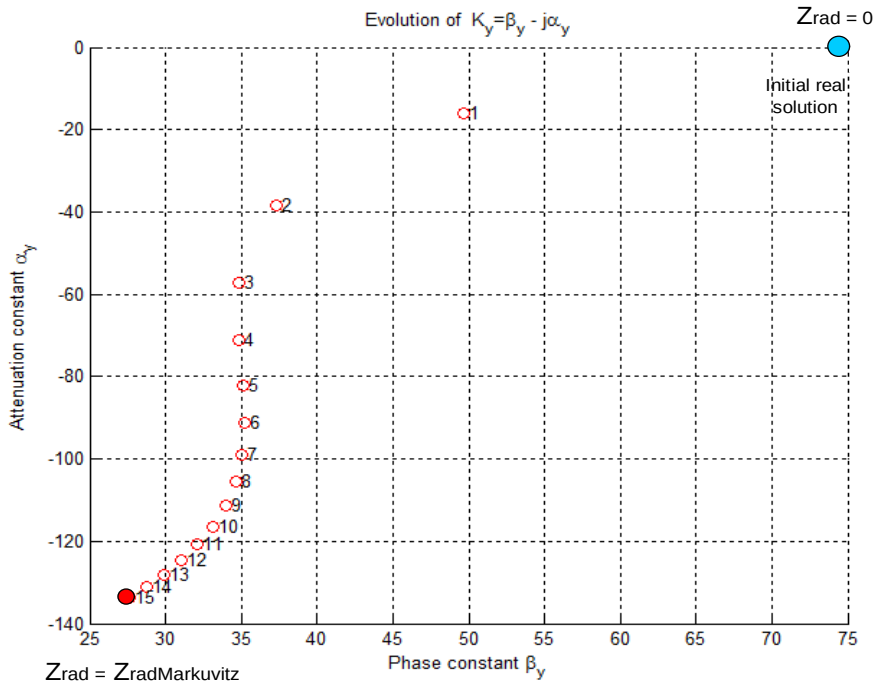

Figure 4.2.4.3 Search for the Det(P) solution in the complex plane.

There is another option for finding the complex solution of the structure, in case the user has an approximate idea of the complex solution of the propagation constant of the mode. The estimated values of β_y and α_y can be introduced in the main window of the program. The user must tick the option '*Find mode from*' and then press the button *Find Mode*. This is very convenient when a structure has been already simulated at some frequency and the user wishes either to go back to that solution or to move in frequency. The user must remember to un-tick said option before sending the found solution to the Fields or Sweep calculations.

Once the complex solution has been found, it is possible to obtain plots for the currents on the periodic printed circuit or the representation for electric and magnetic fields in the antenna. This can be done for both the closed and open case solutions by introducing which type of fields, where and the number of points to plot, then pressing *Plot Currents* or the *Plot Fields* button (see Figure 4.2.4.2).

As an example, the transversal electric field for the TE_{01} at 10.5GHz in the open structure is showed in Figure 4.2.4.4. a). One may compare it with the electric field for the same mode in Figure 4.2.3.7 in the closed WG. It can be seen how the TE_{01} mode now is also

perturbed by the periodic printed circuit and, since it has an inherent horizontal polarization from one of the metallic plates to the opposite, it reaches the aperture and will radiate, in opposition to the Strip mode, which has a vertical polarization and does not reach the top of the parallel plates (see Figure 4.2.4.5. b). The same occurred to the Strip mode with the closed tap.

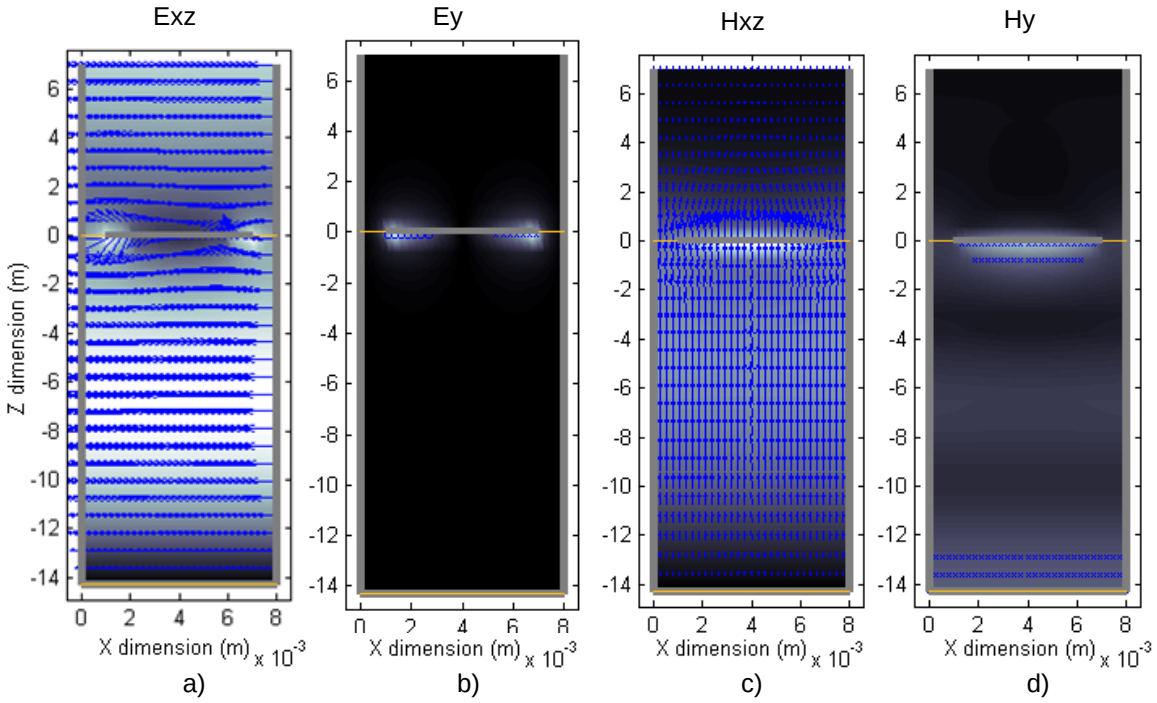

Figure 4.2.4.4 Electric and magnetic fields for the TE mode in the open LWA.

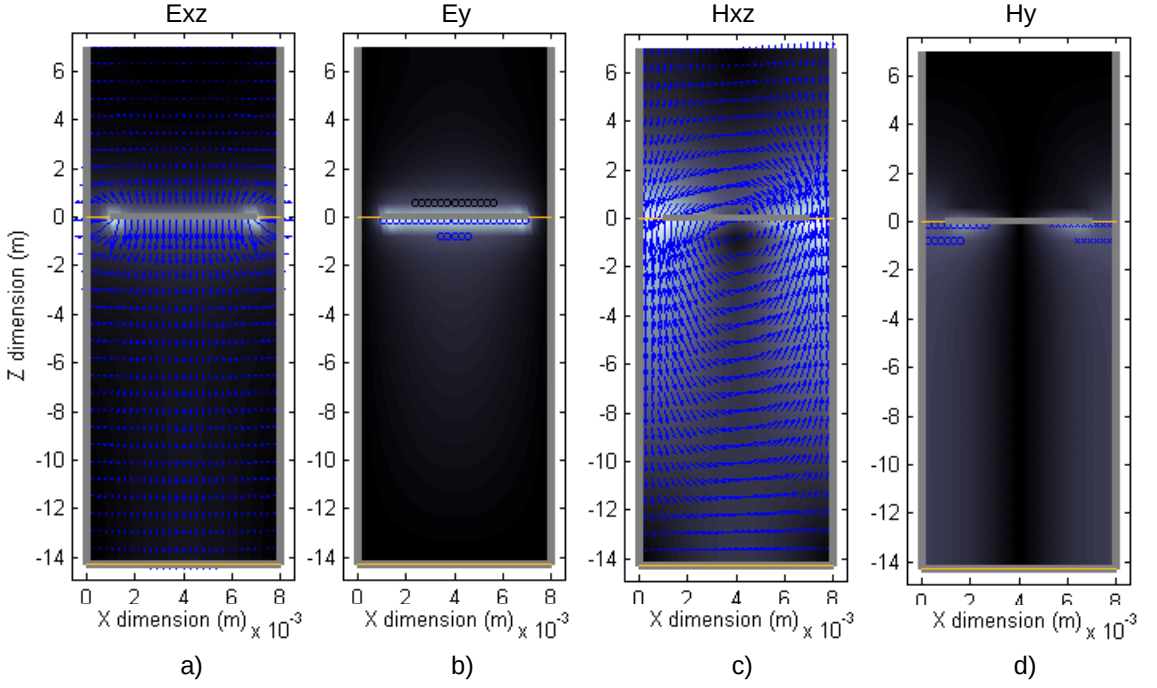

Figure 4.2.4.5 Electric and magnetic fields for the Strip mode in the open LWA.

The same way, the currents for the mode TE_{01} in the closed structure and those for the qTEM or Strip mode in the open LWA are presented in Figure 4.2.4.6 and 4.2.4.7 below. Note that the 2D current representation is for the XZ and YZ planes crossing at the mesh centre. In the two different modes, it can be seen how the currents for the metallic square loop are in order with the conditions expected at the edges of the printed circuit, as seen in Chapter 3. Also, for the qTEM mode the currents directed in the x direction does not exist. This can be reasoned by looking at the fields' distributions of said modes in Figures 4.2.4.4 and 4.2.4.5 above. The existence of induced currents in the x direction depends on the longitudinal magnetic field (y direction) surrounding the metallization. It can be seen that, in the case of the TE mode, this Hy field is directed towards the +y direction, creating a Jx on the patch. On the other hand, the magnetic field Hy for the Strip mode is directed in the +y and -y direction on each side of the patch, cancelling the currents that could be induced on the perpendicular x direction. To the author, the capability to plot the field and currents for each propagative mode separately is crucial to study and truly understand the inside workings of the LWAs, which can not be achieved with commercial software.

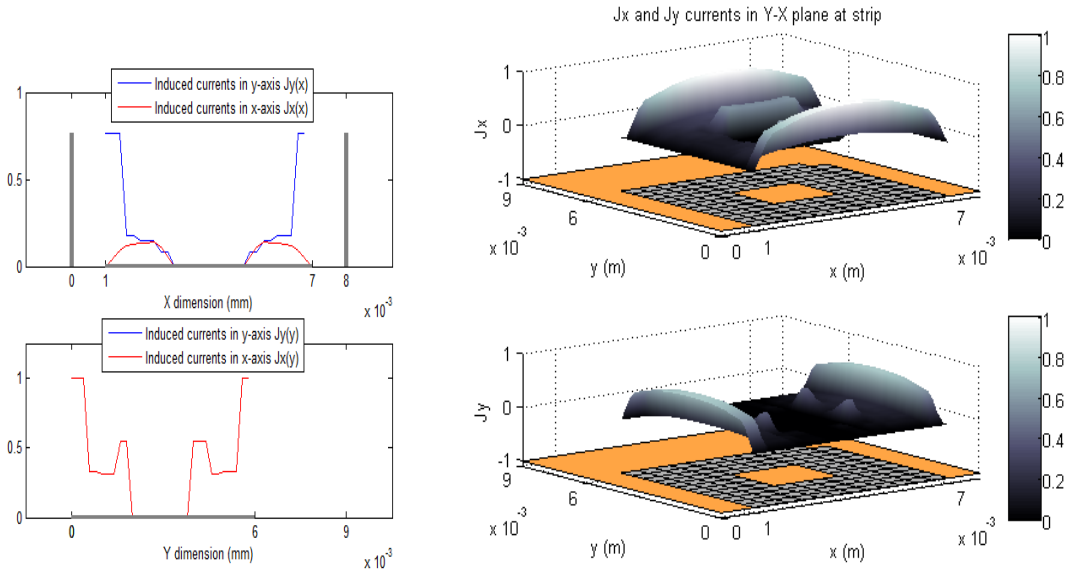

Figure 4.2.4.6 Currents distribution for the TE mode in the open LWA.

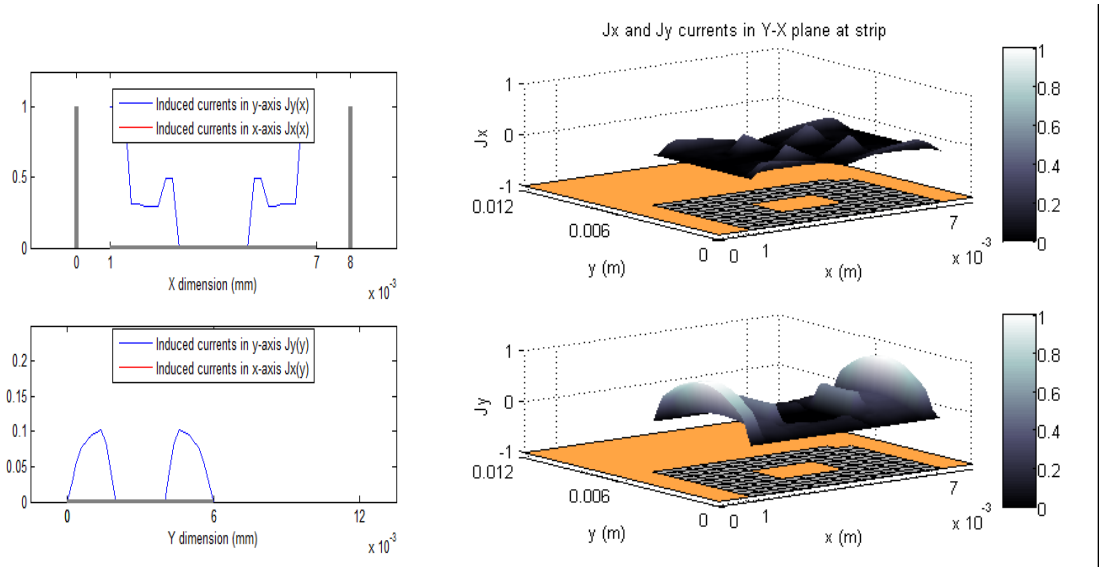

Figure 4.2.4.7 Currents distribution for Strip mode in the open LWA.

Apart from the validation results presented in Chapter 3 by comparison with previously analyzed structures by other authors, it is particularly interesting to check that resulting fields are compliant with the boundary conditions applied in the EFIE (2.8.1.5) used to solve the MoM and also in both MFIEs (2.8.1.6) and (2.8.1.7), at the interface between the dielectric and air, where the metallization lies. Figure 4.2.4.8 shows a 2D plot of electric field at the printed circuit (z = 0), for the TE_{01} mode at 10.5GHz. These plots represent the variation of the three components in the ZX and ZY planes, situated at the centre of the square loop metallization.

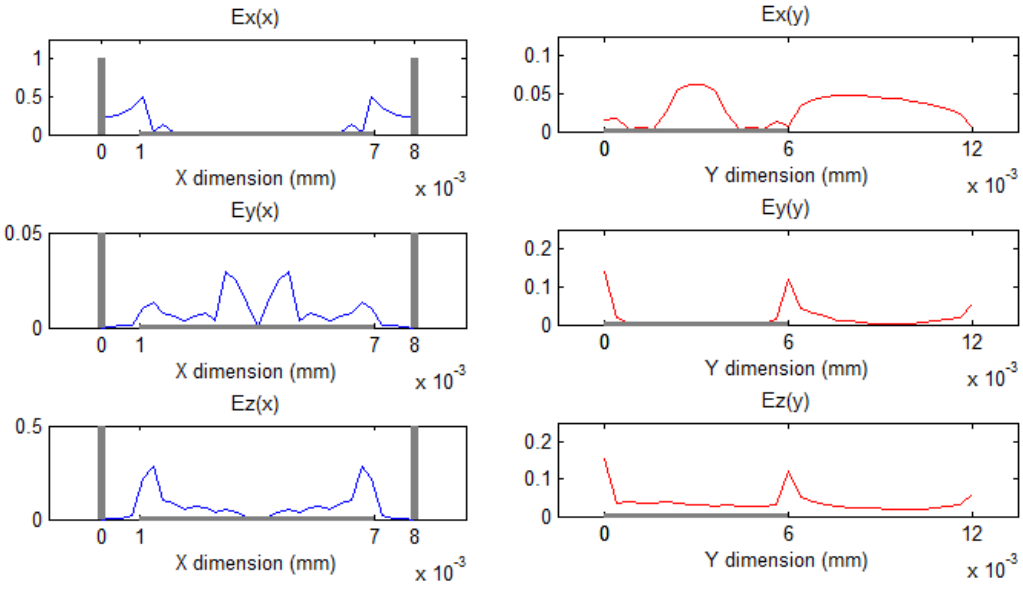

Figure 4.2.4.8 2D Electric field at the metallization (z = 0).

It can be seen how the Ex and Ey fields are practically zero on the printed circuit. Different scales are applied to each component, so the shape of the field can be easily seen. The results are coherent with the EFIE. Figure 4.2.4.9 presents the 3D electric fields, showing how it is null above the whole metallic loop.

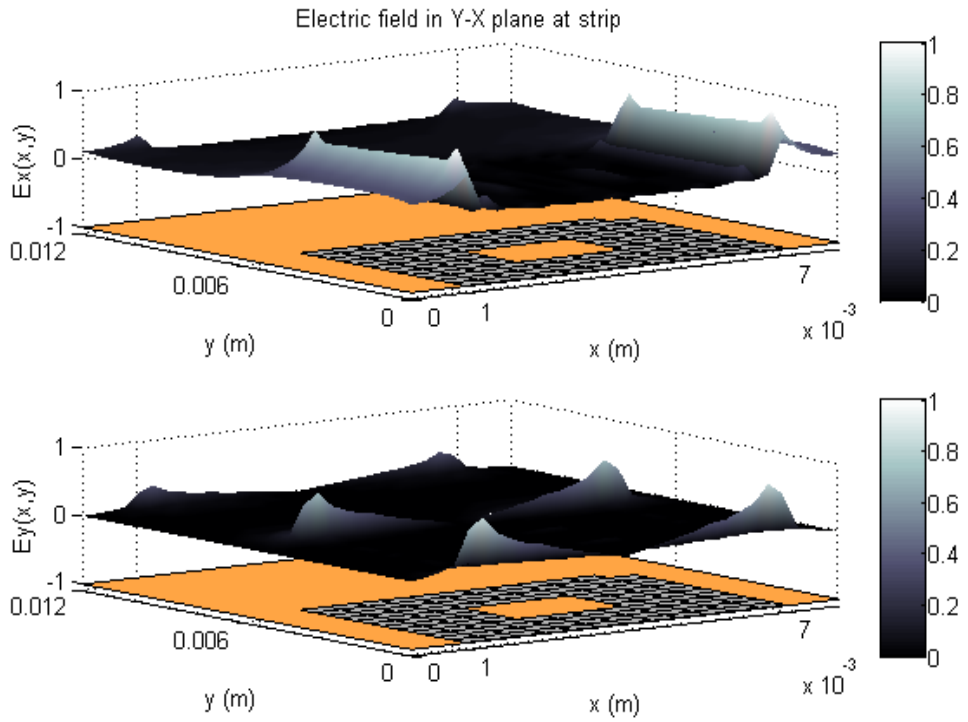

Fi

gure 4.2.4.9 3D Electric field at the metallization (z = 0).

To check that the magnetic field H is discontinuous at the interface where metal is present, inducing the existence of electric currents on the printed square loop, and a continuous function elsewhere, the currents will be calculated again, but this time from the obtained results of H. This is showed in Figure 4.2.4.10, where the difference of the H above the metallization and below it is represented. Comparing with Figure 4.2.4.6, the currents obtained matches perfectly with those calculated with the Roof-Top basis functions. Also, the currents are zero where there is no metal, probing that the magnetic field is exactly the same above and below z = 0. In conclusion, the obtained results agree with the boundary conditions expected in the structure, validating in a different way the developed method.

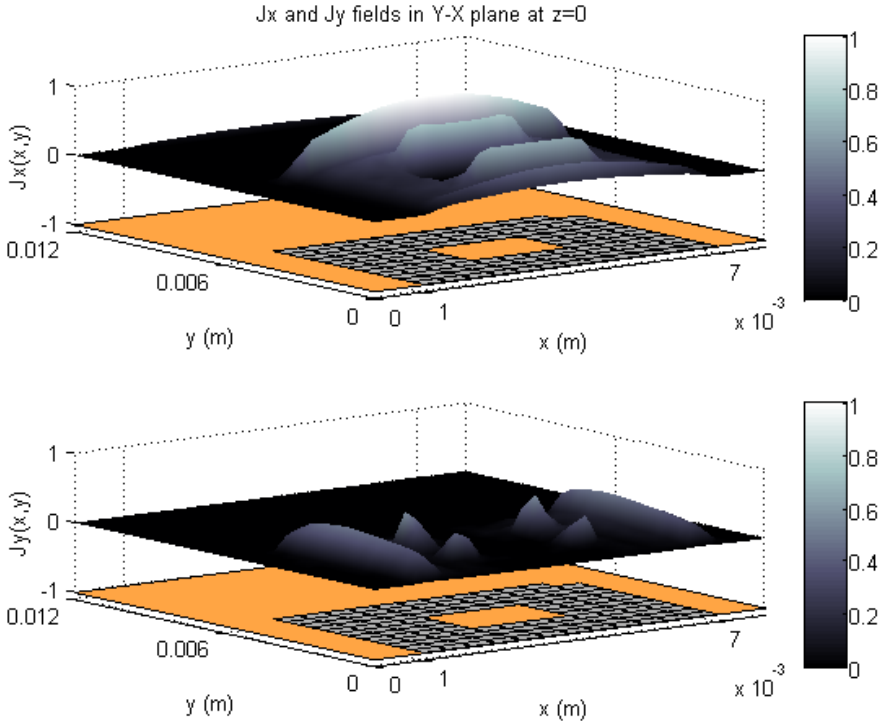

Figure 4.2.4.10 Currents on the metallization induced by H.

4.2.5. User´s guide: Dispersion Analysis.

Starting from a complex solution for a specific mode, the dispersion curves can be obtained, not only for the variation with frequency, but also for other geometrical parameters. This will allow studying the effect they have on the complex propagation constant and therefore, the radiation of the LWA. Fist of all, the complex solution must be selected as the Initial value of the sweep, by pressing the button *Send to Sweep* . Then a parameter, step and limit to sweep must be introduced. When the dispersion curve is obtained, the final point can be sent pressing *Send to Fields* to plot the fields and currents to make sure the results are correct and also *Set as Initial Value* to carry on with the sweep from the last swept point.

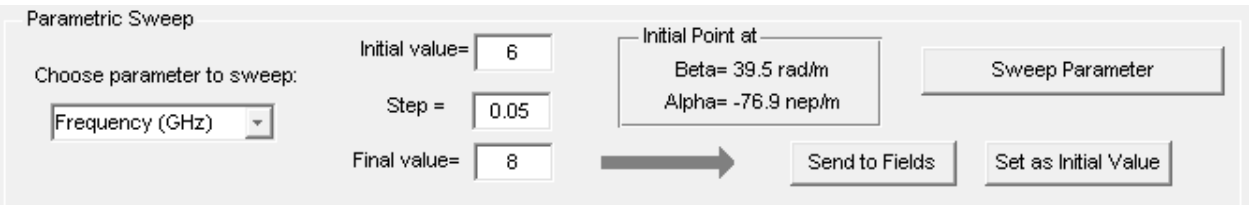

Figure 4.2.5.1 Parametric Sweep dialog box.

Figures 4.2.5.3, 4.2.5.4 and 4.2.5.5 show the dispersion curves with the frequency for the LWA studied in previous sections. These curves provide with most of the information needed to 'know' the structure. In Figure 4.2.5.3, the **phase constant** divided by the propagation constant in vacuum is represented vs. frequency. The modes supported by the LWA appear in different colours, TE_{01} in blue, TE_{02} in red and the qTEM or Strip mode in green. As was introduced in Chapter 2.3, in periodic structures, the modes are composed by a sum of **Floquet harmonics**, related by:

$$k_{my} = k_{y0} + k_{ym} = k_{y0} + my\frac{2\pi}{P} \qquad (2.3.7)$$

So there will be a main harmonic my=0 propagating at the lowest frequencies and a series of higher order harmonics that will start propagating as frequency increases, with a propagation constant related directly with that of the main harmonic. This is the case of the mode TE_{01} in Figure 4.2.5.3, where the main harmonic is plotted in a blue continuous line and the second Floquet harmonic that starts propagating at 10.2GHz in blue dash-dot line.

Since this is an open structure, one or more of the harmonics that exist in the LWA may be radiating. In this case, the propagation constant for the whole family of harmonics belonging to the same mode is complex, of the form:

$$k_{my} = k_{y0} + k_{ym} = (\beta_{y0} - j\alpha_y) + my\frac{2\pi}{P} = \left(\beta_{y0} + my\frac{2\pi}{P}\right) - j\alpha_y \qquad (2.3.8)$$

Where the attenuation constant accounts for the losses due to radiation. The condition for the phase constant to be in the radiation zone was:

$$\left|\frac{k_y}{k_0}\right| \le 1 \rightarrow \quad \boxed{k_z = \beta_z} \qquad (2.4.6)$$

Which means that all those harmonics with a normalized phase constant $\frac{\beta_{my}}{k_0}$ between -1 and 1 will be radiating. The phase constant of these harmonics will determine the angle of maximum radiation θ_{my}, following the equation:

$$\sin\theta_{my} = \frac{\beta_{my}}{k_0} \qquad (4.2.5.1)$$

Figure 4.2.5.4 comes directly from this relation. It shows the **angle of maximum radiation** of the first two TE modes. Note that the Strip mode does not appear in this Figure, since it cannot radiate by definition, as seen in last section. The main harmonic of the TE_{01} has its cut-off frequency at 6.4GHz where it starts radiating very close to *Broadside* with an angle of $\theta_0 = 18^o$, and, as the frequency increases, so does the radiation angle towards *Forward-endfire*, until it reaches the $\theta_0 = 90^o$ at 9.3GHz. The second harmonic my=-1 starts radiating at 10.2GHz in *Backward-endfire* ($\theta_{-1} = -90^o$). Since higher Floquet harmonics have a negative β_{my} at low frequency, they have the inherent ability to radiate backwards. It will carry on with frequency until reaching Forward-endfire, passing through *Broadside* at about 14GHz. The harmonics stop radiating and become bounded after reaching *Forward-endfire*, and they continue propagating with frequency as s**urface waves**. This same behaviour can be observed in Figure 4.2.5.4 for the harmonics of the TE_{02} mode. A graphic explanation the radiation sweep with frequency can be found in Figure 4.2.5.2

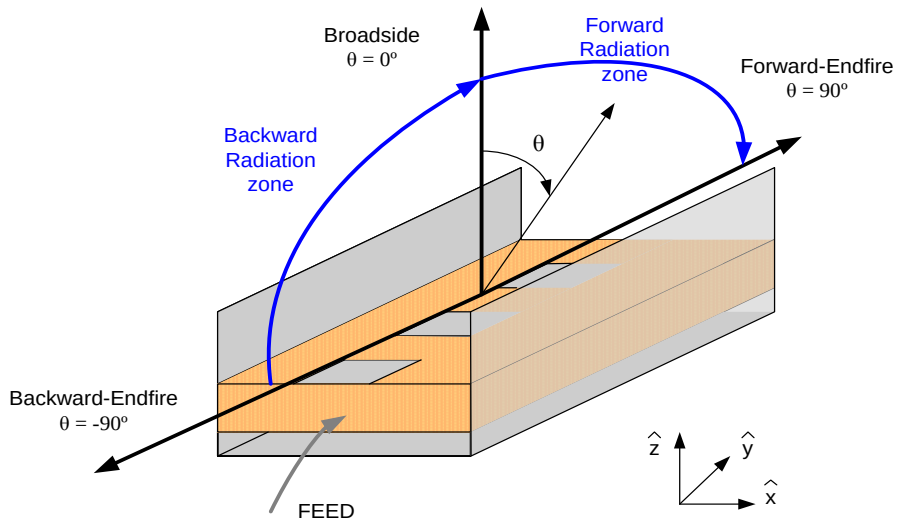

Figure 4.2.5.2 Typical radiation behaviour for a periodic LWA.

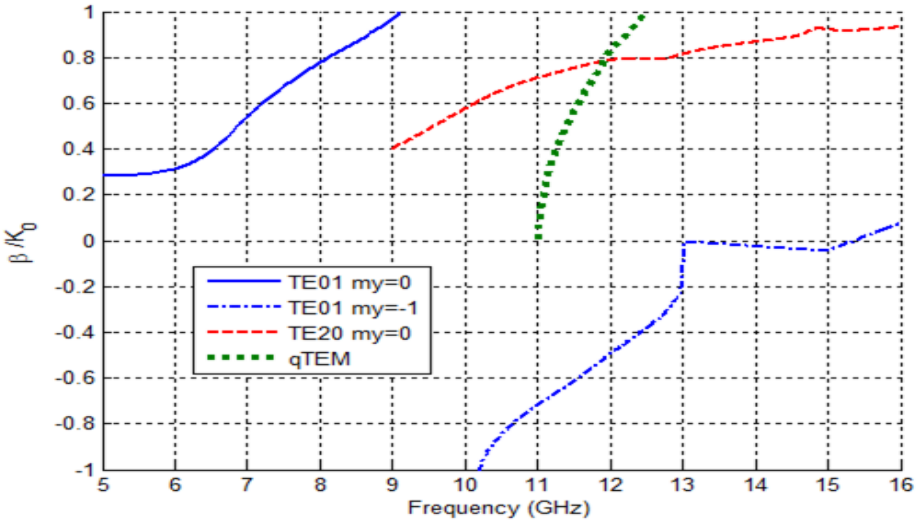

Figure 4.2.5.3 Normalized phase constant dispersion for the SSL LWA.

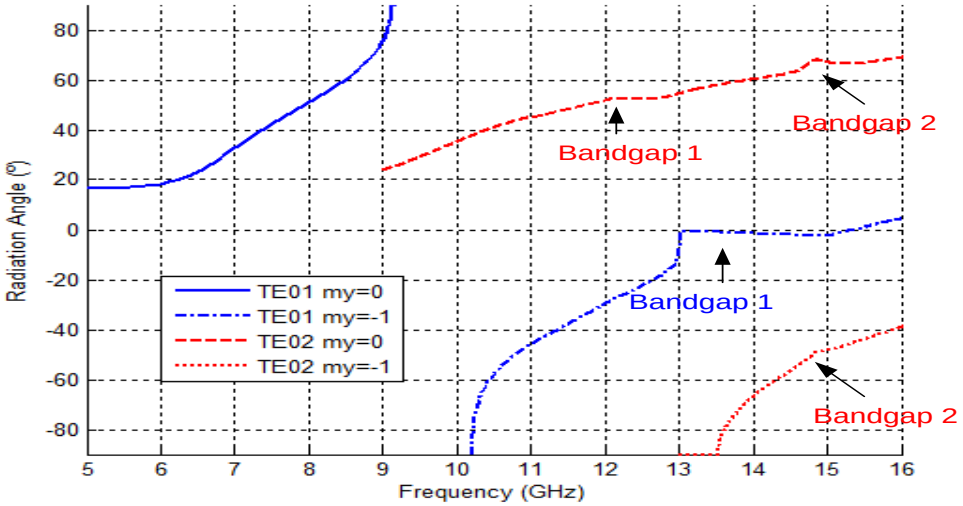

Figure 4.2.5.4 Radiation angle dispersion for the SSL LWA.

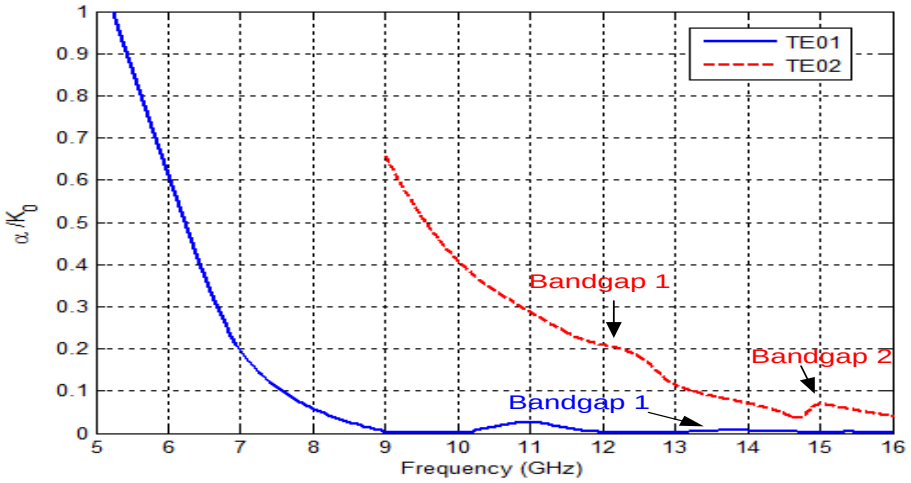

Figure 4.2.5.5 Normalized attenuation constant dispersion for the SSL LWA.

It may happen that at a certain frequency more than one harmonic and/or mode is radiating at the same time. At 11.5GHz TE_{01} second harmonic and TE_{02} main harmonic are radiating with $\theta_{-1} = -37.5^{o}$ and $\theta_0 = 48^{o}$ respectively, and at 13.5GHz, the TE_{02} second harmonic will start radiating too. This situation degrades the radiation performance of the antenna, since there are several main radiation beams. To avoid this, the geometrical parameters of the antenna should be modified. Observing equation 2.3.7, it can be deduced that decreasing the periodicity P will separate the Floquet harmonics one from another, extending the range of frequency in which only one harmonic will be radiating.

Figure 4.2.5.5 shows the **attenuation constant** α in the same band of frequencies. It can be seen how, as frequency increases, the α decreases exponentially. All harmonics from the same mode have the same attenuation constant, whether or not are radiative. The α for the Strip mode does not appear since it is zero. The radiation zone for a specific harmonic is defined by both the phase and attenuation constants. A widely accepted **cut-off frequency criteria** for a mode is the frequency where the attenuation constant and the phase constant reach the same value. Observing Figure 4.2.5.6, the cut-off frequency for the first two modes propagating in the metallic square loop LWA are 6.4GHz and 9.55GHz respectively.

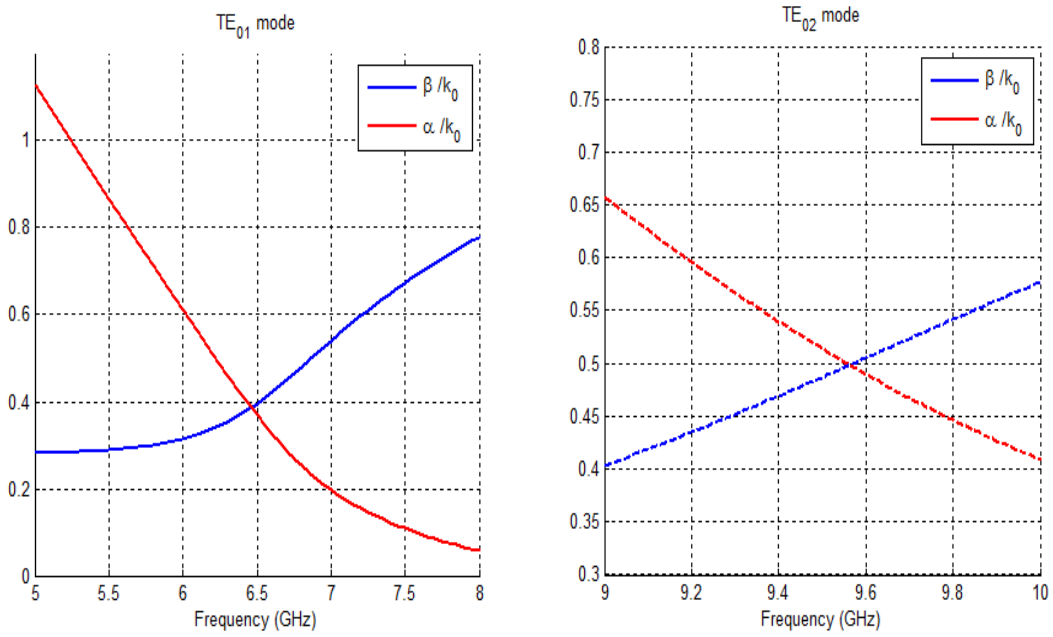

Figure 4.2.5.6 Normalized attenuation constant dispersion for the SSL LWA.

A very important phenomenon that appears in periodic structures is the existence of band of frequency in which there is no propagation or **Bandgaps**. Within these frequency bands, the modes do not propagate, nor radiate. The phase constant β_{my} will stay constant or even decrease slightly as the frequency increases, meaning that the group velocity, $v_g = \left(\frac{\partial \beta_{my}}{\partial \omega} \right)^{-1}$, is zero or negative and no energy is being propagated by the mode. At the same time, the attenuation constant will increase locally. In Figures 4.2.5.3 and 4.2.5.4 these bandgaps can be easily identified. In the TE_{01} mode it can be seen the bandgap that always occurs at broadside $\theta_{-1} = 0^o$, at 13GHz as Bandgap 1 . Several other bandgaps unrelated with broadside occur in TE_{02} mode, the first one Bandgap 1 seems to be related with the presence of the Strip mode and Bandgap 2 at 15 GHz is the second most common kind of bandgap in periodic structures. It happens when two harmonics interfere with each other, in this case the TE_{02} main harmonic has a $\beta_0 = 289.4$ and the TE02 second harmonic is $\beta_{-1} = -289.4$, meaning they are radiating at $\theta_0 = 67^o$ and $\theta_{-1} = -67^o$. These two harmonics cancel each other.

To understand this, the attenuation constant α has to be seen as the sum of three contributions: the **radiation losses** α_{rad}, the **ohmic losses** due to the material conductivity α_{mat} and a **reactive contribution** α_{reac}. Material losses will be considered negligible throughout this work. During the bandgaps, the major contribution to α is reactive and there is no α_{rad}. It can be physically interpreted as the effect of a destructive interference between the ongoing wave and a regressive wave formed by reflexion on the periodic discontinuities. Note that the high value for the attenuation constant when the mode is below cut-off is reactive too.

Depending on the final purpose of the structure, these bandgaps are an undesired effect to avoid, in the case of a LWA, or in the case of FSS, they may be useful to block a specified band of frequency. The conclusion is that, either to avoid or use them, it is important to have a clear idea of where those bandgaps may appear and how to control them by modifying some of the structure geometrical parameters and studying how the different harmonics react.

4.2.6. User´s guide: Radiation Pattern and Modal contribution.

Those propagative modes that excite the PPM mx=0 and are within the *fast-wave* or radiation zone, will radiate outwards with a certain radiation pattern. This pattern will be determined by the propagation constant of the harmonic that is radiating, $k_{my} = \beta_{my} - \alpha i$, and also of the family of Parallel Plate modes that compose said harmonic. Out of those PPmodes propagating in the harmonic, only the first order mode mx=0 has the horizontal polarization required to propagate in the outwards direction and radiate, but there may be other propagating longitudinally (y direction) higher order PPmodes that may reach the aperture, depending on the longitude L of the parallel metallic walls at the top of the structure. Previous works found in the literature and already mentioned (Guglielmi, Lampariello, Oliner….), that studied before the radiation pattern of these leaky wave antennas assumed a L large enough to ensure that only the PPM mx=0 was radiating. Only [Gómez 2004] considered for the first time the effects on radiation of higher order parallel plate modes, but only for the E plane radiation pattern and using an approximation based on a spherical wave from a radiating infinite wire of magnetic current on a ground plane. In the present work, a **rigorous analysis for both the E and H radiation planes considering the contribution of all PPM is developed for the first time**. Analytical expressions are obtained by applying the Fourier transform of the induced magnetic currents at the top aperture. And, on top of this main contribution, WELAST is not limited to the radiation of simple rectangular periodic patches, but is prepared to analyze more complex structures, such as the square loop used as example in this chapter.

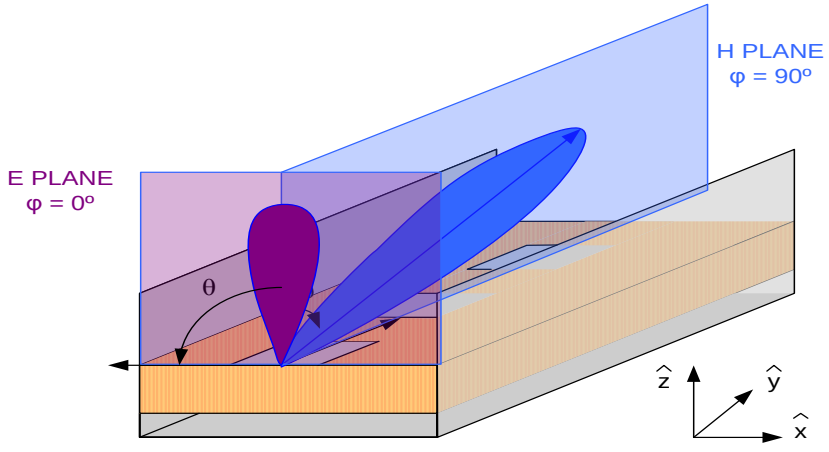

Figure 4.2.6.1 Main radiation planes in the LWA.

In Chapter 2, the expression for the transversal electric field was obtained as:

$$\vec{E}_t(r) = \sum_{p}^{TE,TM} \sum_{mx=0}^{\infty} \sum_{my=-\infty}^{\infty} A_m^{(p)} \hat{V}_m^{(p)}(z) \cdot \vec{e}_{mx}^{(p)}(x) e^{-jk_{my}y} \tag{2.6.32}$$

Where $$\vec{e}_m^{\,TE}(x) = \frac{-jk_{ym}\cos(k_{xm}x)\hat{x} + k_{xm}\sin(k_{xm}x)\hat{y}}{N_m} \tag{2.2.6}$$

$$\vec{e}_m^{\,TM}(x) = \frac{+k_{xm}\cos(k_{xm}x)\hat{x} - jk_{ym}\sin(k_{xm}x)\hat{y}}{N_m} \tag{2.2.7}$$

$\hat{V}_m^{(p)}(z)$ are the modal voltages obtained from the resolution of the equivalent transmission line, and depend on the situation point in the z direction. $\vec{e}_{mx}^{(p)}(x)$ are the parallel plate mode expressions for the transversal propagation, and depend on the situation point in the x direction. The same way, $e^{-jk_{my}y}$ represents the longitudinal propagation of the leaky mode and depends on the situation point in the y direction. Finally, $A_m^{(p)}$ can be defined as the **modal contribution to propagation**, since it depends on the modal indexes my and mx, but is independent from the observation point.

$$A_m^{(p)} = \int_{S'} \frac{\vec{e}_{mx}^{\,x,(p)*}(x') - C_m \vec{e}_{mx}^{\,x,(q)*}(x')}{1 - C_m^2} \frac{e^{jmy\frac{2\pi}{P}y'}}{P} J_t(r') \tag{2.6.31}$$

To obtain the rigorous expressions for the radiation pattern, the top of the LWA will be considered as a radiating aperture, and the Equivalence Principle [Balanis 1982] will be applied to calculate the equivalent magnetic currents induced on said aperture. This principle says that the magnetic currents are rotational of the transverse electric field at the aperture:

$$\vec{M}_s = 2\hat{n} \times \vec{E}_t = M_y + M_x = 2E_t^{\hat{x}}\hat{y} - 2E_t^{\hat{y}}\hat{x} \tag{4.2.6.1}$$

Knowing that:

$$\vec{E}_t(x, y, z = L) = \sum_{p}^{TE,TM} \sum_{mx=0}^{\infty} \sum_{my=-\infty}^{\infty} A_m^{(p)} \hat{V}_m^{(p)}(z = L) \cdot \vec{e}_{mx}^{(p)}(x) e^{-jk_{my}y} \tag{4.2.6.2}$$

The magnetic currents at the top aperture of the LWA are of the form:

$$M_y = \frac{2}{N_m}\left(\sum A_m^{TE} V_m^{TE}(z=L)(-j)k_{my}\cos(k_{mx}x)e^{-jk_{my}\cdot y} + \sum A_m^{TM} V_m^{TM}(z=L)k_{mx}\cos(k_{mx}x)e^{-jk_{my}\cdot y}\right) \quad (4.2.6.3)$$

$$M_x = \frac{-2}{N_m}\left(\sum A_m^{TE} V_m^{TE}(z=L)k_{mx}\sin(k_{mx}x)e^{-jk_{my}\cdot y} + \sum A_m^{TM} V_m^{TM}(z=L)(-j)k_{my}\sin(k_{mx}x)e^{-jk_{my}\cdot y}\right) \quad (4.2.6.4)$$

Analyzing now the resulting expressions for the magnetic currents at the top aperture, it can be deduced that the amount of contribution that each PPM will have to the radiation pattern will depend on *'how much they were propagating'*, $A_m^{(p)}$, now combined with *'how much intensity are reaching each PPM the top aperture with'*, $\hat{V}_m^{(p)}(z=L)$. This is why the product $A_m^{(p)}\hat{V}_m^{(p)}(z=L)$ will be defined as the **modal contribution to radiation**. Note that both coefficients depend on mx and my but no on the positioning coordinates.

The expression for the radiation pattern in the far-field of an aperture, based on the Fourier transform of its induced magnetic currents can be found in [Balanis 1982]:

$$L_\theta = \iint_S \left(Mx\cos\theta\cos\varphi + My\cos\theta\sin\varphi\right)e^{jk(x\sin\theta\cos\varphi + y\sin\theta\sin\varphi)}ds \quad (4.2.6.5)$$

$$L_\varphi = \iint_S \left(-Mx\sin\varphi + My\cos\varphi\right)e^{jk(x\sin\theta\cos\varphi + y\sin\theta\sin\varphi)}ds \quad (4.2.6.6)$$

L_θ corresponds to the horizontal polarization and L_φ correspond to the vertical polarization. An optimum pure polarized radiation pattern will be composed mainly by horizontal polarization and a negligible part of vertically polarized signal.

Introducing (4.2.6.3) and (4.2.6.4) into (4.2.6.5) and (4.2.6.6), and resolving the integrals, the radiation patterns for the two main radiation planes can be easily obtained. Starting with the **H radiation plane**, or the main plane with the pointing angle, it is considered $\varphi = 90^o$, and the following expressions are obtained:

$$L_\theta = \cos\theta\frac{2}{N_m}\left(\sum A_m^{TE} V_m^{TE}(z=L)(-j)k_{my} + \sum A_m^{TM} V_m^{TM}(z=L)k_{mx}\right)\cdot \quad (4.2.6.7)$$

$$\cdot\frac{1}{k_{mx}}\left[\sin\left(k_{mx}\frac{a}{2}+\frac{a}{2}\right)-\sin\left(k_{mx}\frac{-a}{2}+\frac{a}{2}\right)\right]jL_{WG}\sin c\left(\frac{L_{WG}}{2}\left(k\sin\theta-k_{my}\right)\right)$$

$$L_{\varphi}=\frac{2}{N_m}\left(\sum A_m^{TE}V_m^{TE}(z=L)k_{mx}+\sum A_m^{TM}V_m^{TM}(z=L)(-j)k_{my}\right)\cdot \qquad (4.2.6.8)$$

$$\cdot\frac{-1}{k_{mx}}\left[\cos\left(k_{mx}\frac{a}{2}+\frac{a}{2}\right)-\cos\left(k_{mx}\frac{-a}{2}+\frac{a}{2}\right)\right]jL_{WG}\sin c\left(\frac{L_{WG}}{2}\left(k\sin\theta-k_{my}\right)\right)$$

It is interesting to mention that for the main parallel plate mode mx=0, the expression obtained with (4.2.6.7) is

$$L_{\theta}=\cos\theta\frac{2}{N_m}\left(\sum A_m^{TE}V_m^{TE}(z=L)(-j)k_{my}\right)\cdot L_{WG}\sin c\left(\frac{L_{WG}}{2}\left(k\sin\theta-k_{my}\right)\right) \qquad (4.2.6.9)$$

Which is exactly of the same shape that the expression used in PAMELA [Gómez 2004] as the radiation pattern for an exponential illumination $\overline{M(y)}=e^{-jk_{my}\cdot y}$ shown below for a waveguide of a finite longitude. It makes sense, since this approximation only takes into account the radiation of the main PPM.

$$R(\theta)=\int_0^{L_{WG}}\overline{M(y)}\cdot e^{jk_0\sin\theta\cdot y}=\frac{-j}{k_0\sin\theta-k_{my}}\left(e^{j(k_0\sin\theta-k_{my})L_{WG}}-1\right) \qquad (4.2.6.10)$$

Now, for the **E radiation plane**, it is $\varphi=0^{\circ}$. Considering $c=jk\sin\theta$, the expressions obtained are:

$$L_{\theta}=\cos\theta\frac{-2}{N_m}\left(\sum A_m^{TE}V_m^{TE}(z=L)k_{mx}+\sum A_m^{TM}V_m^{TM}(z=L)(-j)k_{my}\right)\cdot\frac{2}{k_{my}}\sin\left(k_{my}\frac{L_{WG}}{2}\right)\cdot \qquad (4.2.6.11)$$

$$\cdot\frac{1}{c^2+k_{mx}^2}\left[e^{\frac{ca}{2}}\left(c\sin\left(k_{mx}\frac{a}{2}+\frac{a}{2}\right)-k_{mx}\cos\left(k_{mx}\frac{a}{2}+\frac{a}{2}\right)\right)-e^{\frac{-ca}{2}}\left(c\sin\left(k_{mx}\frac{-a}{2}+\frac{a}{2}\right)-k_{mx}\cos\left(k_{mx}\frac{-a}{2}+\frac{a}{2}\right)\right)\right]$$

$$L_{\varphi}=\frac{2}{N_m}\left(\sum A_m^{TE}V_m^{TE}(z=L)(-j)k_{my}+\sum A_m^{TM}V_m^{TM}(z=L)k_{mx}\right)\cdot\frac{2}{k_{my}}\sin\left(k_{my}\frac{L_{WG}}{2}\right)\cdot \qquad (4.2.6.12)$$

$$\cdot\frac{1}{c^2+k_{mx}^2}\left[e^{\frac{ca}{2}}\left(c\cos\left(k_{mx}\frac{a}{2}+\frac{a}{2}\right)+k_{mx}\sin\left(k_{mx}\frac{a}{2}+\frac{a}{2}\right)\right)-e^{\frac{-ca}{2}}\left(c\cos\left(k_{mx}\frac{-a}{2}+\frac{a}{2}\right)+k_{mx}\sin\left(k_{mx}\frac{-a}{2}+\frac{a}{2}\right)\right)\right]$$

In Figure 4.2.4.2 there were still two buttons to discuss about. Once a complex solution for a given radiating mode is sent to Fields, different radiation results may be displayed the same way that those for the electric and magnetic fields. By pressing the button *Modal Contribution* the weights each parallel plate mode contributes to both propagation and radiation with are presented as bar plots. For the solution of the TE_{01} second harmonic my=-1 at 12GHz for a lateral walls of L=12mm, Ky= -128.8 -0.8i, the modal spectra is shown in Figure 4.2.6.2 below.

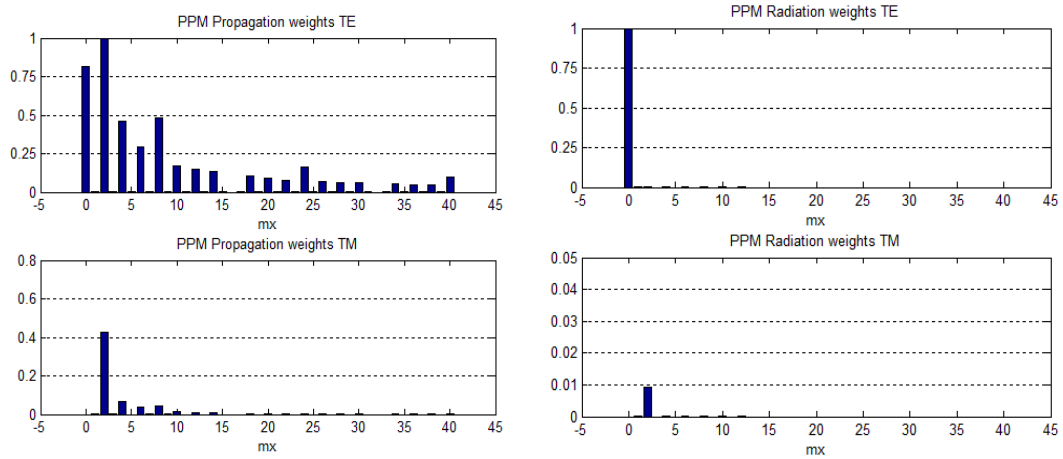

Figure 4.2.6.2 TE_{01} 2nd harmonic Modal Contribution at 12 GHz, for L=12mm.

As can be seen in Figure 4.2.6.2 a), many PPModes are propagating along the structure for the same harmonic, if fact all 40 modes required for the method to converge are propagating. On the other hand, Figure 4.2.6.2 b) shows that, from those propagative modes, only the main parallel plate mode mx=0 is contributing significantly to the radiation pattern. This will have an impact on the polarization purity of the radiation pattern. Now, clicking on the button *Plot Radiation* the radiation patterns for the H plane, E plane or both will be displayed, depending on the radio buttons selected. In Figure 4.2.6.3, the **radiation pattern for the H plane** is presented for a LWA of $10\,\lambda_0$ long. The TE_{01} my=-1 is radiating backwards with a pointing angle of -31º, with secondary lobes at about 13dB below the main lobe, as expected for an exponential illumination of the aperture. Due to the nature of the main PPM, this PLWA are horizontally polarized, as can be seen in this Figure plotted in continuous blue line. A comparison between the approximation done in [Gomez 2004] in red and this work is presented, as a validation of the results. It can be seen how they present a very good

agreement, since, as shown in the modal contribution plots, this structure has all higher order PPModes under cut-off at the aperture, with the only contribution to radiation coming from the main parallel plate mode. As expected, the vertical polarization, shown in the same Figure, is negligible.

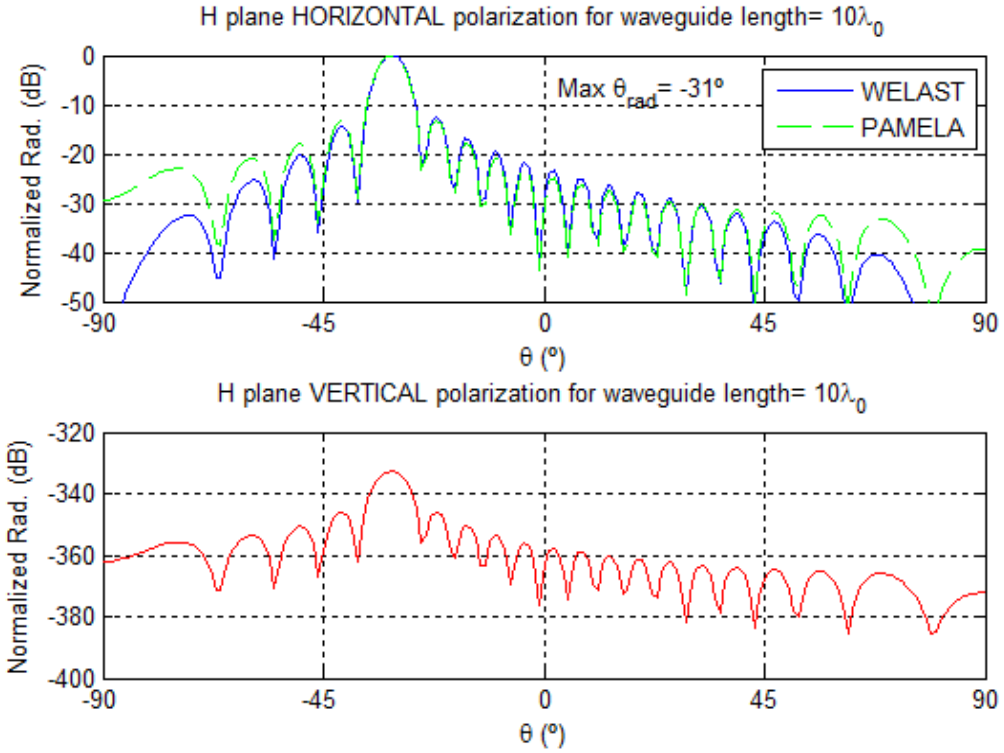

Figure 4.2.6.3 TE_{01} 2nd harmonic H plane radiation pattern at 12 GHz, for L=12mm.

The **radiation pattern for the E plane** is presented in Figure 4.2.6.4 a), as the sum of all PPM contributions, as a single main broadside lobe centered in $\theta = 0^{o}$, with no side lobes. The patterns for the parallel plate modes mx=0, 1 and 2 are represented in Figure 4.2.6.4 b) c) and d) respectively. As was expected too, the main contribution comes from the PPM mx=0, and it has no vertical polarization. The radiation patterns for the higher order modes are shown merely for illustrative purposes, as they not radiate, but it can be seen how their patterns are formed by several main beams, which will degrade the performance of the antenna. In these plots, it can be seen the correspondence between the modal contribution to radiation already seen in Figure 4.2.6.2 and the scales of the patterns for each mode. As the order of the PPM increases, the more tilted are the main lobes and the higher is the vertical polarization. Based on the radiation patterns, it can be concluded that the length of the metallic walls L=12mm was enough to avoid radiation

from higher order modes, which is, most of the times, a design objective to ensure a single directive main lobe.

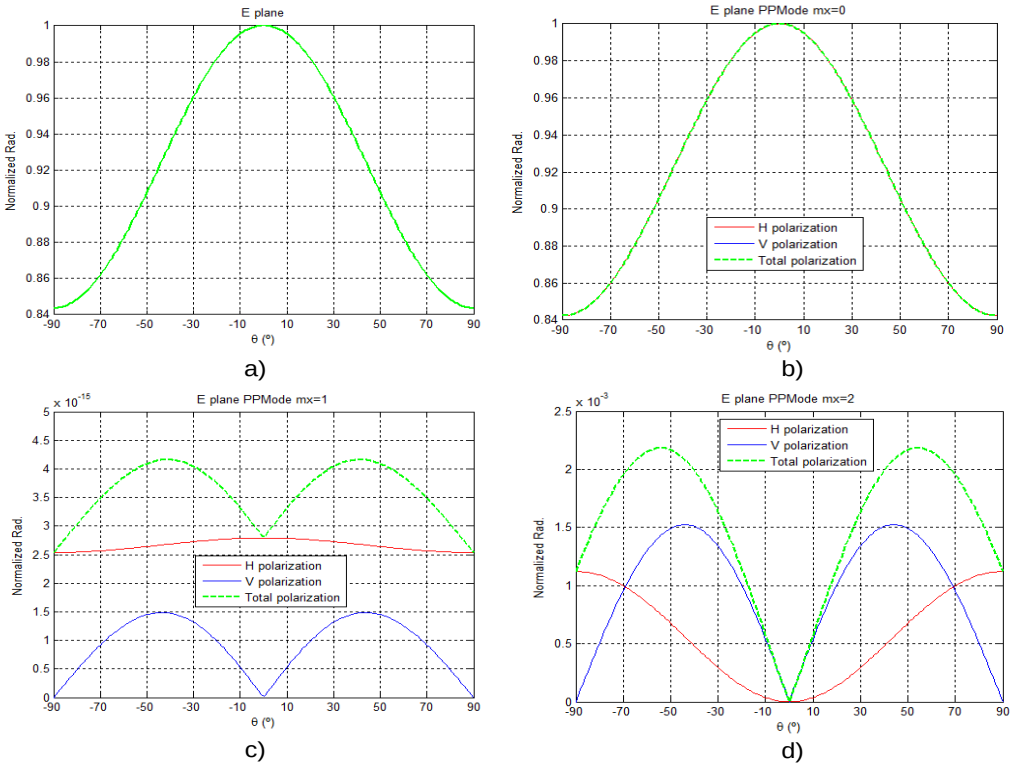

Figure 4.2.6.4 TE_{01} 2nd harmonic E plane radiation pattern at 12 GHz, for L=12mm.

To test the effects that radiative higher order PPModes may have on the radiation properties of the antenna, the same TE_{01} my=-1 at 12GHz will be analyzed, now for a length of the lateral walls of L=1mm. This length is positively not enough to make sure all the high order modes are under cut-off, and do not contribute to the radiation pattern. First, the modal contribution to propagation and radiation is shown in Figure 4.2.6.5. :

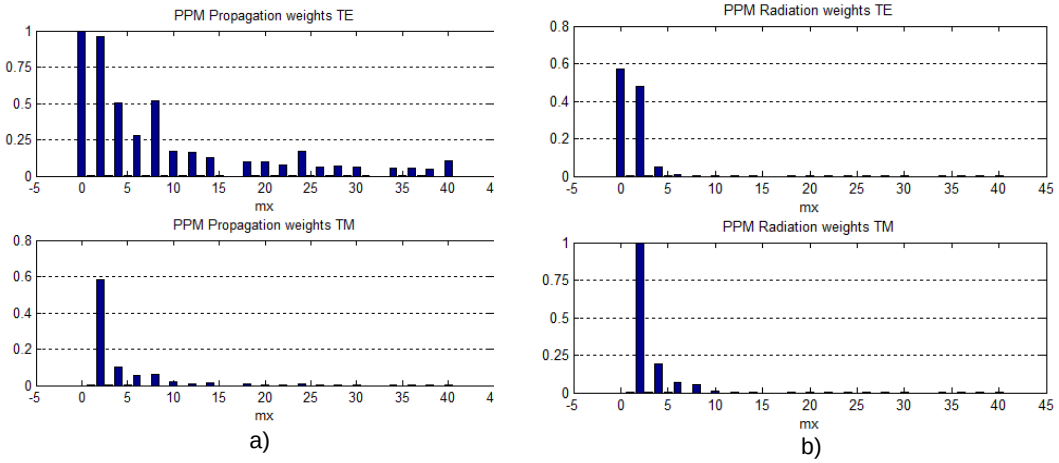

Figure 4.2.6.5 TE01 2nd harmonic Modal Contribution at 12 GHz, for L=1mm.

Although the propagation modal spectra remains basically the same, the radiation has now two main contributors, since the PPM mx=0 and the mx=2 are now able to excite equivalent magnetic currents at the top aperture. The main impact of this second contribution can be seen on the E plane radiation pattern, see Figure 4.2.6.6 a), where there is no longer a neat single beam aiming to $\theta = 0^{o}$, but two tilted lobes. It can be seen in Figure 4.2.6.6 d) how the contribution of the mx=2 is now significant. This degradation of the pattern is to be avoided.

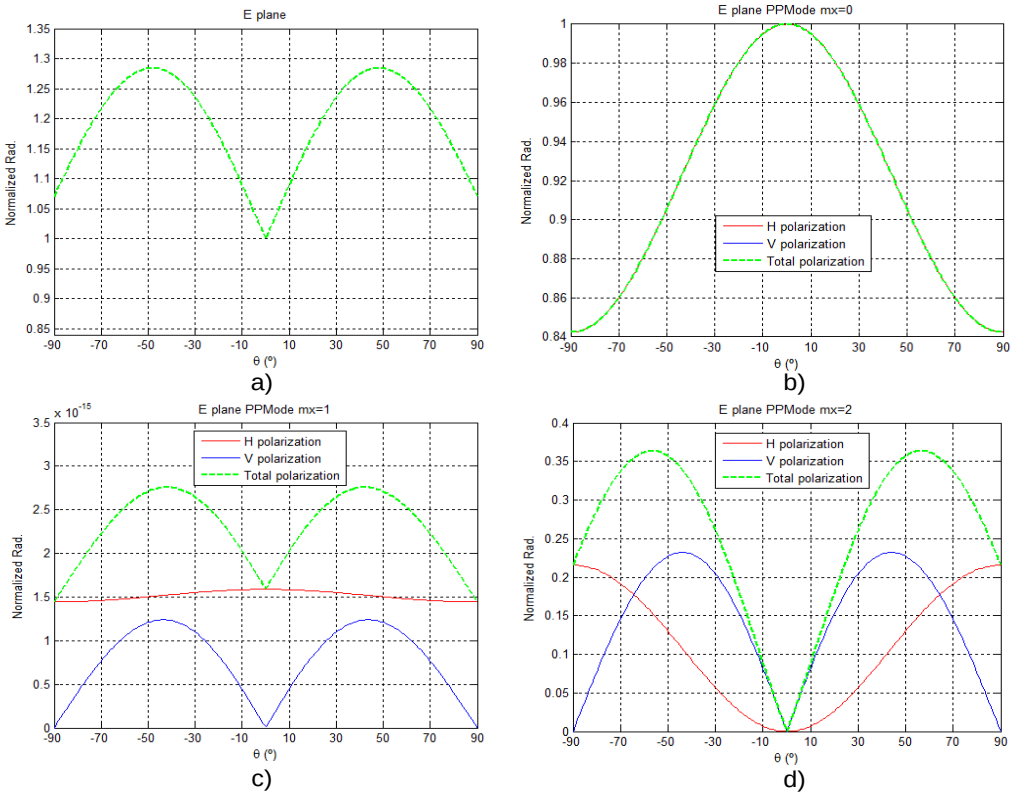

Figure 4.2.6.6 TE_{01} 2nd harmonic E plane radiation pattern at 12 GHz, for L=1mm.

As a conclusion, it is of extreme importance to chose an appropriate value for the length of the lateral walls, long enough to make sure the PPM mx=0 is the only contribution to radiation, but at the same time, it must be not too long to allow the energy to couple from one wall to the other, creating new propagative modes called 'Channel modes', that may be radiating at the same frequency with a different angle. These modes have been studied in the literature already mentioned, and are one of the main drawbacks of the so called 'Inset' structures (those with the aperture in the shortest wall of the waveguide). The other main drawback is that the leakage rate can be controlled to a very small extent, due to the horizontally polarized nature of the TE_{01} in these LWA. This translate in two consequences: one, the attenuation constant α has very large values right after cut-off, so

all the energy is radiated in a very short longitude. This reduces the effective aperture and renders the antenna useless due to extremely low directivities. And second, tapering on the illumination is most of the time not possible.

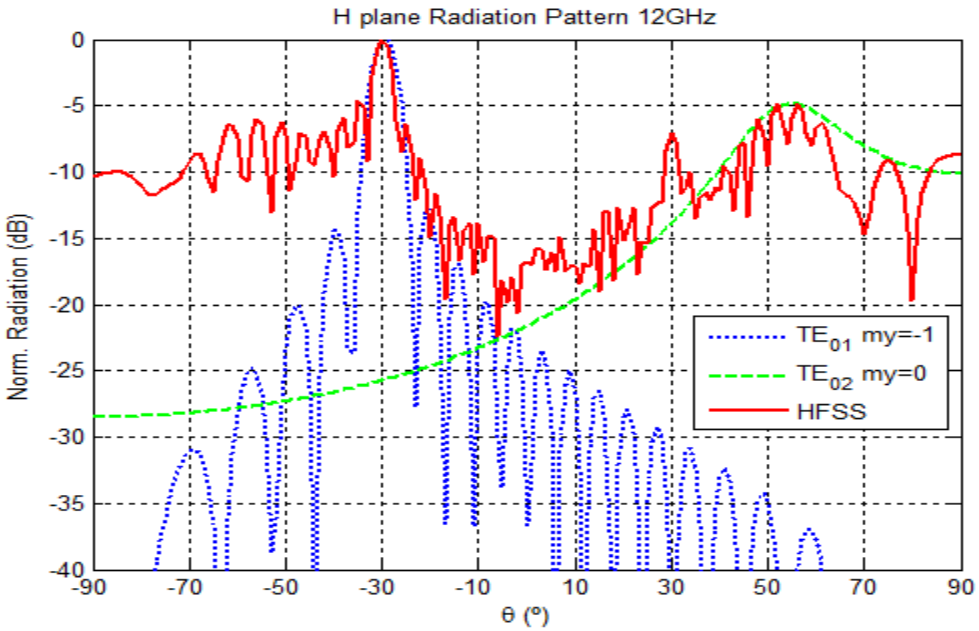

Figure 4.2.6.7 H plane modal radiation pattern comparison with HFSS at 12 GHz.

To check the radiation results calculated with this method, the structure was simulated in HFSS with $10\,\lambda_0$ of longitude, at 12 GHz. As seen in Figure 4.2.5.4, at that frequency there are two harmonics radiating with different pointing angle, the TE_{01} mode Floquet harmonic my=-1, radiating backwards with $\theta_{-1} = -31^{o}$ in blue dotted line and the TE_{02} main harmonic my=0 radiating forward with broad main lobe at $\theta_0 = 54^{o}$, due to his high leakage constant, in green dashed line. The total radiation pattern obtained with HFSS is shown in Figure 4.2.6.7 in red continuous line. The two main pointing angles estimated with the developed method agree very well with those in the HFSS simulation. Also, in the HFSS simulation, another main lobe can be found at +31º and a much higher level of signal that expected is radiated around -54º. On top of that, the total radiation pattern seems to have some 'noise'. All these added effects are due to the finite length of the real simulated structure.

One must take into account that the developed method analyses an infinite periodic open waveguide, and the finite length of the real aperture is introduced when calculating the

radiation pattern from the equivalent magnetic currents at the aperture. The efficiency of a LWA is given by:

$$\eta = 1 - e^{-2\alpha L_{WG}} \qquad (4.2.6.13)$$

For the TE01 mode my=-1 and the length of this LWA, with an attenuation constant of $\alpha = 0.8 nep/m$, the calculated efficiency is about a 33%. This means that a 66% of the energy is not radiated and reaches the end of the waveguide, creating a reflecting wave radiating backwards. It is obvious that a much larger open waveguide is needed to increase the efficiency of the LWA, which would translate in ridiculously long times of simulation with commercial software. The reflected wave is too high to obtain clear results with HFSS that could be used to validate those obtained with the present method. To minimize this effect, a port at the end of the LWA and a tapered transition were added in the structure simulated in HFSS (see Figure 4.2.6.8). Analyzing the S parameters, the attenuation of the now much lower reflected wave was calculated. This way, the sum of the radiating forward wave and the reflected backward wave can be plotted versus the HFSS result. This estimation was done too for the reflected wave corresponding to the TE01 mode. The previously mentioned 'noise' is unavoidable, since the transitions also radiate, due to the horizontal polarization of the TE_{01} and TE_{02} modes.

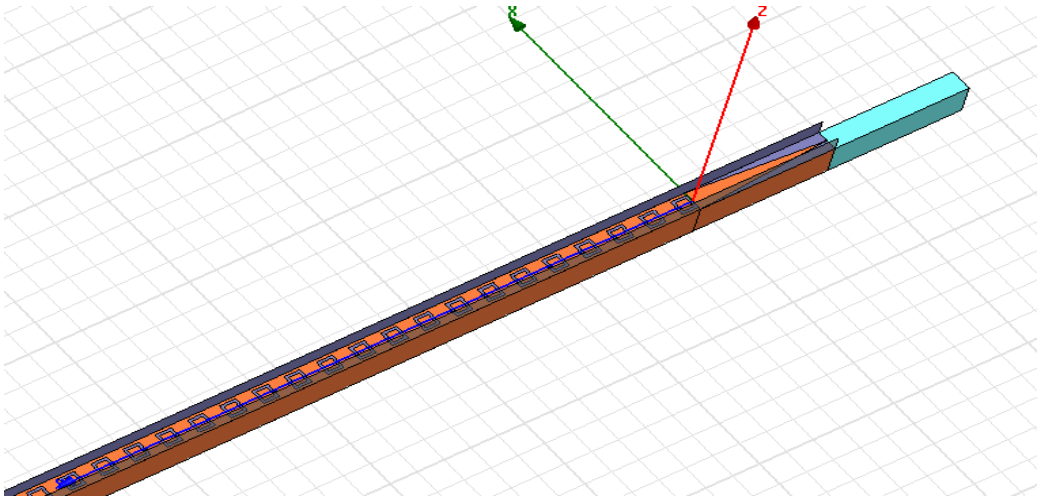

Figure 4.2.6.8 HFSS modelled LWA at 12 GHz.

To make a final validation of the method, all four contributions will be taken into account, the radiation from the two modes TE_{01} and TE_{02} calculated directly with the method, and the radiation coming from the reflected waves of those two modes. Figure 4.2.6.9 presents the comparison between the HFSS radiation pattern in red continuous

line and the sum of all WELAST radiation contributions in blue dotted line. It can be seen how the method developed in this work produces very reliable results.

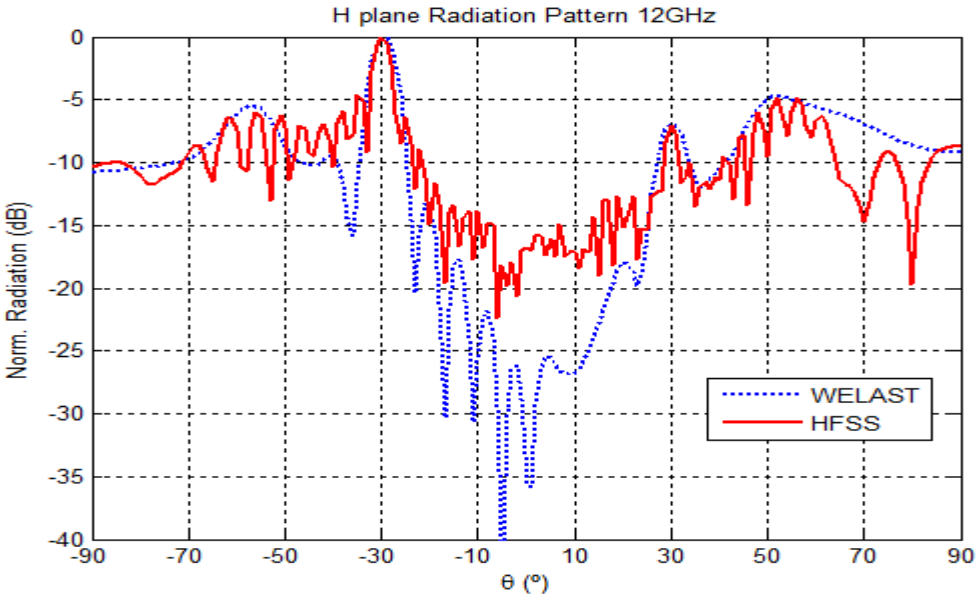

Figure 4.2.6.9 H plane TOTAL radiation pattern comparison with HFSS at 12 GHz.

It would have been impossible to discriminate the different contributions to radiation from the HFSS results. The capability to analyze each mode and harmonic separately is one of the main advantages of the present method. A **rigorous modal analysis** allows the user to understand where all the different contributions to radiation come from, why and where to expect a bandgap due to harmonic interference, since it can be foreseen once the modal spectra supported by the leaky wave antenna is known.

Another very important advantage is the simulation time consumption. The simulation with HFSS took 19 minutes to simulate the structure, with an error below 0.1, with a Core2Duo Centrino. WELAST took 5.5 minutes to reach the complex solution, in a similar computer, with an iterative search of 10 steps. It must be said that same result can be obtained in 2.5 minutes for only 5 steps, but the user is recommended to start with more steps than necessary in order to ensure the correct result. And it takes 25 seconds to move from one result in frequency in steps of 0.1GHz. It can be seen that the present software is **much faster than 3D full wave based software**, since it applies a 2.5D analysis, and only the metallization of one single cell has to be meshed. In HFSS the simulation time grows exponentially when increasing the length of the structure,

necessary to achieve higher efficiency. WELAST simulation time is not affected by the waveguide longitude.

4.2.7. User´s guide: Resonance Study.

One of the most important features when working with periodic metallization is the resonance phenomenon. The main motivation to develop a method able to support subdomain basis functions was to allow the user to study shapes that have interesting resonant behaviour, such a dipoles, square loops, split square loops, crosses… These circuits may be used to create a FSS to avoid the leaky wave antenna radiating at undesired frequencies, or even more, to use the nulls that the resonance will cause in the attenuation constant in order to modify the radiation at will, so the illumination along the aperture is shaped into a more convenient tapered radiation pattern. The concept of tapering is well known [Balanis 1982], and has been used before in very simple LWA structures [Gomez March-2006]. This tapering procedure was based on the radiation controlled by asymmetry, so it was achieved by modifying the position of the printed circuit on the dielectric. With this new simulation tool, not only the variation of the leakage constant due to is position can be analyzed, but also the combined effect of positioning with the different resonance effects of complex printed circuits can be studied.

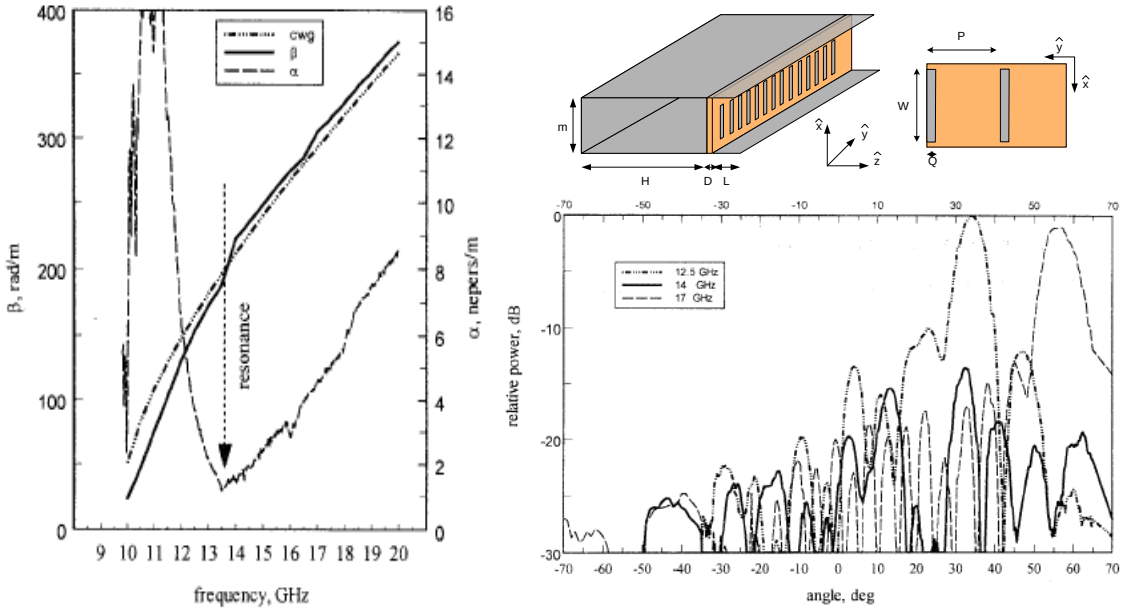

Figure 4.2.7.1 Blanos and Vardaxoglou structure and measured results.

As an example of this, the dipole based Blanos and Vardaxoglou structure will be taken into the software. The button *Resonance Study* is the only feature of this simulation tool that is completely open to the user to be modified. It is basically a tool to plot the dispersion of the phase of the induced currents on the metallization versus the frequency. This way, the resonances can be identified as nulls in the phase of the current. The author had it programmed so the centre point of the dipole was analyzed when studying the current distribution. This file must be modified to adapt to the structure under analysis, since the exact point of interest on the printed circuit may be different, depending on the shape, or maybe more than one interest point may be required. The user will have to edit the file 'currents_vs_frec.m', and modify it accordingly with his chosen printed circuit. It is easy and only basic Matlab programming knowledge is needed. In any case, this feature is a verification tool for resonances, since this information may be deduced by the analysis of the phase β and attenuation α constants dispersion versus frequency.

In 1997, the results for the phase and leakage constant obtained directly from radiation pattern measurements reflected a resonance at 14GHz. It was then checked as the radiation pattern did not show any main lobe radiating at said frequency (continuous line). This can be seen in Figure 4.2.7.1. The geometry of the structure introduced in WELAST is a=9mm, H=14mm, D=0.3mm, L=7mm, P=7mm, the length of the dipole is W=8mm and Q=0.2mm thick. Figure 4.2.7.2 shows the main beam angle and attenuation constant dispersion curves for different values of the dipole length. At the sight of these two results, two bandgaps can be clearly identified, the first near 14GHz and the second close to 24GHz.

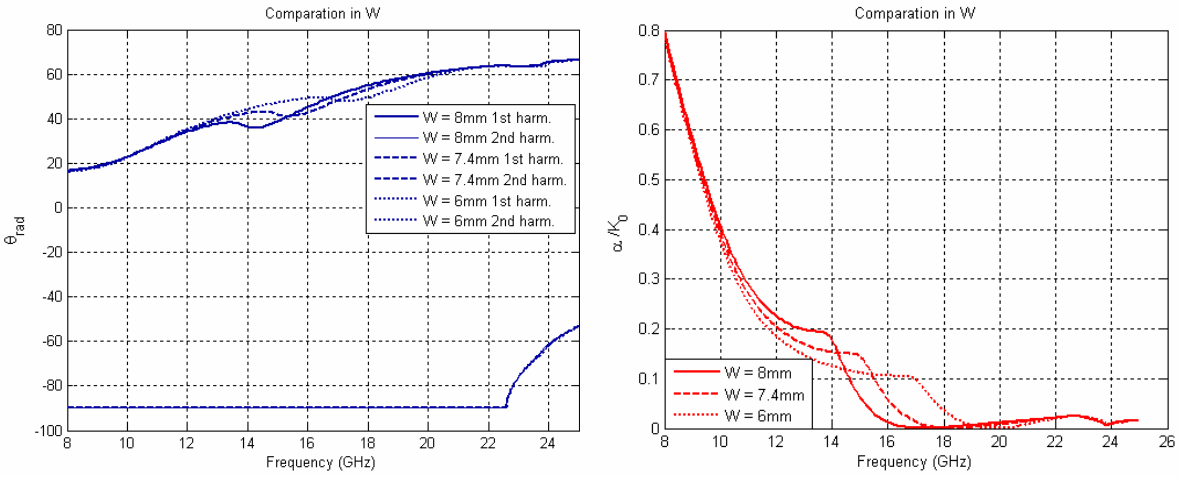

Figure 4.2.7.2 Pointing angle and attenuation constant: W variation.

In the same Figure, the results for the length of the dipoles W= 7.4mm and W=6mm are also plotted. It can be seen how, as the length of the dipole decreases, the first bandgap moves up in frequency. On the other hand, the second bandgap remains at the same frequency for all dipole lengths. From this, it is easily concluded that the first is a **resonance bandgap** is due to the resonance effect of the dipole FSS, and the second is an **interference bandgap** is a consequence of the destructive interference between the harmonic my=0, radiating at $\theta_0 = 63^o$ at 23.8GHz and the second harmonic of the TE_{01} mode my=-1 radiating at $\theta_{-1} = -63^o$ at the same frequency.

This same conclusion can be reached via a resonance study. Figure 4.2.7.3 shows the value of the phase of the induced current on the metallic dipole. Only the current along the dipole (x direction) is of interest. In the zoom at the middle of this figure, it can be appreciated how the null in the current phase moves from 14GHz to above 17GHz as the length of the dipole decreases. Regarding the second bandgap, the current phase tends to be zero at 23.8GHz for all cases.

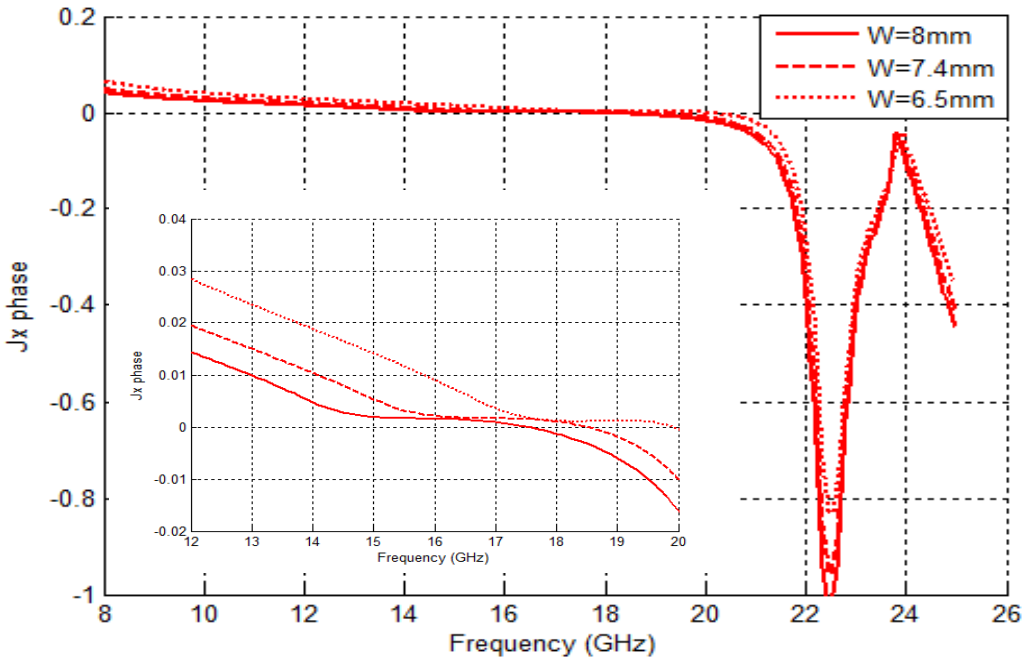

Figure 4.2.7.3 Pointing angle and attenuation constant for the Blanos structure.

For tapering purposes, it is clear that the variation of the leakage constant due to the resonance bandgap can be controlled to an extent by modifying the dipole length.

In previous sections, it was studied that the position of the Floquet second harmonic can be controlled by modifying the periodicity P. Figure 4.2.7.4 shows the main beam radiation angle and the attenuation constant for a fixed length of the dipole W=8mm. It can be seen how, as the periodicity decreases, the second harmonic separates from the main harmonic, which means that the forward wave of the my=0 and the backward wave of the my=-1 will be radiating with the same angle at a higher frequency, so the bandgap moves up from 21GHz to above 24GHz. Do notice that the resonance bandgap remains unmovable, since the W of the dipole is fixed.

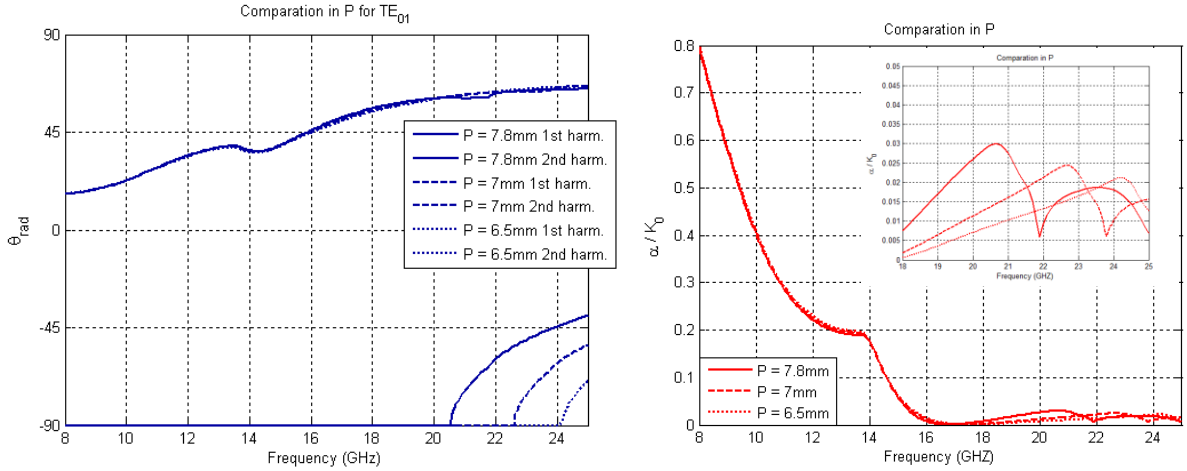

Figure 4.2.7.4 Pointing angle and attenuation constant: P variation.

Again, bearing in mind a future tapering on the illumination of the antenna, there is a second variation of the leakage constant, although within a smaller range, related to interference bandgaps that can be controlled separately modifying the periodicity P.

Finally, a study of the power radiated for the variation of the dipole length W and the periodicity P is shown on Figure 4.2.7.5. The Pointing vector in the z direction was calculated at the centre point of the aperture in the x direction.

$$P_z = \frac{1}{2}\int_{x=0}^{a}\left(\vec{E}(z=L)\times\vec{H}(z=L)\right)\cdot\hat{z}\partial x \qquad (4.2.7.1)$$

The same variation observed for the zero of the current phase in both cases of P variation and W variation can be identified for the null of the radiated power. For the resonance bandgap, the zero of the Poyinting vector moves up in frequency as W decreases.

Considering the interference bandgap, the smaller the periodicity, the higher up in frequency said zero appears. All results are consistent with each other.

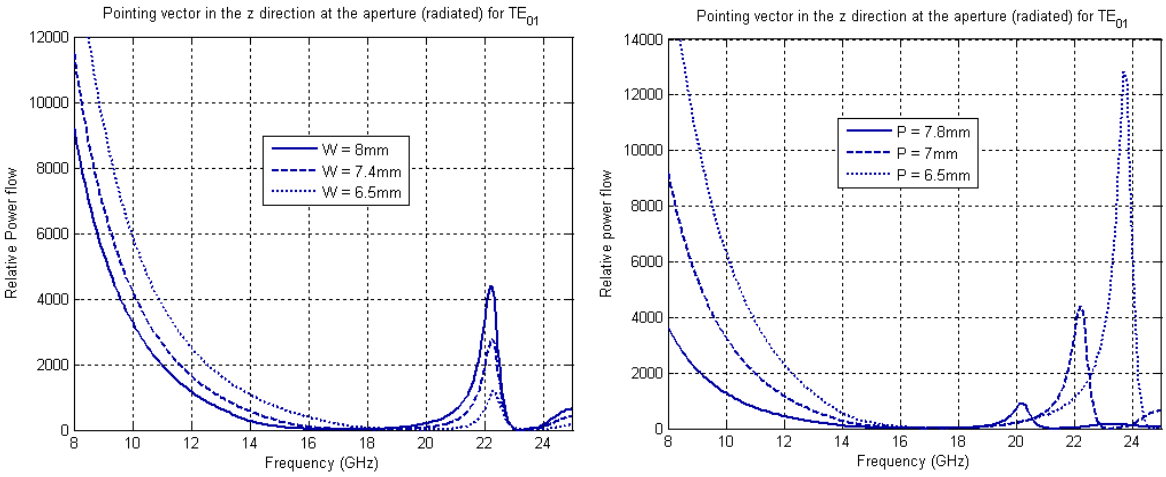

Figure 4.2.7.5 Radiated power at aperture: W and P variation.

4.2.8. User´s guide: Introducing new geometries.

As previously explained, the Roof-top basis functions can model the induced currents on metallizations of certain complexity. Examples have been mentioned as crosses, single and double square loops, splitted square loops, Jerusalem crosses… even periodic printed circuits consisting of two or more components, as dipoles of different length. As long as it has not rounded sections (the number of cells to model this would be prohibitive), almost every arbitrary shape can be modelled. WELAST is already loaded with the meshing files necessary to analyse some of these shapes, but it will happen that a new geometry is needed. Another of the advantages of this software is how easy is to add a new shape, it is only necessary to create a meshing file of said geometry, following some very basic rules, and since there are two ways to fill in the MoM matrix depending on the meshing, as seen in section 2 of this Chapter, there will be two types of meshing files, the **spatial-based meshing** and the **unknowns-based meshing** files.

a) The **spatial-based** meshing file.

It starts with SD1_ and then the name of the new geometry. It meshes a rectangle that will contain all the metallization. This means that there will be empty cells that will be taken into account. The function is of the form:

```
function [vertix,ies,equis,Cx,Cy]=SD1_name (W,Q,t,x1,y1,nx,ny)
```

where nx: number of cells in the x direction

ny: number of cells in the y direction

vertix = [posY posX y_{n-1} y_n y_{n+1} x_{n-1} x_n x_{n+1}]

posY: ordinal position of the cell in the y direction (from 1 to ny)

posX: ordinal position of the cell in the x direction (from 1 to nx)

y, x: absolute position in meters. It is given for two adjacent cells.

ies: [y_{n-1} y_n y_{n+1}]

equis: [x_{n-1} x_n x_{n+1}]

Cx: number of unknowns in the x direction

Cy: number of unknowns in the y direction

b) The **unknown-based** meshing file.

It starts with SD2_ and then the name of the new geometry. It only meshes the actual printed circuit so all the cells will be filled with metal. The function is of the form:

```
function [vertixX,vertixY,Cx,Cy,ies,equis]=SD2_name (W,Q,t,x1,y1,nx,ny)
```

As explained in section 2, the number of unknowns or Roof-tops functions in each direction may not be the same. The only difference now is that each direction has a 'vertixY' vector for the Roof-tops modelling the current in the y direction and another 'vertixX' vector for those in the y direction. All the other output variables remain as the previous case.

As can be seen, this method of introducing new geometries is extremely simple and flexible, since it is based on matrices containing the positioning coordinates of the cells. The plots for the currents and other results receive these absolute positions in the x-y plane to draw the metallization in 3D plots, so they are valid for all new shapes, as long as the format of the inputs is observed carefully.

CONCLUSION

In this Chapter, a new simulation software has been presented, based on the Roof-tops basis functions method introduced in Chapters 2 and 3. This program allows studying for the first time leaky wave antennas based on an open waveguide loaded with complex periodic printed circuits, such as loops, crosses, or an arbitrary shape of the kind. A complete and rigorous modal analysis is carried out on the single square metallic loop LWA, as an example used to explore the features implemented in this simulation tool. An intuitive and simple graphical interface and the fact that results are plotted in real time, makes WELAST not only fast but extremely easy going. It is very flexible, since the user may choose between Entire Domain of Sub-domain based method, and from a wide range of plots of currents, fields, power and dispersion curves not only with frequency, but also significant geometrical parameters. The obtained results have been compared and validated with other authors' methods and commercial software. This makes **WELAST** a **powerful, reliable and versatile tool** able to analyse novel PLWAs with printed circuits of certain complexity that could not be modelled until now. It also counts with the possibility to study resonances, based on the induced currents, characteristic of FSS metallization shapes mentioned before. But the most remarkable feature, in the author eyes, is that this software not only produces graphs and results characterizing a given LWA. Thanks to the modal analysis, the user can achieve a **deep understanding of the electromagnetic phenomena** taking place in the open structure, and use this knowledge to modify and optimize it at will.

CHAPTER 5 - CONCLUSIONS AND FUTURE WORK

Where real applications of the developed simulation tool are presented and future extensions for the code are proposed. Finally, the conclusions of the presented work are synthesized.

5.1. Potential Applications.

Once the simulation tool is coded, provided with a graphical interface and validated, it is ready to use. In this section a wide range of possible applications for WELAST is presented, not only the straight forward ones, but also other possibilities the author came across during the method development stages. Most of the proposed applications are complex enough to become the initial triggering idea of new PhDs based on the electromagnetic software created in this work.

5.1.1. 1D PLWAs

This is the obvious main application of the simulation software developed in this work. As explained throughout previous chapters, this type of periodic LWA was studied in the Polytechnic University of Cartagena using a similar MoM based method with Floquet

and Parallel Plate modes expansion, to model the propagation characteristics in the laterally shielded waveguide for simple printed geometries, as strips or slots [Gomez March-2006]. Therefore, this full-wave method takes into account the radiation of higher order harmonics and phenomena related with the interference between harmonics, such as bandgaps. Said method was greatly limited by the use of Entire Domain basis functions to model the currents on the printed circuits. In the last years, another method has been used to analyze laterally shielded PLWA, based on a Transverse Equivalent Network (TEN) combined with the pole-zero matching method [García-Vigueras 2010]. Although considerably fast and reasonably accurate, this method only works for single Floquet mode propagation, and also shares the geometrical limitation to simple patches.

The method coded in this thesis overcomes this major drawback by introducing Sub-domain basis functions in the MoM to allow complex geometries in the design. With this, the possibility to combine the laterally-shielded PLWA with known FSS and even with metamaterial planar surfaces is open for research. In Chapter 4, a square loop PLWA was presented and used to introduce the simulation program. The same way, WELAST can be used to analyze, understand and efficiently design PLWAs based on loops, crosses, double dipoles or any combination or new element the user may decide is more convenient, since its modular nature makes it easy to extend to new geometries.

It is most interesting the **capability of tapering** that this type of PLWA posses, that is, the ability to independently control the pointing direction and illumination function. The tapering procedure is well-known, the radiation pattern obtained by the conventional exponential illumination has 13dB side lobe level [Schwering 1983], which is not acceptable for some antenna applications. The illumination must be tapered with some specific pattern (cosine, triangular…) to reduce the side lobe level. An excellent discussion on different kinds of illumination and corresponding performances can be found in [Balanis 1982]. In [Gomez Sept-2005] a PLWA based on rectangular slots was studied to probe how the leakage rate could be controlled while the phase constant was maintained simultaneously changing two geometrical parameters of the periodic cell, see Figure 5.1.1.1 below. A cosine tapered illumination was achieved, with 23dB of side lobe level.

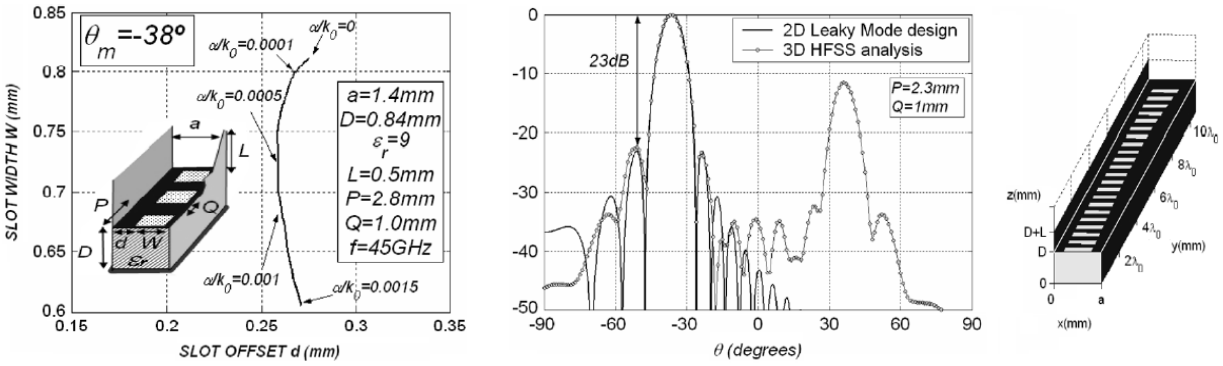

Figure 5.1.1.1 Tapered PLWA design in [Tornero Sept-2005].

This tapering was developed by running parametric analyses on the selected geometrical parameters and creating a cross-table for a given pointing angle. As seen in Chapter 4, WELAST is prepared to run parametrics on geometrical parameters, with the added advantage of dealing with complex elements. Circuits as double loops, double dipoles etc. offer more geometrical parameters to modify in order to achieve the proper tapering. Furthermore, they can be treated as resonant elements choosing the appropriate range of frequency, and the leakage constant can be controlled over a range by working near the resonance frequency by changing physical dimensions of the elements. This effect can be seen in Figures of section 4.2.7. in the resonance study. This way, there is no need to resort solely to the control of radiation by asymmetry to design a taper.

5.1.2. 2D PLWAs

2D periodic LWAs are cavities with a PRS at the top, at about half-wavelength, designed to obtain a pencil beam radiating at broadside, as was explained in Chapter 1. Although WELAST is a simulation software specifically developed for 1D periodic LWA, by applying the **Equivalence Principle**, it can be used to analyze 2D structures. This concept is illustrated in Figure 5.1.2.1 on a 2D PLWA with printed dipoles orientated in the x direction.

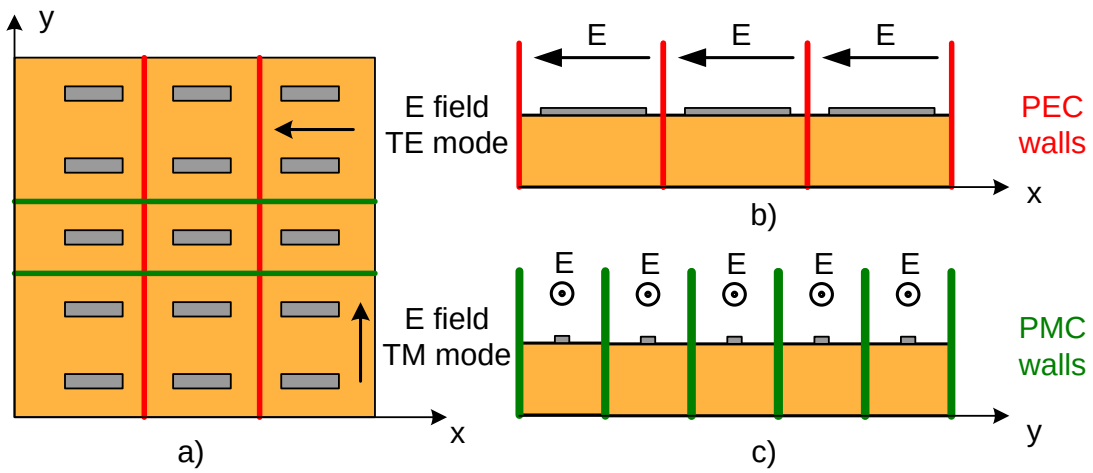

Figure 5.1.2.1 Equivalence Principle applied on a 2D PLWA.

The structure above supports both TE and TM modes, the field of each represented by the arrow along the y axis and the x axis respectively, in Figure 5.1.2.1 a). To effectively model the E field corresponding to the TE mode, Perfect Electric Conductor (PEC) boundaries or Perfect Magnetic Conductor (PMC) boundaries are applied depending on the propagating direction. In Figure 5.1.2.1 b) PEC walls are applied along the y direction for the E field to exist normal to the z-y plane. Alternately, PMC walls can be applied along the x direction, with the same result, see Figure 5.1.2.1 c). It is easy to see that the analysis for the TM mode will be complementary. This kind of LWA works almost at cut-off condition, when $\beta = \alpha \approx 0$, radiating at broadside. As seen in Chapter 1, in this condition, TE mode and TM mode share the same propagation constant values, so only the analysis of the TE mode is necessary. As a conclusion, the study of a laterally shielded 1D PLWA will be equivalent to the infinitely periodic 2D structure.

Until now, these doubly periodic structures were analyzed applying Floquet harmonics expansion on both directions. In [García-Vigueras 2010] this equivalence between 2D LWAs and laterally shielded 1D LWAs is used in combination with a method based on the TEN/pole-zero technique. As mentioned in last section, this method has notable limitations. Also, in [Mateo 2011] the double Floquet expansion is used in conjunction with a spectral domain MoM with Entire Domain basis functions for the study of 2D PLWA made of metallic patches. It can be seen how the most recently developed methods share the inherent limitations of the use of ED basis functions.

Now, with the use of subdomain functions, 2D PLWAs based on printed circuits of arbitrary shape can be analyzed. The mixed Floquet-Parallel Plate mode expansion used in this work, allows a complete modal study, modelling the undesired effect of higher order radiating harmonics and avoiding them in the final design, with the optimum length of the lateral walls.

5.1.3. 1D Metamaterial LWAs.

As introduced in Chapter 1, metamaterial leaky wave antennas have the capability to scan from backward to forward, as conventional PLWAs, but without the need to work with higher order harmonics. Since the new developed code allows complex elements as printed circuit, **laterally shielded left-handed media can be fast and accurately analyzed**. LH media found in the literature can be applied to hybrid waveguide printed circuit technology, as the one shown in Figure 5.1.3.1 from [Liu 2002]. In this Figure a new LH PLWA is proposed with the same features but some added advantages.

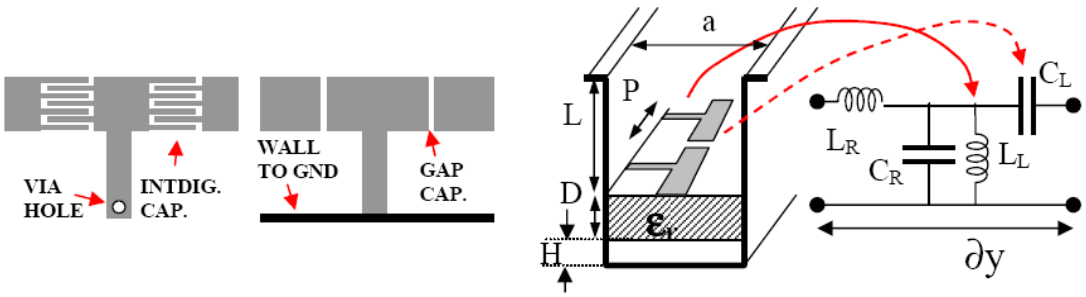

Figure 5.1.3.1 Proposed antenna based on [Liu 2002].

The parallel-plates provide a better focus of the radiated energy and also act as a direct way to connect the shunt inductive line to the ground, avoiding via-holes. The series capacitance is achieved by a simple capacitive gap, instead of the more complex interdigital capacitor. Also, the disposition of the open waveguide shown in Figure 5.1.3.1 b) offers the possibility to control the leakage rate by the asymmetry mechanism explained in Chapter 2. Another example that can be used to design this kind of LH LWA was presented in [Grbic 2002-II] and can be seen in Figure 5.1.3.2.

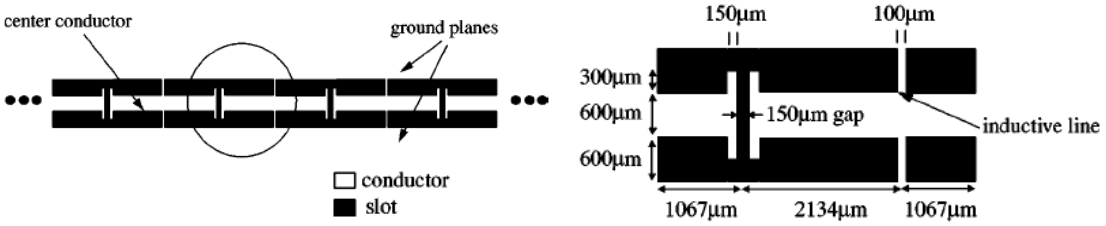

Figure 5.1.3.2 Coplanar backward-wave radiating metamaterial [Grbic 2002-II].

So far, only commercial software has been used to analyze this type of LH LWA, which is too slow for an effective optimized design. In Loughborough University, several studies were carried out on modelling novel uniplanar LH materials, such as loaded dipoles [Goussetis 2006], rectangular loops and spiral loops [Guo 2005], as can be seen in Figure 5.1.3.3. The application of these geometries to the design of a 1D LH periodic LWA would be reasonably straight forward. In these studies, a MoM method combined with interpolation techniques was used with reasonably accuracy, but it did not contemplate any radiation performances, or the effect of lateral walls.

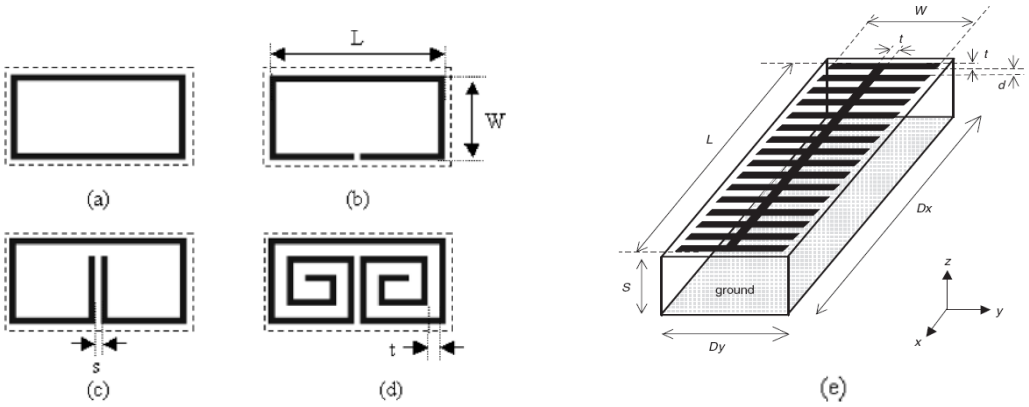

Figure 5.1.3.3 Unit cells proposed in [Guo 2005] a) rectangular loop, b) split loop, c) loaded loop, d) spiral loop and in [Goussetis 2006] e) periodically loaded dipole.

5.1.4. Closed Waveguides.

The simulation tool WELAST is specifically developed for laterally-shielded radiating structures, but it does not mean that closed waveguide based devices cannot be analyzed the same. In Chapter 2 it was explained how, to achieve a solution in the complex plane for the leaky wave, it was necessary to start from the real solution of the closed structure. This analysis is especially interesting when designing waveguides with FSS inserted

within. In 1993, Langley designed a *dual-band waveguide* that could work in two separate frequency bands by creating a waveguide within a waveguide, using a single FSS layer as separator [Langley 1993], as can be seen in Figure 5.1.4.1. This idea can be adapted to other frequencies or requirements by using different geometries in the FSS.

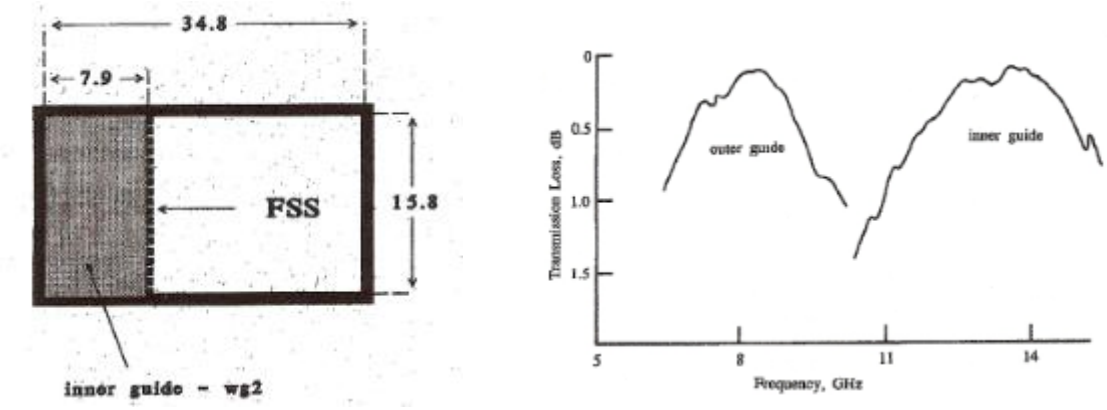

a) b)

Figure 5.1.4.1 Dual band WG proposed in [Langley 1993] a) Cross-section and b) frequency response.

Using Langley configuration, virtually any kind of *waveguide filter* may be designed by studying the modal propagation of the appropriate FSS. Another examples using this configuration are the broadband transmission below the cutoff frequency of a given waveguide, achieved introducing a FSS layer of split ring resonators in [Lubkowski 2007] and the idea for *cavity miniaturization* using 'gangbuster' dipoles FSS in [Caiazzo 2004]. Even without stepping into the metamaterial field, this configuration may be used as a stop-band filter by controlling the electromagnetic bandgaps induced by the FSS, see [Goussetis 2007].

5.2. Future Code Extensions.

The developed method is, as anything else, susceptible of extensions and improvements. Some of the code modifications proposed in this section were not implemented by the author due to time restrictions. It was more pressing the need to establish a solid base for the code, and now that this is achieved in the present PhD, limitless options to give even more versatility to the present method are open for the taking.

5.2.1. Stacked Metallizations Code.

The current version of WELAST is able to analyze one layer of printed metallization on top of a dielectric substrate. The code can be extended to allow structures with stacked layers of printed circuit, as shown in Figure 5.2.1.1, by modifying the method presented in Chapter 2 to allow more than one current source. The boundary condition to obtain the EFIE should be applied on both metallizations, where the E field should be zero. Also, the 'coupling' between both current sources has to be taken into account when solving the equivalent transmission line and deriving the fields in the structure. The geometries of each layer would be treated separately and their induced currents modelled by Roof-top functions, meaning they can be different from each other.

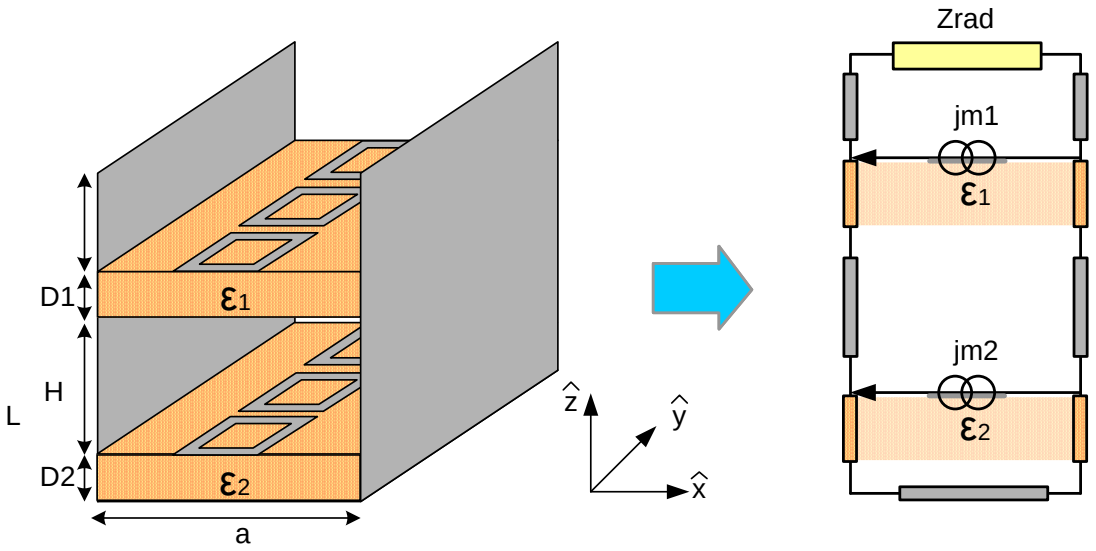

Figure 5.2.1.1. 1D PLWA stacked disposition Equivalent Transmission Line.

In [García-Vigueras 2011] a second printed circuit was added at the bottom of the 1D PLWA acting as a HIS to increase the scanning angle sensitivity with frequency. Traditionally, when a 1D LWA has to scan a large range of angles, it requires a considerably frequency bandwidth, which translates in a complex feeding network. Said bandwidth can be reduced using dielectric filled LWA, with the increase of material losses. With the addition of the second printed layer, the hollow LWA may be designed to radiate from broadside to endfire within the desired frequency bandwidth and a minimum amount of dielectric. The TEN + pole-zero matching method [García-Vigueras 2010], described in section 5.1.2. and limited to rectangular patches, is used.

The same way, 2D PLWAs with two layers of printed circuit could be analyzed. In Chapter 1, it was seen how the typical half-wavelength antenna profile could be reduced to quarter-wavelength or even less with the addition of a PMC at the bottom of the cavity. An example of this can be found in [Mateo 2011].

This code extension could be used also in the field of **closed waveguides**, introduced in previous sections. As seen in Chapter 1, using EBGs acting as PMC inside waveguides could induce an abnormal TEM mode, with *higher illumination efficiency* for feeding purposes. In [Yang 1999-II] this is achieved by using EBGs on both sidewalls to provide magnetic boundary conditions, see Figure 5.2.1.2, generating a relatively uniform field distribution over a certain bandwidth.

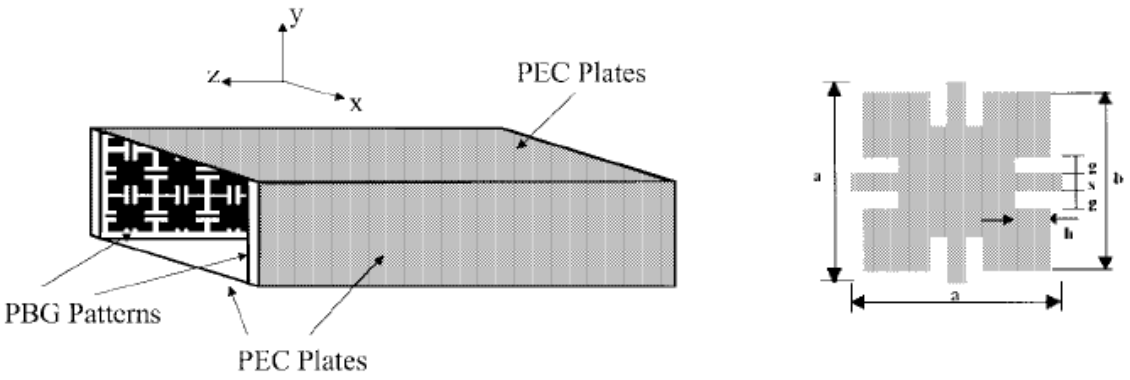

Figure 5.2.1.2 a) Feeding waveguide proposed in [Yang 1999-II] and b) single cell detail.

5.2.2. Arrays of 1D PLWAs

As seen through this work, the 1D PLWA presents an inherent pointing angle scanning with the frequency in the H plane (along propagation direction). To obtain this same scanning capability in the E plane, an array of these antennas must be assembled. This mechanism is well known and has been used before, but the array of this type of antennas has the advantage of not needing complex spatial distributions, as they will be placed in parallel and feed from the same side. A clear and complete explanation about this kind of arrays can be found in [Volakis 2007], as well as several examples of related literature.

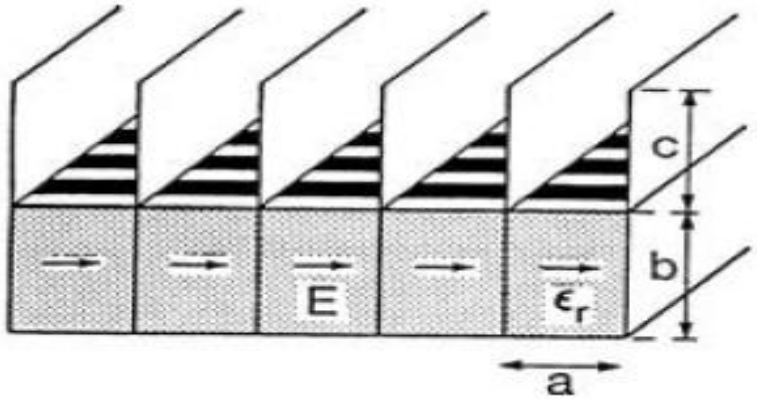

Figure 5.2.2.1 Array of 1D PLWAs (from [Volakis 2007]).

The code extension proposed is based on the study of the equivalent currents induced at the apertures of the 1D LWAs, and the application of Floquet expansion to them, since they will be periodic on a second dimension thanks to the parallel walls separating them. This way, it will be possible to predict the behaviour of the whole array by studying the single antenna, including grating lobes and bandgaps, depending on the separation of the elements of the array.

5.2.3. Design Side CAD tools.

It has been previously introduced the importance of the tapering procedure in the design of LWAs. By appropriately choosing the illumination of the LWA aperture, desired performance in terms of directivity and side lobe level can be achieved [Balanis 1982]. It is based on the *normalized illumination* created by a leaky-mode with propagation constant $\gamma(y) = \beta(y) - i\alpha(y)$, along the antenna aperture in the propagation direction y:

$$M(y) = |M(y)| e^{-j\beta(y)y} \qquad (5.2.3.1)$$

This illumination function depends directly on the phase constant and the attenuation constant of the leaky mode. All related formulation can be found in [Johnson 1993] Ch. 10. To understand the basic, it is sufficient so say that the radiation pattern is calculated

directly by the Fourier transform of (5.2.3.1) and that a simple expression for the attenuation constant $\alpha(y)$ can be obtained, based on the desired illumination function:

$$\alpha(y_0) = 0.5 \frac{|M(y_0)|^2}{\frac{1}{\eta}\int_{y=0}^{y=Lg} |M(y)|^2 dy - \int_{y=0}^{y=y_0} |M(y)|^2 dy} \qquad (5.2.3.2)$$

This expression is based on the efficiency η, which is usually chosen not to be higher of 90%, and the total length of the antenna Lg. With this, a single value of the attenuation constant is given for each point sampled in along the propagation direction y.

It is possible to obtain a semi-automated design of tapered PLWAs, by using side CAD tools developed specifically for that purpose. Two additional programs were developed for PAMELA in [Gómez-Tornero July-2006]. The first one, **LWA Designer** is devoted to calculate the leakage function $\alpha(y)$ needed to obtain the desired radiation pattern, for a specified frequency, guide length Lg and a given radiation angle. Then, the **Layout Designer** uses PAMELA to run the simulations necessary to obtain a dispersion curve for the variation of the leakage constant for a fixed value of the phase constant. The program is coded so a map containing the combined variation of two geometrical parameters is plotted and the appropriate dimensions of said parameters identified in order to obtain the function of $\alpha(y)$ defined by the LWA Designer. This process is defined graphically in Figure 5.2.3.1. and the contour plot obtained for the variation of the asymmetry d and the width of the metallization W is shown in Figure 5.2.3.2. Following the green continuous line corresponding to the pointing angle of interest, in can be chosen the required value of the leakage constant. The correspondence with the dimensions of the geometrical parameters is straight forward.

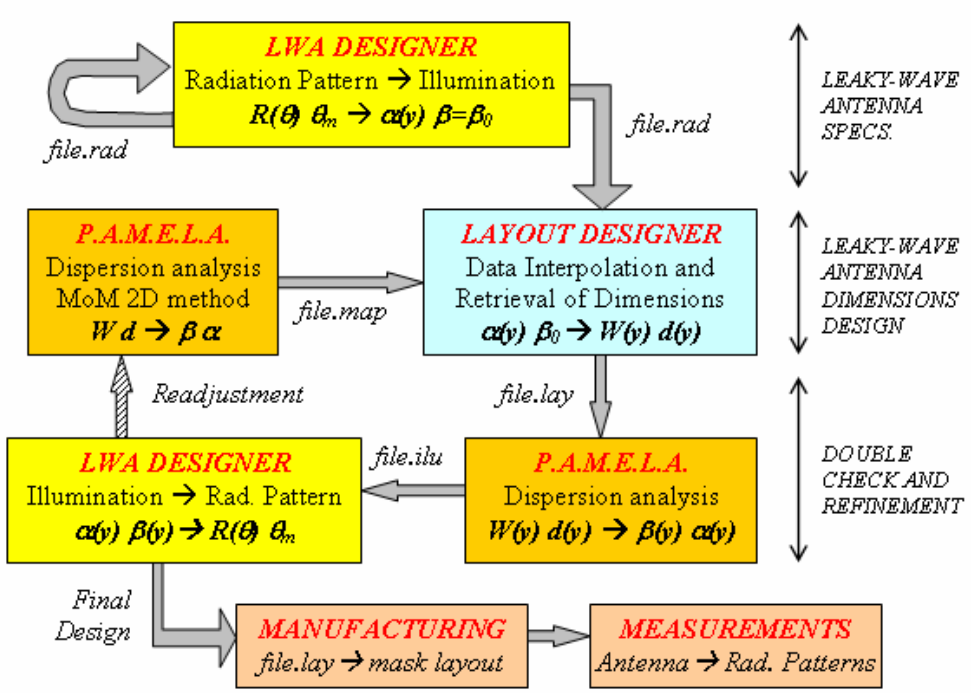

Figure 5.2.3.1 Semi-automated tapering process developed in [Gomez-Tornero July-2006].

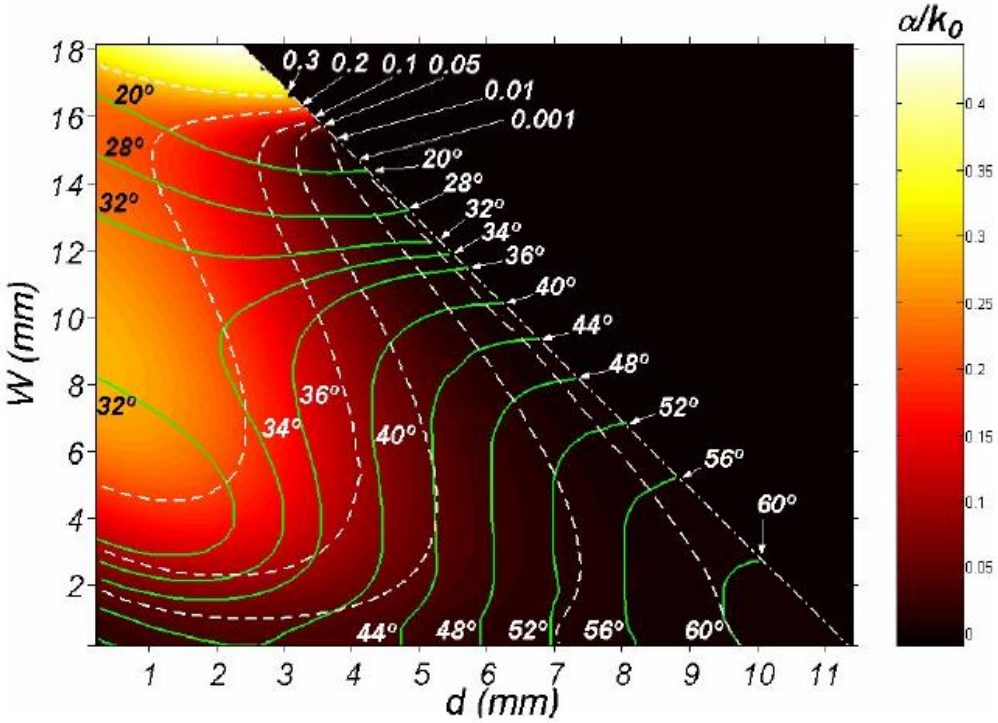

Figure 5.2.3.1 Example of contour plot for two parameters variation [Gomez-Tornero July-2006].

The same extension of the simulation software can be applied to WELAST, where the LWA Designer will have exactly the same functions, but the Layout Designer will require dealing with the combined variation of more than two geometrical parameters, since the main advantage of analyzing more complex cell elements is to obtain more grades of liberty. The full-wave analysis of the 2D cross section of the antenna to obtain the dispersion curves makes this method much faster than the analysis with commercial 3D electromagnetic software. In terms of optimization, where a large number of simulations are required to reach the goal, the proposed design process will provide a fast an accurate tool to obtain the final design in a fraction of the computational time commercial software will take.

5.2.4. Curved Surfaces Basis Functions.

The aim of this present thesis was to develop a new method of modal analysis of leaky wave antennas that could reduce a 3D problem into a 2.5D one, and that could deal with not only regular structures, as the precedent methods to date could, but with more complex geometries. Roof-tops functions are able to deal in an efficient way with the type of structures of interest in this present work: square loops, double square loops, split square loops and so on. These are basically rectangular geometries with rectangular kind of alteration.

Roof-tops functions require a uniformly meshed surface with rectangular cells to operate. This is an obvious limitation in the capabilities of this mesh, since electrically large metallizations with very complex shapes, small discontinuities or curvatures will need a huge amount of cells to include these irregular parts of the geometry, meaning the MoM matrix size will become unbearable. If, in a future, this software is required to handle circular shapes or very intricate designs, it should be optimized to fit these new geometries, avoiding the considerable increase of the computational cost. There could be two possible solutions:

- The modification of the method to make it able to deal with Roof-top basis functions which operate on a rectangular and triangular mixed grid, as described in [Chang 1992].

- Use Rao, Wilton and Glisson (RWG) basis functions, with a triangular mesh. This type of cells can model practically any arbitrary shaped structure, and its size may adapt to the geometrical variation, optimizing the total number of cells, and so the computational cost. These functions are well known and can be easily found in literature, see for instance [Rao 1982].

The first option would be a mix between the method developed in the present work and the use of the RWG functions. The author personally sees the second option as the logical next step for the future work in the evolution of the method.

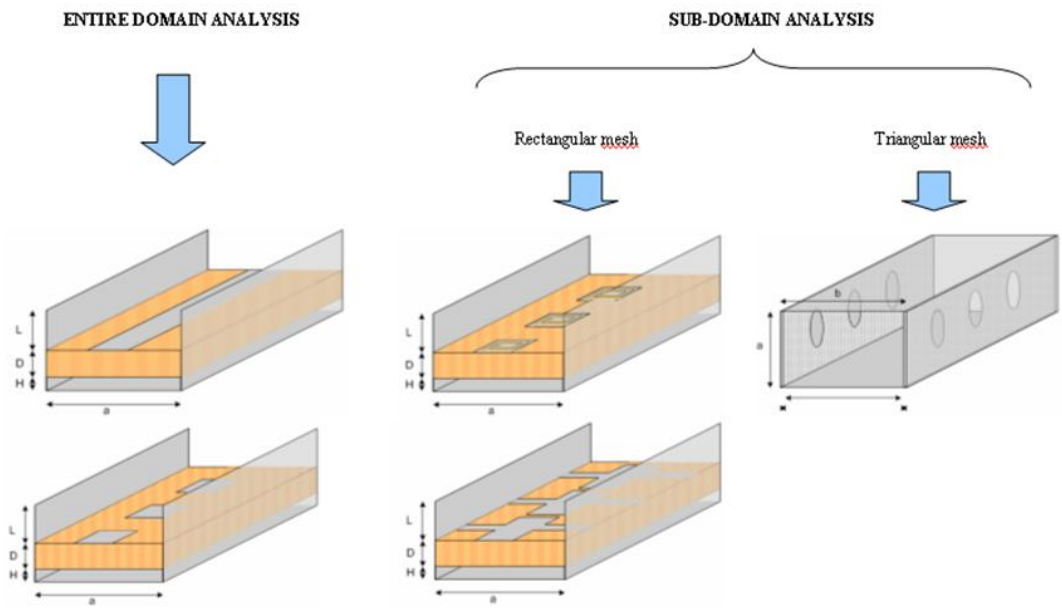

Figure 5.2.4.1 Correspondence between basis functions and analyzable structures.

5.2.5. Accurate Modelling of the Aperture

Traditionally, hybrid waveguide-planar LWAs have been employed to produce pure horizontally polarized radiation. It was desirable that only the main PPMode reached the aperture at the top of the lateral walls. But it is also possible to control the polarization properties of these antennas, in order to obtain vertical and even circular polarization, in a simple manner by controlling the radiation of the first higher order PPMode. In [Gomez-Tornero 2007] it is shown how by modifying the asymmetry of a 1D LWA and the height of the parallel plates, pure horizontal, pure vertical and also balanced horizontal-vertical (circular) polarization can be achieved. Said studies were carried out using commercial software on uniform leaky-wave antennas, with an enormous computational cost, since the whole structure had to be analyzed.

The method presented in Chapter 2 uses the Markuvitz Radiation Impedance [Markuvitz 1951-I] to model the aperture at the top of the LWA. This impedance is a valid approximation for the fundamental PPMode, with pure horizontal polarization. However, said approximation is less accurate when modelling the radiation of the higher order PPMode. In [Gomez-Tornero 2008] a specific TEN is developed, based on the works of Sanchez and Oliner (see same reference), to obtain accurate expressions for the radiation impedance of the evanescent first higher order parallel plate mode. These expressions could be added to WELAST code to allow, for the first time, a *rigorous and efficient analysis of circular polarization in periodic leaky wave antennas, with printed circuit of arbitrary shape*. The computational cost would be considerably reduced, since only the chosen unit cell would be meshed.

In any case, second and higher order PPModes, although never used, have not ever been modelled accurately. An extension of the analysis method to rigorously model the antenna aperture could be formulated. It is possible to model the antenna aperture using the equivalence principle, by expanding the equivalent magnetic currents at the top aperture. The original problem will be separated into two complementary ones, as seen in Figure 5.2.5.1, that must be solved and added to obtain an analytical expression for the rigorous **modal impedance radiation** of the aperture. It must be noted that for the second equivalent structure of the original problem, two conditions must be applied, the known EFIE on the metallization and a new MFIE to assure field continuity on the

aperture, which must be observed for both, the induced electric currents on the printed circuit and the induced magnetic currents in the aperture.

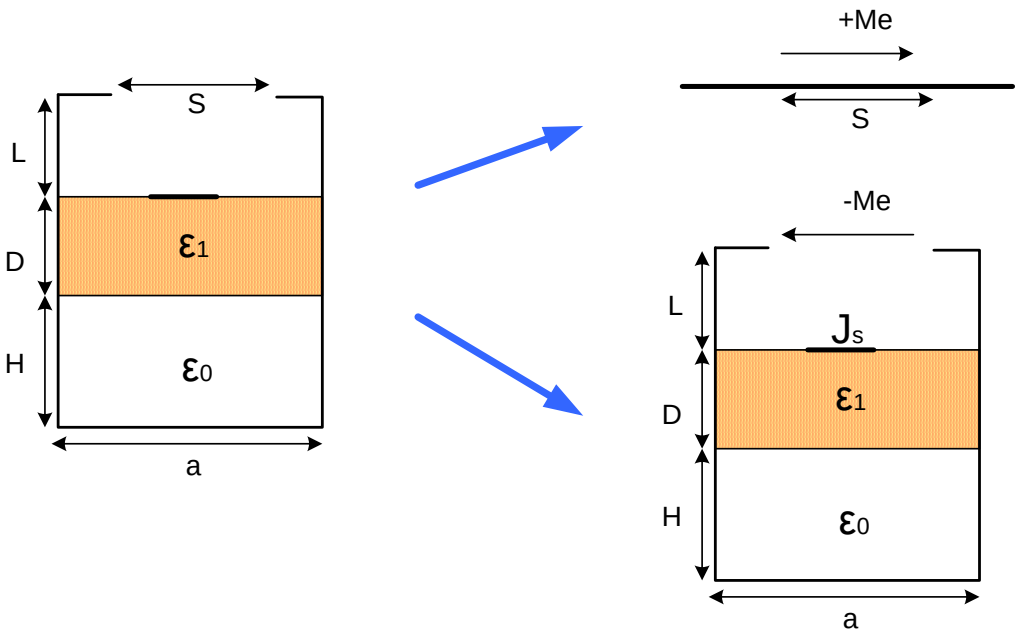

Figure 5.2.5.1 Equivalence theorem applied on the aperture.

This new extension of the code will yield:

- Perfectly accurate results (no approximation will be assumed).
- No limitations in the shape of the aperture S (so far the parallel plates must be completely open to free space). See Figure 5.2.5.2 for illustration.

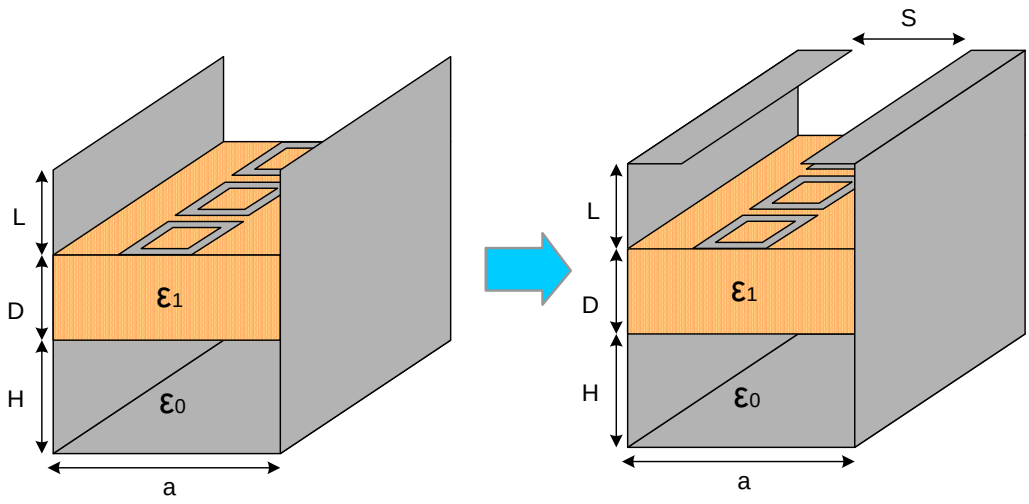

Figure 5.2.5.2 Evolution of Lateral Walls in PLWAs.

CONCLUSION

The following points are a resume of the main contributions of the present work:

- A **rigorous full-wave method** has been developed for the analysis of periodic leaky wave antennas laterally shielded and with planar metallization printed on dielectric substrate. The method is based on modal Floquet harmonics expansion along the propagation direction combined with Parallel-Plate modes expansion in the cross-section. A modal version of the Markuvitz Radiation Impedance has been used to model the top aperture. Method of moments was used to solve the EFIE applied on the printed circuit, and Green functions in combination with Subdomain basis functions were employed to model the fields and currents in the structure. It is the first time a method of these characteristics is **able to analyze arbitrary shaped unit cell geometries.**

- A **complete study of the Roof-tops basis functions** has been carried out. The previously assumed behaviour of Relative Convergence for this kind of modal analysis has been checked and discarded, contrary to the precursors of this method. Also, a comparison between the results obtained with Entire Domain functions and Roof-top functions is presented.

- The **accuracy of the method** is validated through comparison with previously coded methods found in the literature and 3D commercial simulation software (HFSS). The analytical nature of the method and the 2D cross-section analysis provides **superior performances in terms of speed** compared to the later.

- A **novel simulation software, WELAST**, doted with an intuitive graphical interface has been developed. It is not only fast and versatile, but its interactive nature, and the wide range of results that it provides, make it easy to understand the propagation and radiation concepts that take place in the LWA. Its educational potential is an added value to its original analysis and design purpose.

- **Two different coding philosophies** have been presented and compared, using a combination of meshing strategies and matricial coding approach. It was found

that computing times could be significantly reduced depending on the chosen approach, even when the number of unknowns to calculate was larger. WELAST allows the user to take advantage of this discovery.

- A **new PLWA** based on printed metallic square loop is analyzed using the novel method. It is also used to show the capabilities of the simulation tool. The parallel-plate expansion allows modelling the effects that higher order modes may have on propagation and radiation, even when multi-harmonic radiation occurs. This way, induced currents, fields, harmonics interferences, bandgaps, modal contribution to both propagation and radiation and cross polarization effects on this novel leaky-wave antenna are studied. Also, a **resonance analysis** based on the effects that the variation of certain geometrical parameters have on the bandgaps of the structure has been carried out for the first time in this type of antennas. The interpretation of said results has given a full understanding of the inside workings of the periodic leaky-wave antenna.

- Finally, the following steps in the study of PLWA and the extension of the developed simulation tool have been proposed and oriented.

The present work means the closure of the first step (and most of the times the most difficult to take), in the open field of study of periodic and/ or metamaterial leaky-wave antennas. It represents the first milestone required to start the analysis and understanding of new behaviours in periodic structures and efficient design of novel PLWAs. The birth of WELAST is just the beginning.

ACRONYMS/ ABREVIATIONS

AIS	Artificial Impedance Surfaces
CAD	Computer Aided Design
CGM	Conjugate Gradient Method
CRLH	Composite Right/Left Handed
EBG	Electromagnetic Band Gap
ED	Entire Domain
EFIE	Electric Field Integral Equation
FDTD	Finite Difference Time Domain
FSS	Frequency Selective Surfaces
GUI	Graphical User Interface
HIS	High Impedance Surfaces
LHM	Left Handed Materials
LWA	Leaky-Wave Antenna
MFIE	Magnetic Field Integral Equation
MoM	Method of Moments
MTM	Metamaterials
NRI	Negative Refractive Index
PBG	Photonic Band Gap
PEC	Perfect Electric Conductor
PLWA	Periodic Leaky-Wave Antenna
PMC	Perfect Magnetic Conductor
PPW	Parallel Plate Waveguide
PRS	Partially Reflective Surfaces
RHM	Right Handed Materials
RWG	Rao-Wilton-Glisson
SD	Sub-Domain
TEN	Transverse Equivalent Method
TL	Transmission Line
WG	Waveguide

REFERENCES

From A to E

[Balanis 1982] C.A. Balanis, *Antenna Theory*, Singapore, John Wiley & Sons, 1982.

[Balanis 2008] C.A. Balanis, *Modern Antenna Handbook*, Canada, John Wiley & Sons, 2008.

[Becks 1992] T. Becks and I. Wolff, "Analysis of 3-D metallization structures by a full-wave spectral domain technique", *IEEE Trans. Microwave Theory Tech.*, Vol. 40, No.12, pp. 2219-2227, Dec. 1992.

[Bozzi 2005] M. Bozzi, S. Germani, L. Minelli, L. Perregrini and P. De Maagt, "Efficient calculation of the Dispersion Diagram of Planar Electromagnetic Band-Gap Structures by the MoM/BI-RME Method", *IEEE Trans. Antennas Propag.*, vol. 53, no. 1, pp. 29–35, Jan. 2005.

[Brillouin 1946] L.Brillouin, *Wave Propagation in Periodic Structures: Electric Filters and Crystal Lattices,* Ed. McGraw-Hill, New York, 1946.

[Brillouin 1960] L.Brillouin, *Wave Propagation and Group Velocity, Ed. Academic Press,* New York, 1960.

[Caiazzo 2004] M. Caiazzo, S. Maci and N. Engheta, "A metamaterial surface for compact cavity resonators", *IEEE Antennas Wireless Prop. Lett..*, vol. 3, pp.261–264, 2004.

[Caloz 2001] C. Caloz, C.-C. Chang and T. Itoh, "Full wave verification of the Fundamental Properties of Left-Handed Materials in Waveguide Configurations", J. *App. Phys.*. Vol.90, N0. 11, pp5483-5486, December 2001.

[Caloz 2005] C. Caloz and T. Itoh, "Metamaterials for high frequency electronics", *Proceeding IEEE*, vol.93, no.10, pp.1744-1752, Oct.2005.

[Caloz 2006] C. Caloz and T. Itoh, *Electromagnetic Metamaterials: Transmission Line Theory and Microwave Applications*, John Wiley & Sons, New Jersey, 2006.

[Caloz 2008] C. Caloz, T. Itoh and A. Rennings, "CRLH Metamaterial Leaky-wave and Resonant Antennas", *IEEE Antennas and Propag. Magazine*, vol. 50, no. 5, pp. 25-39, Oct. 2008

[Chan 1990] C. H. Chan and R. Mittra, "On the analysis of Frequency-Selective Surfaces using subdomain basis functions", *IEEE Trans. Antennas Propag.*, vol. 38, no. 1, pp. 40–50, Jan. 1990.

[Chang 1992] D. C. Chang and J. X. Zheng, "Electromagnetic Modelling of Passive Circuits Elements in MMIC", *IEEE Trans. Microwave Theory Tech.*, Vol. 40, No.9, pp. 1741-1747, Sept. 1992.

[Chantalat 2008] R. Chantalat, C. Menudier, M. Thevenot, T. Monediere, E. Arnaud and P. Dumon, "Enhanced EBG resonator antenna as feed of a reflector antenna in the Ka band", *IEEE Antennas Wireless Propag.Letters*, vol.7, pp.349-353, 2008.

[Chen 1970] C.C. Chen, 'Scattering by a two-dimensional periodic array of conducting plates', *IEEE Trans. Antennas Propag.*, vol.18, no.5, pp.660-665, 1970.

[Cheng 1989] D. K. Cheng, *Field and Wave Electromagnetics*, Ed. Addison Wesley, 2nd ed., 1989

[Cheng 1997] D. K. Cheng, *Fundamentos de Electromagnetismo para Ingeniería*, Ed. Addison Wesley- Longman, 1997

[Collin 1960] R.E. Collin, *Field Theory of Guided Waves*, McGraw-Hill, New York, 1960

[Collins 1969] R.E. Collins and F.J. Zucker, *Antenna Theory*, part 2, McGraw-Hill, New York, 1969, ch. 19-20

[Cwik 1987] T. A. Cwik and R. Mittra, "Scattering from a Periodic Array of Free-Standing Arbitrarily Shaped Perfectly Conducting or Resistive Patches", *IEEE Trans. Antennas Propag.*, vol.AP-35, no.11, pp.1226-1234, 1987.

[Diblanc 2005] M. Diblanc, E. Rodes, A, Arnaud, M. Thevenot, T. Monediere and B. Jecko, "Circularly polarized metallic EBG antenna", *IEEE Microw. Wireless Comp. Letters*, vol.15, no.10, pp.638-640, Oct. 2005.

[Eleftheriades 2002] G. V. Eleftheriades, A. K. Iyer and P.C. Kremer, "Planar Negative Refractive Index Media using Periodically L-C Loaded Transmision Lines", IEEE, *Trans. Microwave Theory Tech*. Vol. 50, pp.2702-2712, 2002

[Eleftheriades 2003] G.V. Eleftheriades, O. Siddiqui and A.K. Iyer, "Transmission line models for negative refractive index media and associated implementation without excess resonators", *IEEE Microw. Wireless Comp. Lett.*, vol.13, no.2, pp.51-53, Feb.2003.

[Eleftheriades 2005] G.V. Eleftheriades and K.G. Balmain, *Negative -Refraction Meramaterials: Fundamental Principles and Applications*, John Wiley & Sons, New Jersey, 2005.

[Eleftheriades 2007] G.V. Eleftheriades, "Enabling RF/microwave devices using negative-refractive-index transmission line (NRI-TL) metamaterials", *IEEE Antennas Propag..*, vol.49, no.2, pp.34-51, Apr.2007.

[Encinar 1990] J. A. Encinar, "Mode-matching and point-matching techniques applied to the analysis of metal-strip-loaded dielectric antennas," *IEEE Trans. Antennas Propag.*, vol. 38, no. 9, pp. 1405–1412, Sep. 1990.

From F to K

[Feresidis 2001] A.P. Feresidis and J.C. Vardaxoglou, "High gain planar antenna using optimized partially reflective surfaces", *IEEE Proc. Microw. Antennas Propag.*, vol.148, no.6, Feb. 2001.

[Feresidis 2005] A.P. Feresidis, G.Goussetis, S. Wang and J.C. Vardaxoglou, "Artificial magnetic conductor sufaces and their application to low-profile high gain antennas", *IEEE Trans. Antennas Propag.*, vol.53, no.1, pp.209-215, Jan. 2005.

[Frezza 1989] F. Frezza, M. Guglielmi and P. Lampariello, "Complex guidance properties of the slitted asymmetric ridge waveguide", 1989 IEEE MIT-S Int. Microwave Symp. Dig, pp. 977-930, 1989.

[Garcia-Vigueras 2010] M. Garcia-Vigueras, J.L. Gomez-Tornero, G. Goussetis, J.S. Gomez-Diaz and A.A. Melcon, "A modified pole-zero technique for the synthesis of waveguide leaky-wave antettas loaded with dipole-based FSS", *IEEE Trans. Antennas Propagat.*, Vol.58, No.6, pp. 1971-1980, Jun. 2010.

[García-Vigueras 2011] M. Garcia-Vigueras, J.L. Gomez-Tornero, G. Goussetis, A.R. Weily and Y.J. Guo, "Enhancing frequency-scanning response of leaky-wave antennas using high-impedances surfaces", *IEEE Antennas and Wireless Propagation Lett.*, Vol.10, pp.7-11, 2011.

[Ghomi 1989] M. Ghomi and H. Baudrand, "Full-wave analysis of microstrip leakywave antenna," *Elect. Lett.*, vol. 25, no. 13, pp. 870–871, Jun. 1989.

[Glisson 1980] A.W. Glisson and D.R. Wilton, "Simple and Efficient Numerical Methods for Problems of Electromagnetic Radiation and Scattering from Surfaces", *IEEE Trans. Antennas Propagat.*, Vol. AP-28, No.5, pp. 593-603, Sept.. 1980.

[Gómez 1994] J.L. Gómez and A.A. Melcón, "Radiation Analysis in the Space Domain of Laterally-Shielded Planar Transmission Lines Structures", 1994 IEEE MTT-S Int. Microwave Symp. Dig, vol. 2, pp.1033-1036, 1994.

[Gómez April-2003] J.L. Gómez and A.A. Melcón, "Leaky and Surface Waves In Multilayered Laterally-Shielded Microstrip Transmission Lines", *Microwave and Optical Technology Letters*, Vol. 37, Nº 2, pp. 88-93, April 2003.

[Gómez March-2004] J.L. Gómez and A.A. Melcón, "Non-Orthogonality Relations between Complex-Hybrid-Modes: an Application for the Leaky-Wave Analysis of Laterally-Shielded Top-Open Planar Transmission Lines", *IEEE Trans. Microwave Theory Tech.*, Vol. 52, No.3, pp. 760-767, March 2004.

[Gómez June-2004I] J.L. Gómez and A.A. Melcón, "Radiation Analysis in the Space Domain of Laterally-Shielded Planar Transmission Lines. Part I: Theory", *Radio Science*, Vol.39, RS3005 pp.1-11, June 2004.

[Gómez June-2004II] J.L. Gómez and A.A. Melcón, "Radiation Analysis in the Space Domain of Laterally-Shielded Planar Transmission Lines. Part II: Applications", *Radio Science*, Vol.39, RS3006 pp.1-10, June 2004.

[Gómez Jan-2005] J.L. Gómez, F.D. Quesada and A.A. Melcón, "A Full-Wave Space-Domain Method for the Analysis of Leaky-Wave modes in Multilayered Planar Open Parallel-Plate Waveguides", *International Journal of RF and Microwave Computer-Aided Engineering*, Vol.15, No.1, pp.128-139, January 2005.

[Gómez April-2005] J.L. Gómez, F.D. Quesada and A.A Melcón, "Application of the High-Gain Substrate-Superstrate Configuration to Dielectric Leaky-Wave Antennas", *IEEE Microwave and Wireless Components Lett.*, Vol.15, No.4, pp. 250-252, April 2005.

[Gómez August-2005I] J.L. Gómez , A. de la Torre, D. Cañete, M. Gugliemi and A.A. Melcón, "Design of Tapered Leaky-Wave Antennas in Hybrid Waveguide-Planar Technology for Millimeter Waveband Applications", *IEEE Trans. Antennas Propagat.: Special Issue on Antennas Propag. Applicat.* pt.I, Vol.53, No.8, pp.2563-2577, August 2005.

[Gómez August-2005II] J. L. Gómez, D. Cañete and A. Álvarez-Melcón, "Printed-Circuit Leaky-Wave Antenna with Pointing and Illumination Flexibility", *IEEE Microwave and Wireless Components Lett.*,Vol.15, No.8, pp.536-538, August 2005.

[Gómez August-2005III] J. L. Gómez, J. Pascual and A. Álvarez-Melcón, "A Novel Leaky-Wave Antenna Combining an Image NRD Guide and a Strip Circuit", *IEEE Antennas and Wireless Propagation Lett.*, Vol.4, pp.289-292, August 2005.

[Gómez September-2005] J.L. Gómez, F.D. Quesada and A.A. Melcón, "Analysis and Design of Periodic Leaky-Wave Antennas for the Millimeter Waveband in Hybrid Waveguide-Planar Technology", *IEEE Trans. Antennas Propagat.*, Vol.53, No.9, pp. 2834-2842, September 2005.

[Gómez March-2006] J. L. Gómez, J. Pascual and A. Álvarez-Melcón, "Efficient Full-Wave Analysis Method of Leaky-Wave Modes in Periodically Loaded Dielectric Waveguides with Application to Backward-to-Forward Frequency-Scannable Antennas and Metamaterials", *Int. Journal of Numerical Modelling: Special Issue on Numerical*

Modelling of Metamaterial Properties, Structures and Devices., Vol.19, No.2, pp.173-193, March 2006.

[Gómez-Tornero July-2006] J.L. Gómez, J. Pascual and A.A. Melcón, "A Novel Full-Wave CAD for the Design of Tapered Leaky-Wave Antennas in Hybrid Waveguide Printed-Circuit Technology", *Int. Journal of RF and Microwave Computer Aided Engineering*, Vol.16, No.4, pp.297-308, July 2006.

[Gómez Aug-2006] J.L. Gómez, D. Cañete and A.A. Melcón, "P.A.M.E.L.A: A Useful Tool for the Study of Leaky-Wave Modes in Strip-Loaded Open Dielectric Waveguide", IEEE *Antennas and Propagat.* Vol.48, No.4, pp.54-72, Aug. 2006.

[Gomez-Tornero 2007] J.L. Gómez, G. Goussetis and A.A. Melcón, "Simple control of the polarisation in uniform hybrid waveguide-planar leaky-wave antennas", *IET Microw. Antennas Propag.* Vol.1, No.4, pp.911-917, Aug. 2007.

[Gomez-Tornero 2008] J.L. Gómez, F.D. Quesada and A.A. Melcón, "Novel microwave network for the leaky-wave analysis of evanescent fields in stub-loaded structures", *IEEE Trans. Microw. Theory Tech.*. Vol.56, No.6, pp.1405-1412, Jun. 2008.

[G. Tornero 2005] Jose Luis Gomez Tornero, "Analisis de modos de fuga en estructuras planares apantalladas lateraltmente y diseño de nuevas antenas leaky-wave en tecnologia hibrida impresa-apantallada", PhD. University of Cartagena, Abril 2005.

[Godara 2002] L.C. Godara, *Handbook of antennas in wireless communications*, CRC Press, 2002

[Goldstone 1959] L.O. Goldstone and A.A. Oliner, "Leaky Wave Antennas I: Rectangular Waveguides", *IEEE Trans. Antenna Propag*., no. 7, pp. 307-319, 1959.

[Gonzalo 1999] R.Gonzalo, P. deMaagt and M. Sorolla, 'Enhanced patch-antenna performance by suppressing surface waves using photonic-bandgap substrates', *IEEE Trans. Microwave Theory Techn.*, vol.47, No. 11, pp. 2131-2138, Nov. 1999.

[Goussetis 2006] G. Goussetis, A.P. Feresidis and J.C. Vardaxoglou, "Tailoring the AMC and EBG characteristics of periodic metallic arrays printed on grounded dielectric substrate", *IEEE Trans. Antennas Propag.*, vol. 54, no. 1, pp. 82–89, Jan. 2006.

[Goussetis 2007] G. Goussetis, "Dispersion characteristics of a perturbed EBG waveguide with periodic resonant loads", Loughborough Antennas and Propagation Conference, Loughborough, UK, April 2007.

[Grbic 2002-I] A. Grbic and C.V. Eleftheriades, "A backward-wave antenna based on negative refractive index LC networks", *IEEE Proc. Antennas Propag. In. Symp. Dig*., vol.4, pp.340-343, Jun. 2002.

[Grbic 2002-II] A. Grbic and C.V. Eleftheriades, "Experimental verificiation of backward-wave radiation from negative refractive index metamaterial", *J. Appl. Phys.*, vol.92, no.10 pp.5930-5935, Nov. 2002.

[Guerin 2006] N. Guerin, S. Enoch, G. Tayeb, P. Sabouroux, P. Vincent and H. Legay, "A metallic Fabry-Perot directive Antenna", *IEEE Trans. Antennas Propag.*, vol. 54, no. 1, pp. 220–224, Jan. 2006.

[Guglielmi 1989] M. Guglielmi and H. Hochstadt, "Multimode network description of a planar periodic metal-strip grating at a dielectric interface: Part III—Rigorous solution," *IEEE Trans. Microwav. Theory Tech.*, vol. 37, no. 5, pp. 902–909, May 1989.

[Guglielmi 1991] M. Guglielmi and G. Boccalone, "A novel theory for dielectric-inset waveguide leaky-wave antennas," *IEEE Trans. Antennas Propag.*, vol. 39, no. 4, pp. 497–504, Apr. 1991.

[Guo 2005] Y. Guo, G. Goussetis, A.P. Feresidis and J.C. Vardaxoglou, "Efficient modeling of novel uniplanar left-handed metamaterials", *IEEE Trans. Microw. Theory Tech.*, vol. 53, no. 4, pp. 1462–1468, Apr. 2005.

[Hansen 1940] W. W. Hansen, "Radiating Electromagnetic Waveguide", U.S. Patent No. 2.402.622, 1940.

[Iriarte 2009] J.C. Iriarte, I. Ederra, R. Gonzalo, Y. Brand, A. Fourmault, Y. Demers, L. Salgetti and P. DeMaagt, "EBG superstrate array configuration for the WAAS space segment", *IEEE Trans. Antennas Propag.*, vol. 57, no. 1, pp. 81–93, Jan. 2009.

[Jackson 1985] D.R. Jackson and N.G. Alexopoulos, "Gain enhancement methods for printed circuits", *IEEE Trans. Antennas Propag.*, vol. 33, no. 9, pp. 976–987, Sep. 1985.

[Jackson 1993] D.R. Jackson and A.A. Oliner, "Leaky-wave propagation and radiation for a narrow beam multiple layer dielectric structure", *IEEE Trans. Antennas Propag.*, vol. 41, no. 3, pp. 344–348, Mar. 1993.

[Jacobsen 1970] J. Jacobsen, "Analytical, numerical and experimental investigation of guidedwaves on a periodically strip-loaded dielectric Slab," *IEEE Trans. Antennas Propag.*, vol. AP-18, no. 3, pp. 379–387, May 1970.

[Johnson 1993] R.C. Johnson, *Antenna Engineering Handbook*, 3rd Ed., McGraw-Hill, New York, 1993.

[Kalhor 1988] H. A. Kalhor, "Electromagnetic scattering by a dielectric slab loaded with a periodic array of strips over a ground plane," *IEEE Trans. Antennas Propag.*, vol. 36, no. 1, pp. 147–151, Jan. 1988.

[Kanso 2009] A. Kanso, R. Chantalat, M. Thevenot, T. Monediere and B. Becko, "Dual band dielectric EBG resonator antenna", 3rd European Conference on Antennas and Propagation, EuCAP 2009, 23-27 March, pp. 3240-3243.

[Kelly 2008] J. R. Kelly, T. Kokkinos and A. Feresidis, "Análysis and Design of Sub-Wavelength Resonant Cavity Type 2-D Leaky Wave Antennas", *IEEE Trans. Antennas Propag.*, vol.56, no. 9, pp. 2817-2825, Sept.. 2008.

[Kosmas 2007] P. Kosmas, A.P. Feresidis and G. Goussetis, "Periodic FDTD analysis of a 2D lealy-wave planar antenna based on dipole frequency selective surfaces", *IEEE Trans. Antennas Propag.*, vol.55, no. 7, pp. 2006–2012, Jul. 2007.

From L to Q

[Lampariello 1985] P. Lampariello and A.A. Oliner, "A new leaky-wave antenna for millimeter waves using an asymmetric strip in groove guide. Part I: Theory", *IEEE Trans. Antennas Propagat.,* vol. 33, pp. 1285-1294, 1985

[Lampariello 1998] P. Lampariello, F. Frezza, H. Shigesawa, M. Tsuji and A.A. Oliner, "A versatile Leaky-Wave Antenna based on Stub-loaded Rectangular Waveguide. Part I: Theory", *IEEE Trans. Antennas Propagat*., vol. 46, no.7, pp1032-1040, July 1998.

[Lampariello 1987] P. Lampariello and A.A. Oliner, "A novel phase array of printed-circuit leaky wave lines sources", Proceedings of 17th European Microwave Conference, Rome, pp. 555-560, 1987

[Lampariello 1990] P. Lampariello, F. Frezza and A.A. Oliner, "The transition region between bound-wave and leakwave ranges for partially dielectric-loaded open guiding structure", *IEEE Trans. Microwave Tech.*, vol. 38, no. 12, pp.1831- 1836, december 1990.

[Langley 1993] R.J. Langley, "A dual frequency band waveguide using FSS", *IEEE Microw. Guided Wave. Lett*., vol.3, no.1, pp.9-10, Jan.1993.

[Lee 1982] S.W. Lee, G. Zarrillo and C.L. Law, 'Simple formulas for transmission through periodic metal grids or plates', *IEEE Trans. Antennas Propag.,* vol.30, no.5, pp.904-909, Sept. 1982.

[Lee 2005] Y.J. Lee, J. Yeo, R. Mittra and W.S. Park, "Application of electromagnetic bandgap (EBG) superstrates with controllable defects for a class of patch antennas as spatial angular filters", *IEEE Trans. Antennas Propag.,* vol.53, no.1, pp.224-235, Jan. 2005.

[Lee 2007] D.H. Lee, Y.J. Lee, J. Yeo, R. Mittra and W.S. Park, "Design of novel thin frequency selective surface superstrates for dual-band directivity enhancement", *IET Microw. Antennas Propag.*, vol.1, no.1, pp.248-254, 2007.

[Lim 2004-I] S. Lim, C. Caloz and T. Itoh, "Electronically scanned composite right/left handed microstrip leaky-wave antenna", *IEEE Microw. Wireless Comp. Lett*., vol.14, no.6, pp.277-279, Jun.2004.

[Lim 2004-II] S. Lim, C. Caloz and T. Itoh, "Metamaterial-based electronically controlled transmission line structure as a novel leaky-wave antenna with tunable radiation angle and beamwidth", *IEEE Trans. Microwave Theory Tech.*, vol.52, no.12, pp.2678-2690, Dec.2004.

[Liu 2002] L. Liu, C. Caloz and T. Itoh, "Dominant mode (DM) leaky-wave antenna with backfire to endfire scanning capability", *Electron. Lett.*, vol.38, no.23, pp.1414-1416, Nov.2002.

[Liu 2007] C. Liu and W. Menzel, "Frequency-scanned leaky wave antenna from negative refractive index transmission lines", *European Conference Antennas Propag*. EuCAP 2007.

[Lubkowski 2007] G. Lubkowski, C. Damm, B. Bandlow, R. Schuhmann, M. Shussler and T. Weiland, "Broadband transmission below the cutoff frequency of a waveguide loaded with resonant scatterer arrays", *IET Microw. Antennas Propag*., vol.1, no.1, pp.165-169, 2007.

[Luukkonen 2008] O. Luukkonen, C. Simovski, G. Granet, G. Goussetis, D. Lioubtchenko, A.V. Räisänen and S.A. Tretyakov, "Simple and accurate analytical model of planar grids and high-impedance surfaces comprising metal strips or patches", *IEEE Trans. Antennas Propag.*, vol.56, no.6, pp.1624-1632, June. 2008.

[Ma 1994] Z. Ma and E. Yamashita, "Space Wave Leakage from higher order modes on various planar transmission lines structures", IEEE MIT-S Int. Microwave Symp. Dig,. Vol. 2, pp. 1033- 1036, 1994

[Maci 2005] S. Maci, M. Caiazzo, A. Cucini and M. Casaletti, "A pole-zero matching method for EBG surfaces composed of a diple FSS printed on a grounded dielectric slab", *IEEE Trans. Antennas Propag.*, vol.53, no.1, pp.70-81, Jan. 2005.

[Marconi 1919] G. Marconi and C.S. Franklin, 'Reflector for use in wireless telegraphy and telephony', US patent 1301473, April 1919.

[Markuvitz 1951-I] N. Markuvitz, *Waveguide Handbook*, MIT Radiation Laboratory Series Vol. 10, New York, McGraw Hill, 1951.

[Markuvitz 1951-II]Markuvitz, N. and J. Schwinger, "On the Representation of Electric and Magnetic Fields Produced by Currents and Discontinuities in Waveguides", J. *App. Phys*.. Vol.22, pp.806-829, June 1951.

[Mateo 2011] C. Mateo-Segura, G. Goussetis and A.P. Feresidis, 'Sub-wavelength profile 2-D leaky-wave antennas with two periodic layers', *IEEE Trans. Antennas Propag.*, vol.59, no.2, pp.416-424, Feb. 2011.

[Milligan 2005] T. A. Milligan, '*Modern Antenna Design*', 2nd Ed., John Wiley & Sons, New Jersey, 2005.

[Mittra 1963] R. Mittra, "Relative Convergence of the solution of a doubly infinite set of equations", J. Nat. Bur. Stand., 67D, 245-254, Mar.-Apr. 1963

[Mittra 1972] R. Mittra, T. Itoh and Ti-Shu Li, "Analytical and numerical studies of the relative convergence phenomenon arising in the solution of an Integral Equation by the Moment Method", *IEEE Trans. Microwave Theory Techn*., vol.20, no.2, pp. 96-1044, Feb. 1972

[Mittra 1981] M. Mittra and R. Kastner, “A Spectral domain approach for computing the radiation characteristics of a leaky-wave antenna for millimeter waves,” *IEEE Trans. Antennas Propag.*, vol. AP-29, no. 4, pp. 652–654, Jul. 1981.

[Mittra 1988] R. Mittra, C.H. Chan and T. Cwik, “Techniques for analyzing frequency selective surfaces – A review”, *Proceedings of the IEEE*, vol. 76, no. 12, pp. 1593-1615, Dec. 1988.

[Mittra 1990] K. J. Webb, P. W. Grounds and R. Mittra, “Convergence in the spectral domain formulation of waveguide and scattering problems”, *IEEE Trans. Antennas Propag.*, vol. 38, no. 6, pp. 869–877, June 1990.

[Montgomery 1975] J. P. Montgomery, "Scattering by an Infinite Periodic Array of Thin Conductors on a Dielectric Sheet", *IEEE Trans. Antennas Propag.*, vol. AP-23, no. 1, pp. 70-75, Jan. 1975.

[Montgomery 1978] J. P. Montgomery, "Scattering by an Infinite Periodic Array of Microstrip Elements", *IEEE Trans. Antennas Propag.*, vol. AP-26, no. 6, pp. 850-854, Nov. 1978.

[Moustafa 2009] L. Moustafa, M. Thevenot, T. Monediere and B. Jecko, “Design method of EBG material with wide defect band”, EuCap2009, European Conference on Antennas and Propagation, pp. 3235-3239, 2009.

[Munk 2000] B. A. Munk, *Frecuency Selective Surfaces: Theory and Desing*, Ed. John Wiley & Sons, Inc., 2000.

[Nallo 1997] C. Di Nallo, F. Frezza, A. Galli and P. Lampariello, “Theoretical and experimental invertigations on the ´stepped´ leaky wave antennas”, Antennas Propagat. Society Int. Symp. Dig., vol 2, pp. 1446- 1449, 1997

[Neto 2007] A. Neto, N. Llombart, G. Gerini, M. Bonnedal and P. deMaagt, “EBG enhanced feeds for the improvement of the aperture efficiency of reflector antennas”, *IEEE Trans. Antennas Propag.*, vol. 55, no. 8, pp. 2185–2193, Aug. 2007.

[Oliner 1987] A.A. Oliner, “Leakage from higher modes on microstrip line with applicarions to antennas”, Radio Sci., Vol. 22, no. 6, pp. 907-912, November 1987.

[Oliner 1993] A.A. Oliner and R.C. Johnson, *Leaky-Wave Antennas, Antenna Engineering Handbook*, 3rd ed., McGraw-Hill, New York, 1993, ch.3.

[Oses 2009] A. Oses, J.C. Iriarte, I. Ederra, R. Gonzalo and P. de Maagt, “Multiband EBG navigation Antenna”, iWAT 2009, *IEEE International Workshop on Antenna Technology*, 2009.

[Park 1998] S.O. Park, C.A. Balanis and C.R. Birtcher, " Analytical Evaluation of the Asymptotic Impedance Matrix of a Grounded Dielectric Slab with Roof-Top Functions", *IEEE Trans. Antennas Propag.*, vol. 46, no. 2, pp. 251–259, Feb. 1998.

[Pearson 1985] L.W. Pearson, " A Technique for Organaizing Large Moment Calculations for Use with Iterative Solution Methods", *IEEE Trans. Antennas Propag.*, vol. AP-33, no. 9, pp. 1031–1033, Sept. 1985.

[Peng 1981-I] S.T. Peng and A.A. Oliner, 'Guidance and leakage properties of a class of open dielectric waveguides: Part I- Mathematical formulations', *IEEE Trans. Microwave Theory Techn.*, vol.29, (special issue on open guided wave structures), pp. 843-855, Sep. 1981.

[Peng 1981-II] S.T. Peng and A.A. Oliner, 'Guidance and leakage properties of a class of open dielectric waveguides: Part I- New physical effects', *IEEE Trans. Microwave Theory Techn.*, vol.29, (special issue on open guided wave structures), pp. 855-869, Sep. 1981.

From R to Z

[Rao 1982] S. M. Rao, A. W. Glisson and D.R. Wilton, "Electromagnetic scattering by surfaces of arbitrary shape", *IEEE Trans. Antennas Propag.*, vol. AP-30, no. 3, pp. 409–418, May 1982.

[Rozzi 1987] T. Rozzi and L. Ma, "Scattering by dipoles in inset dielectric guide and application to millimetric leaky wave antennas," in *Proc. 17th Eur. Microwave Conf.*, Rome, Italy, Sep. 1987, pp. 543–548.

[Rubin 1983] B.J. Rubin and H.L. Bertoni, "Reflection from a Periodically Perforated Plane Using a Subsectional Current Approximation", ", *IEEE Trans. Antennas Propag.*, vol. AP-31, no. 6, pp. 829–835, Nov. 1983.

[Sanada 2004] A. Sanada, C. Caloz and T. Itoh, "Characteristics of the composite right/left handed transmission lines", *IEEE Microw. Wireless Comp. Lett*., vol.14, no.2, pp.68-70, Feb.2004.

[Sauleau 1999] R. Sauleau, Ph. Coquet, J.P. Daniel, T. Matsui and N. Hirose, "Analysis of millimetre-wave Fabry-Perot cavities using the FDTD technique", *IEEE Microwave Guided Wave Letters*, vol.9, no.5, pp.189- 191, May 1999.

[Schwering 1983] F. Schwering and S. T. Peng, "Design of dielectric grating antennas for millimeter-wave applications", *IEEE Trans. Microwave Theory Tech.*, vol.31,1983, pp. 199–209.

[Shigesawa 1986] H. Shigesawa, M. Tsuji and A.A. Oliner, "Effects of air gap and finite metal plate width on NRD guide", IEEE MIT-S Int. Microwave Symp. Dig, pp 119-122, Baltimore, June 1986

[Shigesawa 1994] H. Shigesawa, P. Lampariello, F. Frezza, M. Tsuji and A.A. Oliner, "Coupling between different leaky-mode types in stub-loaded leaky waveguides", *IEEE Trans. Microwave Tech.*, vol. 42, pp.1548- 1560, August 1994.

[Smith 2000] D. R. Smith, W. J. Padilla, D. C. Vier, S. C. Nemat-Nasser, and S. Schultz, "Composite medium with simultaneously negative permeability and permittivity," *Phys. Rev. Lett.*, vol. 84, no. 18, pp. 4184–4187, May 2000.

[Sievenpiper 1999] D. Sievenpiper, Z. Lijun, R.F. Broas, N.G. Alexopoulos and E. Yablonovitch, 'High impedance electromagnetic surfaces with a forbidden frequency band', *IEEE Trans. Microwave Theory Techn.*, vol.47, No. 11, pp. 2059-2074, Nov. 1999.

[Tamir 1963-I] T. Tamir and A. A. Oliner, "Guided Complex Waves, Part I: Fields at an Interface", *Proc. Inst. Elec. Eng.*, Vol. 110, pp. 310-324, Feb. 1963.

[Tamir 1963-I] T. Tamir and A. A. Oliner, "Guided Complex Waves, Part II: Relation to Radiation Patterns", *Proc. Inst. Elec. Eng.*, Vol. 110, pp. 325-334, Feb. 1963.

[Thevenot 1999] M. Thevenot, C. Cheype, A. Reineix and B. Jecko, "Directive photonic-bandgap antennas", *IEEE Trans. Microwave Tech.*, vol. 47, no.11, pp.2115- 2122, Nov. 1999.

[Trentini 1956] G.V. Trentini, "Partially reflecting sheet arrays", *IRE Trans. Antennas Propag.*, vol.4, pp.666-671, 1956.

[Tsao 1984] C. H. Tsao and R. Mittra, "Spectral-domain analysis of frequency selective surfaces comprised of periodic arrays of cross dipoles and Jesusalem crosses", *IEEE Trans. Antennas Propag.*, vol. AP-32, no. 5, pp. 478–486, May. 1984.

[Tzuang 2000] C.-K. C. Tzuang and Y.-C. Chen, "Dispersion characteristics of microstrip with periodic perturbations," in *Proc. IEEE Microwave Int.Symp. Dig.*, vol. 3, 2000, pp. 1537–1540.

[Vardaxoglou Apr-1997] J.C. Vardaxoglou, A. Blanos and D. Trinchero, "Leaky wave performance of Rectangular Frequency Selective Guides", *IEEE Trans. Antennas Propag: Tenth International Conference on.* Conf. publ. no. 436., vol. 1, pp. 318–321, April. 1997.

[Vardaxoglou 1997] J.C. Vardaxoglou, *Frequency Selective Surfaces: Analysis and Design*, Electronic and Electrical Engineering Research Studies, Antenna Series 10, 1997.

[Veselago 1968] V. Veselago, "The electrodynamics of substances of simultaneously negative values of ε and μ", Soviet Physics Uspekhi, vol.10, no.4, pp.509-514, 1968.

[Volakis 2007] John. L. Volakis, *Antenna Engineering Handbook*, 4th ed., Ed. McGraw-Hill, New York, 2007.

[Walter 1965] C.H. Walter, *Travelling Wave Antennas*, Ed. McGraw-Hill, New York, 1965.

[Wang 1991] Johnson J. h. Wang, *Generalized Moment Methods in Electromagnetics*, Ed. John Wiley & Sons, New York, 1991.

[Wang 1999] Z. L. Wang, K. Hashimoto, N. Shinohara and H. Matsumoto, 'Frequency selective surface for microwave power transmission', *IEEE Trans. Microwave Theory Techn.*, vol.47, No. 10, pp. 2039-2042, Oct. 1999.

[Wang 2006] S. Wang, A.P. Feresidis, G. Goussetis, and J.C. Vardaxoglou, "High-gain subwavelength resonant cavity antennas based on metamaterial ground planes", *IEEE Trans. Antennas Propag.*, vol.153, no.1, pp.1-6, Feb. 2006.

[Wu 1995] T. K. Wu, *Frequency Selective Surface and Grid Array*, Ed. John Wiley & Sons, New York, 1995.

[Yang 1999-I] F.R. Yang, K.P. Ma, Y. Quian and T. Itoh, 'A uniplanar compact photonic-bandgap structure and its applications for microwave circuits', *IEEE Trans. Microwave Theory Techn.*, vol.47, No. 8, pp. 1509-1514, Aug. 1999.

[Yang 1999-II] F.R. Yang, K.P. Ma, Y. Quian and T. Itoh, 'A novel TEM waveguide using uniplanar compact photonic-bandgap structure', *IEEE Trans. Microwave Theory Techn.*, vol.47, No. 11, pp. 2092-2098, Nov. 1999.

[Yang 2001] F. Yang and Y. Rahmat-Samii, 'A low profile circularly polarized curl antenna over electromagnetic band-gap (EBG) surface', *Microwave Optical Tech. Lett.*, vol. 31, no. 4, 264–7, November 2001

[Yang 2003] F. Yang and Y. Rahmat-Samii, 'Microstrip antennas integrated with electromagnetic band-gap (EBG) structures: a low mutual coupling design for array applications', *IEEE Trans. Antennas Propagat*, vol. 51, no. 10, part 2, 2936–46, 2003.

[Yang 2009] F. Yang and Y. Rahmat-Samii, *Electomagnetic Band Gap Structures in Antenna Engineering*, Cambridge University Press, New York, 2009.

[Zhao 2005-I] T. Zhao, D.R. Jackson, J.T. Williams and A.A. Oliner, "General formulas for 2-D leaky-wave antennas", *IEEE Trans. Antennas Propag.*, vol.53, no.11, pp.3525-3533, nov.2005.

[Zhao 2005-II] T. Zhao, D.R. Jackson, J.T. Williams, H.D. Yang and A.A. Oliner, "2-D periodic leaky-wave antennas - Part I: Metal patch design", *IEEE Trans. Antennas Propag.*, vol.53, no.11, pp.3505-3515, nov.2005.

[Zhao 2005-III] T. Zhao, D.R. Jackson, J.T. Williams, H.D. Yang and A.A. Oliner, "2-D periodic leaky-wave antennas - Part II: Slot design", *IEEE Trans. Antennas Propag.*, vol.53, no.11, pp.3515-3524, nov.2005.

[Zarrillo 1987] G. Zarrillo and K. Aguiar, 'Closed form low frequency solutions for electromagnetic waves through a FSS', *IEEE Trans. Antennas Propag.*, vol.AP-35, pp.1406-1417, Dec. 1987.

APPENDIX A

Supplement to Chapter 2 and Chapter 3.

WORKOUT 1

The transverse-longitudinal fields are defined as:

$$\vec{E} = \vec{E}_t + \hat{z}E_z \qquad (2.1.3)$$

$$\vec{H} = \vec{H}_t + \hat{z}H_z \qquad (2.1.4)$$

The expression of the nabla operator in the transverse-longitudinal notation is:

$$\vec{\nabla} = \hat{x}\frac{\partial}{\partial x} + \hat{y}\frac{\partial}{\partial y} + \hat{z}\frac{\partial}{\partial z} = \vec{\nabla}_t + \hat{z}\frac{\partial}{\partial z} \qquad (2.1.5)$$

Combining these expressions and replacing in (2.1.1) and (2.1.2) the transverse-longitudinal notation Maxwell's Equations are obtained. The first Maxwell Equation (1.1) can be rewritten as follows:

$$\vec{\nabla}\times\vec{E} = -j\omega\mu\vec{H} \qquad (2.1.1)$$

$$\vec{\nabla}\times(\vec{E}_t + \hat{z}E_z) = -j\omega\mu(\vec{H}_t + \hat{z}H_z) \qquad (2.1.6)$$

$$\left(\vec{\nabla}_t + \hat{z}\frac{\partial}{\partial z}\right)\times(\vec{E}_t + \hat{z}E_z) = -j\omega\mu(\vec{H}_t + \hat{z}H_z) \qquad (2.1.7)$$

Applying the distributive law of cross-product, it is obtained:

$$\left(\vec{\nabla}_t\times\vec{E}_t\right) + \left(\vec{\nabla}_t\times\hat{z}E_z\right) + \left(\hat{z}\frac{\partial}{\partial z}\times\vec{E}_t\right) + \left(\hat{z}\frac{\partial}{\partial z}\times\hat{z}E_z\right) = -j\omega\mu(\vec{H}_t + \hat{z}H_z) \qquad (2.1.8)$$

This expression can be split into two terms, one of them containing the transverse component (1.9) and the other one containing the longitudinal component (2.1.10). Note that the cross-product of two vectors with the same direction is zero $\left(\hat{z}\frac{\partial}{\partial z}\times\hat{z}E_z = 0\right)$.

$$\boxed{\vec{\nabla}_t\times\vec{E}_t = -j\omega\mu\hat{z}H_z} \qquad (2.1.9)$$

$$\left(\vec{\nabla}_t\times\hat{z}E_z\right) + \left(\hat{z}\frac{\partial}{\partial z}\times\vec{E}_t\right) = -j\omega\mu\vec{H}_t \qquad (2.1.10)$$

The resulting expression for the transverse fields (1.10) can be simplified using the following vector identity, $\vec{\nabla}\times(\vec{A}f)=f(\vec{\nabla}\times\vec{A})+(\vec{\nabla}f)\times\vec{A}$, obtaining:

$$E_z\left(\vec{\nabla}_t\times\hat{z}\right)+\left(\vec{\nabla}_t E_z\right)\times\hat{z}+\left(\hat{z}\frac{\partial}{\partial z}\times\vec{E}_t\right)=-j\omega\mu\vec{H}_t \qquad (2.1.11)$$

Taking into account that, since $\hat{z}$ is a vector constant, then $\vec{\nabla}_t\times\hat{z}=0$ and that $\hat{z}\frac{\partial}{\partial z}\times\vec{E}_t$ can be rewritten as $\hat{z}\times\frac{\partial\vec{E}_t}{\partial z}$, the resulting expression is:

$$\left(\vec{\nabla}_t E_z\right)\times\hat{z}+\left(\hat{z}\times\frac{\partial\vec{E}_t}{\partial z}\right)=-j\omega\mu\vec{H}_t \qquad (2.1.12)$$

$$\hat{z}\times\left(\frac{\partial\vec{E}_t}{\partial z}-\vec{\nabla}_t E_z\right)=-j\omega\mu\vec{H}_t \qquad (2.1.13)$$

Crossing equation (2.1.13) with $\hat{z}$ and making use of a second vector identity $\left(\vec{A}\times\vec{B}\right)\times\vec{C}=\left(\vec{A}\cdot\vec{C}\right)\vec{B}-\left(\vec{B}\cdot\vec{C}\right)\vec{A}$, where it is considered $\vec{A}=\vec{C}=\hat{z}$ and $\vec{B}=\frac{\partial\vec{E}_t}{\partial z}-\vec{\nabla}_t E_z$, leads to the next expressions:

$$\left[\hat{z}\times\left(\frac{\partial\vec{E}_t}{\partial z}-\vec{\nabla}_t E_z\right)\right]\times\hat{z}=-j\omega\mu\left(\vec{H}_t\times\hat{z}\right) \qquad (2.1.14)$$

$$(\hat{z}\cdot\hat{z})\left(\frac{\partial\vec{E}_t}{\partial z}-\vec{\nabla}_t E_z\right)-\left(\left(\frac{\partial\vec{E}_t}{\partial z}-\vec{\nabla}_t E_z\right)\cdot\hat{z}\right)\hat{z}=-j\omega\mu\left(\vec{H}_t\times\hat{z}\right) \qquad (2.1.15)$$

Since $\hat{z}\cdot\hat{z}=1$ and $\left(\frac{\partial\vec{E}_t}{\partial z}-\vec{\nabla}_t E_z\right)\cdot\hat{z}=0$, (1.15) can be finally expressed as:

$$\boxed{\frac{\partial\vec{E}_t}{\partial z}-\vec{\nabla}_t E_z=-j\omega\mu\left(\vec{H}_t\times\hat{z}\right)} \qquad (2.1.16)$$

The same process is applied to the second Maxwell Equation (2.1.2), and it will lead to a pair of similar equations to (2.1.9) and (2.1.16), one for the transverse term and the second one for the longitudinal term. Since the metallization plane is the x-y plane, only the transverse currents are taken into account, that is to say, $\vec{J}_s=\vec{J}_t+J_z=\vec{J}_t$.

$$\vec{\nabla}\times\vec{H}=\vec{J}_s+j\omega\varepsilon\vec{E} \qquad (2.1.2)$$

$$\vec{\nabla}\times(\vec{H}_t+\hat{z}H_z)=\vec{J}_t+j\omega\varepsilon(\vec{E}_t+\hat{z}E_z) \qquad (2.1.17)$$

$$\left(\vec{\nabla}_t+\hat{z}\frac{\partial}{\partial z}\right)\times(\vec{H}_t+\hat{z}H_z)=\vec{J}_t+j\omega\varepsilon(\vec{E}_t+\hat{z}E_z) \qquad (2.1.18)$$

$$\left(\vec{\nabla}_t\times\vec{H}_t\right)+\left(\vec{\nabla}_t\times\hat{z}H_z\right)+\left(\hat{z}\frac{\partial}{\partial z}\times\vec{H}_t\right)+\left(\hat{z}\frac{\partial}{\partial z}\times\hat{z}H_z\right)=\vec{J}_t+j\omega\varepsilon(\vec{E}_t+\hat{z}E_z) \qquad (2.1.19)$$

Again, it is known that $\hat{z}\frac{\partial}{\partial z}\times\hat{z}H_z=0$, so it is obtained the transverse-longitudinal notation:

$$\boxed{\vec{\nabla}_t\times\vec{H}_t=+j\omega\varepsilon\hat{z}E_z} \qquad (2.1.20)$$

$$\left(\vec{\nabla}_t\times\hat{z}H_z\right)+\left(\hat{z}\frac{\partial}{\partial z}\times\vec{H}_t\right)=\vec{J}_t+j\omega\varepsilon\vec{E}_t \qquad (2.1.21)$$

The transverse component (2.1.21) can be simplified applying the same vector identity than used in the first case $\vec{\nabla}\times(\vec{A}f)=f(\vec{\nabla}\times\vec{A})+(\vec{\nabla}f)\times\vec{A}$, $\vec{\nabla}_t\times\hat{z}=0$ and, as seen before, that $\hat{z}\frac{\partial}{\partial z}\times\vec{H}_t$ can be rewritten as $\hat{z}\times\frac{\partial\vec{H}_t}{\partial z}$, resulting:

$$H_z\left(\vec{\nabla}_t\times\hat{z}\right)+\left(\vec{\nabla}_t H_z\right)\times\hat{z}+\left(\hat{z}\frac{\partial}{\partial z}\times\vec{H}_t\right)=\vec{J}_t+j\omega\varepsilon\vec{E}_t \qquad (2.1.22)$$

$$\left(\vec{\nabla}_t H_z\right)\times\hat{z}+\left(\hat{z}\times\frac{\partial\vec{H}_t}{\partial z}\right)=\vec{J}_t+j\omega\varepsilon\vec{E}_t \qquad (2.1.23)$$

$$\hat{z}\times\left(\frac{\partial\vec{H}_t}{\partial z}-\vec{\nabla}_t H_z\right)=\vec{J}_t+j\omega\varepsilon\vec{E}_t \qquad (2.1.24)$$

Repeating the same process applied to equation (2.1.13) to the equation (2.1.24) now using the assignment $\vec{B}=\frac{\partial\vec{H}_t}{\partial z}-\vec{\nabla}_t H_z$, it is obtained:

$$\left[\hat{z}\times\left(\frac{\partial\vec{H}_t}{\partial z}-\vec{\nabla}_t H_z\right)\right]\times\hat{z}=\left(\vec{J}_t+j\omega\varepsilon\vec{E}_t\right)\times\hat{z} \qquad (2.1.25)$$

$$(\hat{z}\hat{z})\left(\frac{\partial\vec{H}_t}{\partial z}-\vec{\nabla}_t H_z\right)-\left(\left(\frac{\partial\vec{H}_t}{\partial z}-\vec{\nabla}_t H_z\right)\hat{z}\right)\hat{z}=\left(\vec{J}_t+j\omega\varepsilon\vec{E}_t\right)\times\hat{z} \qquad (2.1.26)$$

$$\frac{\partial \vec{H}_t}{\partial z} - \vec{\nabla}_t H_z = \left(\vec{J}_t + j\omega\varepsilon\vec{E}_t\right)\times\hat{z} \qquad (2.1.27)$$

$$\frac{\partial \vec{H}_t}{\partial z} - \vec{\nabla}_t H_z = \vec{J}_t\times\hat{z} + j\omega\varepsilon\left(\vec{E}_t\times\hat{z}\right) \qquad (2.1.28)$$

$$\boxed{\frac{\partial \vec{H}_t}{\partial z} - \vec{\nabla}_t H_z = -j\omega\varepsilon\left(\hat{z}\times\vec{E}_t\right) - \hat{z}\times\vec{J}_t} \qquad (2.1.29)$$

WORKOUT 2

Taking equation (2.1.9), the longitudinal magnetic field H_z can be rewritten:

$$\vec{\nabla}_t\times\vec{E}_t = -j\omega\mu\hat{z}H_z \qquad (2.1.9)$$

$$\hat{z}(\vec{\nabla}_t\times\vec{E}_t) = \hat{z}(-j\omega\mu\hat{z}H_z) \qquad (2.1.30)$$

$$\hat{z}(\vec{\nabla}_t\times\vec{E}_t) = -j\omega\mu H_z \qquad (2.1.31)$$

The left hand side of the last equation can be transformed, so equation (2.1.33) is obtained.

$$\hat{z}(\vec{\nabla}_t\times\vec{E}_t) = \vec{E}_t(\hat{z}\times\vec{\nabla}_t) = \vec{\nabla}_t(\vec{E}_t\times\hat{z}) = -\vec{\nabla}_t(\hat{z}\times\vec{E}_t) \qquad (2.1.32)$$

$$-\vec{\nabla}_t(\hat{z}\times\vec{E}_t) = -j\omega\mu H_z \qquad (2.1.33)$$

$$\boxed{H_z = \frac{\vec{\nabla}_t(\hat{z}\times\vec{E}_t)}{j\omega\mu}} \qquad (2.1.34)$$

The same development is applied to equation (1.20) to obtain a similar expression for the longitudinal electric field E_z:

$$\vec{\nabla}_t\times\vec{H}_t = +j\omega\varepsilon\hat{z}E_z \qquad (2.1.20)$$

$$\hat{z}(\vec{\nabla}_t\times\vec{H}_t) = \hat{z}(j\omega\varepsilon\hat{z}E_z) \qquad (2.1.35)$$

$$\hat{z}(\vec{\nabla}_t\times\vec{H}_t) = j\omega\varepsilon E_z \qquad (2.1.36)$$

$$\hat{z}(\vec{\nabla}_t\times\vec{H}_t) = \vec{H}_t(\hat{z}\times\vec{\nabla}_t) = \vec{\nabla}_t(\vec{H}_t\times\hat{z}) \qquad (2.1.37)$$

$$\vec{\nabla}_t(\vec{H}_t\times\hat{z}) = j\omega\varepsilon E_z \qquad (2.1.38)$$

$$\boxed{E_z = \frac{\vec{\nabla}_t(\vec{H}_t\times\hat{z})}{j\omega\varepsilon}} \qquad (2.1.39)$$

Now if equations (2.1.34) and (2.1.39) are introduced into equations (2.1.9) and (2.1.20) respectively, the final set of transverse Maxwell's equations is formulated:

$$\frac{\partial \vec{E}_t}{\partial z} = -j\omega\mu\left(\vec{H}_t \times \hat{z}\right) + \frac{1}{j\omega\varepsilon}\vec{\nabla}_t\left[\vec{\nabla}_t(\vec{H}_t \times \hat{z})\right] \qquad (2.1.40)$$

$$\frac{\partial \vec{H}_t}{\partial z} = -j\omega\varepsilon\left(\hat{z} \times \vec{E}_t\right) + \frac{1}{j\omega\mu}\vec{\nabla}_t\left[\vec{\nabla}_t(\hat{z} \times \vec{E}_t)\right] - \hat{z} \times \vec{J}_t \qquad (2.1.41)$$

WORKOUT 3

From (2.4.1), the two different polarizations, p=TE and p=TM, are going to be considered separately, and taking into account that $\vec{e}^{(p)}_{mx,my}(x,y) = \vec{h}^{(p)}_{mx,my}(x,y) \times \hat{z}$, it is obtained:

$$\sum_{mx=0}^{\infty}\sum_{my=-\infty}^{\infty}\frac{dV^{TE}_{mx,my}(z)}{dz}\vec{e}^{TE}_{mx,my}(x,y) + \sum_{mx=0}^{\infty}\sum_{my=-\infty}^{\infty}\frac{dV^{TM}_{mx,my}(z)}{dz}\vec{e}^{TM}_{mx,my}(x,y) =$$

$$-j\omega\mu\sum_{mx=0}^{\infty}\sum_{my=-\infty}^{\infty}I^{TE}_{mx,my}(z)\vec{e}^{TE}_{mx,my}(x,y) - j\omega\mu\sum_{mx=0}^{\infty}\sum_{my=-\infty}^{\infty}I^{TM}_{mx,my}(z)\vec{e}^{TM}_{mx,my}(x,y) + \qquad (2.5.4)$$

$$+\frac{1}{j\omega\varepsilon}\sum_{mx=0}^{\infty}\sum_{my=-\infty}^{\infty}I^{TE}_{mx,my}(z)\vec{\nabla}_t\left(\vec{\nabla}_t\vec{e}^{TE}_{mx,my}(x,y)\right) + \frac{1}{j\omega\varepsilon}\sum_{mx=0}^{\infty}\sum_{my=-\infty}^{\infty}I^{TM}_{mx,my}(z)\vec{\nabla}_t\left(\vec{\nabla}_t\vec{e}^{TM}_{mx,my}(x,y)\right)$$

Applying the following properties of the PPM (2.5.5) and (2.5.6), leads to (2.5.7):

$$\vec{\nabla}_t\left(\vec{\nabla}_t\vec{e}^{TE}_{mx,my}(x,y)\right) = 0 \qquad (2.5.5)$$

$$\vec{\nabla}_t\left(\vec{\nabla}_t\vec{e}^{TM}_{mx,my}(x,y)\right) = -k^2_{cm}\vec{e}^{TM}_{mx,my}(x,y) \qquad (2.5.6)$$

$$\sum_{mx=0}^{\infty}\sum_{my=-\infty}^{\infty}\frac{dV^{TE}_{mx,my}(z)}{dz}\vec{e}^{TE}_{mx,my}(x,y) + \sum_{mx=0}^{\infty}\sum_{my=-\infty}^{\infty}\frac{dV^{TM}_{mx,my}(z)}{dz}\vec{e}^{TM}_{mx,my}(x,y) =$$

$$-j\omega\mu\sum_{mx=0}^{\infty}\sum_{my=-\infty}^{\infty}I^{TE}_{mx,my}(z)\vec{e}^{TE}_{mx,my}(x,y) - j\omega\mu\sum_{mx=0}^{\infty}\sum_{my=-\infty}^{\infty}I^{TM}_{mx,my}(z)\vec{e}^{TM}_{mx,my}(x,y) +$$

$$-\frac{1}{j\omega\varepsilon}\sum_{mx=0}^{\infty}\sum_{my=-\infty}^{\infty}I^{TM}_{mx,my}(z)k^2_{cm}\vec{e}^{TM}_{mx,my}(x,y) \qquad (2.5.7)$$

If (2.5.7) is multiplied by $\vec{e}_{mx}^{(p)*}(x,y)$ and integrated in the interval from x=0 to x=a, that is equivalent to the definition of the inner product applied in the PPW modal expansion:

$$I_{P_m Q_n^*} = \int_0^a \vec{e}_m^{\,(p)}(x)\cdot\vec{e}_n^{\,(q)*}(x)dx = \begin{cases} 1 & \text{if p=q and m=n} \\ 0 & \text{if m} \neq \text{n} \\ C_m & \text{if p} \neq \text{q and m=n} \end{cases} \qquad (2.2.17)$$

The aim of this procedure is to eliminate the summation in x from the equation, so it can be obtained a expression for the equivalent transmission line. Hence, the resulting expression for $\int_{x=0}^{a} (4.7)\cdot\vec{e}_{mx}^{(p)*}(x,y)dx$ is:

$$\sum_{my=-\infty}^{\infty} \frac{dV_{mx,my}^{TE}(z)}{dz} e^{-jk_{my}y} + \sum_{my=-\infty}^{\infty} \frac{dV_{mx,my}^{TM}(z)}{dz} C_m e^{-jk_{my}y} = \qquad (2.5.8)$$

$$= -\left(j\omega\mu + \frac{k_{cm}^2}{j\omega\varepsilon} \right) \sum_{my=-\infty}^{\infty} I_{mx,my}^{TM}(z) C_m e^{-jk_{my}y} - j\omega\mu \sum_{my=-\infty}^{\infty} I_{mx,my}^{TE}(z) e^{-jk_{my}y}$$

And the result for $\int_{x=0}^{a} (4.7)\cdot\vec{e}_{mx}^{TM*}(x,y)dx$ is:

$$\sum_{my=-\infty}^{\infty} \frac{dV_{mx,my}^{TE}(z)}{dz} C_m e^{-jk_{my}y} + \sum_{my=-\infty}^{\infty} \frac{dV_{mx,my}^{TM}(z)}{dz} e^{-jk_{my}y} = \qquad (2.5.9)$$

$$= -\left(j\omega\mu + \frac{k_{cm}^2}{j\omega\varepsilon} \right) \sum_{my=-\infty}^{\infty} I_{mx,my}^{TM}(z) e^{-jk_{my}y} - j\omega\mu \sum_{my=-\infty}^{\infty} I_{mx,my}^{TE}(z) C_m e^{-jk_{my}y}$$

It is known that:
$$k_0^2 = k_{mx}^2 + k_{my}^2 + k_z^2 = \omega^2\mu\varepsilon$$
$$k_z^2 = k_0^2 - k_{mx}^2 - k_{my}^2 = k_0^2 - k_{cm}^2$$

where k_{cm} is the **transverse wave number** and $\varepsilon = \varepsilon_0 \cdot \varepsilon_r$, so k_0^2 is the propagation constant for whichever medium (actually it is more accurate to say $k_0^2\sqrt{\varepsilon_r}$). Hence it can be written:

$$j\omega\mu + \frac{k_{cm}^2}{j\omega\varepsilon} = \frac{1}{j\omega\varepsilon}\left(-\omega^2\mu\varepsilon + k_{cm}^2\right) = \frac{1}{j\omega\varepsilon}\left(k_{cm}^2 - k_0^2\right) = \frac{jk_z^2}{\omega\varepsilon} \qquad (2.5.10)$$

It is important to notice that there will be a different value of k_z^2 for every couple of values of (mx,my), so from this moment on it will be referred as k_{zm}^2 . If the transverse impedances are defined as follows:

$$Z_{0m}{}^{TE} = \frac{\omega\mu}{k_{zm}} \qquad (2.5.11)$$

$$Z_{0m}{}^{TM} = \frac{k_{zm}}{\omega\varepsilon} \qquad (2.5.12)$$

Introducing this expressions in (4.8) and (4.9):

$$\sum_{my=-\infty}^{\infty} \frac{dV_{mx,my}^{TE}(z)}{dz} e^{-jk_{my}y} + \sum_{my=-\infty}^{\infty} \frac{dV_{mx,my}^{TM}(z)}{dz} C_m e^{-jk_{my}y} = \qquad (2.5.13)$$

$$= -j \sum_{my=-\infty}^{\infty} C_m Z_{0m}^{TM} k_{zm} I_{mx,my}^{TM}(z) e^{-jk_{my}y} - j \sum_{my=-\infty}^{\infty} Z_{0m}^{TE} k_{zm} I_{mx,my}^{TE}(z) e^{-jk_{my}y}$$

$$\sum_{my=-\infty}^{\infty} \frac{dV_{mx,my}^{TE}(z)}{dz} C_m e^{-jk_{my}y} + \sum_{my=-\infty}^{\infty} \frac{dV_{mx,my}^{TM}(z)}{dz} e^{-jk_{my}y} = \qquad (2.5.14)$$

$$= -j \sum_{my=-\infty}^{\infty} Z_{0m}^{TM} k_{zm} I_{mx,my}^{TM}(z) e^{-jk_{my}y} - j \sum_{my=-\infty}^{\infty} C_m Z_{0m}^{TE} k_{zm} I_{mx,my}^{TE}(z) e^{-jk_{my}y}$$

These two previous equations can be expressed as a single one, using the indexes p and q to refer to the different polarizations:

$$\sum_{my=-\infty}^{\infty} \frac{dV_{mx,my}^{(p)}(z)}{dz} e^{-jk_{my}y} + \sum_{my=-\infty}^{\infty} \frac{dV_{mx,my}^{(q)}(z)}{dz} C_m e^{-jk_{my}y} = \qquad (2.5.15)$$

$$= -j \sum_{my=-\infty}^{\infty} Z_{0m}^{(p)} k_{zm} I_{mx,my}^{(p)}(z) e^{-jk_{my}y} - j \sum_{my=-\infty}^{\infty} C_m Z_{0m}^{(q)} k_{zm} I_{mx,my}^{(q)}(z) e^{-jk_{my}y}$$

where, if p=TE then q=TM.

The same procedure applied to (2.4.1) is going to be applied now to (2.4.2), taking the polarizations TE and TM separately and taking into account that $\vec{h}_{mx,my}^{(p)}(x,y) = \hat{z} \times \vec{e}_{mx,my}^{(p)}(x,y)$:

$$\sum_{mx=0}^{\infty}\sum_{my=-\infty}^{\infty} \frac{dI_{mx,my}^{(TE)}(z)}{dz}\vec{h}_{mx,my}^{(TE)}(x,y) + \sum_{mx=0}^{\infty}\sum_{my=-\infty}^{\infty} \frac{dI_{mx,my}^{(TM)}(z)}{dz}\vec{h}_{mx,my}^{(TM)}(x,y)$$

$$= -j\omega\varepsilon\left(\sum_{mx=0}^{\infty}\sum_{my=-\infty}^{\infty} V_{mx,my}^{(TE)}(z)\vec{h}_{mx,my}^{(TE)}(x,y) + \sum_{mx=0}^{\infty}\sum_{my=-\infty}^{\infty} V_{mx,my}^{(TM)}(z)\vec{h}_{mx,my}^{(TM)}(x,y)\right) +$$

$$+\frac{1}{j\omega\mu}\left(\sum_{mx=0}^{\infty}\sum_{my=-\infty}^{\infty} V_{mx,my}^{(TE)}(z)\vec{\nabla}_t\left(\vec{\nabla}_t\vec{h}_{mx,my}^{(TE)}(x,y)\right) + \sum_{mx=0}^{\infty}\sum_{my=-\infty}^{\infty} V_{mx,my}^{(TM)}(z)\vec{\nabla}_t\left(\vec{\nabla}_t\vec{h}_{mx,my}^{(TM)}(x,y)\right)\right) -$$

$$-\sum_{mx=0}^{\infty}\sum_{my=-\infty}^{\infty} j_{mx,my}^{(TE)}(z)\vec{h}_{mx,my}^{(TE)}(x,y) - \sum_{mx=0}^{\infty}\sum_{my=-\infty}^{\infty} j_{mx,my}^{(TM)}(z)\vec{h}_{mx,my}^{(TM)}(x,y) \qquad (2.5.16)$$

Applying the following PPM properties (2.5.17) and (2.5.18) to (2.5.16), (2.5.19) is obtained:

$$\vec{\nabla}_t\left(\vec{\nabla}_t\vec{h}_{mx,my}^{(TE)}(x,y)\right) = -k_{cm}^2\vec{h}_{mx,my}^{(TE)}(x,y) \qquad (2.5.17)$$

$$\vec{\nabla}_t\left(\vec{\nabla}_t\vec{h}_{mx,my}^{(TM)}(x,y)\right) = 0 \qquad (2.5.18)$$

$$\sum_{mx=0}^{\infty}\sum_{my=-\infty}^{\infty} \frac{dI_{mx,my}^{(TE)}(z)}{dz}\vec{h}_{mx,my}^{(TE)}(x,y) + \sum_{mx=0}^{\infty}\sum_{my=-\infty}^{\infty} \frac{dI_{mx,my}^{(TM)}(z)}{dz}\vec{h}_{mx,my}^{(TM)}(x,y)$$

$$= -j\omega\varepsilon\left(\sum_{mx=0}^{\infty}\sum_{my=-\infty}^{\infty} V_{mx,my}^{(TE)}(z)\vec{h}_{mx,my}^{(TE)}(x,y) + \sum_{mx=0}^{\infty}\sum_{my=-\infty}^{\infty} V_{mx,my}^{(TM)}(z)\vec{h}_{mx,my}^{(TM)}(x,y)\right) + \qquad (2.5.19)$$

$$-\frac{1}{j\omega\mu}\sum_{mx=0}^{\infty}\sum_{my=-\infty}^{\infty} V_{mx,my}^{(TE)}(z)k_{cm}^2\vec{h}_{mx,my}^{(TE)}(x,y) - \sum_{mx=0}^{\infty}\sum_{my=-\infty}^{\infty} j_{mx,my}^{(TE)}(z)\vec{h}_{mx,my}^{(TE)}(x,y) - \sum_{mx=0}^{\infty}\sum_{my=-\infty}^{\infty} j_{mx,my}^{(TM)}(z)\vec{h}_{mx,my}^{(TM)}(x,y)$$

The definition of the inner product is used again this time on (2.5.19):

$$I_{P_mQ_n^*} = \int_0^a \vec{h}_m^{(p)}(x)\cdot\vec{h}_n^{(q)*}(x)dx = \begin{cases} 1 & \text{if p=q and m=n} \\ 0 & \text{if m} \neq \text{n} \\ C_m & \text{if p} \neq \text{q and m=n} \end{cases} \qquad (2.2.17)$$

Hence, the resulting expression for $\int_{x=0}^{a} (2.5.19)\cdot \vec{h}_{mx}^{(TE)*}(x,y)dx$ is:

$$\sum_{my=-\infty}^{\infty} \frac{dI_{mx,my}^{(TE)}(z)}{dz} + \sum_{my=-\infty}^{\infty} \frac{dI_{mx,my}^{(TM)}(z)}{dz} C_m = -\left(j\omega\varepsilon + \frac{k_{cm}^2}{j\omega\mu} \right) \sum_{my=-\infty}^{\infty} V_{mx,my}^{(TE)}(z) -$$

$$- \sum_{my=-\infty}^{\infty} j_{mx,my}^{(TE)}(z) - j\omega\varepsilon \sum_{my=-\infty}^{\infty} V_{mx,my}^{(TM)}(z) C_m - \sum_{my=-\infty}^{\infty} j_{mx,my}^{(TM)}(z) C_m \qquad (2.5.20)$$

And the resulting expression for $\int_{x=0}^{a} (2.5.19)\cdot \vec{h}_{mx}^{(TM)*}(x,y)dx$ is:

$$\sum_{my=-\infty}^{\infty} \frac{dI_{mx,my}^{(TE)}(z)}{dz} C_m + \sum_{my=-\infty}^{\infty} \frac{dI_{mx,my}^{(TM)}(z)}{dz} = -\left(j\omega\varepsilon + \frac{k_{cm}^2}{j\omega\mu} \right) \sum_{my=-\infty}^{\infty} V_{mx,my}^{(TE)}(z) C_m -$$

$$- \sum_{my=-\infty}^{\infty} j_{mx,my}^{(TE)}(z) C_m - j\omega\varepsilon \sum_{my=-\infty}^{\infty} V_{mx,my}^{(TM)}(z) - \sum_{my=-\infty}^{\infty} j_{mx,my}^{(TM)}(z) \qquad (2.5.21)$$

Using again the same equalities than before , $\begin{aligned} k_0^2 &= k_{mx}^2 + k_{my}^2 + k_z^2 = \omega^2\mu\varepsilon \\ k_z^2 &= k_0^2 - k_{mx}^2 - k_{my}^2 = k_0^2 - k_{cm}^2 \end{aligned}$, it can be written as follows:

$$j\omega\varepsilon + \frac{k_{cm}^2}{j\omega\mu} = \frac{1}{j\omega\mu}\left(-\omega^2\mu\varepsilon + k_{cm}^2 \right) = \frac{1}{j\omega\mu}\left(k_{cm}^2 - k_0^2 \right) = \frac{jk_z^2}{\omega\mu} \qquad (2.5.22)$$

And applying again the transverse impedances' definitions already seen in (2.4.11) and (2.4.12), it is finally obtained:

$$\sum_{my=-\infty}^{\infty} \frac{dI_{mx,my}^{(TE)}(z)}{dz} + \sum_{my=-\infty}^{\infty} \frac{dI_{mx,my}^{(TM)}(z)}{dz} C_m = -j\frac{k_z^2}{Z_{0m}^{TE}} \sum_{my=-\infty}^{\infty} V_{mx,my}^{(TE)}(z) -$$

$$- \sum_{my=-\infty}^{\infty} j_{mx,my}^{(TE)}(z) + C_m \left(-j\frac{k_z^2}{Z_{0m}^{TM}} \sum_{my=-\infty}^{\infty} V_{mx,my}^{(TM)}(z) - \sum_{my=-\infty}^{\infty} j_{mx,my}^{(TM)}(z) \right) \qquad (2.5.23)$$

$$\sum_{my=-\infty}^{\infty} \frac{dI_{mx,my}^{(TE)}(z)}{dz} C_m + \sum_{my=-\infty}^{\infty} \frac{dI_{mx,my}^{(TM)}(z)}{dz} = -j\frac{k_z^2}{Z_{0m}^{TM}} \sum_{my=-\infty}^{\infty} V_{mx,my}^{(TM)}(z) -$$

$$- \sum_{my=-\infty}^{\infty} j_{mx,my}^{(TM)}(z) + C_m \left(-j\frac{k_z^2}{Z_{0m}^{TE}} \sum_{my=-\infty}^{\infty} V_{mx,my}^{(TE)}(z) - \sum_{my=-\infty}^{\infty} j_{mx,my}^{(TE)}(z) \right) \qquad (2.5.24)$$

And these two equations can easily be expressed as a single one:

$$\sum_{my=-\infty}^{\infty}\frac{dI_{mx,my}^{(p)}(z)}{dz}e^{-jk_{my}y}+\sum_{my=-\infty}^{\infty}\frac{dI_{mx,my}^{(q)}(z)}{dz}C_m e^{-jk_{my}y}=-j\frac{k_z^2}{Z_{0m}^{(p)}}\sum_{my=-\infty}^{\infty}V_{mx,my}^{(p)}(z)e^{-jk_{my}y}-$$

$$-\sum_{my=-\infty}^{\infty}j_{mx,my}^{(p)}(z)e^{-jk_{my}y}+C_m\left(-j\frac{k_z^2}{Z_{0m}^{(q)}}\sum_{my=-\infty}^{\infty}V_{mx,my}^{(q)}(z)e^{-jk_{my}y}-\sum_{my=-\infty}^{\infty}j_{mx,my}^{(q)}(z)e^{-jk_{my}y}\right) \qquad (2.5.25)$$

where, if p=TE then q=TM and vice versa.

Following the step no.3 in Chapter 2.5, the definition of the inner product (2.3.13) for the Floquet modes will be applied to (2.5.15) and (2.5.25). In the previous section, the electric and magnetic basis functions were defined as follows:

$$\vec{e}_{mx,my}^{(p)}(x,y)=\vec{e}_{mx}^{(p)}(x)e^{-jk_{my}y} \qquad (2.3.11)$$

$$\vec{h}_{mx,my}^{(p)}(x,y)=\vec{h}_{mx}^{(p)}(x)e^{-jk_{my}y} \qquad (2.3.12)$$

So far the x summation has been eliminated from (2.4.15) and (2.4.25) applying the PPM inner product definition. The same process will be followed on those equations to eliminate the y summation.

$$I_{P_{my}Q_{ny}^*}=\int_{x=0}^{P}e^{-jk_{my}y}\cdot e^{+jk_{ny}y}\partial y=\begin{cases}0 & \text{if } m\neq n\\ P & \text{if } m=n\end{cases} \qquad (2.3.13)$$

If that definition is applied to (2.4.15), $I_{P_{my}Q_{ny}^*}=\int_{x=0}^{P}(2.5.15)\cdot e^{+jk_{ny}y}\partial y$, is obtained:

$$P\left(\frac{dV_{mx,my}^{(p)}(z)}{dz}+\frac{dV_{mx,my}^{(q)}(z)}{dz}C_m\right)=P\left(-jZ_{0m}^{(p)}k_{zm}I_{mx,my}^{(p)}(z)-jC_mZ_{0m}^{(q)}k_{zm}I_{mx,my}^{(q)}(z)\right) \qquad (2.5.26)$$

$$\frac{dV_{mx,my}^{(p)}(z)}{dz}+\frac{dV_{mx,my}^{(q)}(z)}{dz}C_m=-jZ_{0m}^{(p)}k_{zm}I_{mx,my}^{(p)}(z)-jC_mZ_{0m}^{(q)}k_{zm}I_{mx,my}^{(q)}(z) \qquad (2.5.27)$$

Again, if it is applied to (2.5.25), $I_{P_{my}Q^*_{ny}} = \int_{x=0}^{P} (2.5.25)\cdot e^{+jk_{ny}y}\partial y$:

$$P\left(\frac{dI^{(p)}_{mx,my}(z)}{dz}+\frac{dI^{(q)}_{mx,my}(z)}{dz}C_m\right)=P\left(-j\frac{k_z^2}{Z^{(p)}_{0m}}V^{(p)}_{mx,my}(z)-j^{(p)}_{mx,my}(z)+C_m\left(-j\frac{k_z^2}{Z^{(q)}_{0m}}V^{(q)}_{mx,my}(z)-j^{(q)}_{mx,my}\right)\right) \quad (2.5.28)$$

$$\frac{dI^{(p)}_{mx,my}(z)}{dz}+\frac{dI^{(q)}_{mx,my}(z)}{dz}C_m=-j\frac{k_z^2}{Z^{(p)}_{0m}}V^{(p)}_{mx,my}(z)-j^{(p)}_{mx,my}(z)+C_m\left(-j\frac{k_z^2}{Z^{(q)}_{0m}}V^{(q)}_{mx,my}(z)-j^{(q)}_{mx,my}\right) \quad (2.5.29)$$

It is important to notice that, due to the orthogonality of the Floquet basis functions, there is no couple between the modes with different polarization.

WORKOUT 4

As done in the previous section, the definition of the inner product for both expansions, PPM in $\hat{x}$ and Floquet modes in $\hat{y}$, is applied, which leads to:

$$\int_0^a\int_0^P \vec{J}_t(x,y,z)\vec{e}^{(p)*}_{mx}(x)e^{+jk_{my}y}dxdy=\int_0^a\int_0^P \vec{J}^x_t\vec{e}^{(p)*}_{mx}(x)e^{+jk_{my}y}dxdy \quad (2.6.4)$$

$$\int_0^a\int_0^P \sum_p^{TE,TM}\sum_{mx=0}^{\infty}\sum_{my=-\infty}^{\infty} j^{(p)}_{mx,my}(z)\vec{e}^{(p)}_{mx}(x)e^{-jk_{my}y}\vec{e}^{(p)*}_{mx}(x)e^{+jk_{my}y}dydx = \quad (2.6.5)$$

$$=\int_0^a\int_0^P \delta(x-x')\cdot\delta(z-z')\cdot\delta(y-y')e^{-jk_{y0}y}\hat{x}\vec{e}^{(p)*}_{mx}(x)e^{+jk_{my}y}dxdy$$

$$\int_0^a P\sum_p^{TE,TM}\sum_{mx=0}^{\infty} j^{(p)}_{mx,my}(z)\vec{e}^{(p)}_{mx}(x)\vec{e}^{(p)*}_{mx}(x)dx = \quad (2.6.6)$$

$$=\int_0^a \delta(x-x')\cdot\delta(z-z')\cdot\hat{x}\vec{e}^{(p)*}_{mx}(x)e^{+j(k_{my}-k_{y0})y'}dx$$

$$P\sum_p^{TE,TM}\left(j^{(p)}_{mx,my}(z)+C_m j^{(q)}_{mx,my}(z)\right)=\delta(z-z')\vec{e}^{(p)*}_{mx}(x)e^{+j(k_{my}-k_{y0})y'}\cdot\hat{x} \quad (2.6.7)$$

Remembering the definition of the propagation constant in the longitudinal direction (2.3.8), last equation can be rewritten as:

$$P\sum_p^{TE,TM}\left(j^{(p)}_{mx,my}(z)+C_m j^{(q)}_{mx,my}(z)\right)=\delta(z-z')\vec{e}^{(p)*}_{mx}(x)e^{+j(my\frac{2\pi}{P})y'}\cdot\hat{x} \quad (2.6.8)$$

The $\hat{x}$ term points out that this expression will only affect to the PPM, since those are the ones that model the variation in $\hat{x}$. Now, aiming to decouple the expression obtained, each polarization is going to be considered separately:

$$\text{A} = P\sum_{p}^{TE,TM}\left(j_{mx,my}^{TE}(z)+C_m j_{mx,my}^{TM}(z)\right)=\delta(z-z')\vec{e}_{mx}^{TE*}(x)e^{+j(my\frac{2\pi}{P})y'} \quad (2.6.9)$$

$$\text{B} = P\sum_{p}^{TE,TM}\left(j_{mx,my}^{TM}(z)+C_m j_{mx,my}^{TE}(z)\right)=\delta(z-z')\vec{e}_{mx}^{TM*}(x)e^{+j(my\frac{2\pi}{P})y'} \quad (2.6.10)$$

$$A-C_m\cdot B$$

$$P\left(j_{mx,my}^{TE}(z)-C_m^2 j_{mx,my}^{TE}(z)\right)=e^{+j(my\frac{2\pi}{P})y'}\delta(z-z')\left(\vec{e}_{mx}^{TE*}(x)-C_m\vec{e}_{mx}^{TM*}(x)\right) \quad (2.6.11)$$

$$B-C_m\cdot A$$

$$P\left(j_{mx,my}^{TM}(z)-C_m^2 j_{mx,my}^{TM}(z)\right)=e^{+j(my\frac{2\pi}{P})y'}\delta(z-z')\left(\vec{e}_{mx}^{TM*}(x)-C_m\vec{e}_{mx}^{TE*}(x)\right) \quad (2.6.12)$$

$$j_{mx,my}^{x,TE}(z)=\frac{e^{+j(my\frac{2\pi}{P})y'}}{P}\frac{\vec{e}_{mx}^{x,TE*}(x)-C_m\vec{e}_{mx}^{x,TM*}(x)}{1-C_m^2}\delta(z-z') \quad (2.6.13)$$

$$j_{mx,my}^{x,TM}(z)=\frac{e^{+j(my\frac{2\pi}{P})y'}}{P}\frac{\vec{e}_{mx}^{x,TM*}(x)-C_m\vec{e}_{mx}^{x,TE*}(x)}{1-C_m^2}\delta(z-z') \quad (2.6.14)$$

It is important to notice that the superscript has been modified in order to indicate that these expressions are to be considered for the variation in $\hat{x}$.

If the same process is repeated again but this time for the elementary source directed in $\hat{y}$ (2.6.2), $\vec{J}_t(x,y,z)=\vec{J}_t^{\,y}$, the following results are obtained:

$$j_{mx,my}^{y,TE}(z)=\frac{e^{+j(my\frac{2\pi}{P})y'}}{P}\frac{\vec{e}_{mx}^{y,TE*}(x)-C_m\vec{e}_{mx}^{y,TM*}(x)}{1-C_m^2}\delta(z-z') \quad (2.6.15)$$

$$j_{mx,my}^{y,TM}(z)=\frac{e^{+j(my\frac{2\pi}{P})y'}}{P}\frac{\vec{e}_{mx}^{y,TM*}(x)-C_m\vec{e}_{mx}^{y,TE*}(x)}{1-C_m^2}\delta(z-z') \quad (2.6.16)$$

WORKOUT 5

$$V^{(p)}_{\substack{mx,my \\ ELEM}}(z)=\hat{V}^{(p)}_{mx,my}(z)\cdot j^{x,(p)}_{mx,my}=\hat{V}^{(p)}_{mx,my}(z)\cdot\frac{e^{+j(my\frac{2\pi}{P})y'}}{P}\frac{\vec{e}^{\,x,(p)^*}_{mx}(x')-C_m\vec{e}^{\,x,(q)^*}_{mx}(x')}{1-C_m^2} \quad (2.6.17)$$

$$I^{(p)}_{\substack{mx,my \\ ELEM}}(z)=\hat{I}^{(p)}_{mx,my}(z)\cdot j^{x,(p)}_{mx,my}=\hat{I}^{(p)}_{mx,my}(z)\cdot\frac{e^{+j(my\frac{2\pi}{P})y'}}{P}\frac{\vec{e}^{\,x,(p)^*}_{mx}(x')-C_m\vec{e}^{\,x,(q)^*}_{mx}(x')}{1-C_m^2} \quad (2.6.18)$$

$$V^{(p)}_{\substack{mx,my \\ ELEM}}(z)=\hat{V}^{(p)}_{mx,my}(z)\cdot j^{y,(p)}_{mx,my}=\hat{V}^{(p)}_{mx,my}(z)\cdot\frac{e^{+j(my\frac{2\pi}{P})y'}}{P}\frac{\vec{e}^{\,y,(p)^*}_{mx}(x')-C_m\vec{e}^{\,y,(q)^*}_{mx}(x')}{1-C_m^2} \quad (2.6.19)$$

$$I^{(p)}_{\substack{mx,my \\ ELEM}}(z)=\hat{I}^{(p)}_{mx,my}(z)\cdot j^{y,(p)}_{mx,my}=\hat{I}^{(p)}_{mx,my}(z)\cdot\frac{e^{+j(my\frac{2\pi}{P})y'}}{P}\frac{\vec{e}^{\,y,(p)^*}_{mx}(x')-C_m\vec{e}^{\,y,(q)^*}_{mx}(x')}{1-C_m^2} \quad (2.6.20)$$

If the elementary tension and current are introduced in the expressions of the fields (2.3.9) and (2.3.10), the elementary transverse fields, or what's the same, the Green Functions are obtained:

$$\vec{E}_{\substack{t \\ ELEM}}(x,y,z)=\bar{\bar{G}}^{tt}_{EJ}(x,y,z,x',y')= \quad (2.6.21)$$

$$=\sum_{p}^{TE,TM}\sum_{mx=0}^{\infty}\sum_{my=-\infty}^{\infty}\hat{V}^{(p)}_{mx,my}(z)\cdot\frac{e^{+j(my\frac{2\pi}{P})y'}}{P}\frac{\vec{e}^{\,(p)^*}_{mx}(x')-C_m\vec{e}^{\,(q)^*}_{mx}(x')}{1-C_m^2}\vec{e}^{\,(p)}_{mx}(x)e^{-jk_{my}y}$$

$$\vec{H}_{\substack{t \\ ELEM}}(x,y,z)=\bar{\bar{G}}^{tt}_{HJ}(x,y,z,x',y')= \quad (2.6.22)$$

$$=\sum_{p}^{TE,TM}\sum_{mx=0}^{\infty}\sum_{my=-\infty}^{\infty}\hat{I}^{(p)}_{mx,my}(z)\cdot\frac{e^{+j(my\frac{2\pi}{P})y'}}{P}\frac{\vec{e}^{\,(p)^*}_{mx}(x')-C_m\vec{e}^{\,(q)^*}_{mx}(x')}{1-C_m^2}\vec{h}^{\,(p)}_{mx}(x)e^{-jk_{my}y}$$

Now, it is renamed: $m=mx,my$

$$\vec{X}^{(p)}_{m}(x')=\frac{\vec{e}^{\,(p)^*}_{mx}(x')-C_m\vec{e}^{\,(q)^*}_{mx}(x')}{1-C_m^2} \quad (2.6.23) \qquad Y^{(p)}_{m}(y')=\frac{e^{+j(my\frac{2\pi}{P})y'}}{P} \quad (2.6.24)$$

$$\bar{\bar{G}}_{EJ}^{tt}(r,r') = \sum_{p}^{TE,TM} \sum_{mx=0}^{\infty} \sum_{my=-\infty}^{\infty} \vec{X}_m^{(p)}(x') Y_m^{(p)}(y') \hat{V}_m^{(p)}(z) \cdot \vec{e}_{mx}^{(p)}(x) e^{-jk_{my}y} \qquad (2.6.25)$$

$$\bar{\bar{G}}_{HJ}^{tt}(r,r') = \sum_{p}^{TE,TM} \sum_{mx=0}^{\infty} \sum_{my=-\infty}^{\infty} \vec{X}_m^{(p)}(x') Y_m^{(p)}(y') \hat{I}_m^{(p)}(z) \cdot \vec{h}_{mx}^{(p)}(x) e^{-jk_{my}y} \qquad (2.6.26)$$

This way the transverse fields existing in the structure can be expressed:

$$\vec{E}_t(x,y,z) = \vec{E}_t(r) = \int_{S'} \bar{\bar{G}}_{EJ}^{tt}(r,r') \square J_t(r') dr \qquad (2.6.27)$$

$$\vec{H}_t(x,y,z) = \vec{H}_t(r) = \int_{S'} \bar{\bar{G}}_{HJ}^{tt}(r,r') \square J_t(r') dr \qquad (2.6.28)$$

$$\vec{E}_t(r) = \int_{S'} \sum_{p}^{TE,TM} \sum_{mx=0}^{\infty} \sum_{my=-\infty}^{\infty} \vec{X}_m^{(p)}(x') Y_m^{(p)}(y') \hat{V}_m^{(p)}(z) \cdot \vec{e}_{mx}^{(p)}(x) e^{-jk_{my}y} \square \vec{J}_t(r') dr \qquad (2.6.29)$$

$$\vec{H}_t(r) = \int_{S'} \sum_{p}^{TE,TM} \sum_{mx=0}^{\infty} \sum_{my=-\infty}^{\infty} \vec{X}_m^{(p)}(x') Y_m^{(p)}(y') \hat{I}_m^{(p)}(z) \cdot \vec{h}_{mx}^{(p)}(x) e^{-jk_{my}y} \square \vec{J}_t(r') dr \qquad (2.6.30)$$

It can be resumed in one coefficient the contributions from the PPModes and the Floquet modes to the fields, for every combination between them:

$$A_m^{(p)} = \int_{S'} \vec{X}_m^{(p)}(x') Y_m^{(p)}(y') \square \vec{J}_t(r') = \qquad (2.6.31)$$

$$= \int_{S'} \frac{\vec{e}_{mx}^{x,(p)*}(x') - C_m \vec{e}_{mx}^{x,(q)*}(x')}{1 - C_m^2} Y_m^{(p)}(y') J_t^x(r') + \int_{S'} \frac{\vec{e}_{mx}^{y,(p)*}(x') - C_m \vec{e}_{mx}^{y,(q)*}(x')}{1 - C_m^2} Y_m^{(p)}(y') J_t^y(r')$$

$$\vec{E}_t(r) = \sum_{p}^{TE,TM} \sum_{mx=0}^{\infty} \sum_{my=-\infty}^{\infty} A_m^{(p)} \hat{V}_m^{(p)}(z) \cdot \vec{e}_{mx}^{(p)}(x) e^{-jk_{my}y} \qquad (2.6.32)$$

$$\vec{H}_t(r) = \sum_{p}^{TE,TM} \sum_{mx=0}^{\infty} \sum_{my=-\infty}^{\infty} A_m^{(p)} \hat{I}_m^{(p)}(z) \cdot \vec{h}_{mx}^{(p)}(x) e^{-jk_{my}y} \qquad (2.6.33)$$

From the transverse fields, the longitudinal electric and magnetic fields can be derived. This relation is expressed in the longitudinal Maxwell Equations:

$$\vec{H}_z = \frac{\vec{\nabla}_t (\hat{z} \times \vec{E}_t)}{j\omega\mu} \qquad (2.6.34)$$

$$\vec{E}_z = \frac{\vec{\nabla}_t (\vec{H}_t \times \hat{z})}{j\omega\varepsilon} \qquad (2.6.35)$$

In the first place, the electric field is obtained:

$$\vec{E}_z = \frac{\vec{\nabla}_t(\vec{H}_t \times \hat{z})}{j\omega\varepsilon} = \frac{1}{j\omega\varepsilon}\vec{\nabla}_t\left(\sum_{p}^{TE,TM}\sum_{mx=0}^{\infty}\sum_{my=-\infty}^{\infty} A_m^{(p)}\hat{I}_m^{(p)}(z)\cdot\vec{h}_{mx}^{(p)}(x)e^{-jk_{my}y}\times\hat{z}\right) =$$

$$= \frac{1}{j\omega\varepsilon}\sum_{p}^{TE,TM}\sum_{mx=0}^{\infty}\sum_{my=-\infty}^{\infty} A_m^{(p)}\hat{I}_m^{(p)}(z)\cdot\vec{\nabla}_t\left(\vec{h}_{mx}^{(p)}(x)e^{-jk_{my}y}\times\hat{z}\right) = \left\{\vec{h}_{mx}^{(p)}\times\hat{z} = \vec{e}_{mx}^{(p)}\right\} =$$

$$= \frac{1}{j\omega\varepsilon}\sum_{p}^{TE,TM}\sum_{mx=0}^{\infty}\sum_{my=-\infty}^{\infty} A_m^{(p)}\hat{I}_m^{(p)}(z)\cdot\vec{\nabla}_t\left(\vec{e}_{mx}^{(p)}(x)\cdot e^{-jk_{my}y}\right) \qquad (2.6.36)$$

Applying: $\vec{\nabla}_t\cdot\vec{e}_{mx}^{TE}(x) = 0$

$$\vec{\nabla}_t\cdot\vec{e}_{mx}^{TM}(x) = k_{cm}^2\hat{\phi}_{mx}^{TM}(x)$$

$$\boxed{\vec{E}_z = \frac{1}{j\omega\varepsilon}\sum_{mx=0}^{\infty}\sum_{my=-\infty}^{\infty} A_m^{TM}\hat{I}_m^{TM}(z)k_{cm}^2\hat{\phi}_{mx}^{TM}(x)e^{-jk_{my}y}} \qquad (2.6.37)$$

where $\hat{\phi}_{mx}^{TM}(x) = \dfrac{-\sin(k_{mx}x)}{N_m}$

$$\vec{H}_z = \frac{\vec{\nabla}_t(\hat{z}\times\vec{E}_t)}{j\omega\mu} = \frac{1}{j\omega\mu}\vec{\nabla}_t\left(\hat{z}\times\sum_{p}^{TE,TM}\sum_{mx=0}^{\infty}\sum_{my=-\infty}^{\infty} A_m^{(p)}\hat{V}_m^{(p)}(z)\cdot\vec{e}_{mx}^{(p)}(x)e^{-jk_{my}y}\right) =$$

$$= \frac{1}{j\omega\mu}\sum_{p}^{TE,TM}\sum_{mx=0}^{\infty}\sum_{my=-\infty}^{\infty} A_m^{(p)}\hat{V}_m^{(p)}(z)\cdot\vec{\nabla}_t\left(\hat{z}\times\vec{e}_{mx}^{(p)}(x)e^{-jk_{my}y}\right) = \left\{\vec{h}_{mx}^{(p)} = \hat{z}\times\vec{e}_{mx}^{(p)}\right\} =$$

$$= \frac{1}{j\omega\mu}\sum_{p}^{TE,TM}\sum_{mx=0}^{\infty}\sum_{my=-\infty}^{\infty} A_m^{(p)}\hat{V}_m^{(p)}(z)\cdot\vec{\nabla}_t\left(\vec{h}_{mx}^{(p)}(x)e^{-jk_{my}y}\right) \qquad (2.6.38)$$

Applying: $\vec{\nabla}_t\cdot\vec{h}_{mx}^{TE}(x) = k_{cm}^2\hat{\phi}_{mx}^{TE}(x)$

$$\vec{\nabla}_t\cdot\vec{h}_{mx}^{TM}(x) = 0$$

$$\boxed{\vec{H}_z = \frac{1}{j\omega\mu}\sum_{mx=0}^{\infty}\sum_{my=-\infty}^{\infty} A_m^{TE}\hat{V}_m^{TE}(z)k_{cm}^2\hat{\phi}_{mx}^{TE}(x)e^{-jk_{my}y}} \qquad (2.6.39)$$

where $\hat{\phi}_{mx}^{TE}(x) = \dfrac{-\cos(k_{mx}x)}{N_m}$.

From the expressions of the longitudinal fields it can be deduced the longitudinal Green Functions:

$$\bar{G}_{EJ}^{zt}(r,r') = \frac{1}{j\omega\varepsilon}\sum_{mx=0}^{\infty}\sum_{my=-\infty}^{\infty}\hat{I}_m^{TM}(z)\vec{X}_m^{TM}(x')Y_m^{TM}(y')k_{cm}^2\hat{\phi}_{mx}^{TM}(x)e^{-jk_{my}y} \quad (2.6.40)$$

$$\bar{G}_{HJ}^{zt}(r,r') = \frac{1}{j\omega\mu}\sum_{mx=0}^{\infty}\sum_{my=-\infty}^{\infty}\hat{V}_m^{TE}(z)\vec{X}_m^{TE}(x')Y_m^{TE}(y')k_{cm}^2\hat{\phi}_{mx}^{TE}(x)e^{-jk_{my}y} \quad (2.6.41)$$

WORKOUT 6

Zone 1: +L

$$\hat{V}_m^{(p)}(z) = \frac{V_m^{(p)}(z)}{j_m^{(p)}} = \hat{V}_m^{(p)+}(0^+)\cdot e^{-jk_{zm}^{VAC}z} + \hat{V}_m^{(p)-}(0^+)\cdot e^{+jk_{zm}^{VAC}z} \quad (2.7.6)$$

$$\hat{V}_m^{(p)+}(0^+) = \frac{\hat{V}_m^{(p)}(0^+)}{1+\rho_{RADm}^{(p)}\cdot e^{-j2k_{zm}^{VAC}L}} \quad (2.7.7) \qquad \hat{V}_m^{(p)-}(0^+) = \rho_{RADm}^{(p)}\cdot\hat{V}_m^{(p)+}(0^+)\cdot e^{-j2k_{zm}^{VAC}L} \quad (2.7.8)$$

$$\hat{V}_m^{(p)}(0^+) = \frac{Z_{Lm}^{(p)}\cdot Z_{Dm}^{(p)}}{Z_{Lm}^{(p)}+Z_{Dm}^{(p)}} \quad (2.7.9)$$

$$\hat{I}_m^{(p)}(z) = \frac{I_m^{(p)}(z)}{j_m^{(p)}} = \hat{I}_m^{(p)+}(0^+)\cdot e^{-jk_{zm}^{VAC}z} - \hat{I}_m^{(p)-}(0^+)\cdot e^{+jk_{zm}^{VAC}z} \quad (2.7.10)$$

$$\hat{I}_m^{(p)+}(0^+) = \frac{\hat{I}_m^{(p)}(0^+)}{1-\rho_{RADm}^{(p)}\cdot e^{-j2k_{zm}^{VAC}L}} \quad (2.7.11) \qquad \hat{I}_m^{(p)-}(0^+) = \rho_{RADm}^{(p)}\cdot\hat{I}_m^{(p)+}(0^+)\cdot e^{-j2k_{zm}^{VAC}L} \quad (2.7.12)$$

$$\hat{I}_m^{(p)}(0^+) = \frac{Z_{Dm}^{(p)}}{Z_{Lm}^{(p)}+Z_{Dm}^{(p)}} \quad (2.7.13)$$

Zone 2: -D

$$\hat{V}_m^{(p)}(z) = \frac{V_m^{(p)}(z)}{j_m^{(p)}} = \hat{V}_m^{(p)+}(0^-)\cdot e^{+jk_{zm}^{DIE}z} + \hat{V}_m^{(p)-}(0^-)\cdot e^{-jk_{zm}^{DIE}z} \quad (2.7.14)$$

$$\hat{V}_m^{(p)+}(0^-) = \frac{\hat{V}_m^{(p)}(0^-)}{1+\rho_{DIEm}^{(p)}\cdot e^{-j2k_{zm}^{DIE}D}} \quad (2.7.15) \qquad \hat{V}_m^{(p)-}(0^-) = \rho_{DIEm}^{(p)}\cdot\hat{V}_m^{(p)+}(0^-)\cdot e^{-j2k_{zm}^{DIE}D} \quad (2.7.16)$$

$$\hat{V}_m^{(p)}(0^-) = \hat{V}_m^{(p)}(0^+) = \frac{Z_{Lm}^{(p)}\cdot Z_{Dm}^{(p)}}{Z_{Lm}^{(p)}+Z_{Dm}^{(p)}} \quad (2.7.17)$$

$$\hat{I}_m^{(p)}(z) = \frac{I_m^{(p)}(z)}{j_m^{(p)}} = \hat{I}_m^{(p)+}(0^-)\cdot e^{+jk_{zm}^{DIE}z} - \hat{I}_m^{(p)-}(0^-)\cdot e^{-jk_{zm}^{DIE}z} \qquad (2.7.18)$$

$$\hat{I}_m^{(p)+}(0^-) = \frac{\hat{I}_m^{(p)}(0^-)}{1-\rho_{DIEm}^{(p)}\cdot e^{-j2k_{zm}^{DIE}D}} \qquad (2.7.19) \qquad \hat{I}_m^{(p)-}(0^-) = \rho_{DIEm}^{(p)}\cdot \hat{I}_m^{(p)+}(0^+)\cdot e^{-j2k_{zm}^{DIE}D} \qquad (2.7.20)$$

$$\hat{I}_m^{(p)}(0^-) = \frac{Z_{Lm}^{(p)}}{Z_{Lm}^{(p)} + Z_{Dm}^{(p)}} \qquad (2.7.21)$$

Zone 3: -D-H

$$\hat{V}_m^{(p)}(z) = \frac{V_m^{(p)}(z)}{j_m^{(p)}} = \hat{V}_m^{(p)+}(D)\cdot e^{+jk_{zm}^{VAC}(z+D)} + \hat{V}_m^{(p)-}(D)\cdot e^{-jk_{zm}^{VAC}(z+D)} \qquad (2.7.22)$$

$$\hat{V}_m^{(p)+}(D) = \frac{\hat{V}_m^{(p)}(D)}{1+\rho_{CORTOm}^{(p)}\cdot e^{-j2k_{zm}^{VAC}H}} \qquad (2.7.23) \qquad \hat{V}_m^{(p)-}(D) = \rho_{CORTOm}^{(p)}\cdot \hat{V}_m^{(p)+}(D)\cdot e^{-j2k_{zm}^{VAC}H} \qquad (2.7.24)$$

$$\hat{V}_m^{(p)}(D) = \hat{V}_m^{(p)+}(0^-)\cdot e^{-jk_{zm}^{DIE}D} + \hat{V}_m^{(p)-}(0^-)\cdot e^{+jk_{zm}^{DIE}D} \qquad (2.7.25)$$

$$\hat{I}_m^{(p)}(z) = \frac{I_m^{(p)}(z)}{j_m^{(p)}} = \hat{I}_m^{(p)+}(D)\cdot e^{+j2k_{zm}^{VAC}(z+D)} - \hat{I}_m^{(p)-}(D)\cdot e^{-j2k_{zm}^{VAC}(z+D)} \qquad (2.7.26)$$

$$\hat{I}_m^{(p)+}(D) = \frac{\hat{I}_m^{(p)}(D)}{1-\rho_{CORTOm}^{(p)}\cdot e^{-j2k_{zm}^{VAC}H}} \qquad (2.7.27) \qquad \hat{I}_m^{(p)-}(D) = \rho_{CORTOm}^{(p)}\cdot \hat{I}_m^{(p)+}(D)\cdot e^{-j2k_{zm}^{VAC}H} \qquad (2.7.28)$$

$$\hat{I}_m^{(p)}(D) = \hat{I}_m^{(p)+}(0^-)\cdot e^{-jk_{zm}^{DIE}D} + \hat{I}_m^{(p)-}(0^-)\cdot e^{+jk_{zm}^{DIE}D} \qquad (2.7.29)$$

$$Z_{Lm}^{(p)} = Z_{0m}^{(p)^{VAC}}\,\frac{Z_{RADm}^{(p)} + j\cdot Z_{0m}^{(p)^{VAC}}\cdot\tan(k_{zm}^{VAC}\cdot L)}{Z_{0m}^{(p)^{VAC}} + j\cdot Z_{RADm}^{(p)}\cdot\tan(k_{zm}^{VAC}\cdot L)} \qquad (2.7.30)$$

$$Z_{Dm}^{(p)} = Z_{0m}^{(p)^{DIE}}\,\frac{Z_{Hm}^{(p)} + j\cdot Z_{0m}^{(p)^{DIE}}\cdot\tan(k_{zm}^{DIE}\cdot D)}{Z_{0m}^{(p)^{DIE}} + j\cdot Z_{Hm}^{(p)}\cdot\tan(k_{zm}^{DIE}\cdot D)} \qquad (2.7.31)$$

$$Z_{Hm}^{(p)} = j\cdot Z_{0m}^{(p)^{VAC}}\cdot\tan(k_{zm}^{VAC}\cdot H) \qquad (2.7.32)$$

$$\rho_{RADm}^{(p)} = \frac{Z_{RADm}^{(p)} - Z_{0m}^{(p)^{VAC}}}{Z_{RADm}^{(p)} + Z_{0m}^{(p)^{VAC}}} \qquad (2.7.33)$$

$$\rho_{DIEm}^{(p)} = \frac{Z_{Hm}^{(p)} - Z_{0m}^{(p)^{DIE}}}{Z_{Hm}^{(p)} + Z_{0m}^{(p)^{DIE}}} \qquad (2.7.34)$$

$$\rho_{CORTOm}^{(p)} = -1 \qquad (2.7.35)$$

WORKOUT 7

To solve the integral equation, the field variations in $\hat{x}$ and $\hat{y}$ will be considered partly. In first place the variation in $\hat{x}$:

$$\int_r \vec{E}t(x,y,0)\cdot f_{lx}^{X}(x)\cdot g_{ly}^{X}(y)\cdot \partial r =$$

$$= \int_r \sum_{p}^{TE,TM}\sum_{mx=0}^{\infty}\sum_{my=-\infty}^{\infty} A_m^{(p)}\hat{V}_m^{(p)}(0)\cdot \vec{e}_{mx}^{(p)}(x)e^{-jk_{my}y}\cdot f_{lx}^{X}(x)\cdot g_{ly}^{X}(y)\cdot \partial r =$$

$$= \int_r \sum_{p}^{TE,TM}\sum_{mx=0}^{\infty}\sum_{my=-\infty}^{\infty} \hat{V}_m^{(p)}(0)\cdot \vec{e}_{mx}^{(p)}(x)e^{-jk_{my}y}\cdot$$

$$\cdot\left[\begin{array}{l}\sum_{Bx=0}^{Cx}\beta_{Bx}^{X}\int_{r'}\vec{X}_{mx}^{(p)}(x')Y_m^{(p)}(y')f_{nx}^{X}(x')g_{ny}^{X}(y')e^{-jk_{y0}y'}\partial r' \\ +\sum_{By=0}^{Cy}\beta_{By}^{Y}\int_{r'}\vec{X}_{mx}^{(p)}(x')Y_m^{(p)}(y')f_{nx}^{Y}(x')g_{ny}^{Y}(y')e^{-jk_{y0}y'}\partial r'\end{array}\right]\cdot f_{lx}^{X}(x)\cdot g_{ly}^{X}(y)\cdot\partial r =$$

$$= \sum_{p}^{TE,TM}\sum_{mx=0}^{\infty}\sum_{my=-\infty}^{\infty}\hat{V}_m^{(p)}(0)\cdot[\sum_{Bx=0}^{Cx}\beta_{Bx}^{X}$$

$$\int_r\int_{r'}\vec{X}_{mx}^{(p)}(x')Y_m^{(p)}(y')f_{nx}^{X}(x')g_{ny}^{X}(y')\vec{e}_{mx}^{(p)}(x)e^{-jk_{my}y}e^{-jk_{y0}y'}f_{lx}^{X}(x)g_{ly}^{X}(y)\partial r'\partial r +$$

$$+\sum_{By=0}^{Cy}\beta_{By}^{Y}\int_r\int_{r'}\vec{X}_{mx}^{(p)}(x')Y_m^{(p)}(y')f_{nx}^{Y}(x')g_{ny}^{Y}(y')\vec{e}_{mx}^{(p)}(x)e^{-jk_{my}y}e^{-jk_{y0}y'}f_{lx}^{X}(x)g_{ly}^{X}(y)\partial r'\partial r] =$$

$$= \sum_{p}^{TE,TM}\sum_{mx=0}^{\infty}\sum_{my=-\infty}^{\infty}\hat{V}_m^{(p)}(0)\cdot[\sum_{Bx=0}^{Cx}\beta_{Bx}^{X}(I_{BX}^{EX}\cdot I_{BY}^{EX}\cdot I_{TX}^{EX}\cdot I_{TY}^{EX})+$$

$$+\sum_{By=0}^{Cy}\beta_{By}^{Y}(I_{BX}^{EY}\cdot I_{BY}^{EY}\cdot I_{TX}^{EX}\cdot I_{TY}^{EX})] \qquad (2.8.2.4)$$

Now the test for the field variation in $\hat{y}$:

$$\int_r \vec{E}t(x,y,0)\cdot f_{lx}^{Y}(x)\cdot g_{ly}^{Y}(y)\cdot \partial r =$$

$$= \int_r \sum_{p}^{TE,TM}\sum_{mx=0}^{\infty}\sum_{my=-\infty}^{\infty} A_m^{(p)}\hat{V}_m^{(p)}(0)\cdot \vec{e}_{mx}^{(p)}(x)e^{-jk_{my}y}\cdot f_{lx}^{Y}(x)\cdot g_{ly}^{Y}(y)\cdot \partial r =$$

$$= \sum_{p}^{TE,TM}\sum_{mx=0}^{\infty}\sum_{my=-\infty}^{\infty}\hat{V}_m^{(p)}(0)\cdot[\sum_{Bx=0}^{Cx}\beta_{Bx}^{X}$$

$$\int_r\int_{r'}\vec{X}_{mx}^{(p)}(x')Y_m^{(p)}(y')f_{nx}^{X}(x')g_{ny}^{X}(y')\vec{e}_{mx}^{(p)}(x)e^{-jk_{my}y}e^{-jk_{y0}y'}f_{lx}^{Y}(x)g_{ly}^{Y}(y)\partial r'\partial r +$$

$$+\sum_{By=0}^{Cy}\beta_{By}^{Y}\int_{r}\int_{r'}\vec{X}_{mx}^{(p)}(x')Y_{m}^{(p)}(y')f_{nx}^{Y}(x')g_{ny}^{Y}(y')\vec{e}_{mx}^{(p)}(x)e^{-jk_{my}y}e^{-jk_{y0}y'}f_{lx}^{Y}(x)g_{ly}^{Y}(y)\partial r'\partial r]=$$

$$=\sum_{p}^{TE,TM}\sum_{mx=0}^{\infty}\sum_{my=-\infty}^{\infty}\hat{V}_{m}^{(p)}(0)\cdot[\sum_{Bx=0}^{Cx}\beta_{Bx}^{X}(I_{BX}^{EX}\cdot I_{BY}^{EX}\cdot I_{TX}^{EY}\cdot I_{TY}^{EY})+$$

$$+\sum_{By=0}^{Cy}\beta_{By}^{Y}(I_{BX}^{EY}\cdot I_{BY}^{EY}\cdot I_{TX}^{EY}\cdot I_{TY}^{EY})] \qquad (2.8.2.5)$$

WORKOUT 8

Before working out the expressions for both the basis and test integrals for the entire domain basis functions, it may be useful remember some of the expressions derived so far in previous sections:

$$\bar{X}_{mx}^{(p)}(x)=\frac{\vec{e}_{mx}^{(p)*}(x)-C_m\cdot\vec{e}_{mx}^{(q)*}(x)}{1-C_m^2} \quad (2.6.23) \qquad Y_{my}(y)=\frac{e^{-jk_{ym}y}}{P} \quad (2.6.24)$$

From eqs, (2.2.6) and (2.2.7), can be directly obtained:

$$e_{mx}^{X^{TE}}(x)=\frac{-jk_{my}}{N_m}\cos\left(mx\frac{\pi}{a}x\right) \qquad e_{mx}^{Y^{TE}}(x)=\frac{mx\frac{\pi}{a}}{N_m}\sin\left(mx\frac{\pi}{a}x\right)$$

$$e_{mx}^{X^{TM}}(x)=\frac{mx\frac{\pi}{a}}{N_m}\cos\left(mx\frac{\pi}{a}x\right) \qquad e_{mx}^{Y^{TM}}(x)=\frac{-jk_{my}}{N_m}\sin\left(mx\frac{\pi}{a}x\right)$$

$$N_m=\sqrt{\frac{a}{2}}\delta\cdot\sqrt{k_{xm}{}^2+\left|k_{ym}\right|^2} \qquad \text{with } \delta=1 \text{ if m=n>0 or } \delta=2 \text{ if m=n=0} \qquad (2.2.14)$$

$$C_m=\frac{jk_{xm}(k_{ym}-k_{ym}^{*})}{\left|N_m\right|^2}\frac{a}{2}\delta \qquad \text{with } \delta=1 \text{ if m=n>0 or } \delta=2 \text{ if m=n=0} \qquad (2.2.16)$$

The basis integrals result as follows (references to equations are not required from this point on):

$$I_{BX}^{EX}=\int_{x'}\bar{X}_{m}^{(p)}(x')\cdot\hat{x}\cdot f_{nx}^{X}(x')dx'=\begin{cases}I_{BX}^{EX}(p=TE)=\dfrac{1}{N_m(1-C_m^2)}\left(jk_{my}-C_m mx\dfrac{\pi}{a}\right)\cdot I_1\\ I_{BX}^{EX}(p=TM)=\dfrac{1}{N_m(1-C_m^2)}\left(mx\dfrac{\pi}{a}-C_m jk_{my}\right)\cdot I_1\end{cases}$$

$$I_{BY}^{EX} = \int_{y'} Y_{my}(y') \cdot g_{ny}^{X}(y') \cdot e^{-jk_0 y'} dy' = \frac{1}{P} \cdot I_2$$

$$I_{BX}^{EY} = \int_{x'} \bar{X}_m^{(p)}(x') \cdot \hat{y} \cdot f_{nx}^{Y}(x') dx' = \begin{cases} I_{BX}^{EY}(p = TE) = \dfrac{1}{N_m(1 - C_m^2)} \left(mx \dfrac{\pi}{a} - C_m jk_{my} \right) \cdot I_3 \\ I_{BX}^{EY}(p = TM) = \dfrac{1}{N_m(1 - C_m^2)} \left(jk_{my} - C_m mx \dfrac{\pi}{a} \right) \cdot I_3 \end{cases}$$

$$I_{BY}^{EY} = \int_{y'} Y_{my}(y') \cdot g_{ny}^{Y}(y') \cdot e^{-jk_0 y'} dy' = \frac{1}{P} \cdot I_4$$

The same way, the resolution for test integrals is shown below:

$$I_{TX}^{EX} = \int_{x} e_{mx}^{(p)}(x) \cdot \hat{x} \cdot f_{lx}^{X}(x) dx = \begin{cases} I_{TX}^{EX}(p = TE) = \dfrac{-jk_{my}}{N_m} \cdot I_1 \\ I_{TX}^{EX}(p = TM) = \dfrac{mx \dfrac{\pi}{a}}{N_m} \cdot I_1 \end{cases}$$

$$I_{TY}^{EX} = \int_{y} e^{-jk_{my} y} \cdot g_{ly}^{X}(y) dy = I_2$$

$$I_{TX}^{EY} = \int_{x'} e_{mx}^{(p)}(x) \cdot \hat{y} \cdot f_{lx}^{Y}(x) dx = \begin{cases} I_{TX}^{EY}(p = TE) = \dfrac{mx \dfrac{\pi}{a}}{N_m} \cdot I_3 \\ I_{TX}^{EY}(p = TM) = \dfrac{-jk_{my}}{N_m} \cdot I_3 \end{cases}$$

$$I_{TY}^{EY} = \int_{y'} e^{-jk_{my} y} \cdot g_{ly}^{Y}(y) dy = I_4$$

The so called temporal integrals (I_1, I_2, I_3, I_4) are taken from the main integrals since they are common for the basis and test integrals, and it makes more “handy” not only its resolution, but the forthcoming coding stage. These integrals are solved using a notation that may vary depending on the integrals they come from, basis or test.

$$I_1 = \int_{x1}^{x2} \cos\left(mx \frac{\pi}{a} \right) \sin\left(nx \frac{\pi}{W} (x - x1) \right) dx = \frac{aW}{\pi} \frac{1}{mx^2 W^2 - nx^2 a^2} \cdot$$

$$\left[\begin{array}{l} nx\cdot a\cdot\cos\left(\frac{\pi mx}{a}x2\right)\cos\left(\frac{\pi nx}{W}x2\right)\cos\left(\frac{\pi nx}{W}x1\right)+ \\ +mx\cdot W\cdot\sin\left(\frac{\pi mx}{a}x2\right)\sin\left(\frac{\pi nx}{W}x2\right)\cos\left(\frac{\pi nx}{W}x1\right)-mx\cdot W\cdot\sin\left(\frac{\pi mx}{a}x2\right)\cos\left(\frac{\pi nx}{W}x2\right)sen\left(\frac{\pi nx}{W}x1\right)+ \\ +nx\cdot a\cdot\cos\left(\frac{\pi mx}{a}x2\right)\sin\left(\frac{\pi nx}{W}x2\right)\sin\left(\frac{\pi nx}{W}x1\right)-nx\cdot a\cdot\cos\left(\frac{\pi mx}{a}x1\right) \end{array}\right]$$

$$I_3=\int_{x1}^{x2}\sin\left(mx\frac{\pi}{a}\right)\cos\left(nx\frac{\pi}{W}(x-x1)\right)dx=\frac{aW}{\pi}\frac{-1}{mx^2W^2-nx^2a^2}\cdot$$

$$\left[\begin{array}{l} nx\cdot a\cdot\sin\left(\frac{\pi mx}{a}x2\right)\sin\left(\frac{\pi nx}{W}x2\right)\cos\left(\frac{\pi nx}{W}x1\right)+ \\ +mx\cdot W\cdot\cos\left(\frac{\pi mx}{a}x2\right)\cos\left(\frac{\pi nx}{W}x2\right)\cos\left(\frac{\pi nx}{W}x1\right)+mx\cdot W\cdot\cos\left(\frac{\pi mx}{a}x2\right)\sin\left(\frac{\pi nx}{W}x2\right)\sin\left(\frac{\pi nx}{W}x1\right)- \\ -nx\cdot a\cdot\sin\left(\frac{\pi mx}{a}x2\right)\cos\left(\frac{\pi nx}{W}x2\right)\sin\left(\frac{\pi nx}{W}x1\right)-mx\cdot W\cdot\cos\left(\frac{\pi mx}{a}x1\right) \end{array}\right]$$

In the case in which $mx\cdot W=nx\cdot a$, the integrals result as follows:

$$I_1=\int_{x1}^{x2}\cos\left(mx\frac{\pi}{a}\right)\sin\left(nx\frac{\pi}{W}(x-x1)\right)dx=\frac{W}{2\pi\cdot nx}\cdot$$

$$\left[\begin{array}{l} -\cos\left(\frac{\pi nx}{W}x1\right)\cos^2\left(\frac{\pi nx}{W}x2\right)+\cos\left(\frac{\pi nx}{W}x1\right)- \\ -\sin\left(\frac{\pi nx}{W}x1\right)\sin\left(\frac{\pi nx}{W}x2\right)\cos\left(\frac{\pi nx}{W}x2\right)-\sin\left(\frac{\pi nx}{W}x1\right)\frac{\pi nx}{W}x2+ \\ +\sin\left(\frac{\pi nx}{W}x1\right)\frac{\pi nx}{W}x1 \end{array}\right]$$

$$I_3=\int_{x1}^{x2}\sin\left(mx\frac{\pi}{a}\right)\cos\left(nx\frac{\pi}{W}(x-x1)\right)dx=\frac{-W}{2\pi\cdot nx}\cdot$$

$$\left[\begin{array}{l} \cos\left(\frac{\pi nx}{W}x1\right)\cos^2\left(\frac{\pi nx}{W}x2\right)-\cos\left(\frac{\pi nx}{W}x1\right)+ \\ +\sin\left(\frac{\pi nx}{W}x1\right)\sin\left(\frac{\pi nx}{W}x2\right)\cos\left(\frac{\pi nx}{W}x2\right)-\sin\left(\frac{\pi nx}{W}x1\right)\frac{\pi nx}{W}x2+ \\ +\sin\left(\frac{\pi nx}{W}x1\right)\frac{\pi nx}{W}x1 \end{array}\right]$$

$$I_2 = \int_0^Q \cos\left(ny\frac{\pi}{Q}y \right) e^{-jk_{my}y} dy = \frac{Q\left(-jk_{my}Qe^{-jk_{my}Q}\cos(\pi n_y) + jk_{my}Q + \pi n_y e^{-jk_{my}Q}\sin(\pi n_y) \right)}{\pi^2 n_y^2 - k_{my}^2 Q^2}$$

$$I_4 = \int_0^Q \sin\left(ny\frac{\pi}{Q}y \right) e^{-jk_{my}y} dy = \frac{-Q\left(\pi n_y e^{-jk_{my}Q}\cos(\pi n_y) + jk_{my}Qe^{-jk_{my}Q}\sin(\pi n_y) - \pi n_y \right)}{\pi^2 n_y^2 - k_{my}^2 Q^2}$$

In the case in which $\pi n_y = k_{my}Q$, the integrals result as follows:

$$I_2 = \frac{1}{2k_{my}}\left(\sin(k_{my}Q)\cos(k_{my}Q) + k_{my}Q + j\cos^2(k_{my}Q) - j \right)$$

$$I_4 = \frac{1}{2k_{my}}\left(j\sin(k_{my}Q)\cos(k_{my}Q) + k_{my}Q - \cos^2(\pi n_y) - jk_{my}Q + 1 \right)$$

WORKOUT 9

It can be noticed that $I_{BY}^{EX} = I_{BY}^{EY}$ and $I_{TY}^{EX} = I_{TY}^{EY}$.

$$\boxed{I_{BX}^{EX} = \int_{x'} \bar{X}_m^{(p)}(x') \cdot \hat{x} \cdot f(x')dx' = \int_{x'} \frac{e_{mx}^{X(p)*}(x) - C_m \cdot e_{mx}^{X(q)*}(x)}{1 - C_m^2} \cdot f(x')dx'}$$

For the ascending ramp:

$$I_{BX}^{EX}(p = TE) = \int_{x'} \bar{X}_m^{(p)}(x') \cdot \hat{x} \cdot f(x')dx' = \int_{x'} \frac{e_{mx}^{X^{TE}*}(x) - C_m \cdot e_{mx}^{X^{TM}*}(x)}{1 - C_m^2} \cdot \frac{x' - x'_{n-1}}{x'_n - x'_{n-1}} dx' =$$

$$= \int_{x'_{n-1}}^{x'_n} \frac{1}{1 - C_m^2}\left(\frac{jk_{my}}{N_m}\cos\left(mx\frac{\pi}{a}x \right) - C_m \cdot \frac{mx\frac{\pi}{a}}{N_m}\cos\left(mx\frac{\pi}{a}x \right) \right) \cdot \frac{x' - x'_{n-1}}{x'_n - x'_{n-1}} dx' =$$

$$= \frac{1}{\left(1 - C_m^2\right)\left(x'_n - x'_{n-1}\right)}\left(\frac{jk_{my}}{N_m} - C_m \cdot \frac{mx\frac{\pi}{a}}{N_m} \right)$$

$$\left(\frac{x'_n}{mx\frac{\pi}{a}}\sin\left(mx\frac{\pi}{a}x'_n\right)-\frac{x'_{n-1}}{mx\frac{\pi}{a}}\sin\left(mx\frac{\pi}{a}x'_{n-1}\right)+\frac{1}{mx^2\frac{\pi^2}{a^2}}\left(\cos\left(mx\frac{\pi}{a}x'_n\right)-\cos\left(mx\frac{\pi}{a}x'_{n-1}\right)\right)\right)-$$

$$-\frac{1}{\left(1-C_m^2\right)\left(x'_n-x'_{n-1}\right)}\left(\frac{jk_{my}}{N_m}x'_{n-1}-C_m\cdot\frac{mx\frac{\pi}{a}}{N_m}x'_{n-1}\right)\frac{1}{mx\frac{\pi}{a}}\left(\sin\left(mx\frac{\pi}{a}x'_n\right)-\sin\left(mx\frac{\pi}{a}x'_{n-1}\right)\right)$$

$$I_{BX}^{EX}(p=TM)=\int_{x'}\bar{X}_m^{(p)}(x')\cdot\hat{x}\cdot f(x')dx'=\int_{x'}\frac{e_{mx}^{X^{TM}*}(x)-C_m\cdot e_{mx}^{X^{TE}*}(x)}{1-C_m^2}\cdot\frac{x'-x'_{n-1}}{x'_n-x'_{n-1}}dx'=$$

$$=\int_{x'_{n-1}}^{x'_n}\frac{1}{1-C_m^2}\left(\frac{mx\frac{\pi}{a}}{N_m}\cos\left(mx\frac{\pi}{a}x\right)-C_m\cdot\frac{jk_{my}}{N_m}\cos\left(mx\frac{\pi}{a}x\right)\right)\cdot\frac{x'-x'_{n-1}}{x'_n-x'_{n-1}}dx'=$$

$$=\frac{1}{\left(1-C_m^2\right)\left(x'_n-x'_{n-1}\right)}\left(\frac{mx\frac{\pi}{a}}{N_m}-C_m\cdot\frac{jk_{my}}{N_m}\right)$$

$$\left(\frac{x'_n}{mx\frac{\pi}{a}}\sin\left(mx\frac{\pi}{a}x'_n\right)-\frac{x'_{n-1}}{mx\frac{\pi}{a}}\sin\left(mx\frac{\pi}{a}x'_{n-1}\right)+\frac{1}{mx^2\frac{\pi^2}{a^2}}\left(\cos\left(mx\frac{\pi}{a}x'_n\right)-\cos\left(mx\frac{\pi}{a}x'_{n-1}\right)\right)\right)-$$

$$-\frac{1}{\left(1-C_m^2\right)\left(x'_n-x'_{n-1}\right)}\left(\frac{mx\frac{\pi}{a}}{N_m}x'_{n-1}-C_m\frac{jk_{my}}{N_m}\cdot x'_{n-1}\right)\frac{1}{mx\frac{\pi}{a}}\left(\sin\left(mx\frac{\pi}{a}x'_n\right)-\sin\left(mx\frac{\pi}{a}x'_{n-1}\right)\right)$$

For the descending ramp:

$$I_{BX}^{EX}(p=TE)=\int_{x'}\bar{X}_m^{(p)}(x')\cdot\hat{x}\cdot f(x')dx'=\int_{x'}\frac{e_{mx}^{X^{TE}*}(x)-C_m\cdot e_{mx}^{X^{TM}*}(x)}{1-C_m^2}\cdot\frac{x'_{n+1}-x'}{x'_{n+1}-x'_n}dx'=$$

$$=\int_{x'_n}^{x'_{n+1}}\frac{1}{1-C_m^2}\left(\frac{jk_{my}}{N_m}\cos\left(mx\frac{\pi}{a}x\right)-C_m\cdot\frac{mx\frac{\pi}{a}}{N_m}\cos\left(mx\frac{\pi}{a}x\right)\right)\cdot\frac{x'_{n+1}-x'}{x'_{n+1}-x'_n}dx'=$$

$$= -\frac{1}{\left(1-C_m^2\right)\left(x'_{n+1}-x'_n\right)}\left(\frac{jk_{my}}{N_m}x'_{n+1}-C_m\frac{mx\frac{\pi}{a}}{N_m}\cdot x'_{n+1}\right)\frac{1}{mx\frac{\pi}{a}}\left(\sin\left(mx\frac{\pi}{a}x'_{n+1}\right)-\sin\left(mx\frac{\pi}{a}x'_n\right)\right)-$$

$$-\frac{1}{\left(1-C_m^2\right)\left(x'_{n+1}-x'_n\right)}\left(\frac{jk_{my}}{N_m}-C_m\cdot\frac{mx\frac{\pi}{a}}{N_m}\right)$$

$$\left(\frac{x'_{n+1}}{mx\frac{\pi}{a}}\sin\left(mx\frac{\pi}{a}x'_{n+1}\right)-\frac{x'_n}{mx\frac{\pi}{a}}\sin\left(mx\frac{\pi}{a}x'_n\right)+\frac{1}{mx^2\frac{\pi^2}{a^2}}\left(\cos\left(mx\frac{\pi}{a}x'_{n+1}\right)-\cos\left(mx\frac{\pi}{a}x'_n\right)\right)\right)$$

$$I_{BX}^{EX}(p=TM)=\int_{x'}\bar{X}_m^{(p)}(x')\cdot\hat{x}\cdot f(x')dx'=\int_{x'}\frac{e_{mx}^{X^{TM}*}(x)-C_m\cdot e_{mx}^{X^{TE}*}(x)}{1-C_m^2}\cdot\frac{x'_{n+1}-x'}{x'_{n+1}-x'_n}dx'=$$

$$=\int_{x'_n}^{x'_{n+1}}\frac{1}{1-C_m^2}\left(\frac{mx\frac{\pi}{a}}{N_m}\cos\left(mx\frac{\pi}{a}x\right)-C_m\cdot\frac{jk_{my}}{N_m}\cos\left(mx\frac{\pi}{a}x\right)\right)\cdot\frac{x'_{n+1}-x'}{x'_{n+1}-x'_n}dx'=$$

$$= -\frac{1}{\left(1-C_m^2\right)\left(x'_{n+1}-x'_n\right)}\left(\frac{mx\frac{\pi}{a}}{N_m}x'_{n+1}-C_m\frac{jk_{my}}{N_m}\cdot x'_{n+1}\right)\frac{1}{mx\frac{\pi}{a}}\left(\sin\left(mx\frac{\pi}{a}x'_{n+1}\right)-\sin\left(mx\frac{\pi}{a}x'_n\right)\right)-$$

$$-\frac{1}{\left(1-C_m^2\right)\left(x'_{n+1}-x'_n\right)}\left(\frac{mx\frac{\pi}{a}}{N_m}-C_m\cdot\frac{jk_{my}}{N_m}\right)$$

$$\left(\frac{x'_{n+1}}{mx\frac{\pi}{a}}\sin\left(mx\frac{\pi}{a}x'_{n+1}\right)-\frac{x'_n}{mx\frac{\pi}{a}}\sin\left(mx\frac{\pi}{a}x'_n\right)+\frac{1}{mx^2\frac{\pi^2}{a^2}}\left(\cos\left(mx\frac{\pi}{a}x'_{n+1}\right)-\cos\left(mx\frac{\pi}{a}x'_n\right)\right)\right)$$

$$I_{BY}^{EX} = \int_{y'} Y_{my}(y') \cdot f(y') \cdot e^{-jk_0 y'} dy' = \int_{y'} \frac{e^{-jk_{ym} y}}{P} \cdot f(y') \cdot e^{-jk_0 y'} dy'$$

For the ascending ramp:

$$= \frac{1}{P(y'_n - y'_{n-1})} \left(\left(\frac{y'_n}{-jk_{my}} + \frac{1}{k_{my}^2} \right) e^{-jk_{ym} y'_n} - \left(\frac{y'_{n-1}}{-jk_{my}} + \frac{1}{k_{my}^2} \right) e^{-jk_{ym} y'_{n-1}} - \frac{y'_{n-1}}{-jk_{my}} \left(e^{-jk_{ym} y'_n} - e^{-jk_{ym} y'_{n-1}} \right) \right)$$

For the descending ramp:

$$= \frac{1}{P(y'_{n+1} - y'_n)} \left(\frac{y'_{n+1}}{-jk_{my}} \left(e^{-jk_{ym} y'_{n+1}} - e^{-jk_{ym} y'_n} \right) - \left(\frac{y'_{n+1}}{-jk_{my}} + \frac{1}{k_{my}^2} \right) e^{-jk_{ym} y'_{n+1}} + \left(\frac{y'_n}{-jk_{my}} + \frac{1}{k_{my}^2} \right) e^{-jk_{ym} y'_n} \right)$$

$$I_{BX}^{EY} = \int_{x'} \bar{X}_m^{(p)}(x') \cdot \hat{y} \cdot f(x') dx' = \int_{x'} \frac{e_{mx}^{Y(p)*}(x) - C_m \cdot e_{mx}^{Y(q)*}(x)}{1 - C_m^2} \cdot f(x') dx'$$

For the ascending ramp:

$$I_{BX}^{EY}(p = TE) = \int_{x'} \bar{X}_m^{(p)}(x') \cdot \hat{y} \cdot f(x') dx' = \int_{x'} \frac{e_{mx}^{Y^{TE}*}(x) - C_m \cdot e_{mx}^{Y^{TM}*}(x)}{1 - C_m^2} \cdot \frac{x' - x'_{n-1}}{x'_n - x'_{n-1}} dx' =$$

$$= \int_{x'_{n-1}}^{x'_n} \frac{1}{1 - C_m^2} \left(\frac{mx\frac{\pi}{a}}{N_m} \sin\left(mx\frac{\pi}{a} x \right) - C_m \cdot \frac{jk_{my}}{N_m} \sin\left(mx\frac{\pi}{a} x \right) \right) \cdot \frac{x'_{n+1} - x'}{x'_{n+1} - x'_n} dx' =$$

$$= -\frac{1}{\left(1 - C_m^2\right)\left(x'_n - x'_{n-1}\right)} \left(\frac{mx\frac{\pi}{a}}{N_m} - C_m \frac{jk_{my}}{N_m} \right)$$

$$\left(\frac{-x'_n}{mx\frac{\pi}{a}} \cos\left(mx\frac{\pi}{a} x'_n \right) + \frac{x'_{n-1}}{mx\frac{\pi}{a}} \cos\left(mx\frac{\pi}{a} x'_{n-1} \right) + \frac{1}{mx^2 \frac{\pi^2}{a^2}} \left(\sin\left(mx\frac{\pi}{a} x'_n \right) - \sin\left(mx\frac{\pi}{a} x'_{n-1} \right) \right) \right) -$$

$$- \frac{1}{\left(1 - C_m^2\right)\left(x'_n - x'_{n-1}\right)} \left(\frac{mx\frac{\pi}{a}}{N_m} x'_{n-1} - C_m \frac{jk_{my}}{N_m} \cdot x'_{n-1} \right) \frac{-1}{mx\frac{\pi}{a}} \left(\cos\left(mx\frac{\pi}{a} x'_n \right) - \cos\left(mx\frac{\pi}{a} x'_{n-1} \right) \right)$$

$$I_{BX}^{EY}(p=TM)=\int_{x'}\bar{X}_m^{(p)}(x')\cdot\hat{y}\cdot f(x')dx'=\int_{x'}\frac{e_{mx}^{Y^{TM}*}(x)-C_m\cdot e_{mx}^{Y^{TE}*}(x)}{1-C_m^2}\cdot\frac{x'-x'_{n-1}}{x'_n-x'_{n-1}}dx'=$$

$$=\int_{x'_{n-1}}^{x'_n}\frac{1}{1-C_m^2}\left(\frac{jk_{my}}{N_m}\sin\left(mx\frac{\pi}{a}x\right)-C_m\cdot\frac{mx\frac{\pi}{a}}{N_m}\sin\left(mx\frac{\pi}{a}x\right)\right)\cdot\frac{x'-x'_{n-1}}{x'_n-x'_{n-1}}dx'=$$

$$=-\frac{1}{\left(1-C_m^2\right)\left(x'_n-x'_{n-1}\right)}\left(\frac{jk_{my}}{N_m}-C_m\frac{mx\frac{\pi}{a}}{N_m}\right)$$

$$\left(\frac{-x'_n}{mx\frac{\pi}{a}}\cos\left(mx\frac{\pi}{a}x'_n\right)+\frac{x'_{n-1}}{mx\frac{\pi}{a}}\cos\left(mx\frac{\pi}{a}x'_{n-1}\right)+\frac{1}{mx^2\frac{\pi^2}{a^2}}\left(\sin\left(mx\frac{\pi}{a}x'_n\right)-\sin\left(mx\frac{\pi}{a}x'_{n-1}\right)\right)\right)-$$

$$-\frac{1}{\left(1-C_m^2\right)\left(x'_n-x'_{n-1}\right)}\left(\frac{jk_{my}}{N_m}x'_{n-1}-C_m\frac{mx\frac{\pi}{a}}{N_m}\cdot x'_{n-1}\right)\frac{-1}{mx\frac{\pi}{a}}\left(\cos\left(mx\frac{\pi}{a}x'_n\right)-\cos\left(mx\frac{\pi}{a}x'_{n-1}\right)\right)$$

For the descending ramp:

$$I_{BX}^{EY}(p=TM)=\int_{x'}\bar{X}_m^{(p)}(x')\cdot\hat{y}\cdot f(x')dx'=\int_{x'}\frac{e_{mx}^{Y^{TM}*}(x)-C_m\cdot e_{mx}^{Y^{TE}*}(x)}{1-C_m^2}\cdot\frac{x'_{n+1}-x'}{x'_{n+1}-x'_n}dx'=$$

$$=\int_{x'_n}^{x'_{n+1}}\frac{1}{1-C_m^2}\left(\frac{jk_{my}}{N_m}\sin\left(mx\frac{\pi}{a}x\right)-C_m\cdot\frac{mx\frac{\pi}{a}}{N_m}\sin\left(mx\frac{\pi}{a}x\right)\right)\cdot\frac{x'_{n+1}-x'}{x'_{n+1}-x'_n}dx'=$$

$$=-\frac{1}{\left(1-C_m^2\right)\left(x'_{n+1}-x'_n\right)}\left(\frac{mx\frac{\pi}{a}}{N_m}x'_{n+1}-C_m\frac{jk_{my}}{N_m}\cdot x'_{n+1}\right)\frac{-1}{mx\frac{\pi}{a}}\left(\cos\left(mx\frac{\pi}{a}x'_{n+1}\right)-\cos\left(mx\frac{\pi}{a}x'_n\right)\right)-$$

$$-\frac{1}{\left(1-C_m^2\right)\left(x'_{n+1}-x'_n\right)}\left(\frac{mx\frac{\pi}{a}}{N_m}-C_m\frac{jk_{my}}{N_m}\right)$$

$$\left(\frac{-x'_{n+1}}{mx\frac{\pi}{a}}\cos\left(mx\frac{\pi}{a}x'_{n+1}\right)+\frac{x'_n}{mx\frac{\pi}{a}}\cos\left(mx\frac{\pi}{a}x'_n\right)+\frac{1}{mx^2\frac{\pi^2}{a^2}}\left(\sin\left(mx\frac{\pi}{a}x'_{n+1}\right)-\sin\left(mx\frac{\pi}{a}x'_n\right)\right)\right)-$$

$$I_{BX}^{EY}(p=TE)=\int_{x'}\bar{X}_m^{(p)}(x')\cdot\hat{y}\cdot f(x')dx'=\int_{x'}\frac{e_{mx}^{Y^{TE}*}(x)-C_m\cdot e_{mx}^{Y^{TM}*}(x)}{1-C_m^2}\cdot\frac{x'_{n+1}-x'}{x'_{n+1}-x'_n}dx'=$$

$$=\int_{x'_n}^{x'_{n+1}}\frac{1}{1-C_m^2}\left(\frac{mx\frac{\pi}{a}}{N_m}\sin\left(mx\frac{\pi}{a}x\right)-C_m\cdot\frac{jk_{my}}{N_m}\sin\left(mx\frac{\pi}{a}x\right)\right)\cdot\frac{x'_{n+1}-x'}{x'_{n+1}-x'_n}dx'=$$

$$=-\frac{1}{\left(1-C_m^2\right)\left(x'_{n+1}-x'_n\right)}\left(\frac{jk_{my}}{N_m}x'_{n+1}-C_m\frac{mx\frac{\pi}{a}}{N_m}\cdot x'_{n+1}\right)\frac{-1}{mx\frac{\pi}{a}}\left(\cos\left(mx\frac{\pi}{a}x'_{n+1}\right)-\cos\left(mx\frac{\pi}{a}x'_n\right)\right)-$$

$$-\frac{1}{\left(1-C_m^2\right)\left(x'_{n+1}-x'_n\right)}\left(\frac{jk_{my}}{N_m}-C_m\cdot\frac{mx\frac{\pi}{a}}{N_m}\right)$$

$$\left(\frac{-x'_{n+1}}{mx\frac{\pi}{a}}\cos\left(mx\frac{\pi}{a}x'_{n+1}\right)+\frac{x'_n}{mx\frac{\pi}{a}}\cos\left(mx\frac{\pi}{a}x'_n\right)+\frac{1}{mx^2\frac{\pi^2}{a^2}}\left(\sin\left(mx\frac{\pi}{a}x'_{n+1}\right)-\sin\left(mx\frac{\pi}{a}x'_n\right)\right)\right)$$